Precision Cold Forming Modelling,

Interfacial Thermal Parameter Investigation

and Tool Design Optimisation

Volume Two

By

XUESHENG CHEN

This thesis is submitted to the Department of Design, Manufacturing Engineering and Management, University of Strathclyde for the degree of Doctor of Philosophy

Glasgow, January 2002

Contents

1. Diagrams for Chapter One 1
2. Diagrams for Chapter Two 36
3. Diagrams for Chapter Three 59
4. Diagrams for Chapter Four 114
5. Diagrams for Chapter Five 150
6. Diagrams for Chapter Six 182

Diagrams for Chapter One

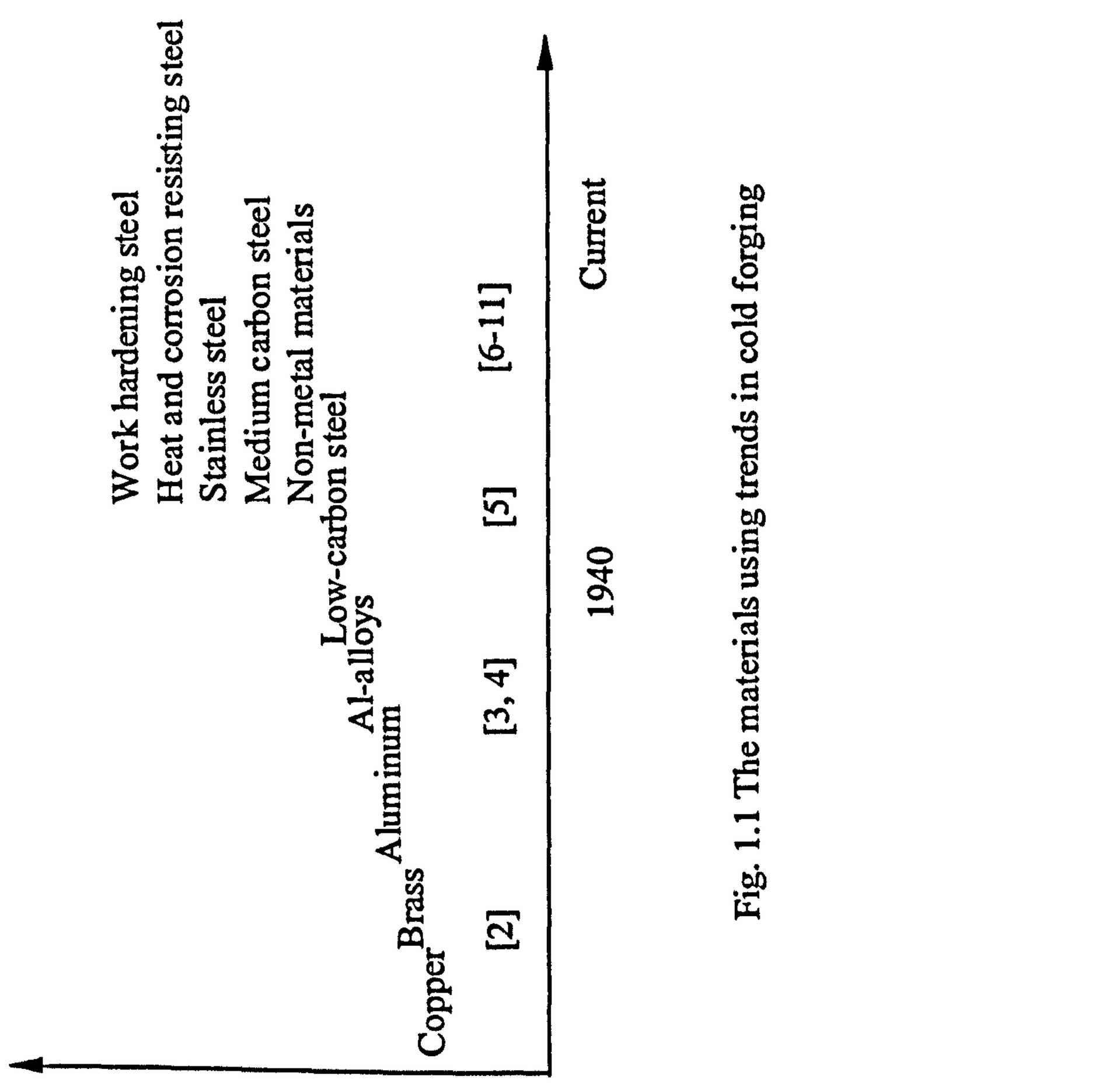

Fig. 1.1 The materials using trends in cold forging

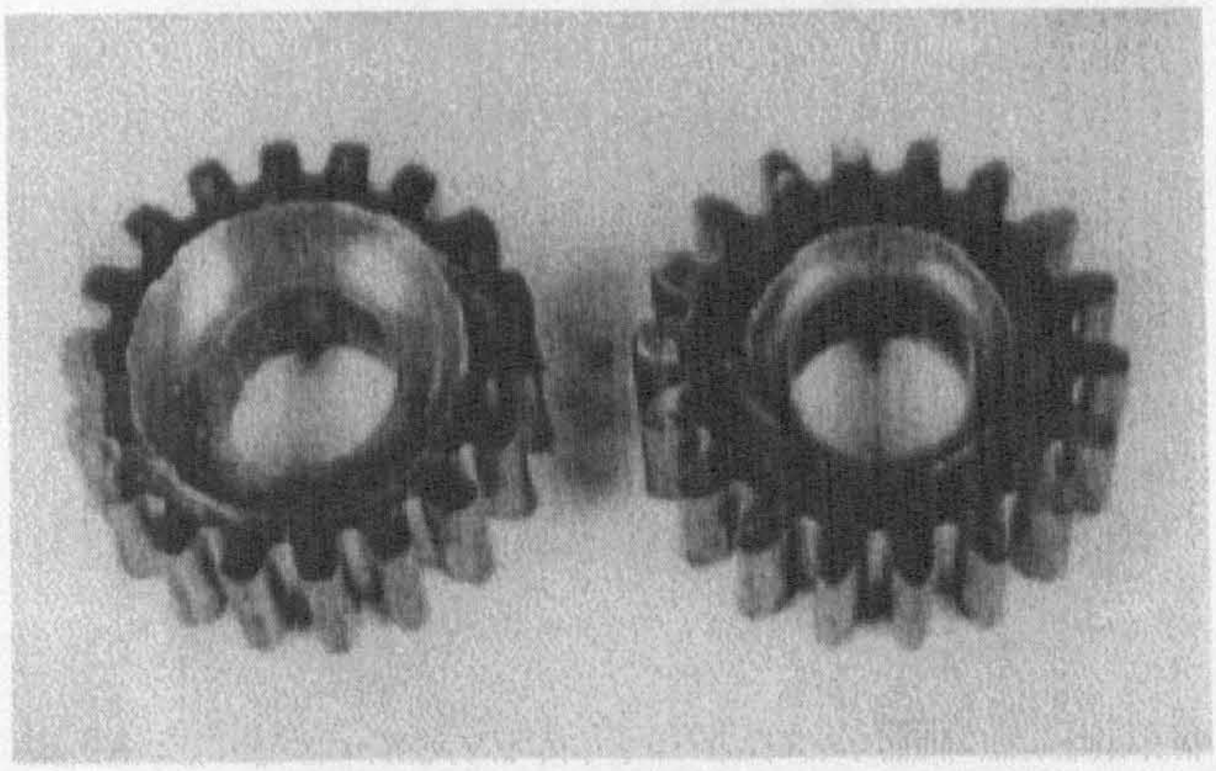

(a)[12]

The first step The second step

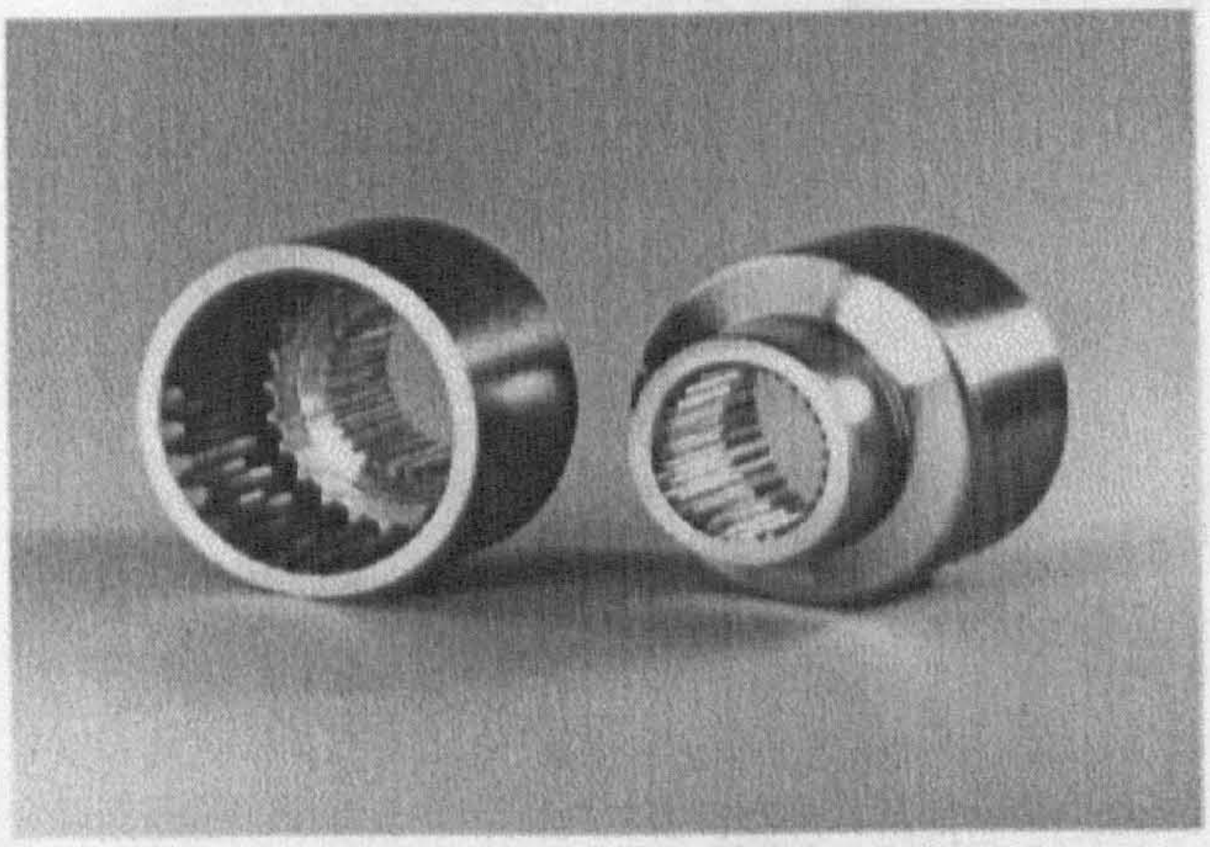

(b)[13]

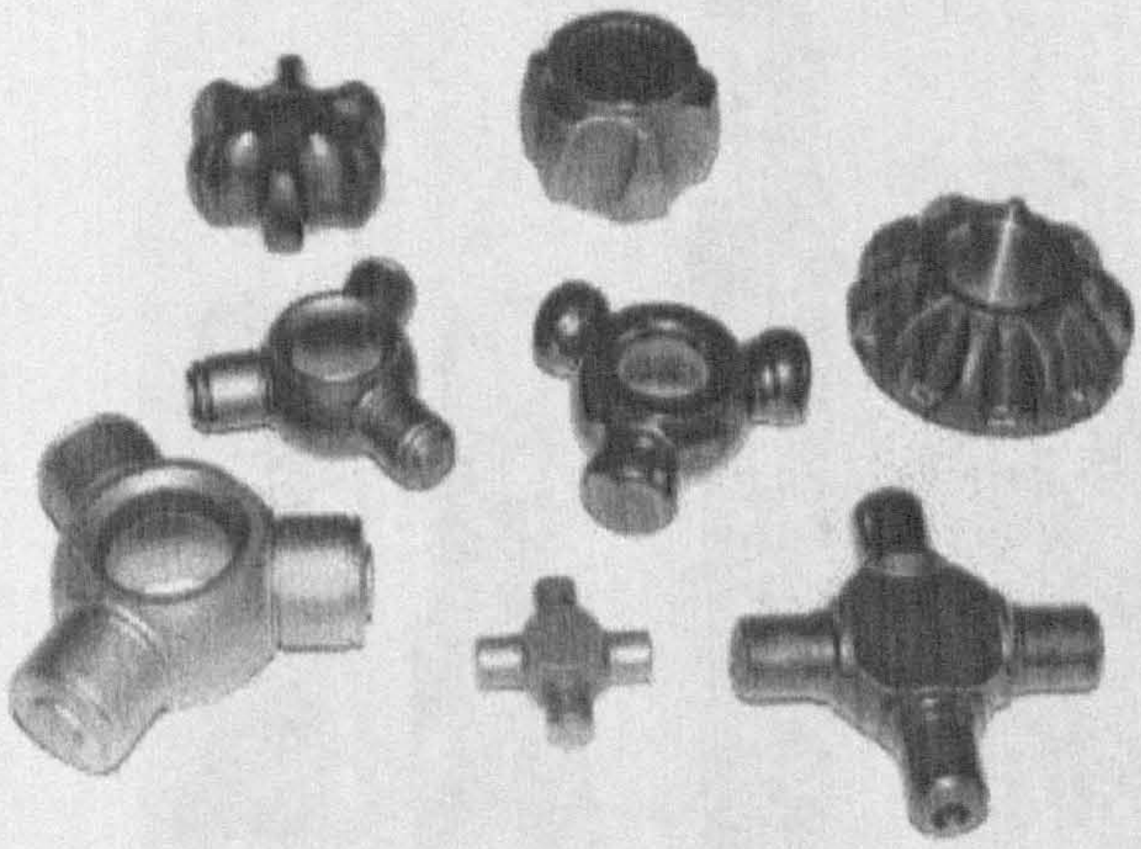

(c)[14]

Fig. 1.2 The typical precision cold forgings

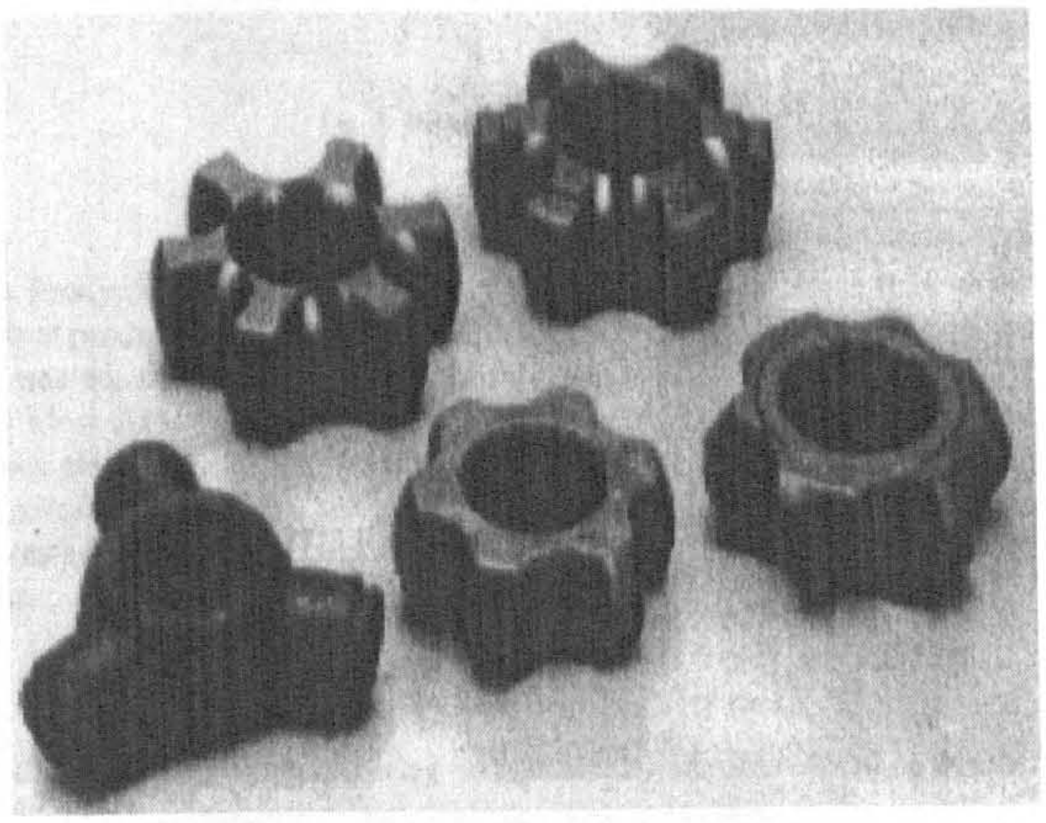

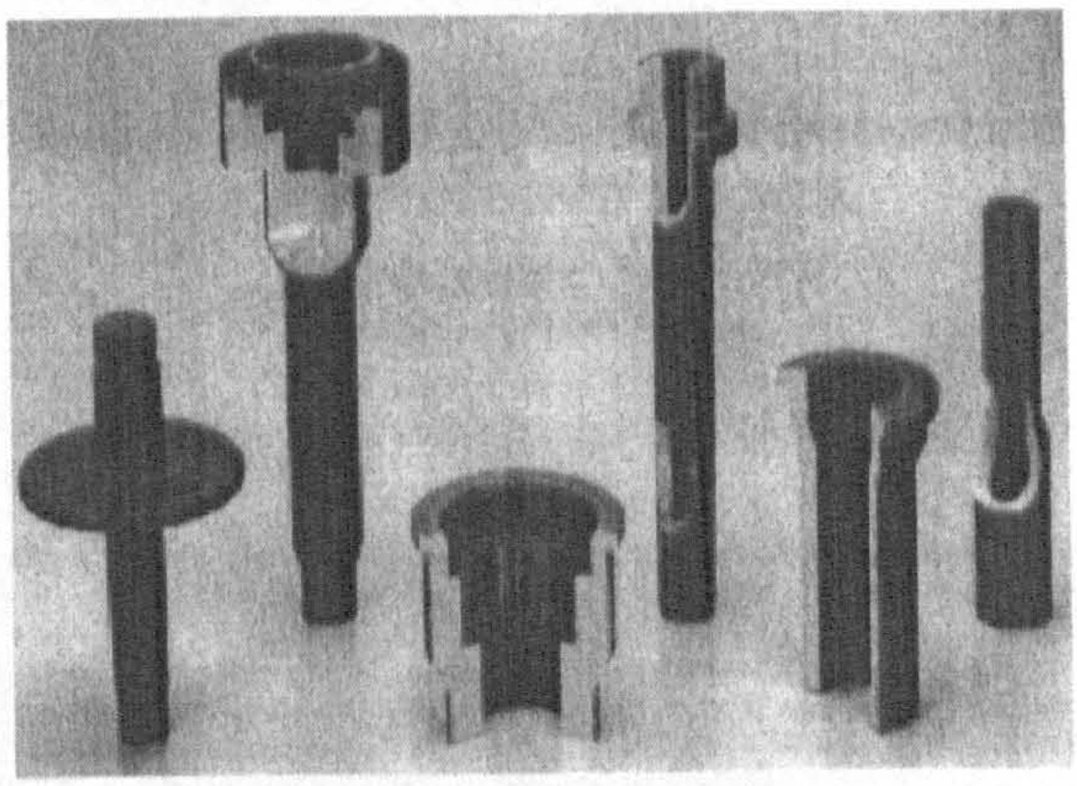

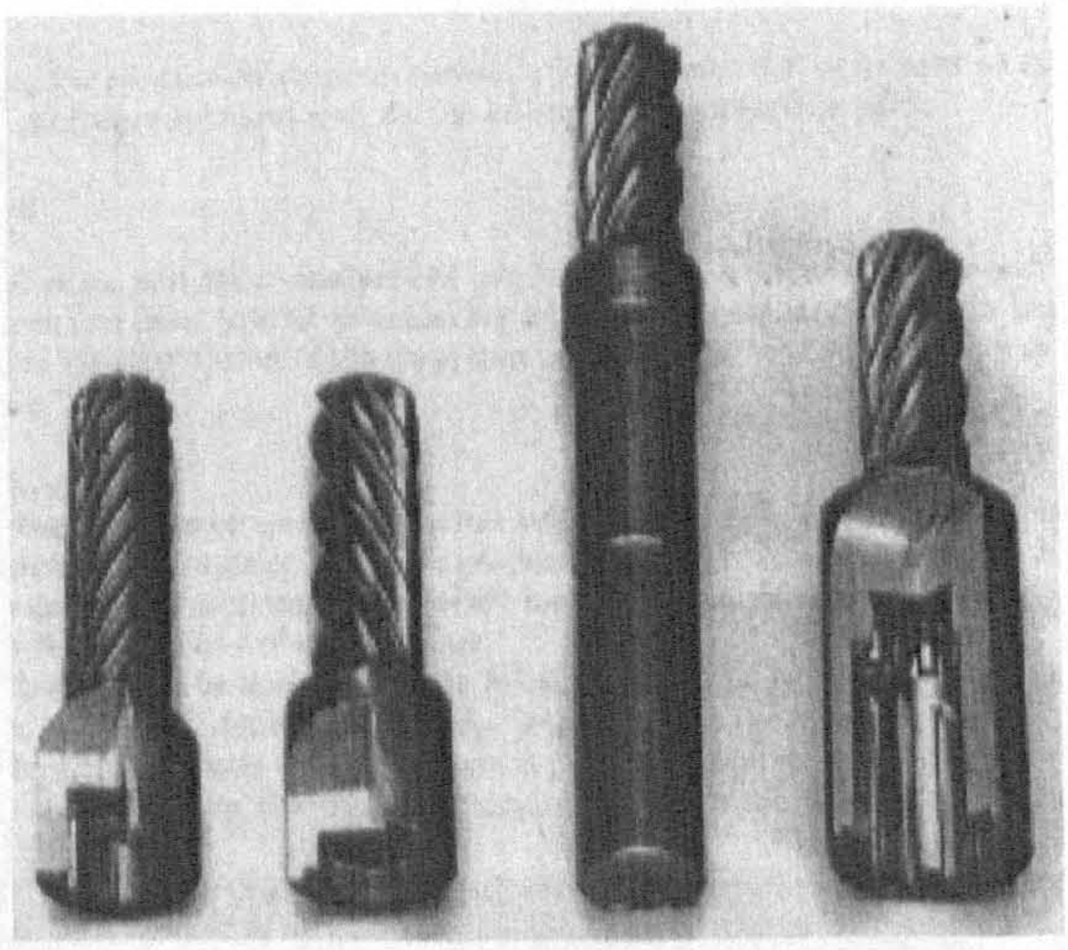

Fig. 1.3 Typical precision cold forgings [26]

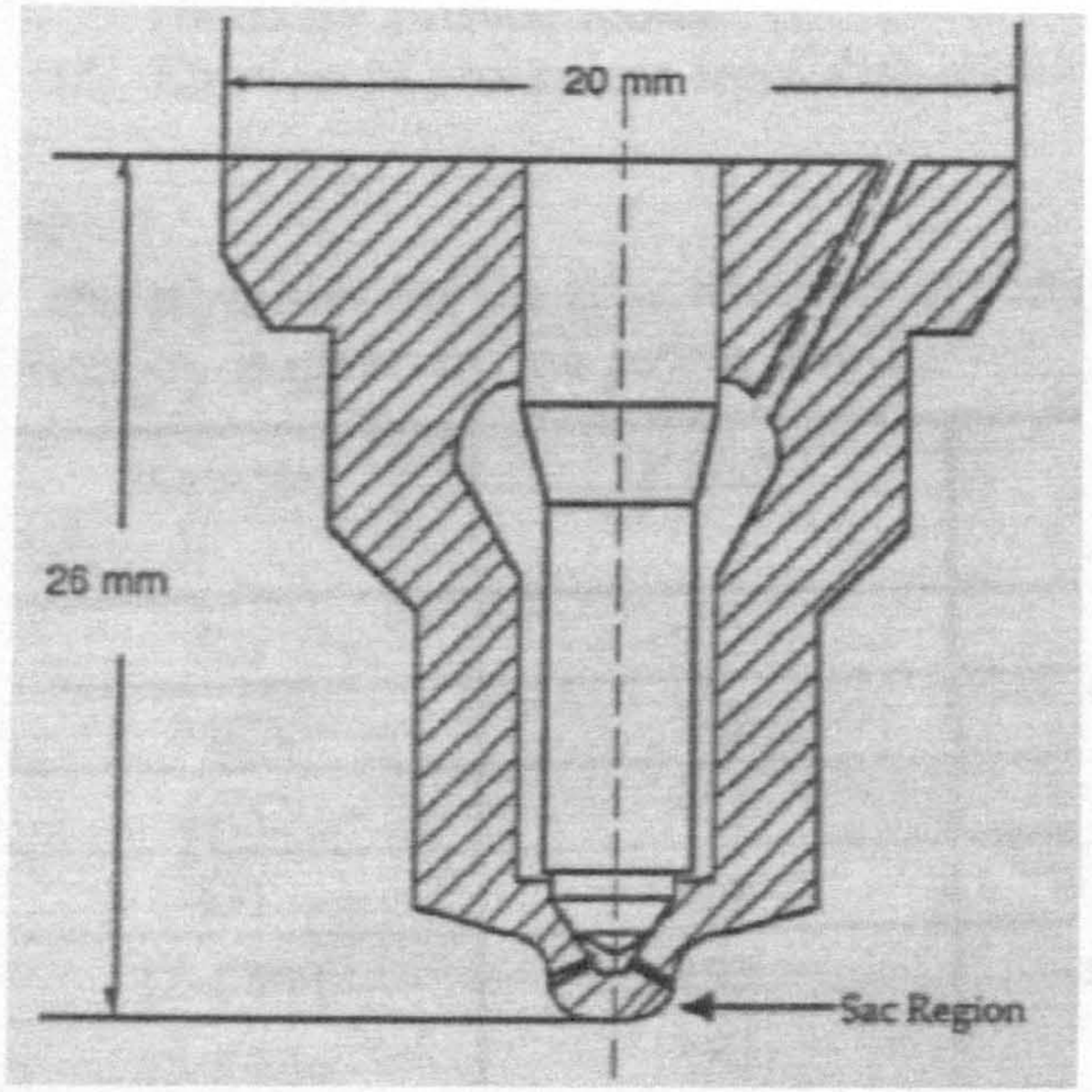

(a) Section view of fuel injector nozzle [9]

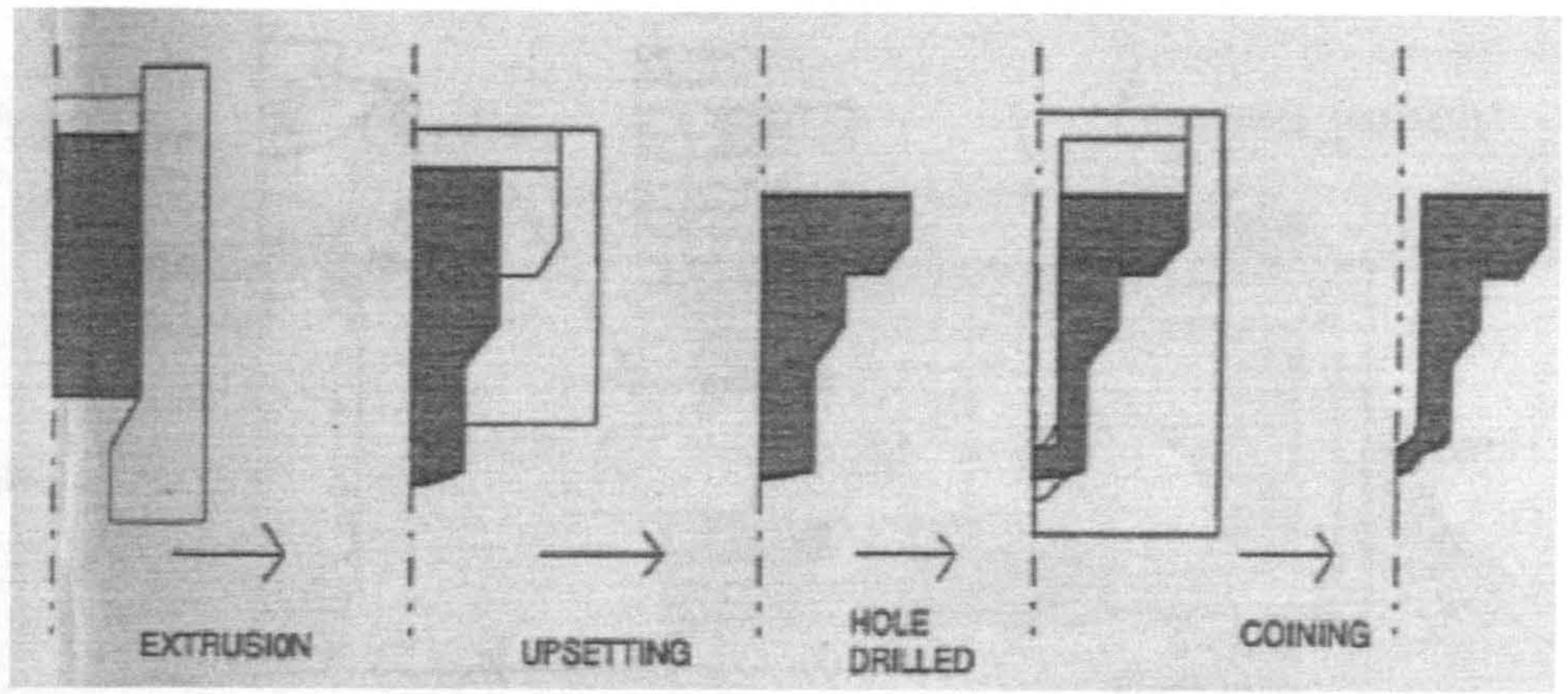

(b) Applied forging sequences [9]

Fig. 1.4 An injection nozzle and the forging sequences

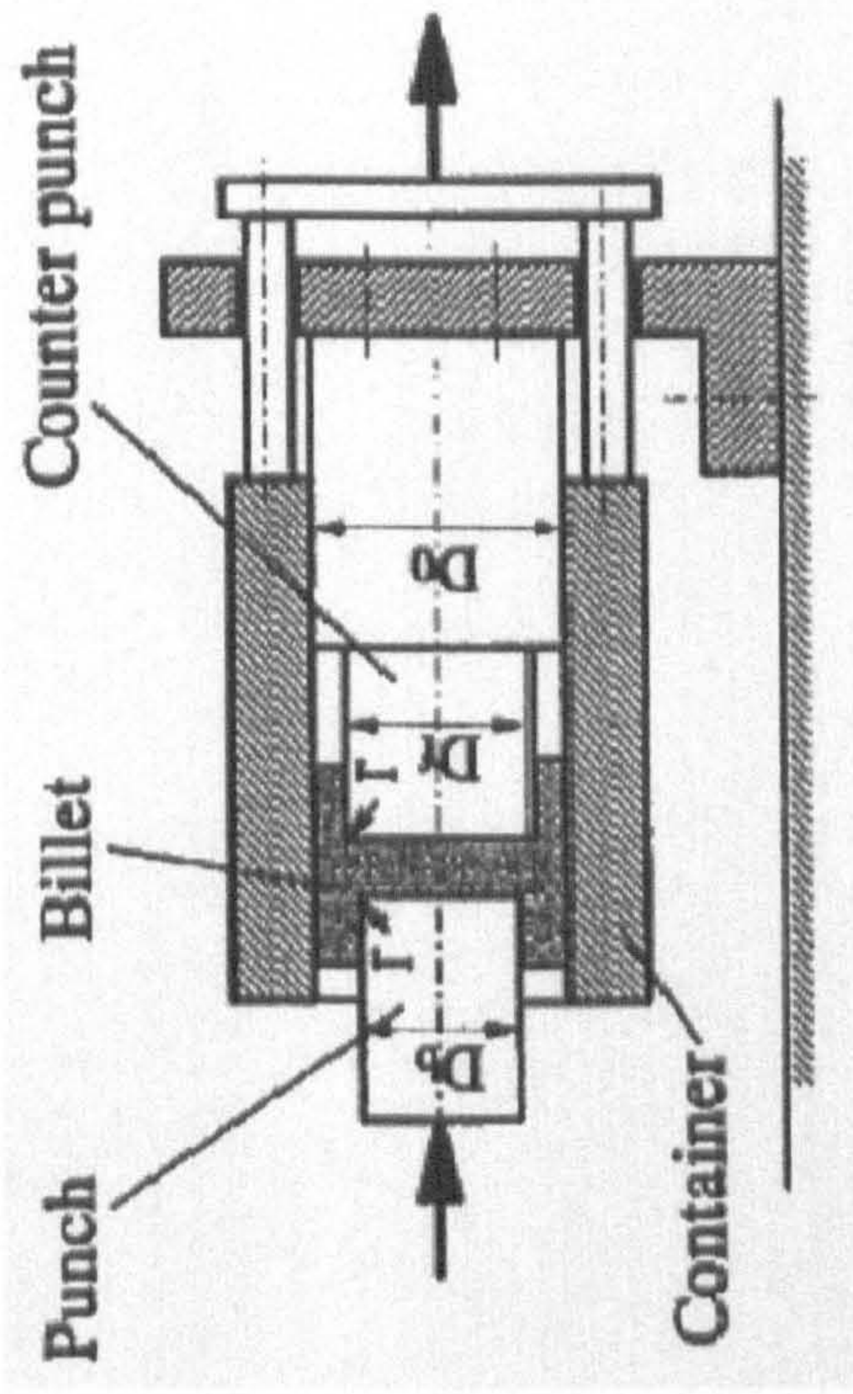

(b)

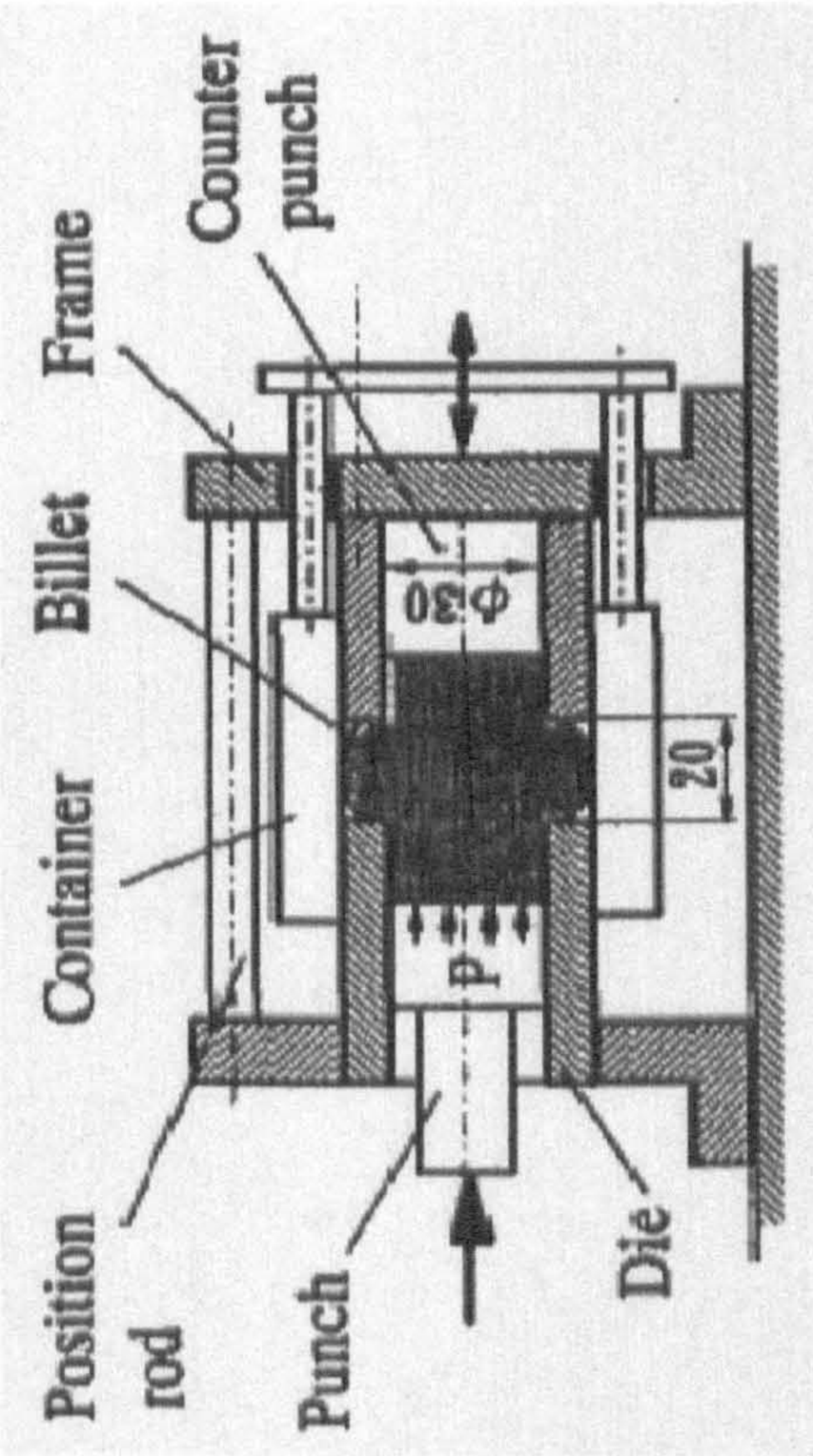

(a)

Fig. 1.5 Conceptual diagram of extrusion with movable container [27]

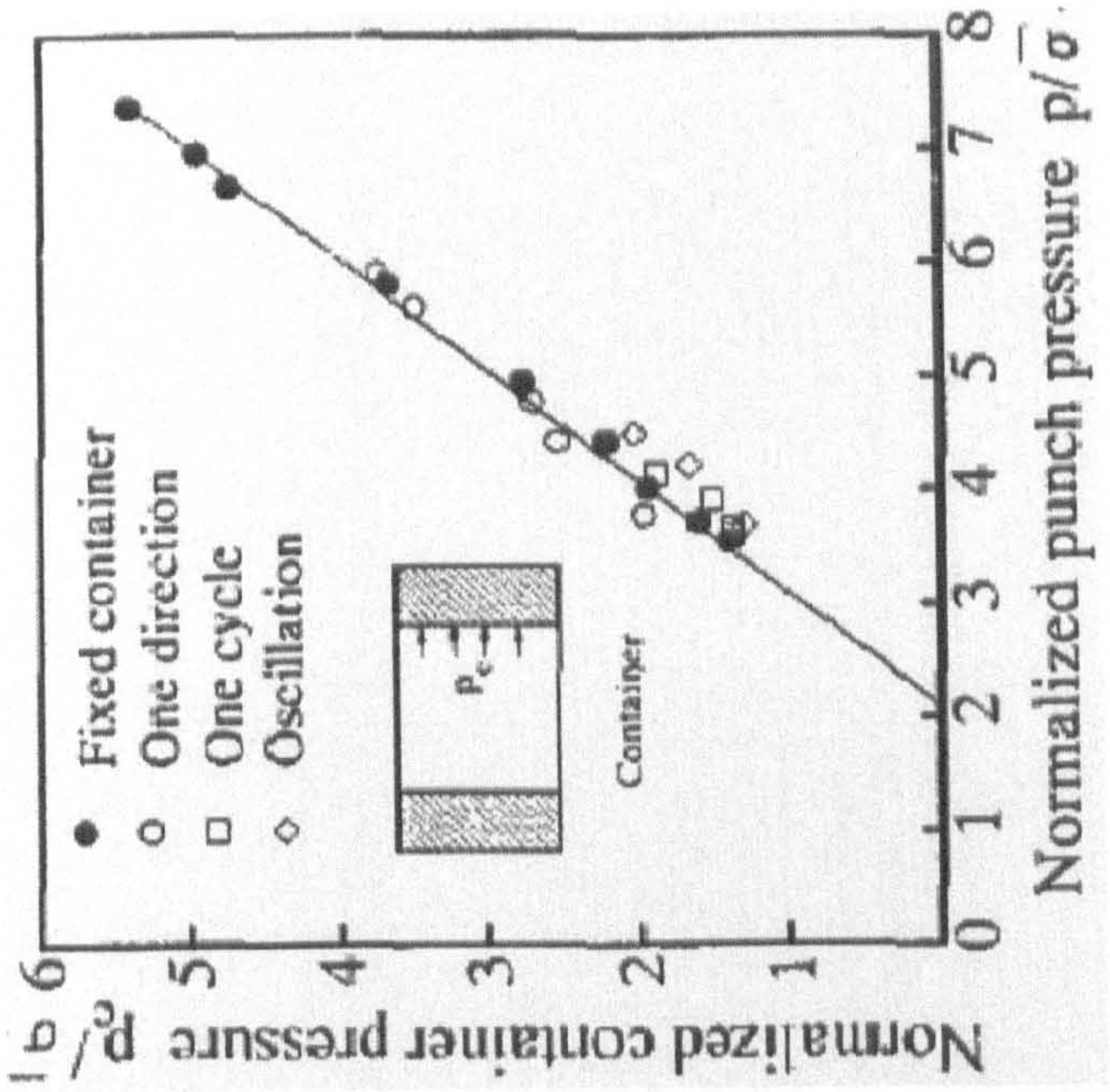

(b) Backward/forward can-can extrusion

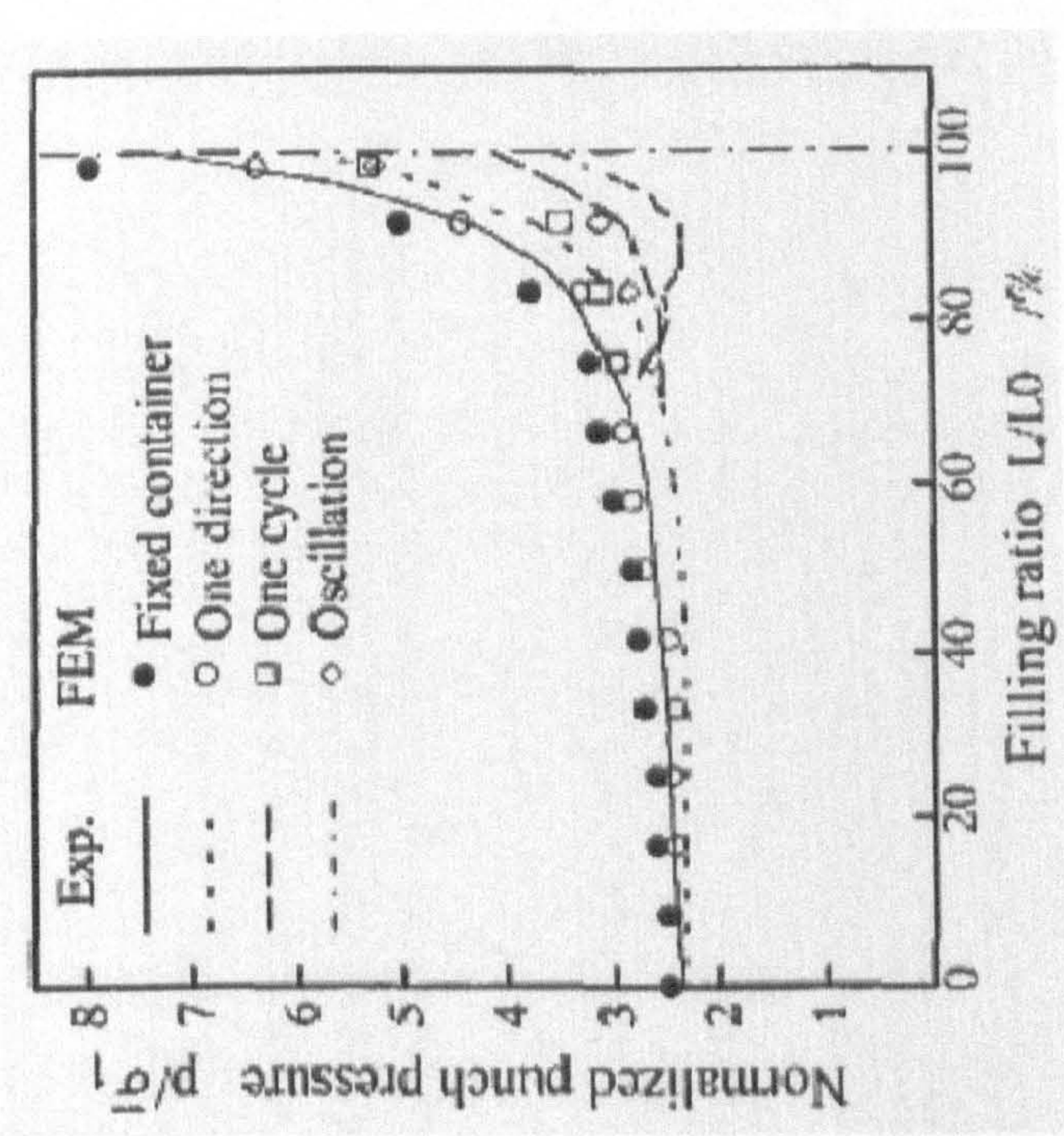

(a) Radial extrusion

Fig. 1.6 The forging force reduction by movable container [27]

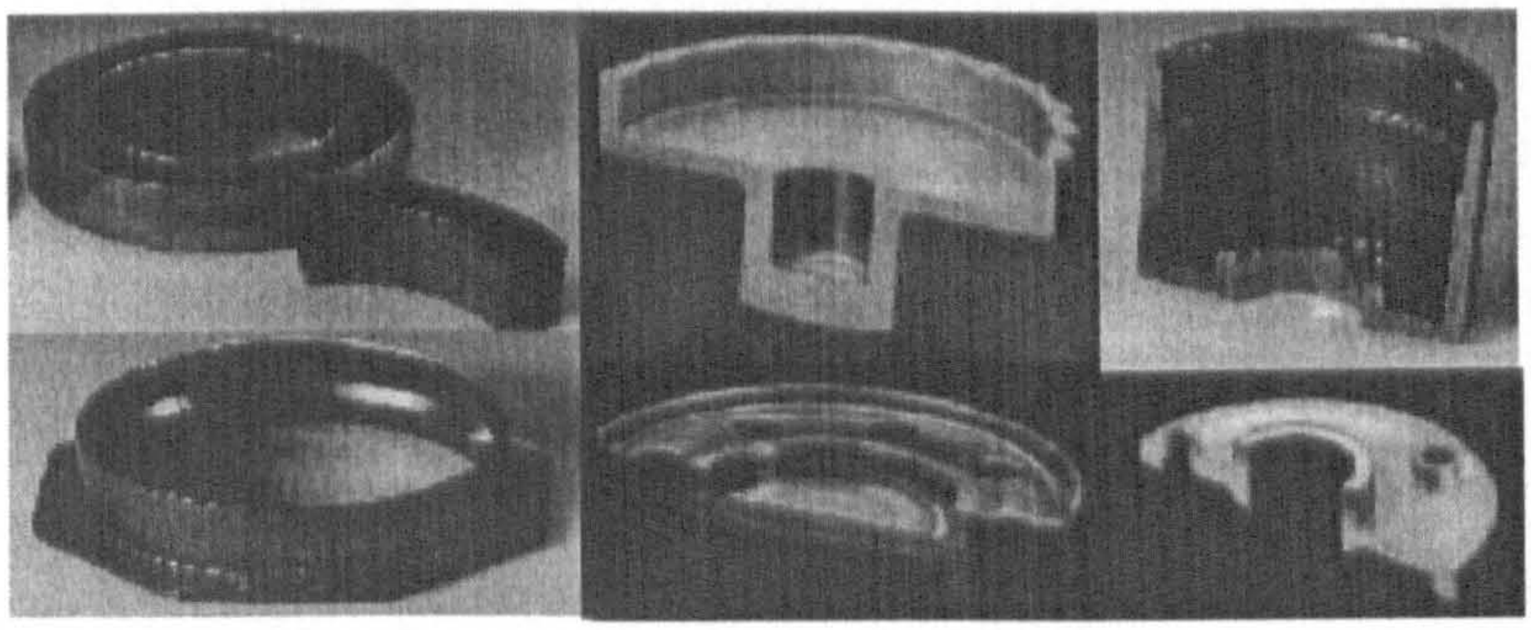

(a) Components by sheet forming and cold forming [28]

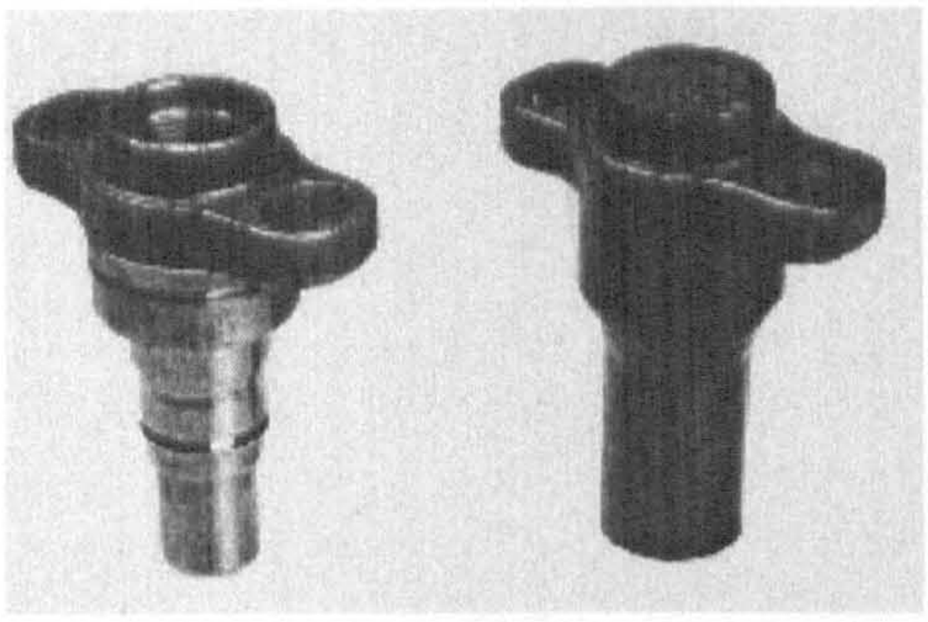

(b) Flanged cylinder after forming and after machining [13]

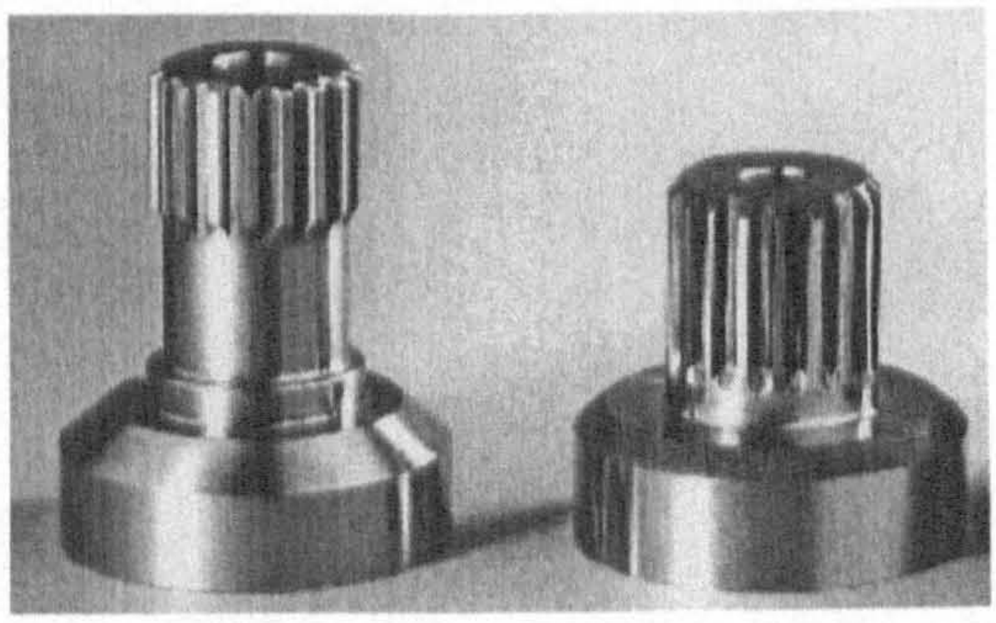

(c) Link shaft original (left) and forged (right) [13]

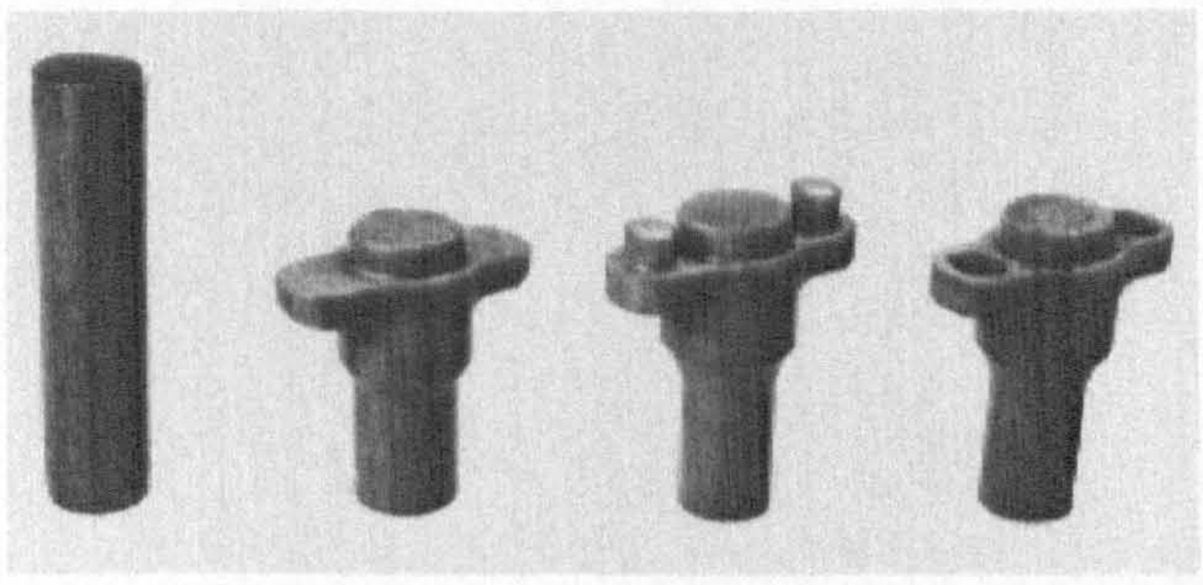

(d) Forming steps of flanged cylinder [13]

Fig. 1.7 Components by sheet-forming and cold forming

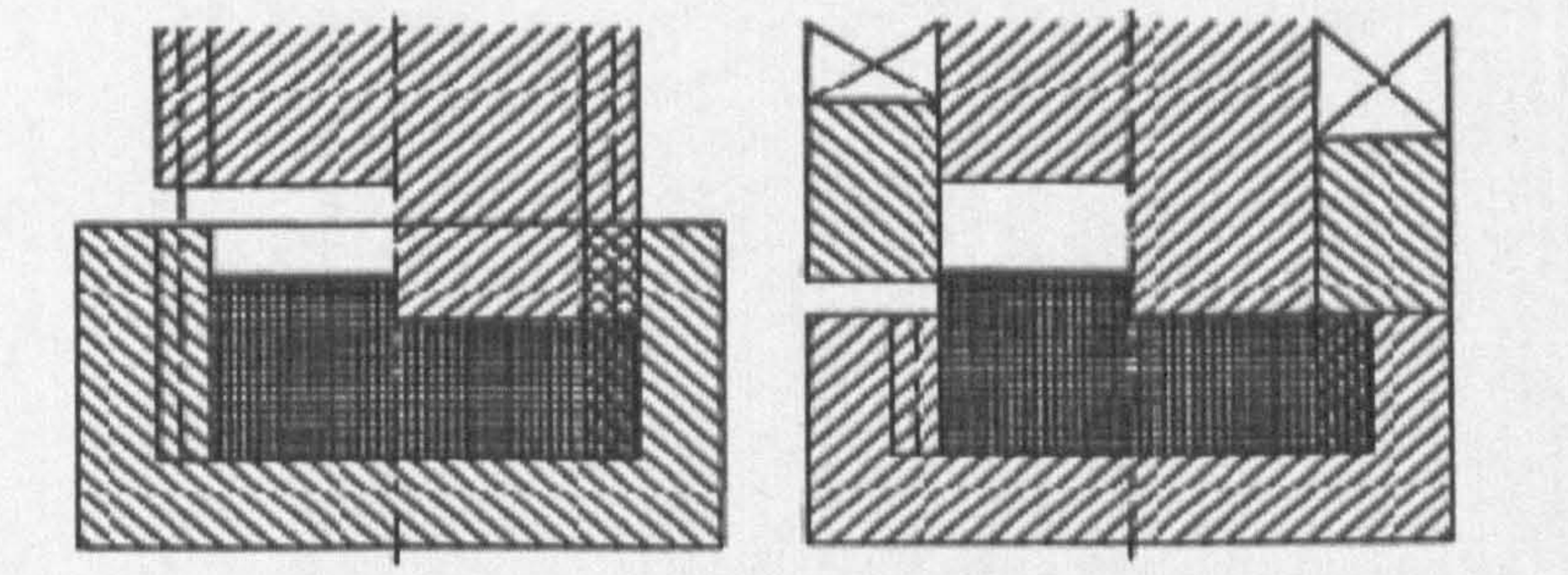

(a) Guiding type

(b) Clamping type

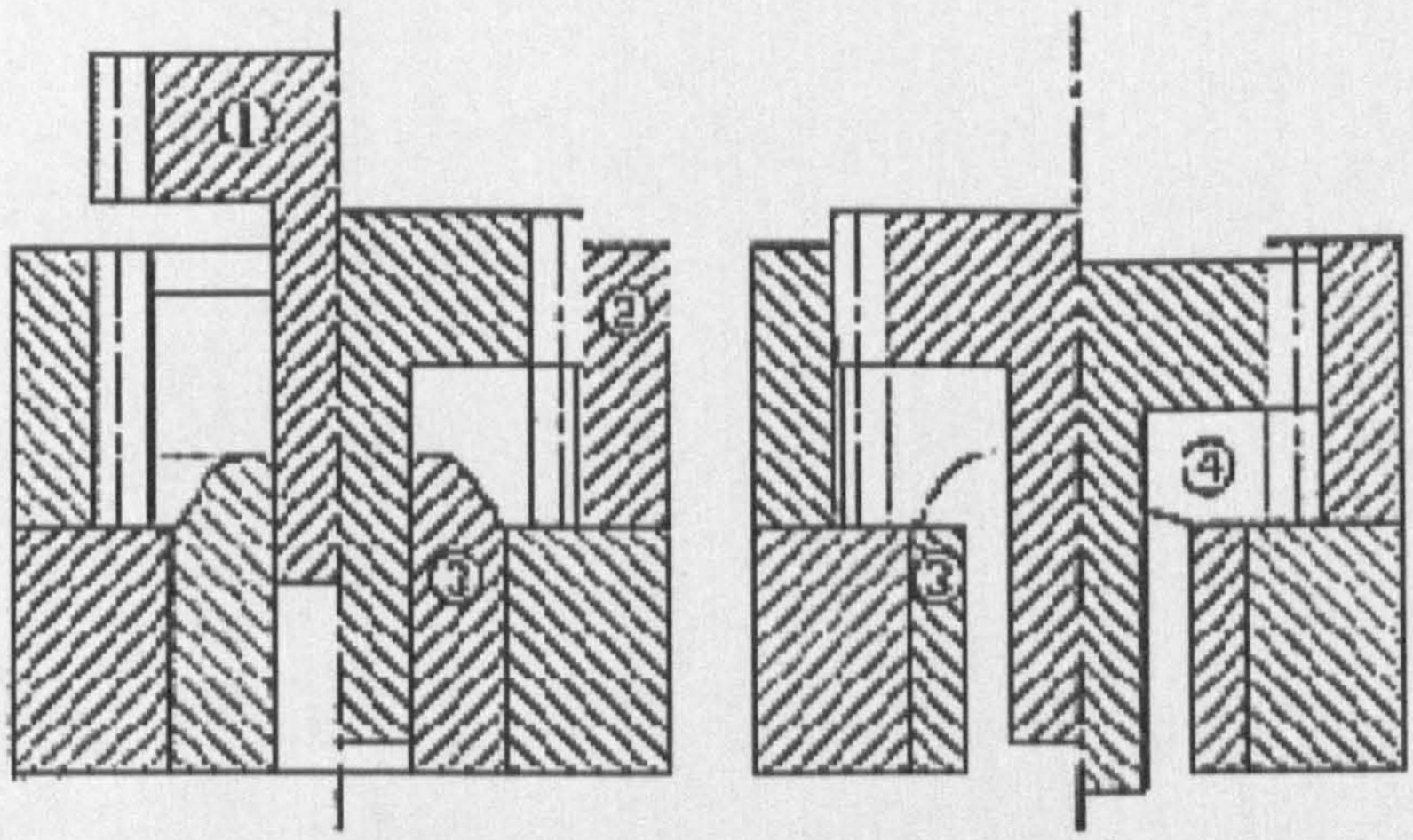

(c) The two-step divided flow method

1 Toothed punch 2 Toothed die 3 Ejector 4 Test material

Fig. 1.8 Die design schematics of cold forging spur gears [12]

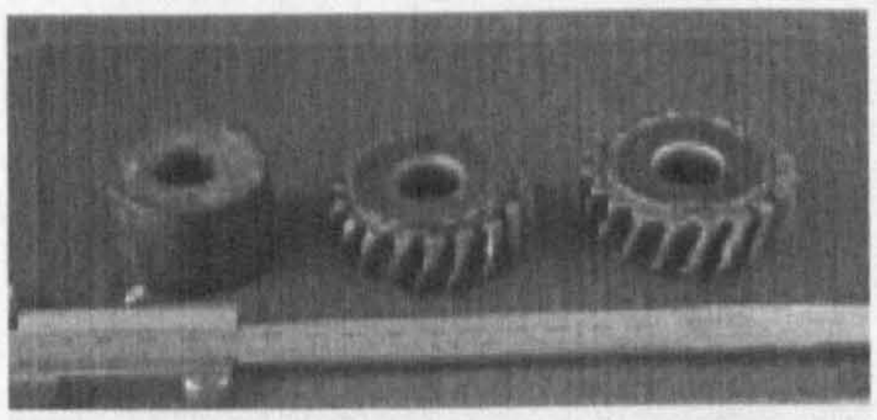

(a) Billet and product [29]

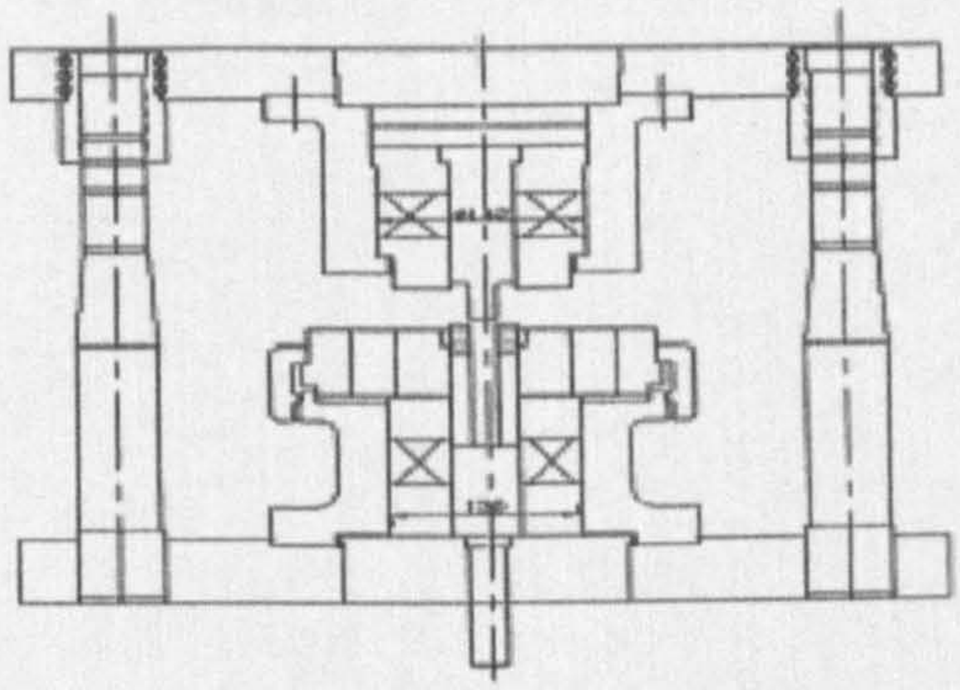

(b) Tooling configuration

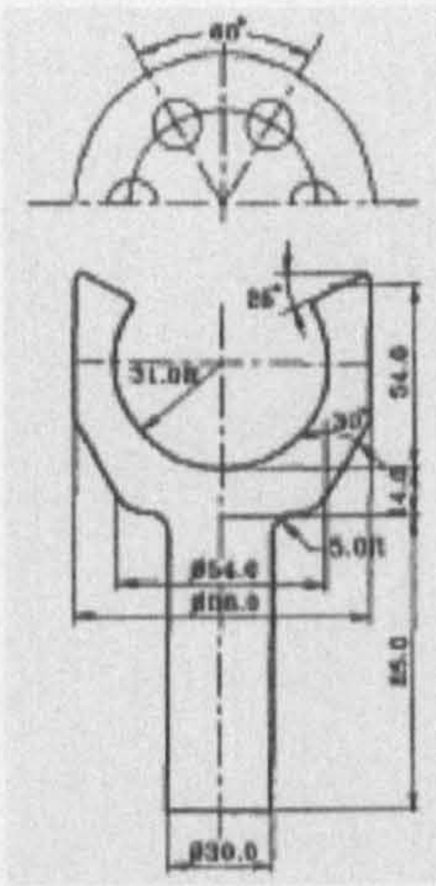

(c) Product [30]

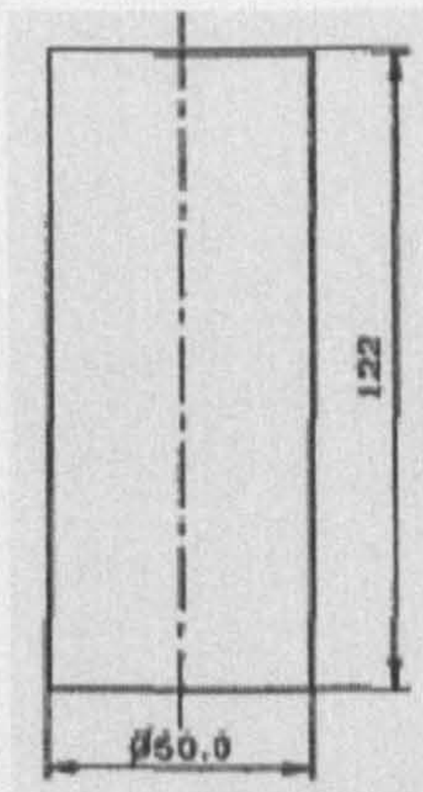

(d) Billet [30]

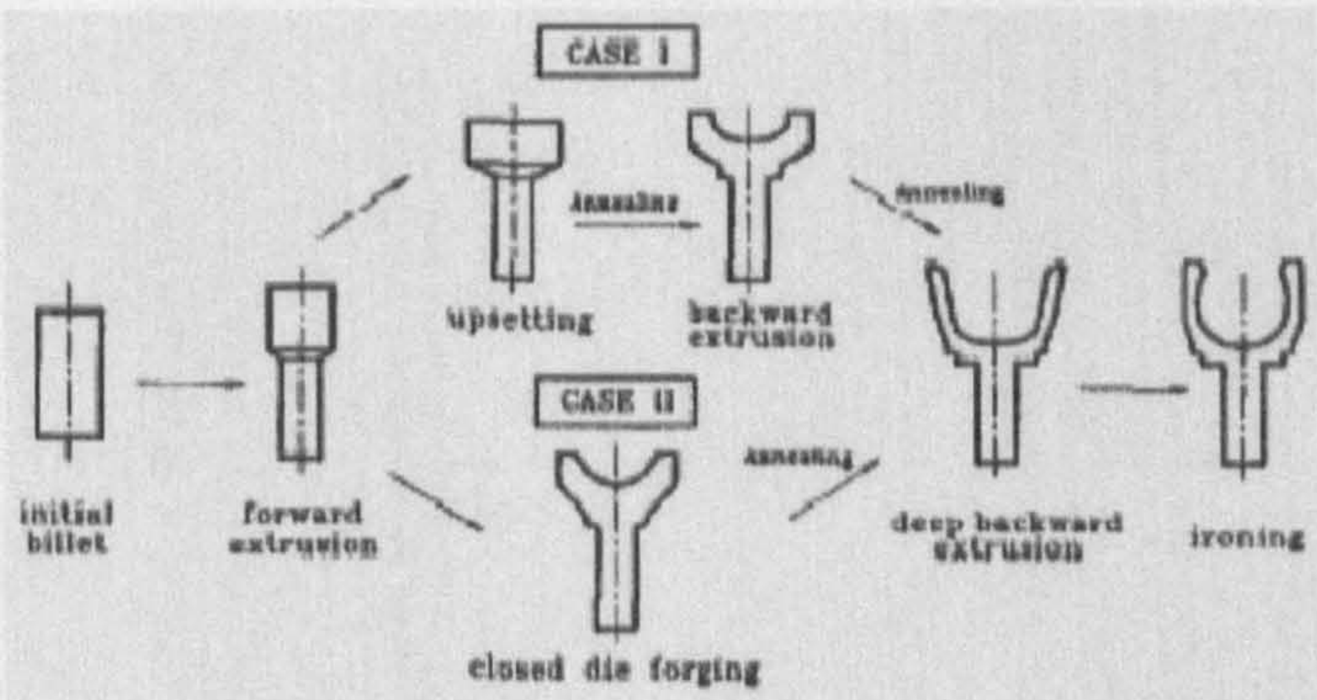

(e) Forging sequence [30]

Fig. 1.9 Cold forging of CVJ housing and helical gear

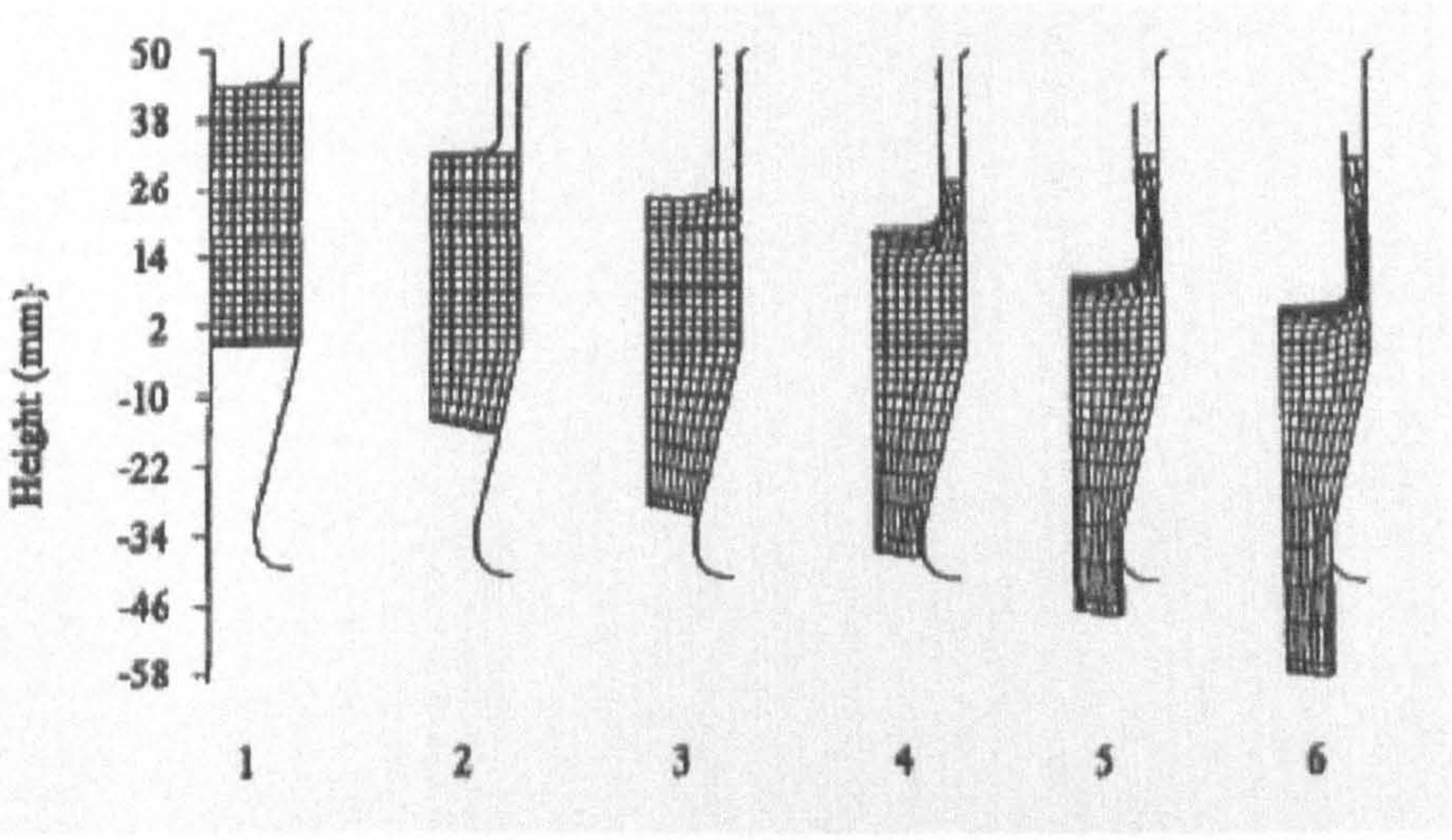

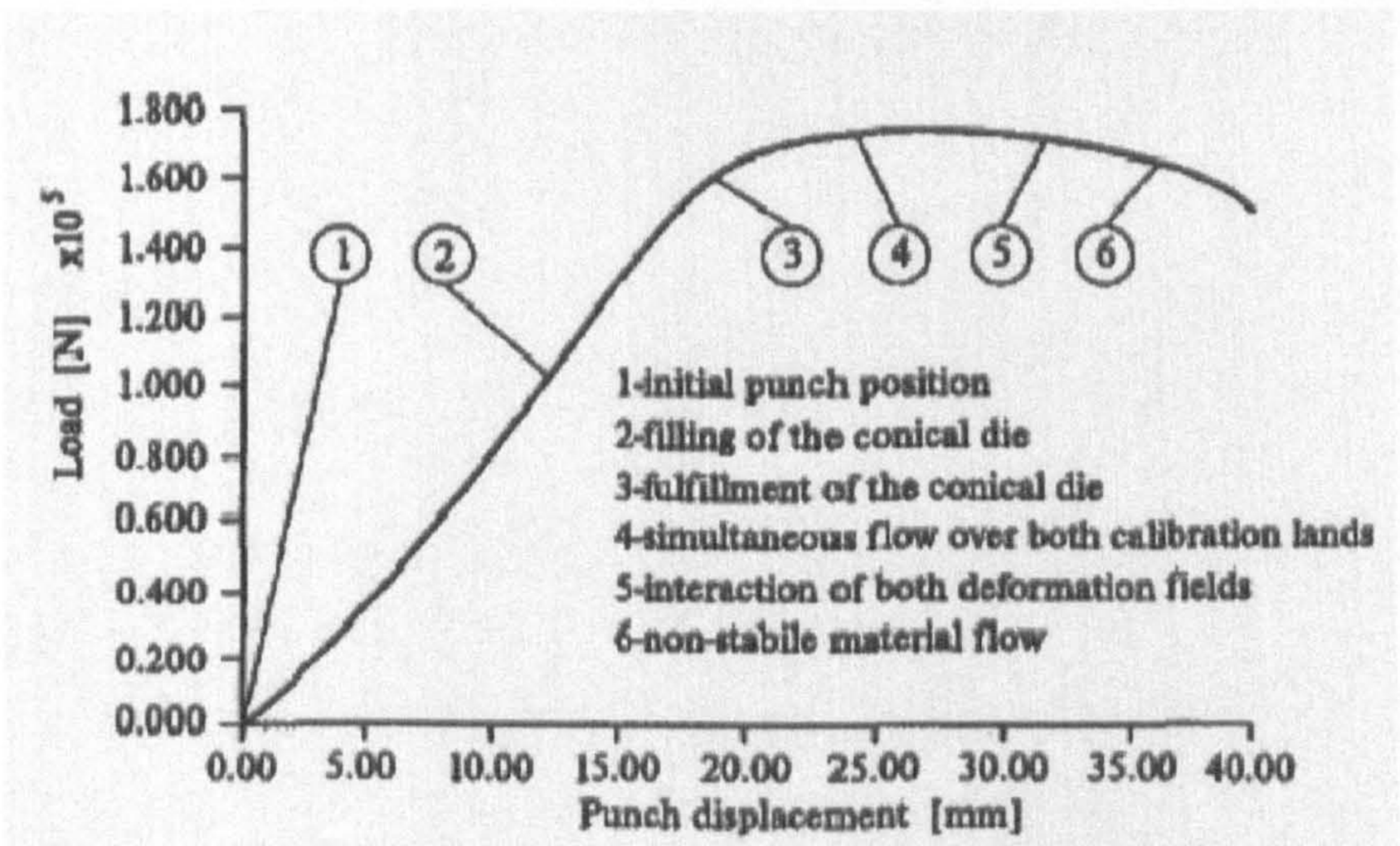

Fig. 1.10 Forging force and material divided flow[31]

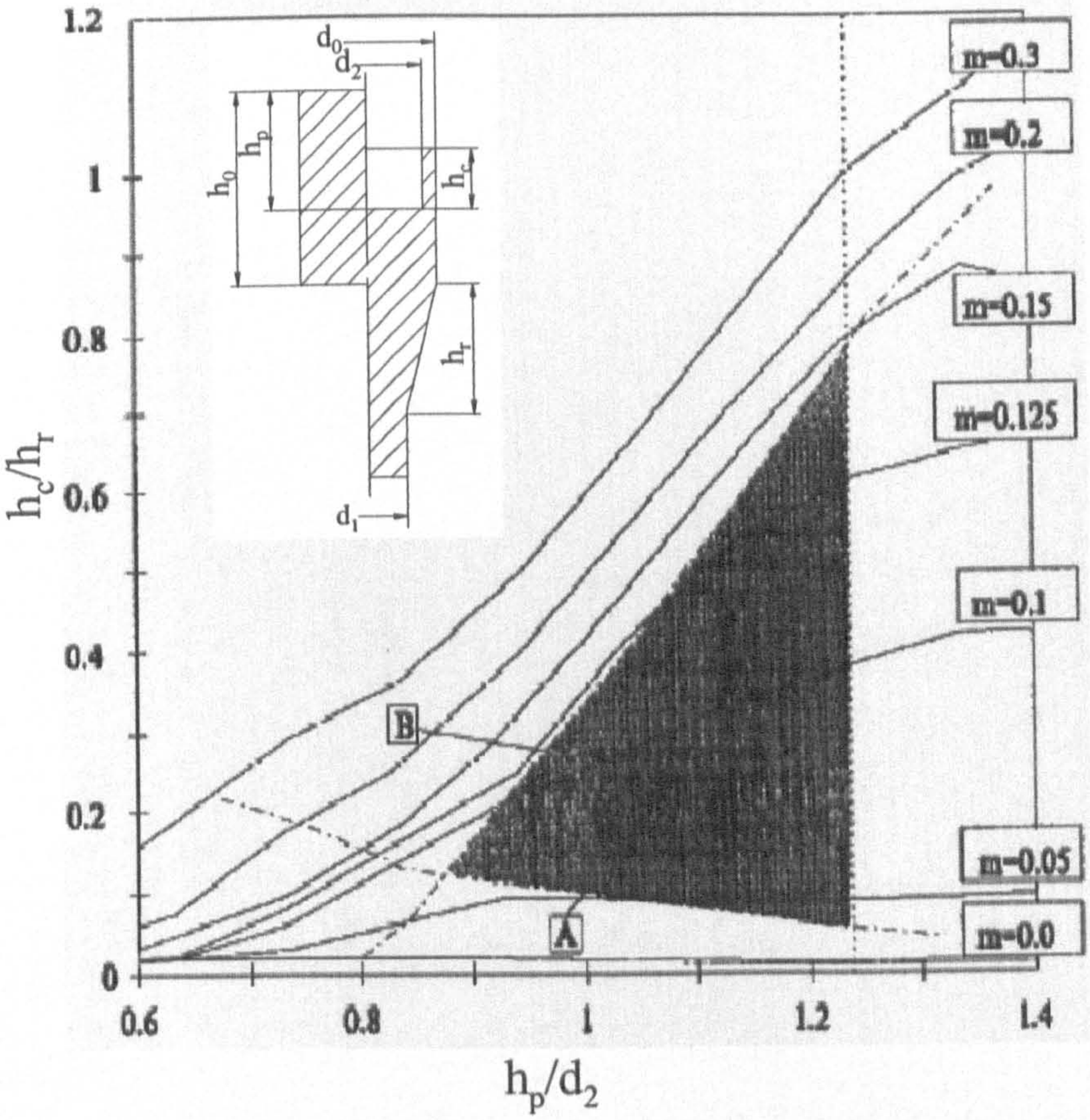

Fig. 1.11 Calibration curve for forward/backward extrusion process design[31]

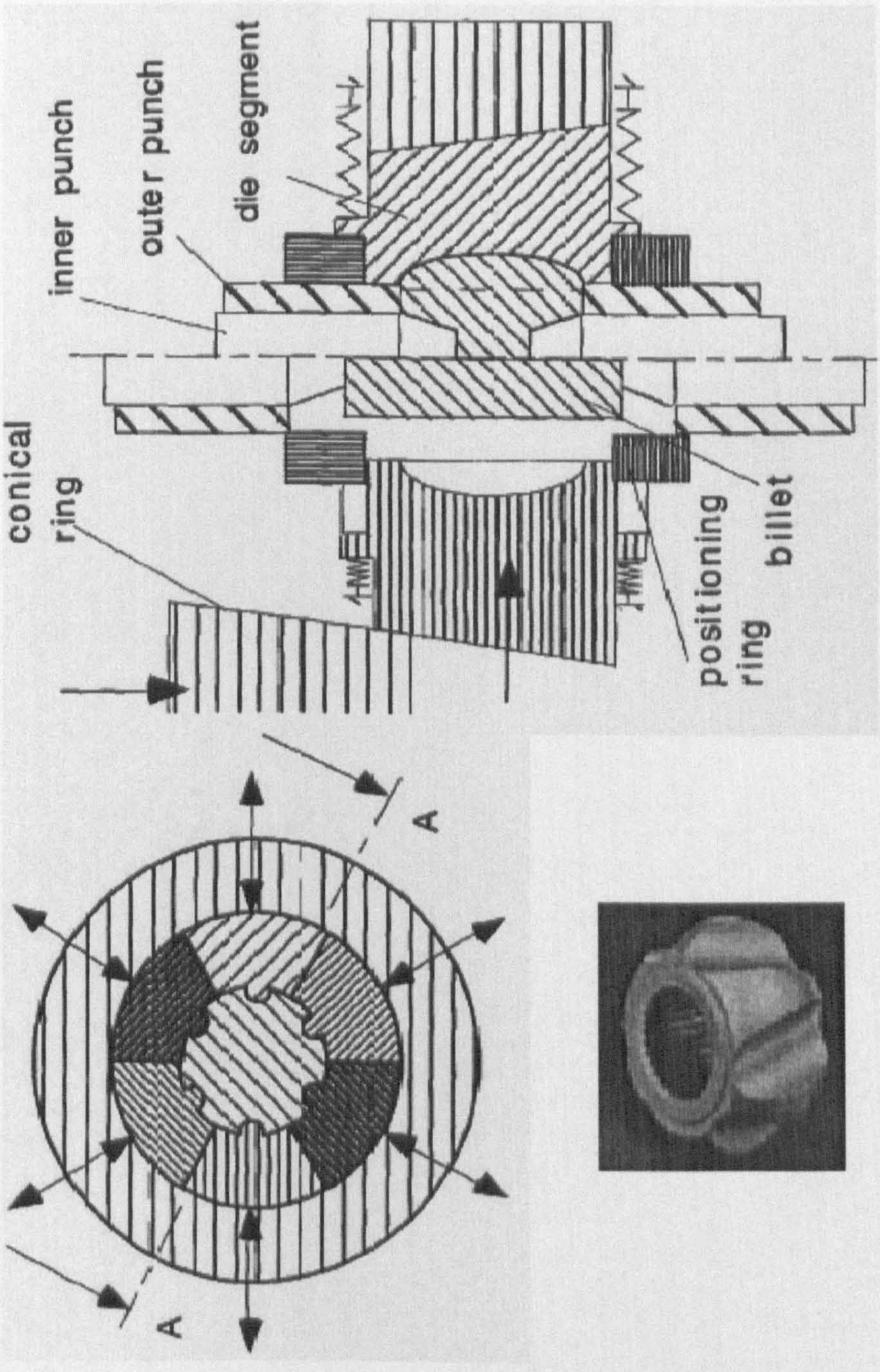

Fig. 1.12 The inner race and the tooling [17]

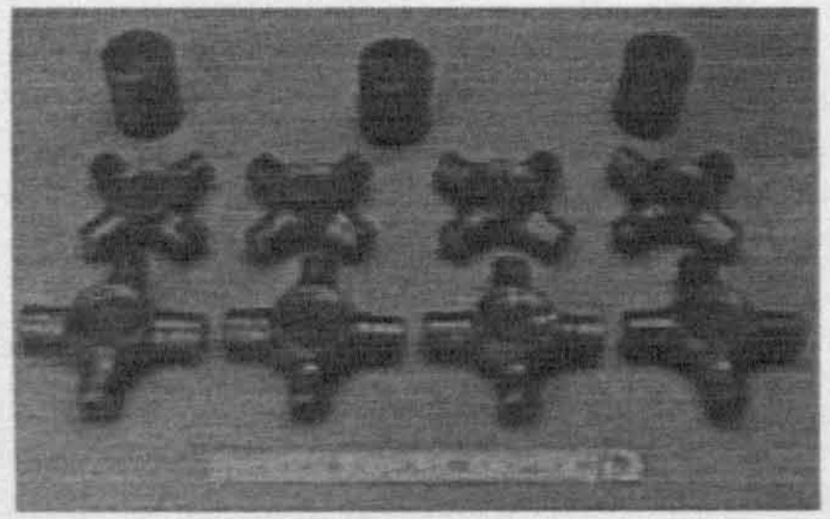

(a) Cross journals

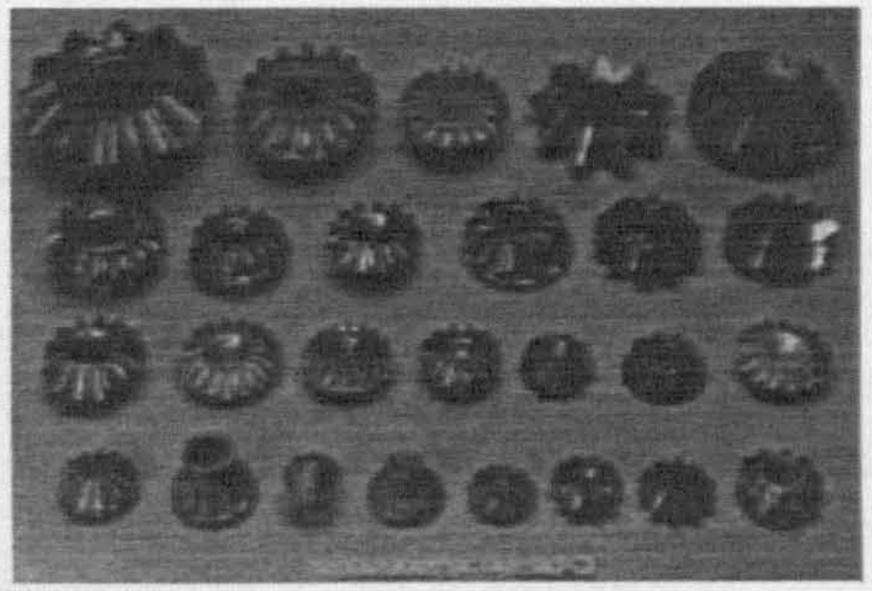

(c) Bevel gears

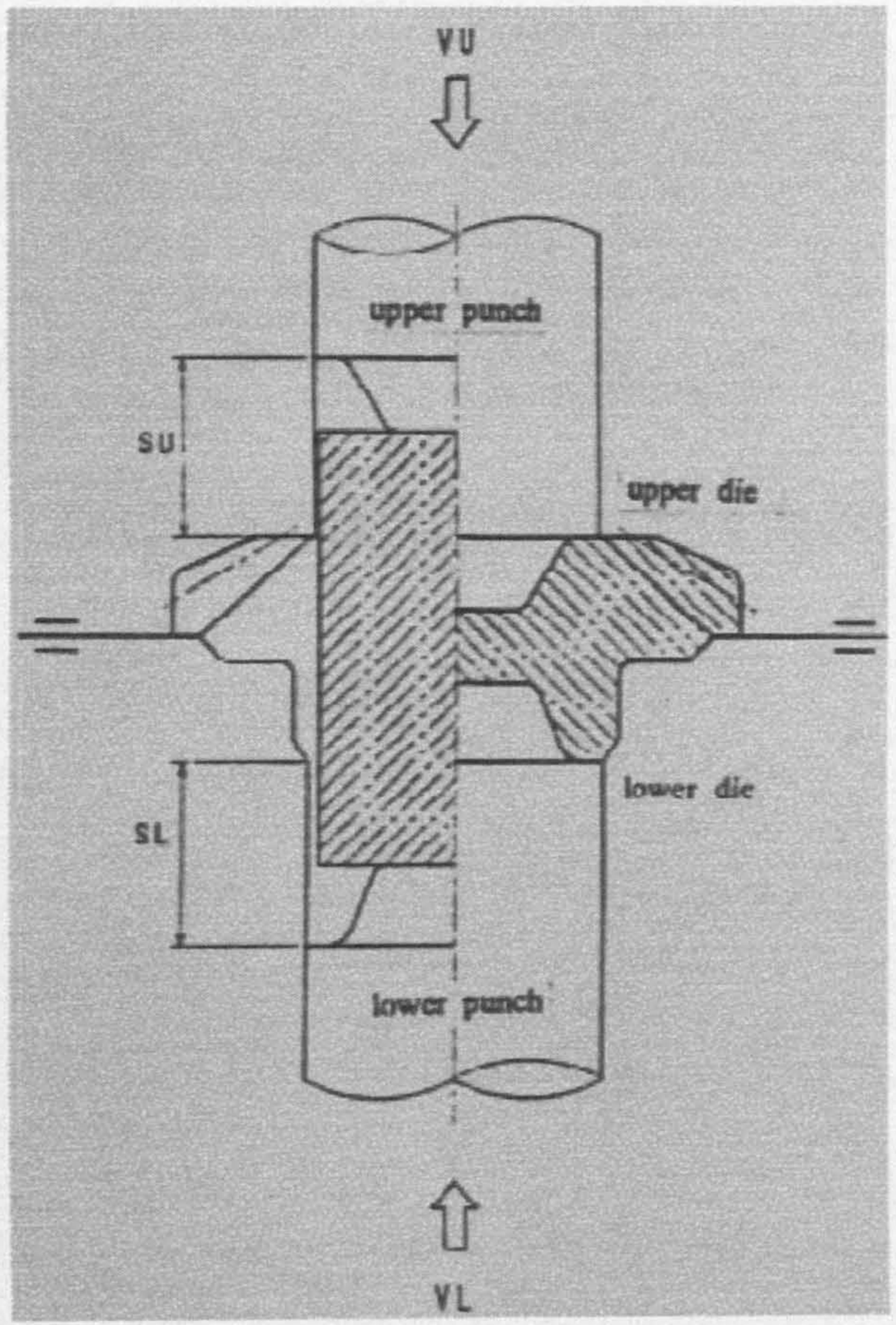

(e) Tooling for bevel gears

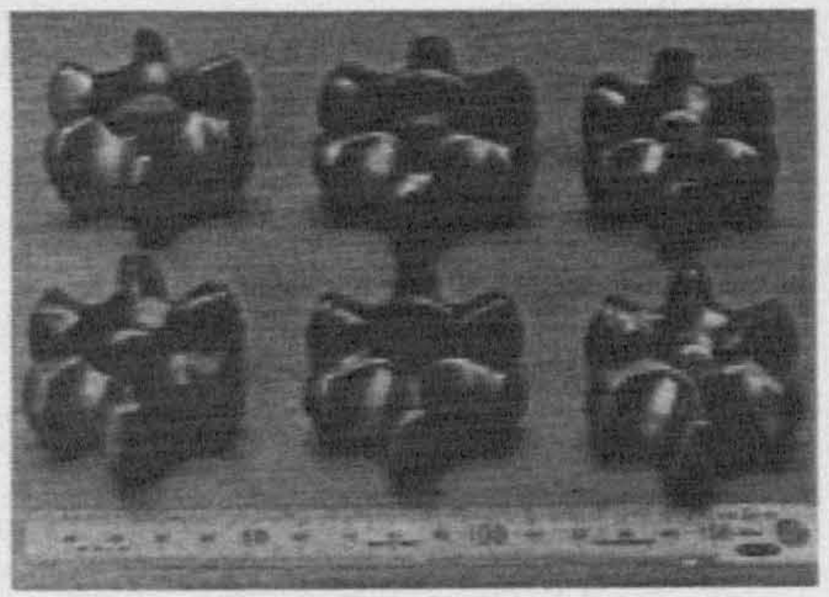

(b) inner racers

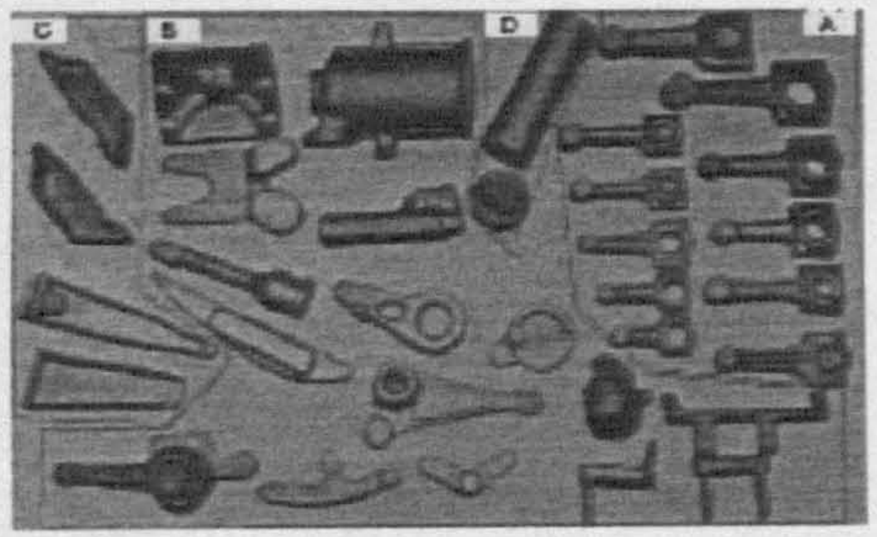

(d) Aluminum products

Fig. 1.13 Different precision cold forgings and tooling for bevel gear [10]

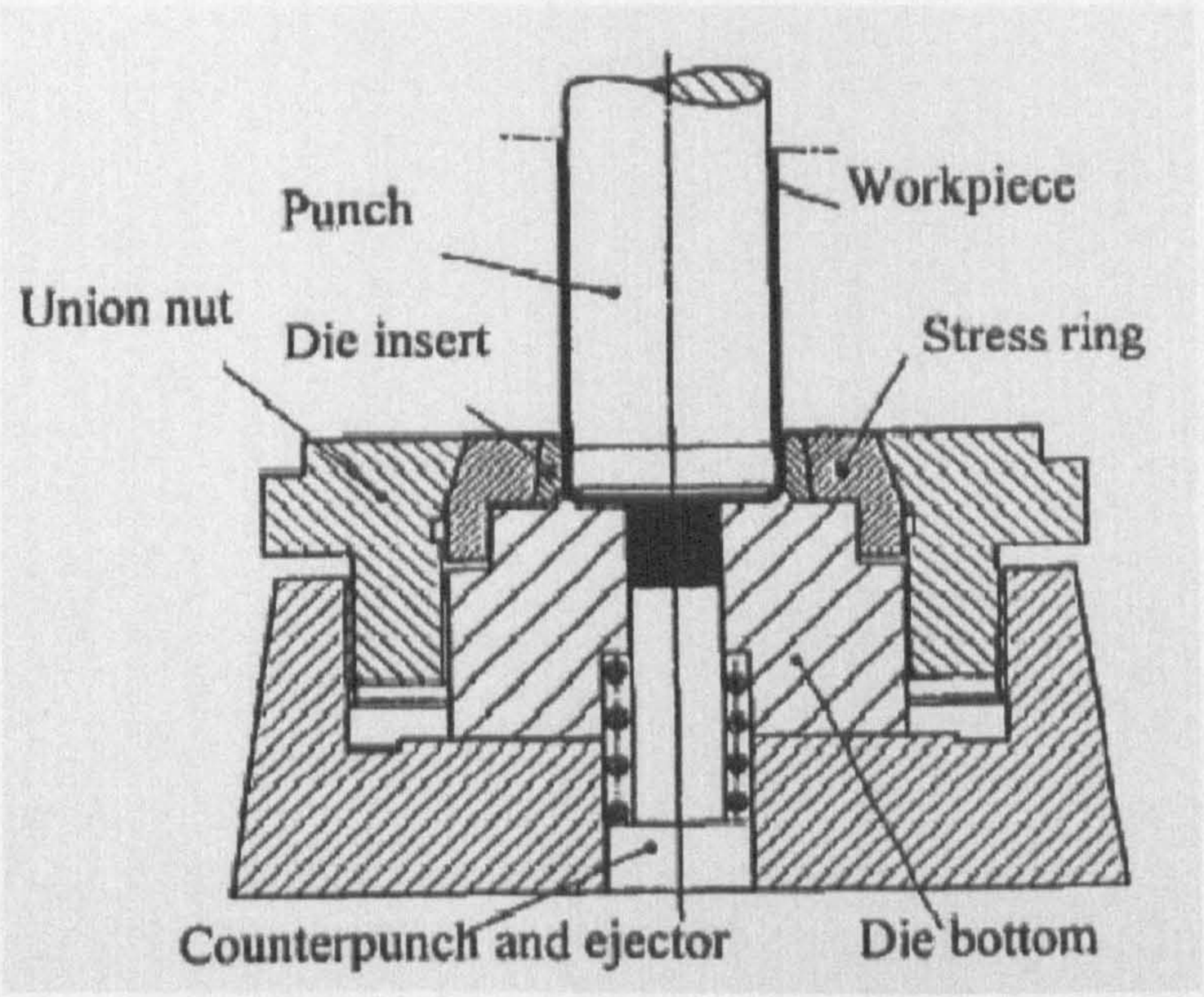

(a) Pre-stressed die

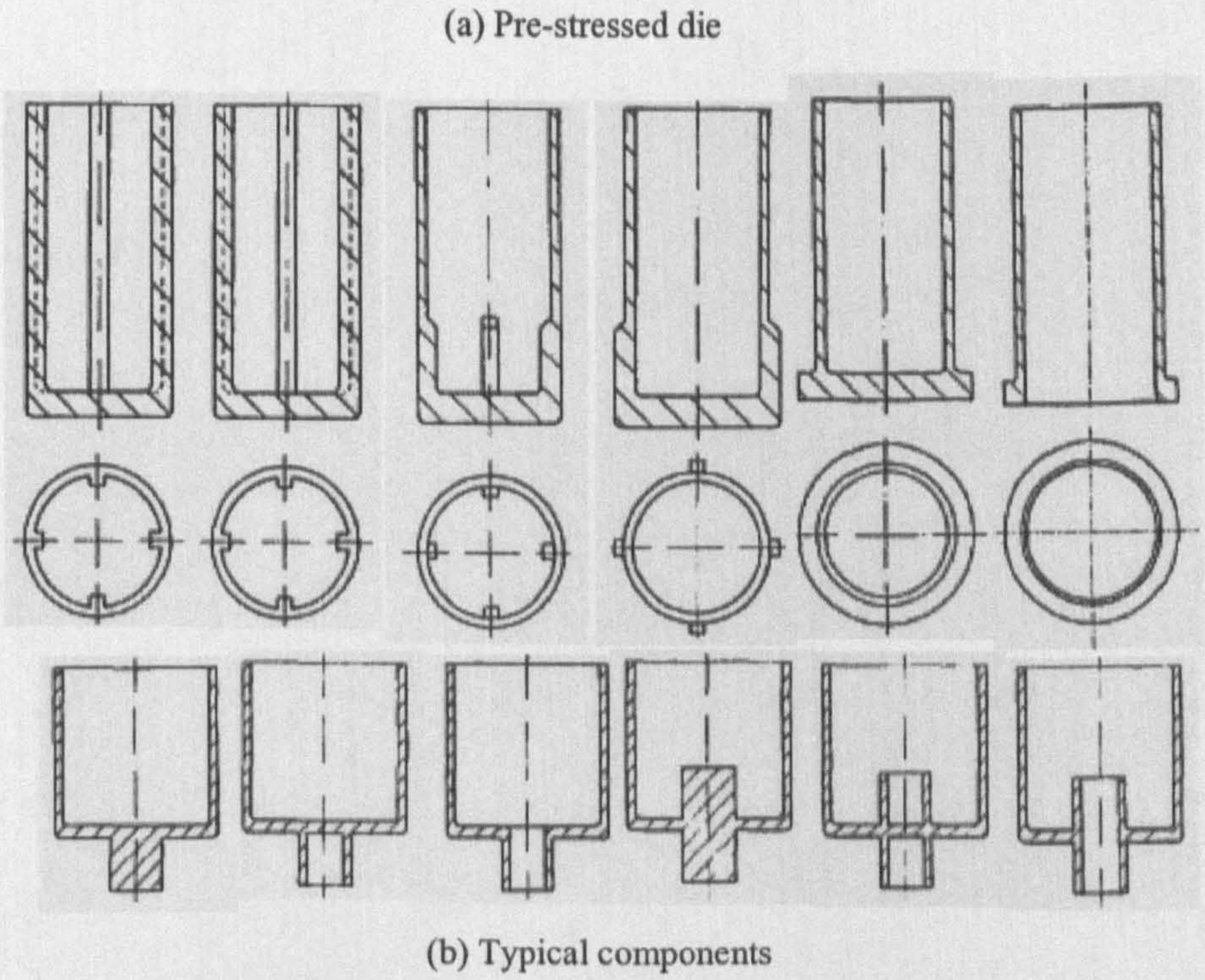

(b) Typical components

Fig. 1.14 Pre-stressed die and typical components [3]

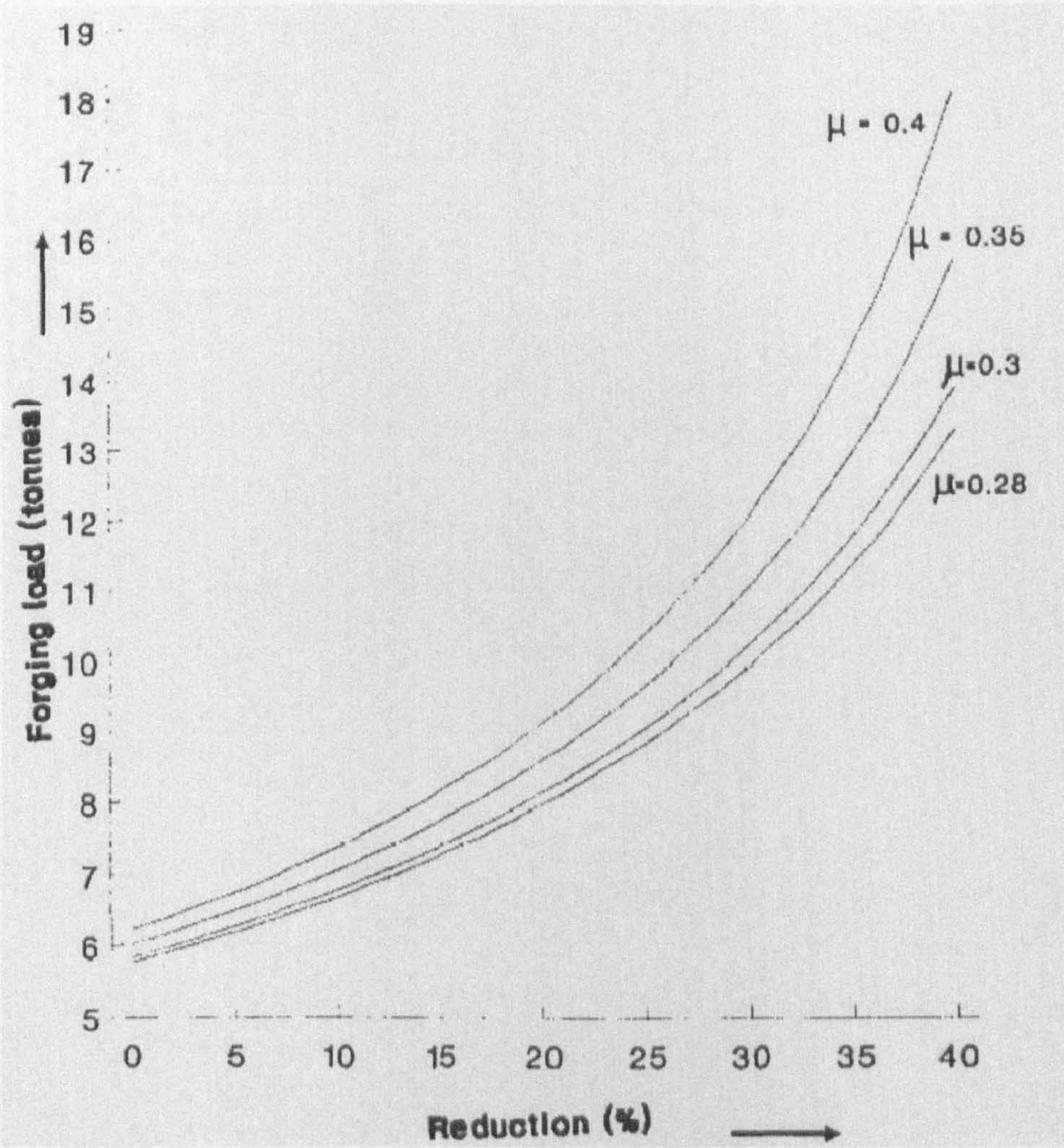

Fig. 1.15 Theoretical and experimental comparison of upsetting load versus height reduction [34]

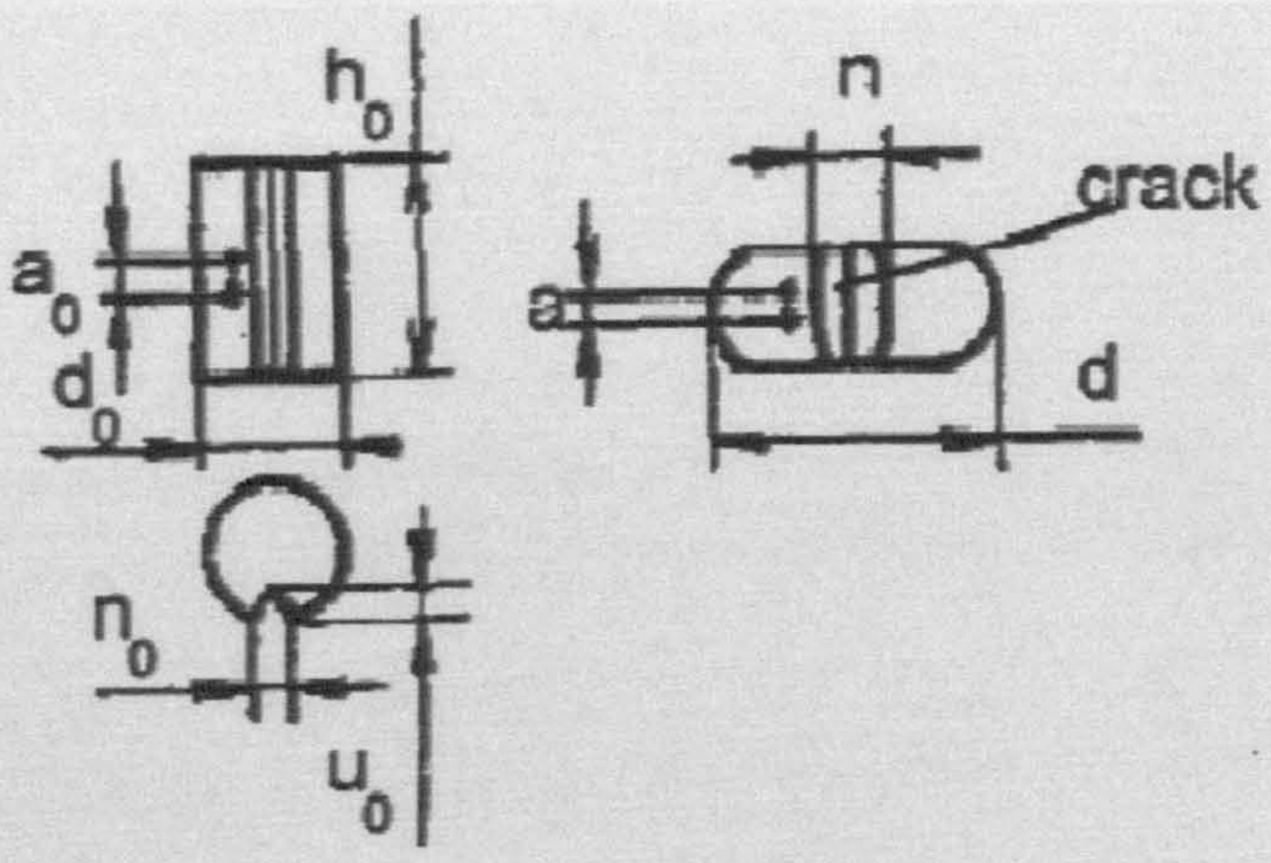

Axial strain $\varphi_z^a = -\ln\frac{a}{a_0}$

Global circumferential strain $\varphi_\Theta^d = \ln\frac{d}{d_0}$

Local circumferential strain $\varphi_\Theta^n = \ln\frac{n}{n_0}$

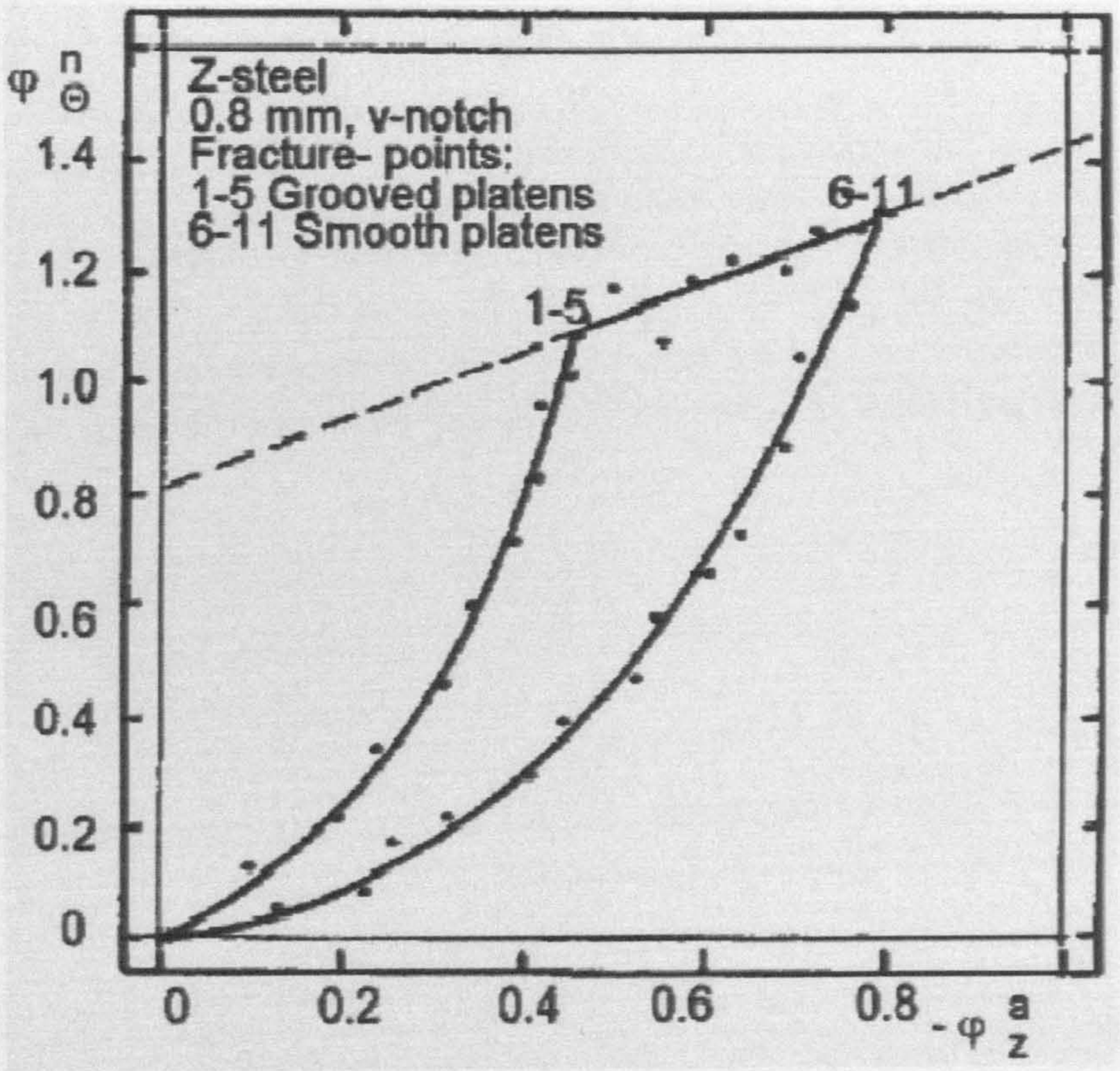

Fig. 1.16 The FLD obtained by upsetting test [35]

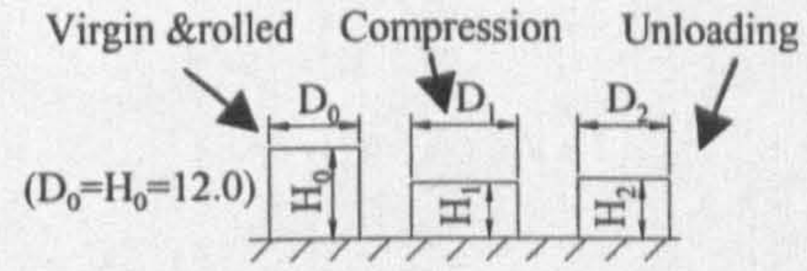

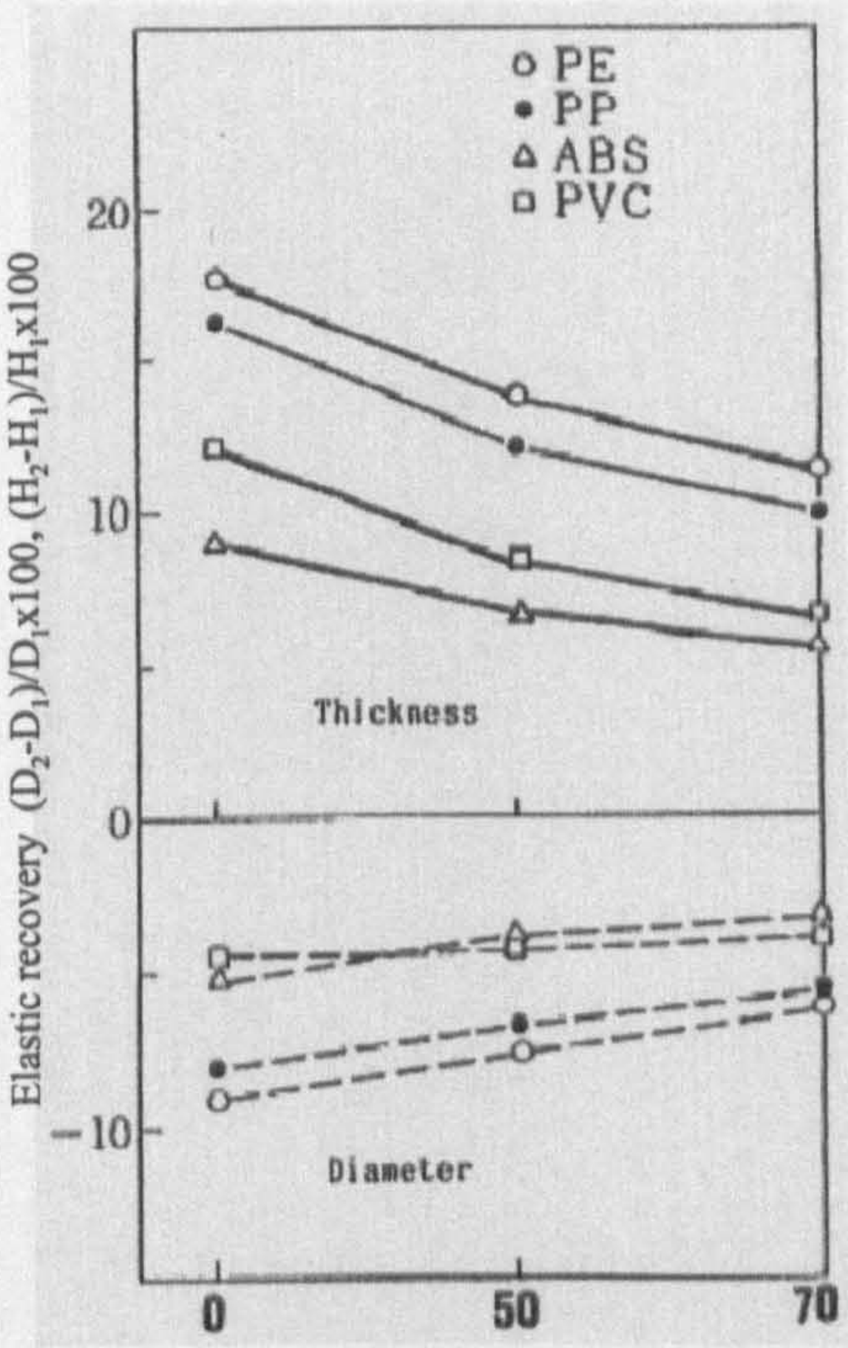

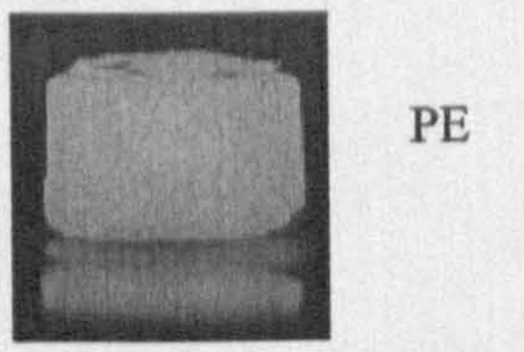
PE

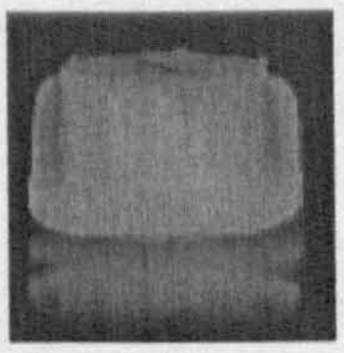
PP

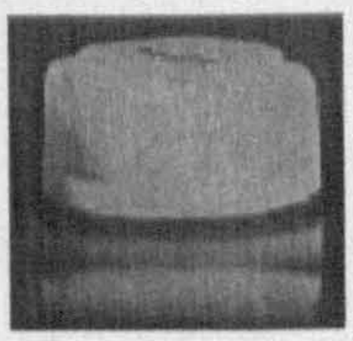
ABS


PVC

Fig. 1.17 Reduction of elastic recovery and product example [36]

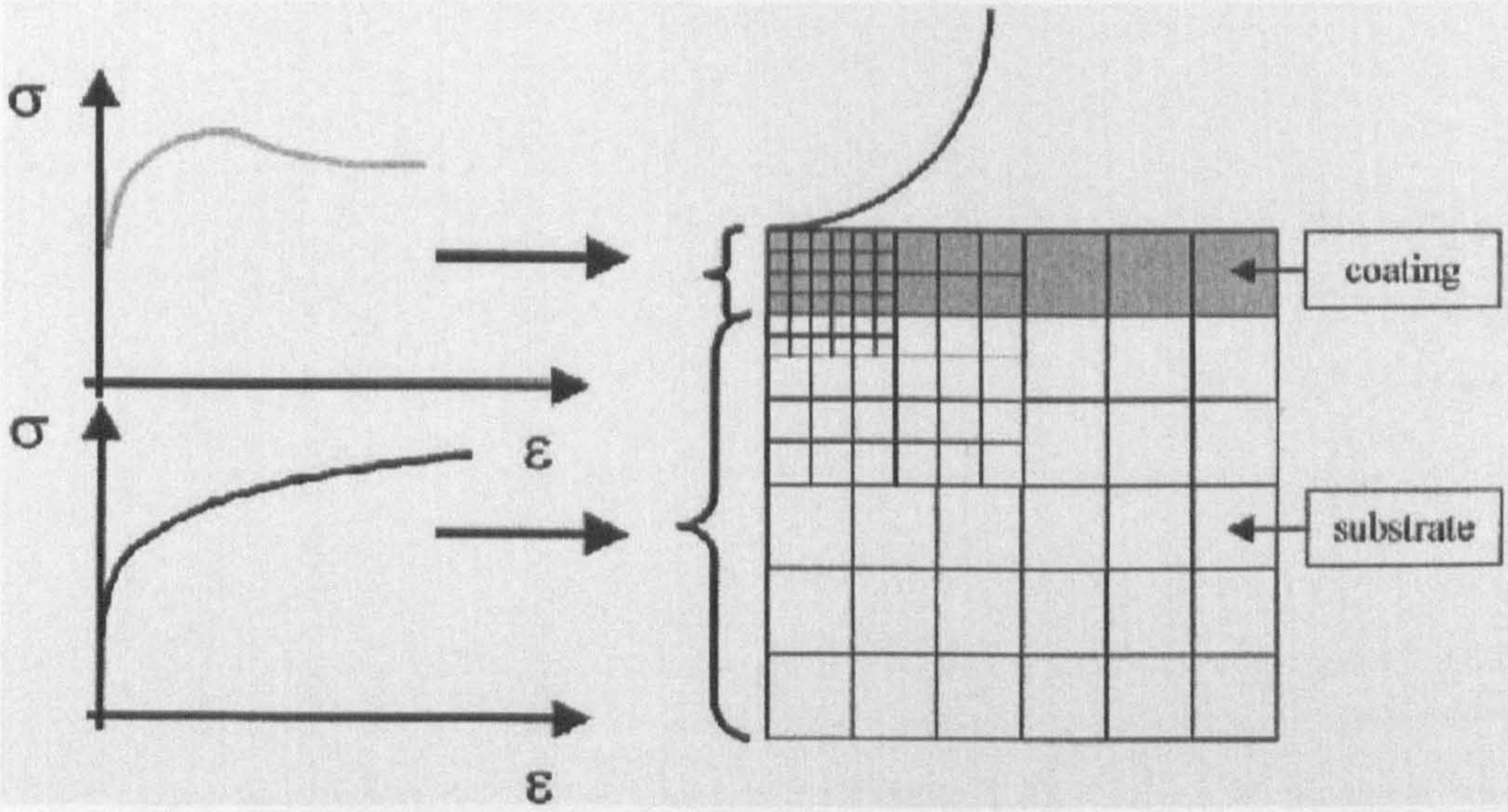

(a)

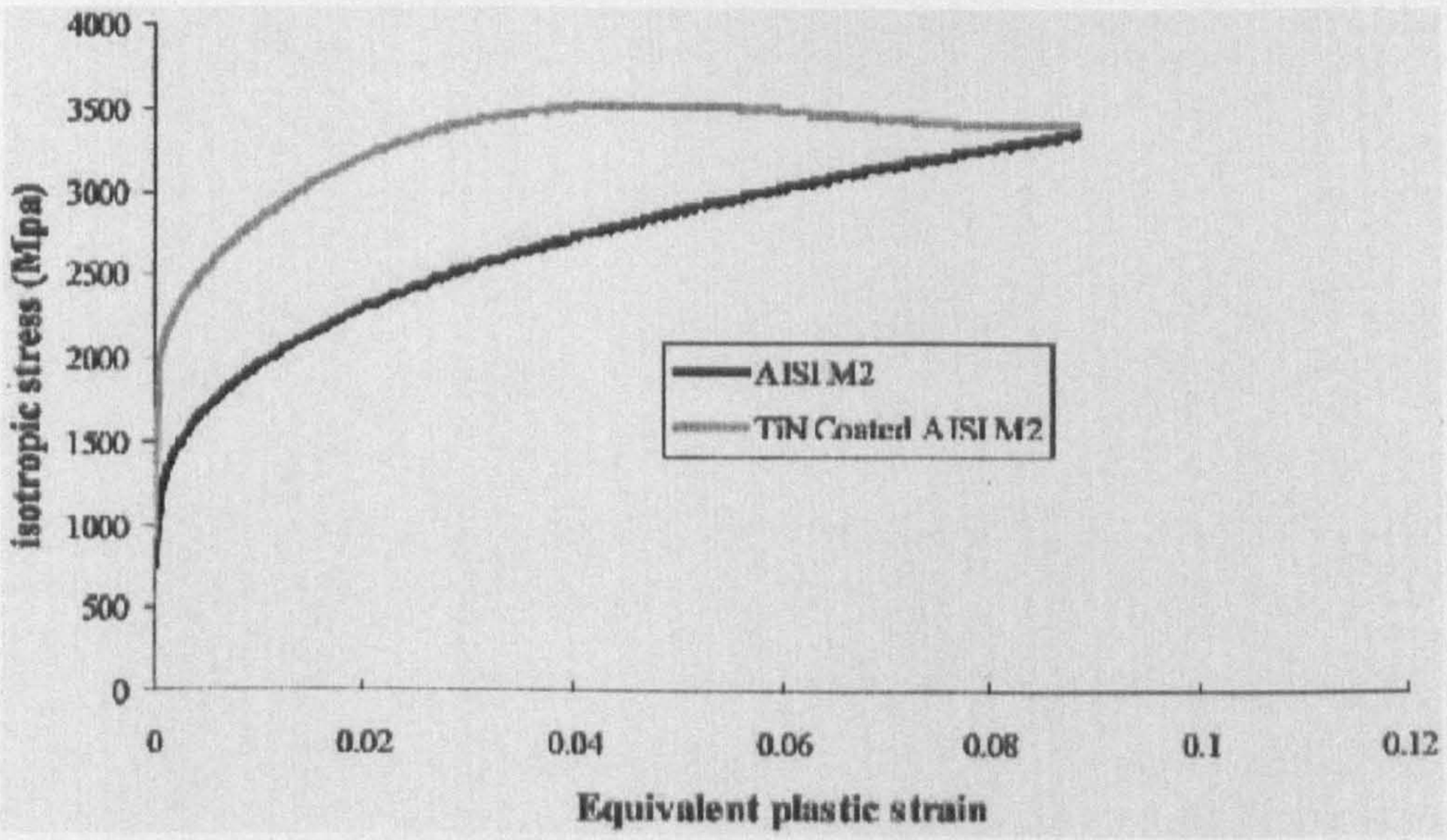

(b)

Fig. 1.18 Hardening law of tool material ASIS M2 with TiN coating [37]

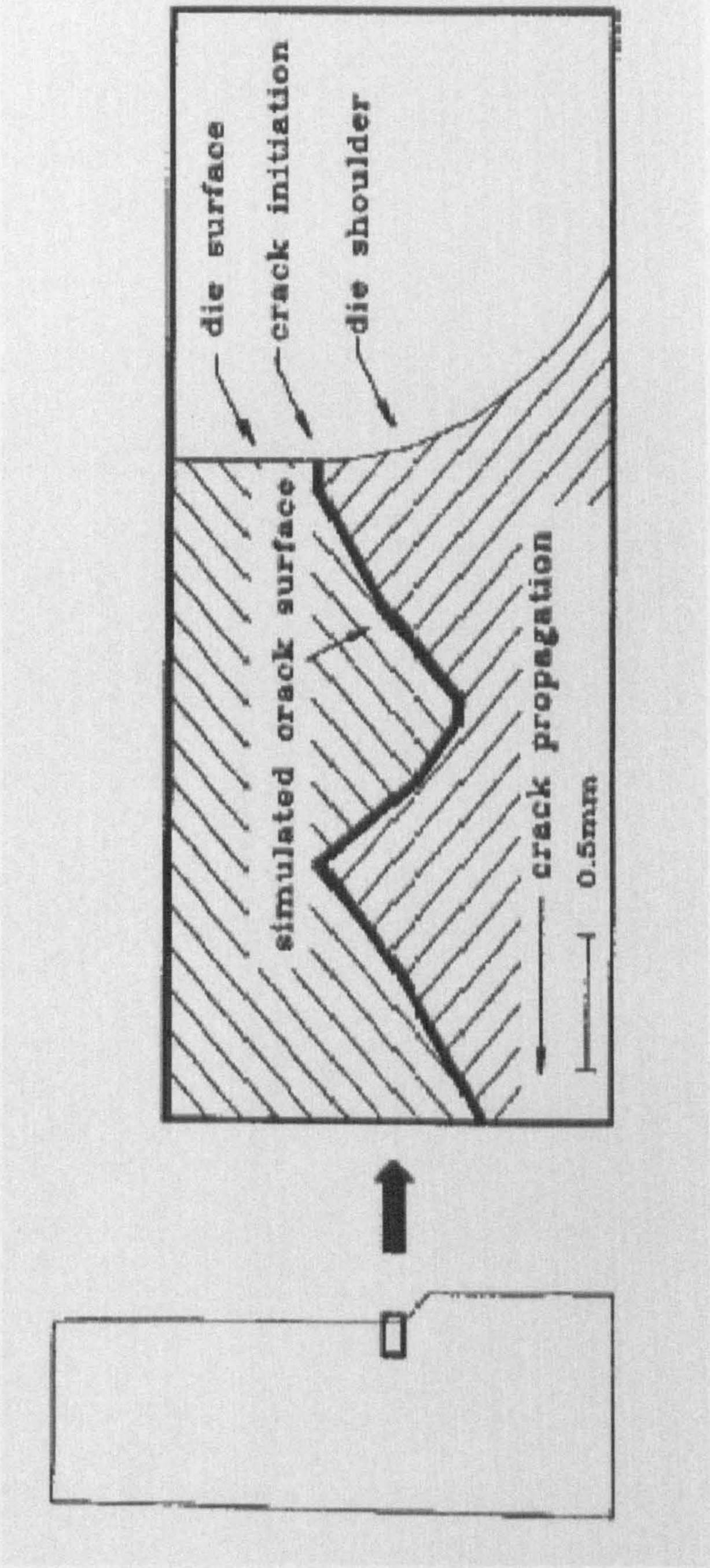

Fig. 1.19 Simulated fatigue crack propagation in the extrusion die [48]

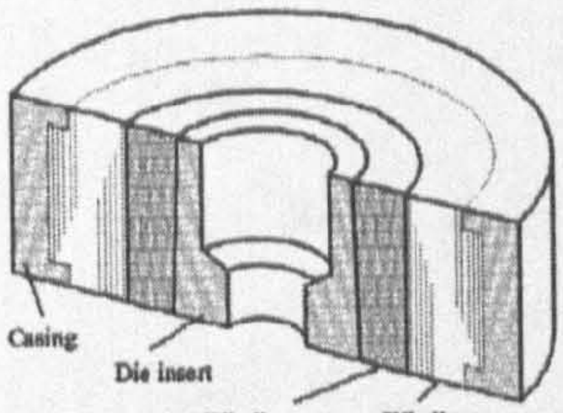

(a) [47]

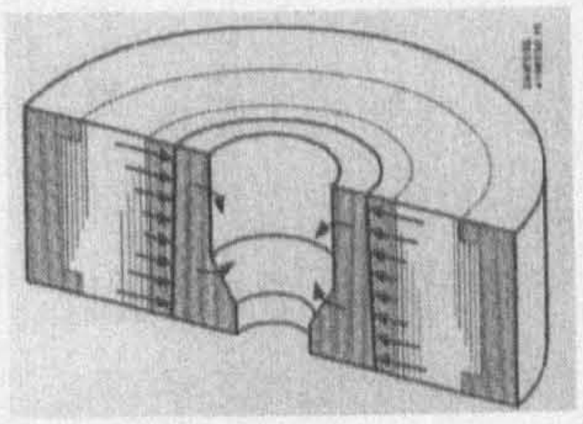

(b) [49]

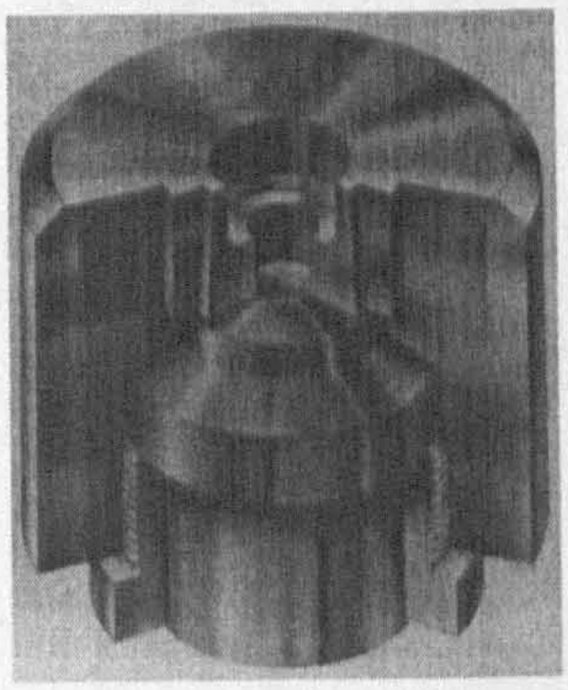

(c) [49]

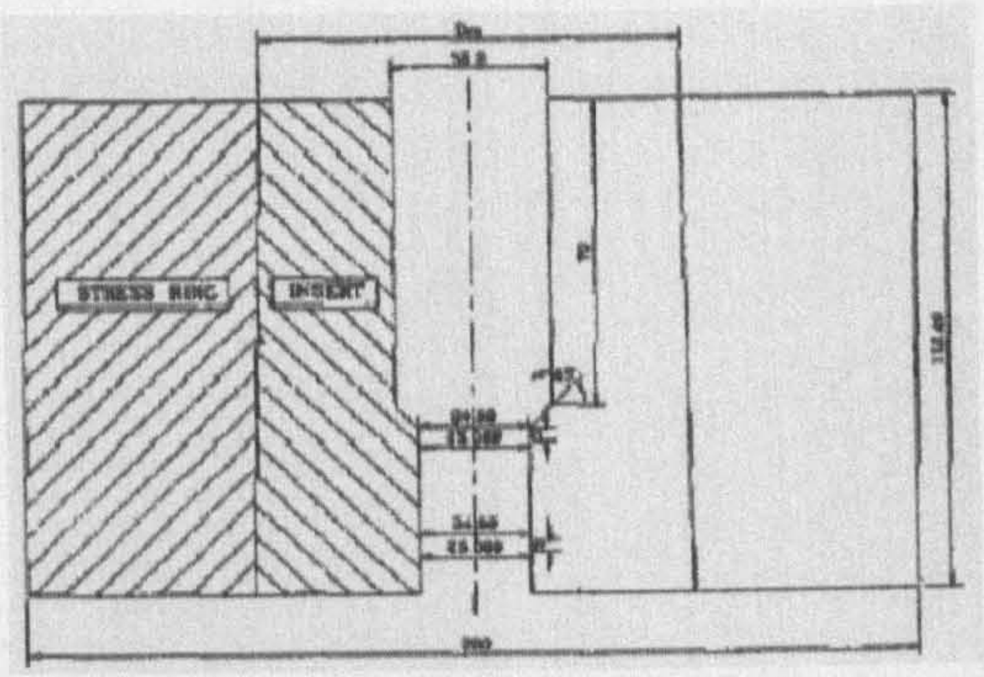

(d) [48]

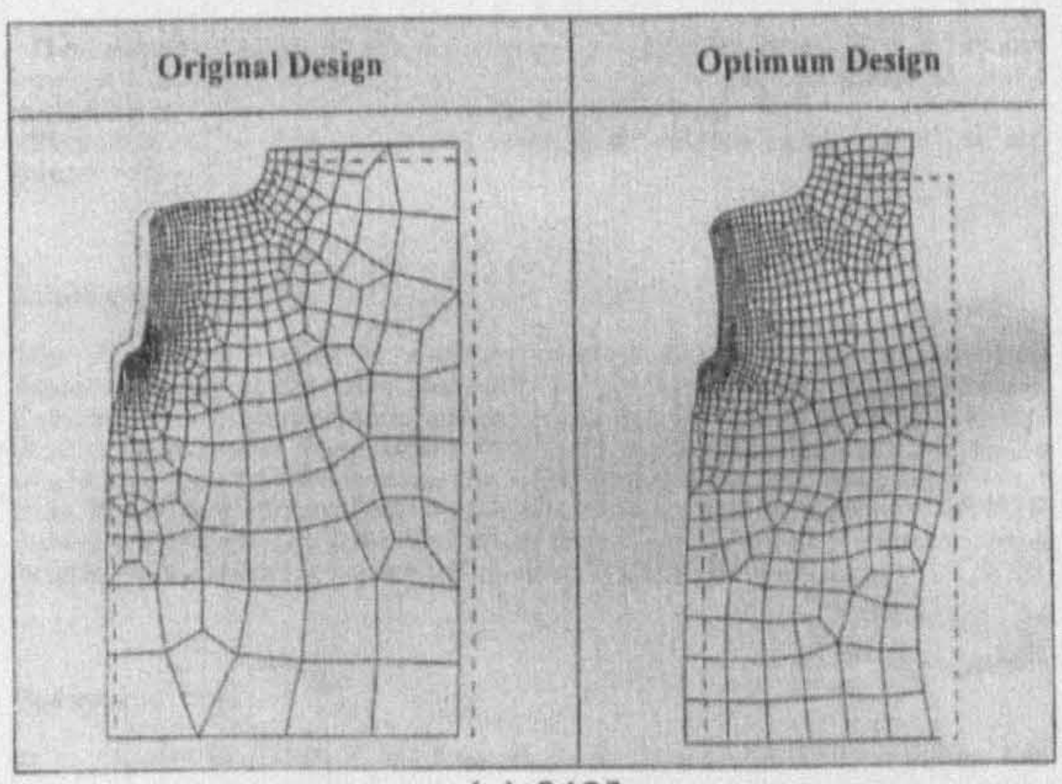

(e) [42]

Fig. 1.20 Different approaches improving cold forging tool fatigue

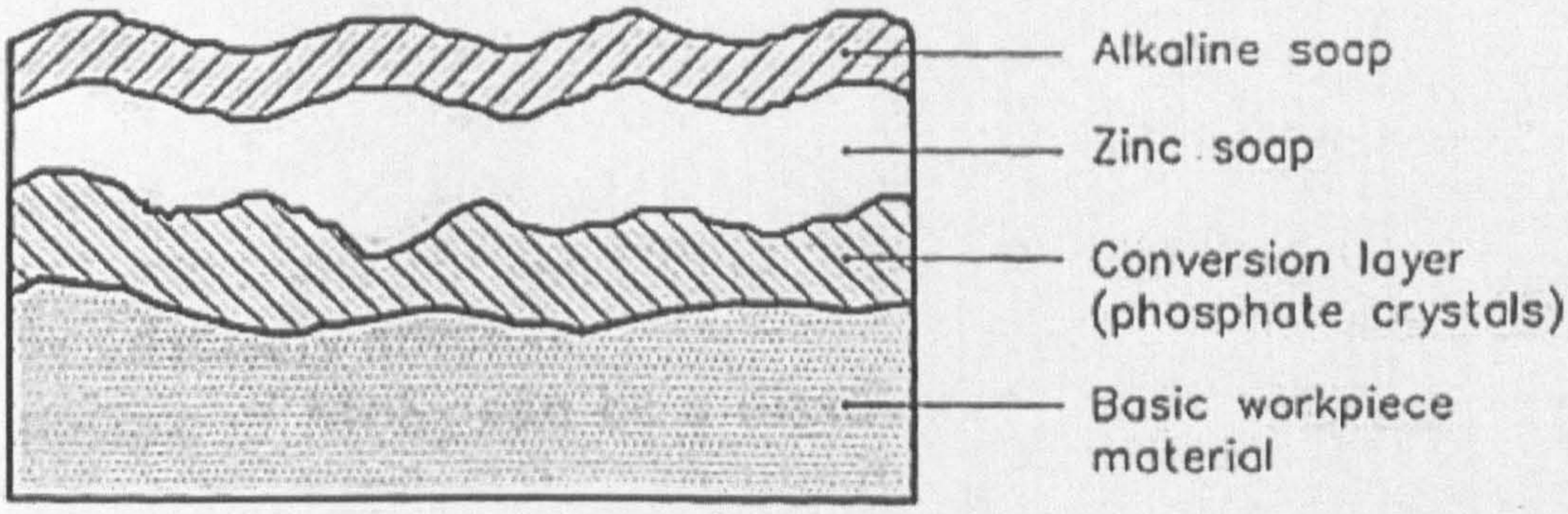

(a) Lubricant layers

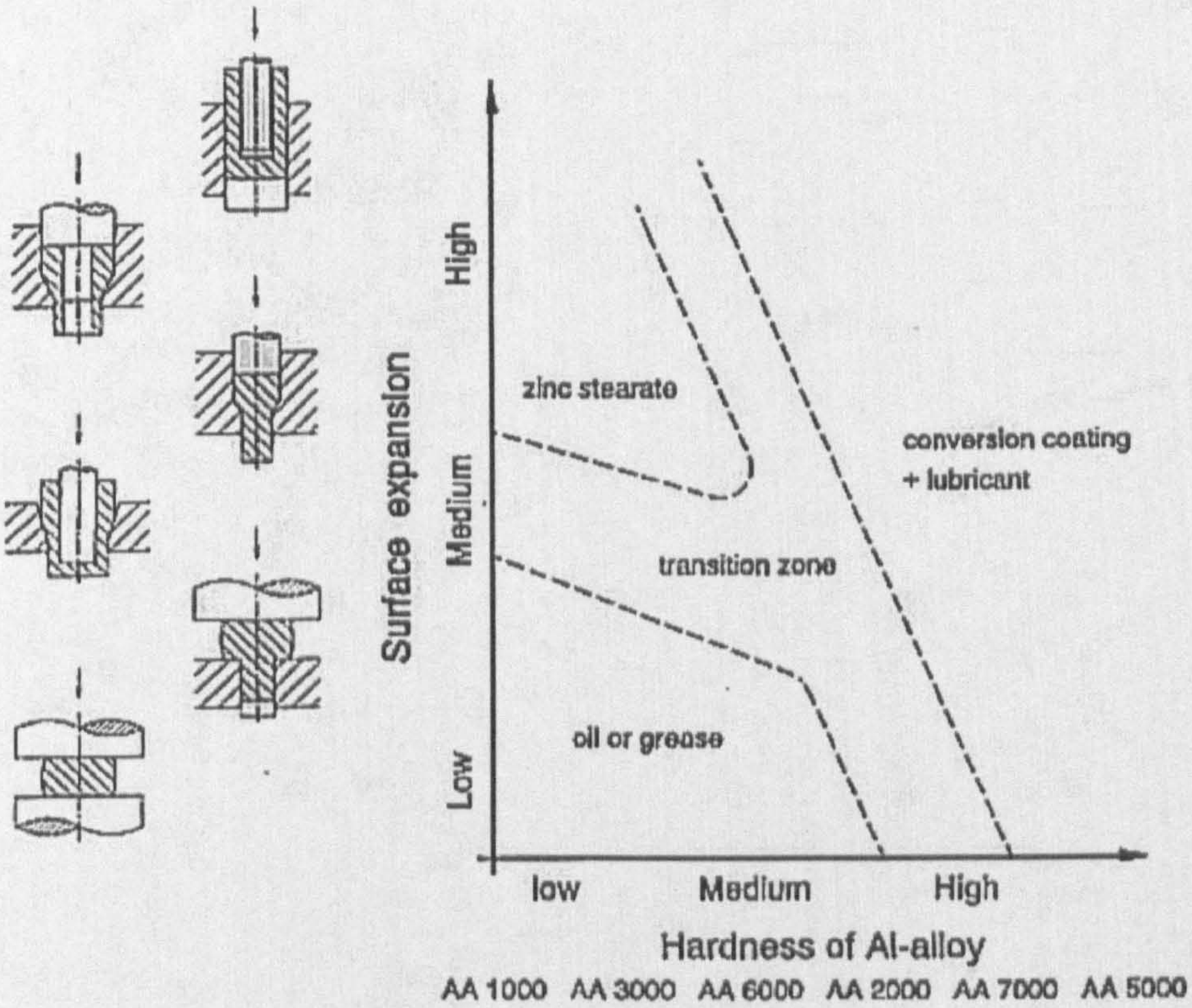

(b) Lubrication choices

Fig. 1.21 Lubrication principle and approaches choice for cold forging aluminum and aluminum alloys [50]

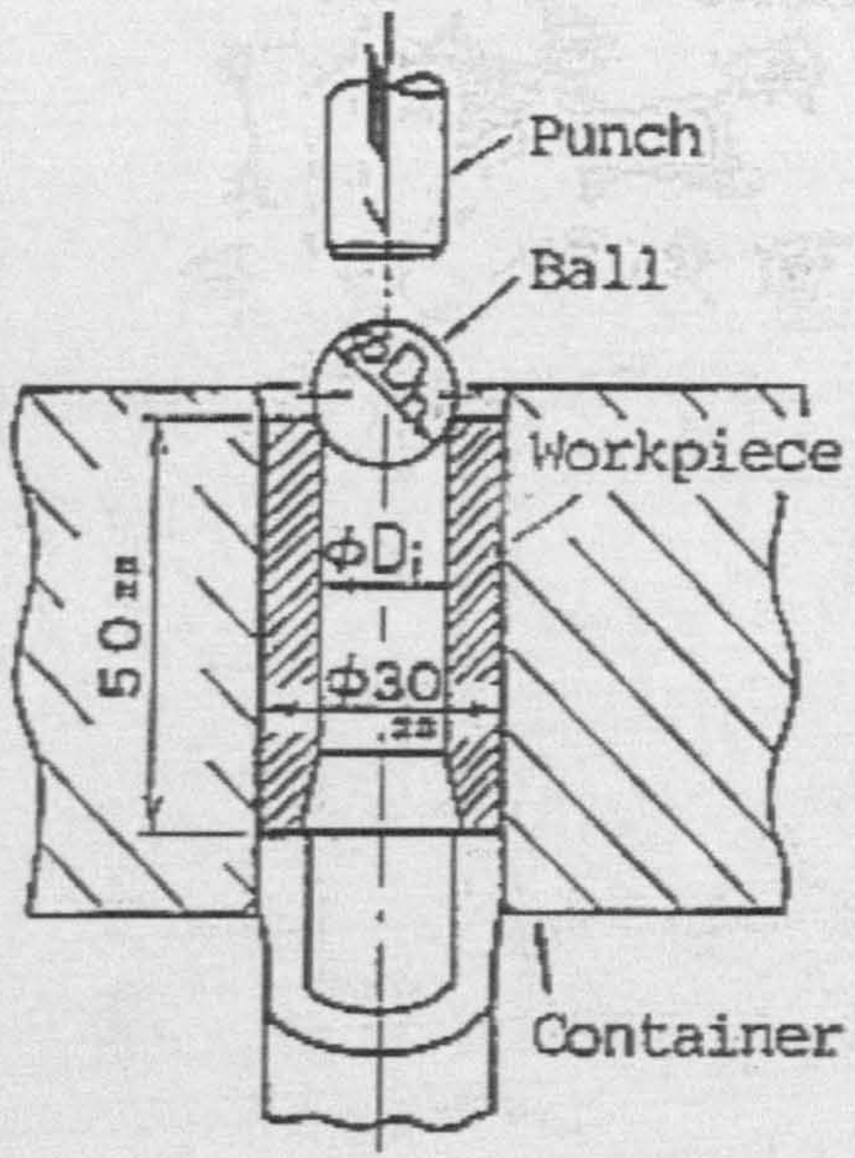

(a)

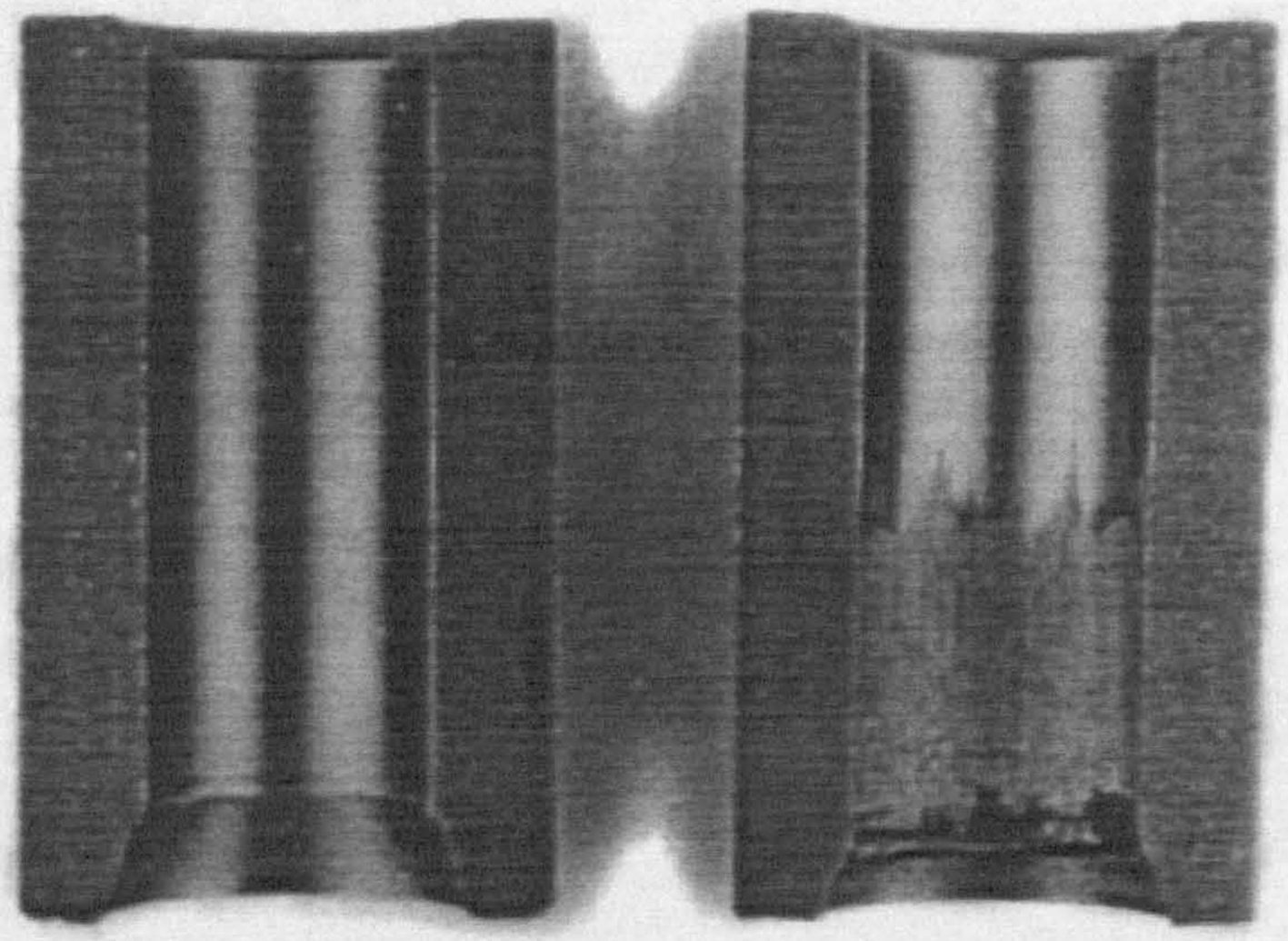

(b)

Fig. 1.22 Ball penetration test (a) and the galling and without galling inside surfaces (b) [51]

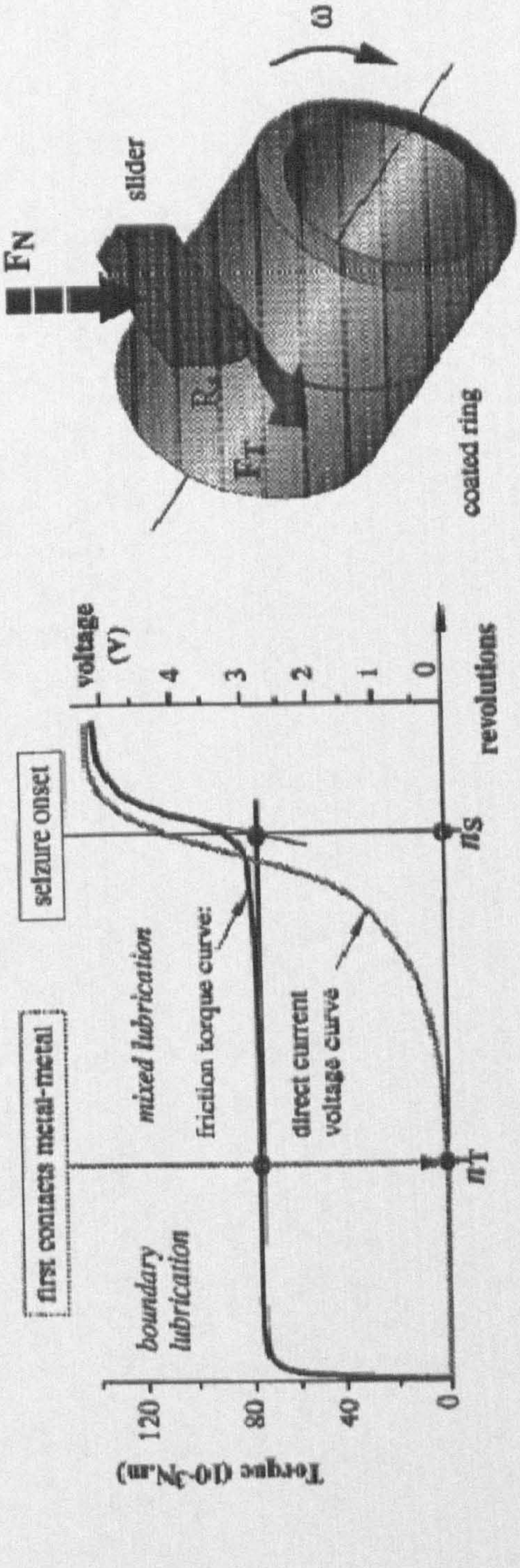

Fig. 1.23 Friction-seizure test of cold forging coatings [53]

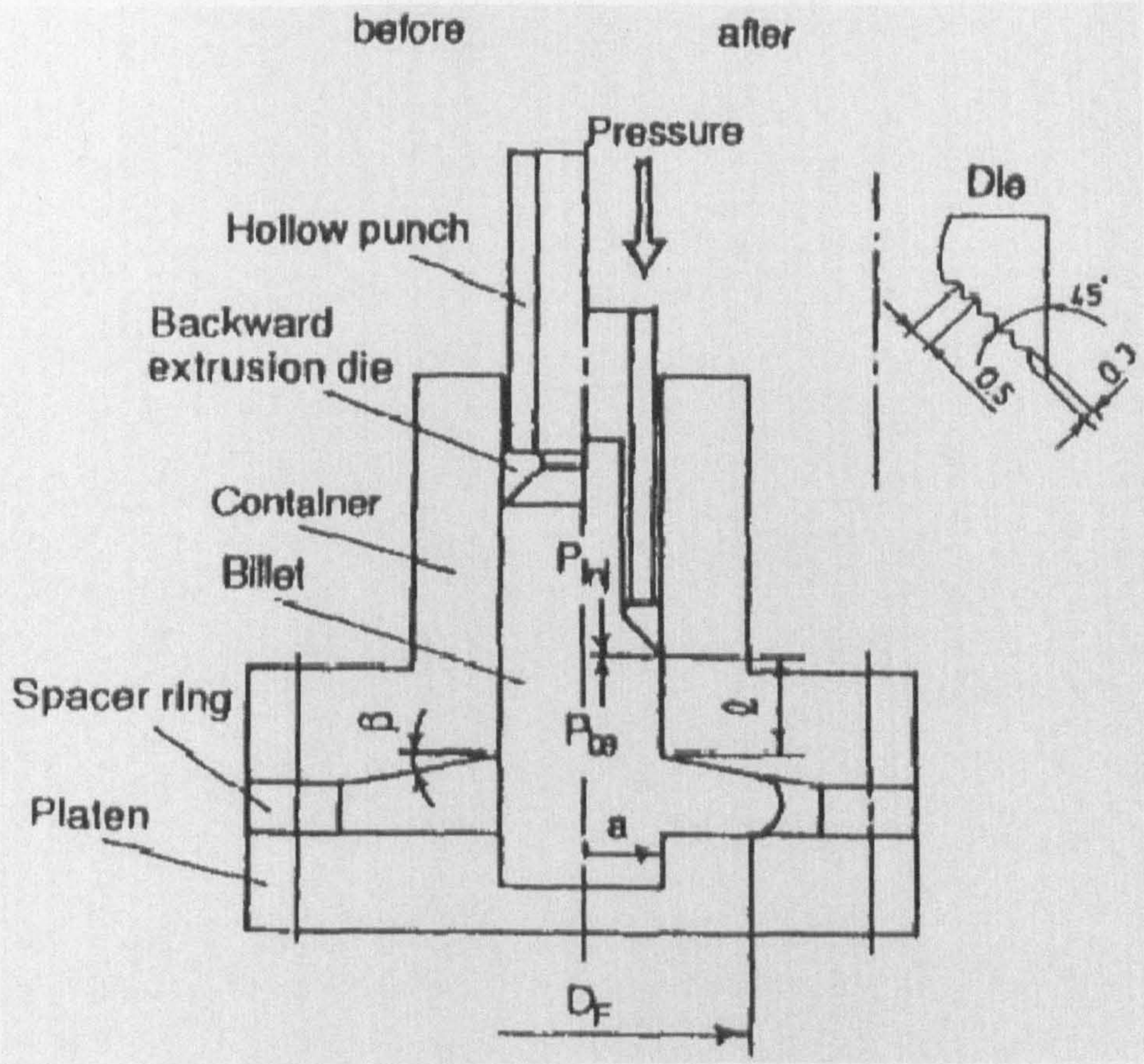

Fig. 1.24 Schematic diagram of injecting experimental device [55]

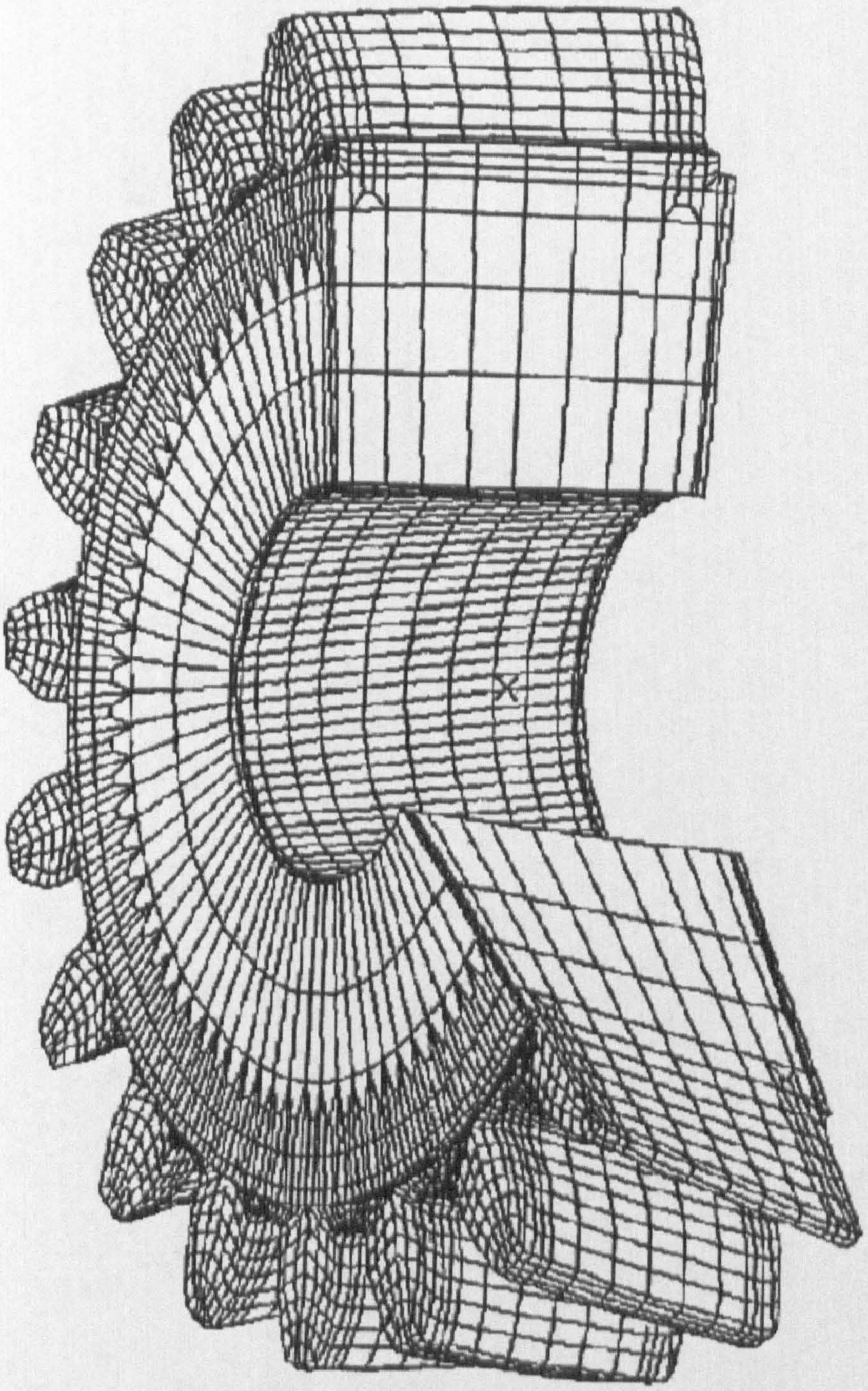

Fig. 1.25 Three-dimensional simulation of cold forging helical gear [29]

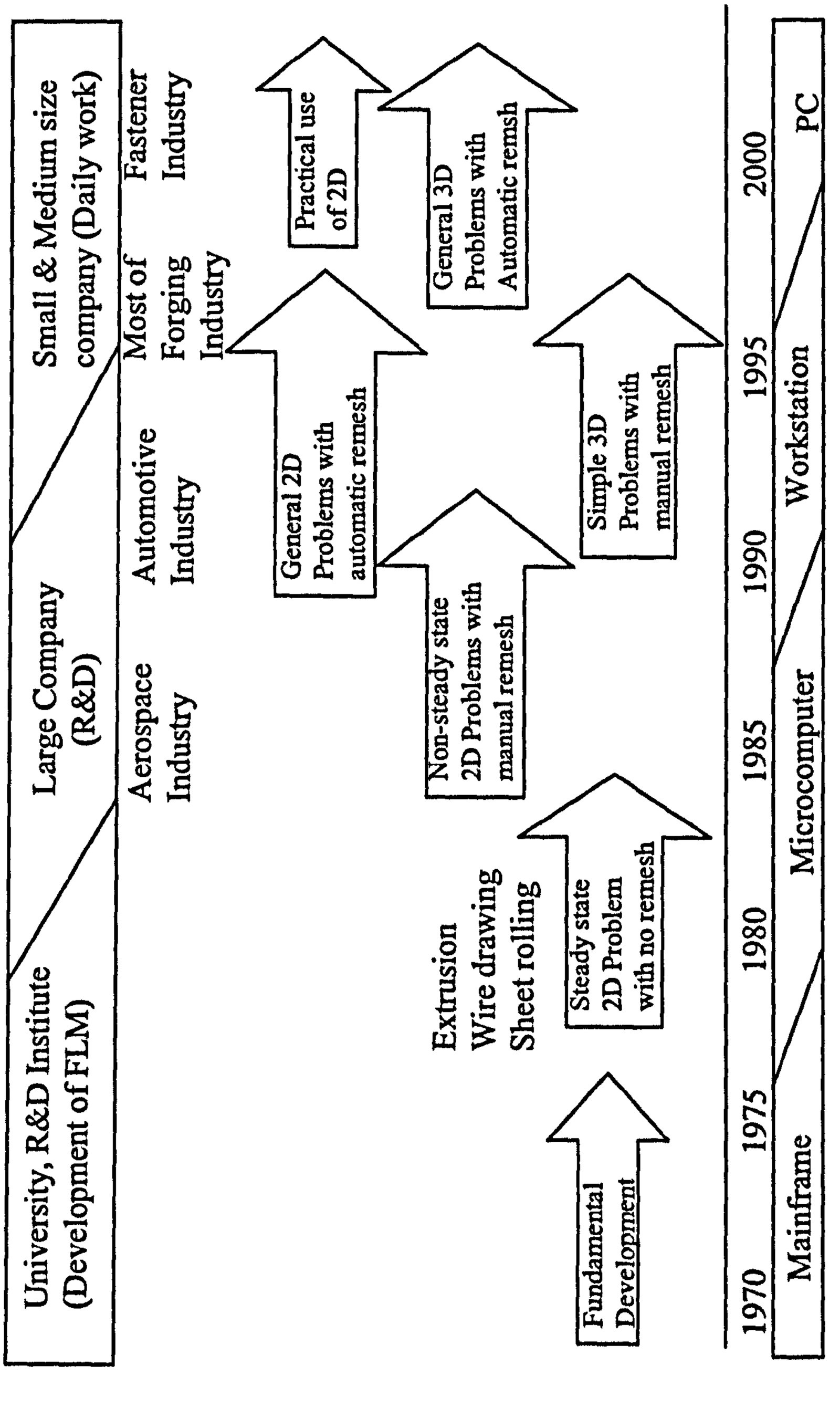

Fig. 1.26 History of practical use of FE simulation in forging [57]

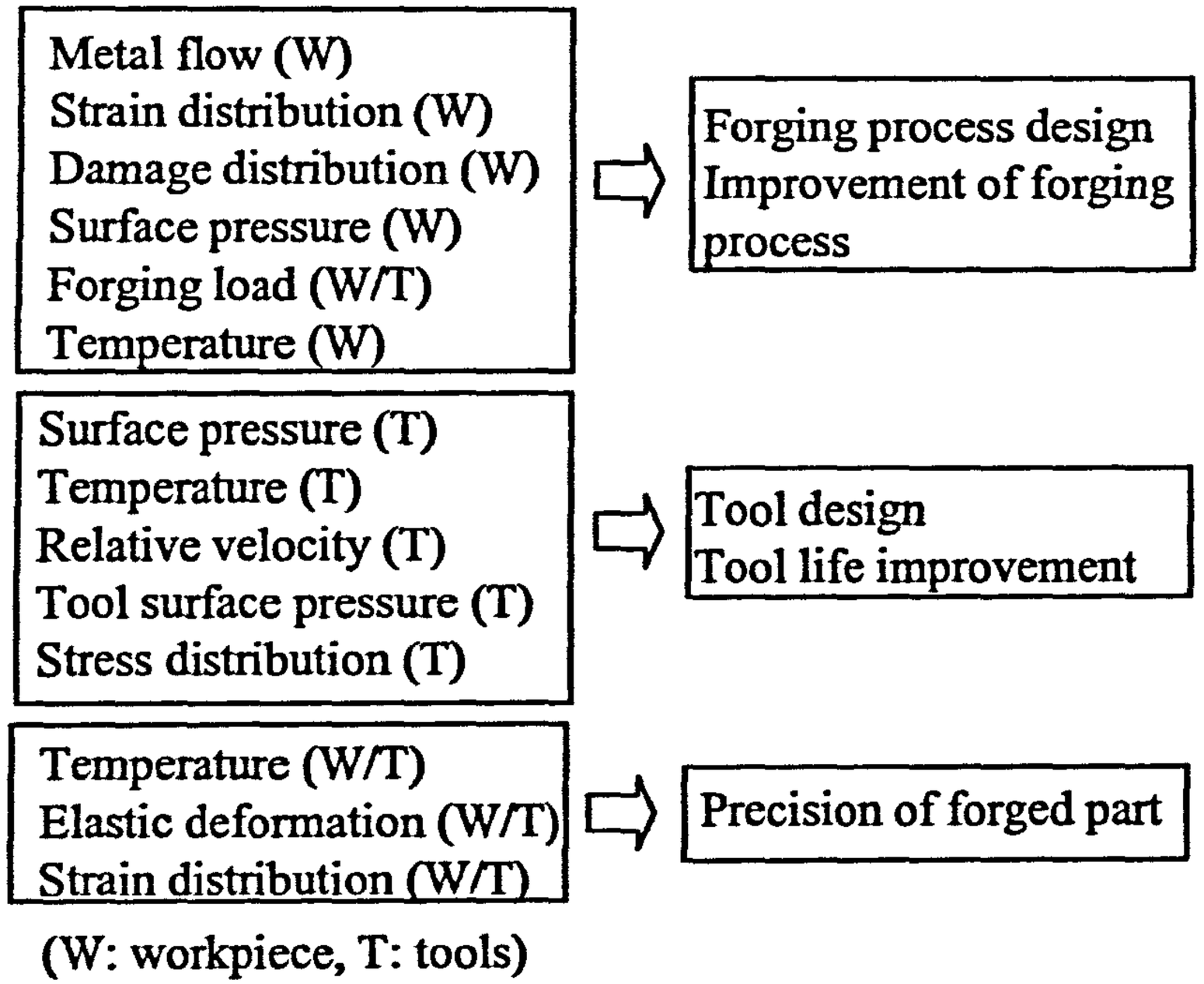

(a) Available information

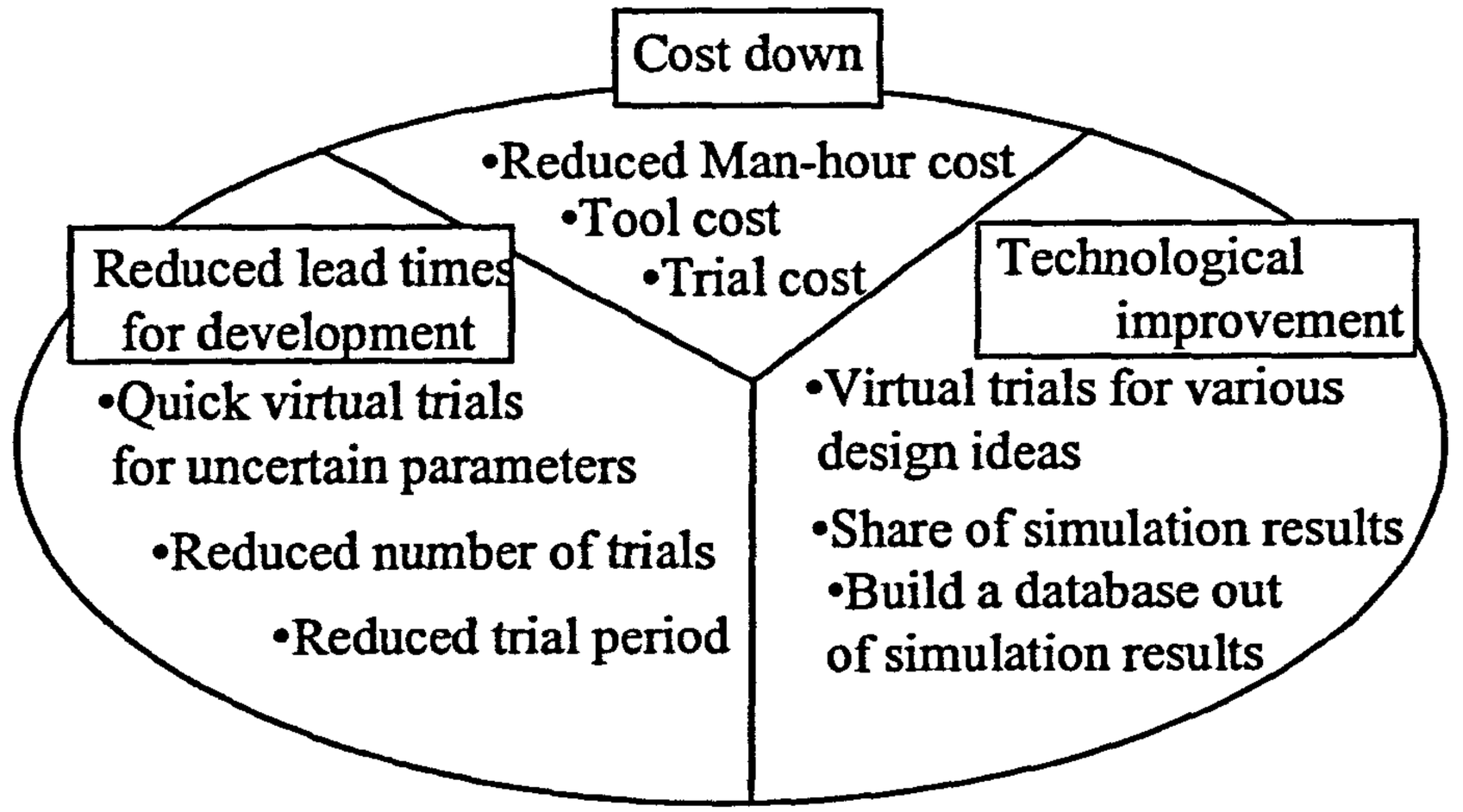

(b) Advantages

Fig. 1.27 Available information and advantages of FE simulation [57]

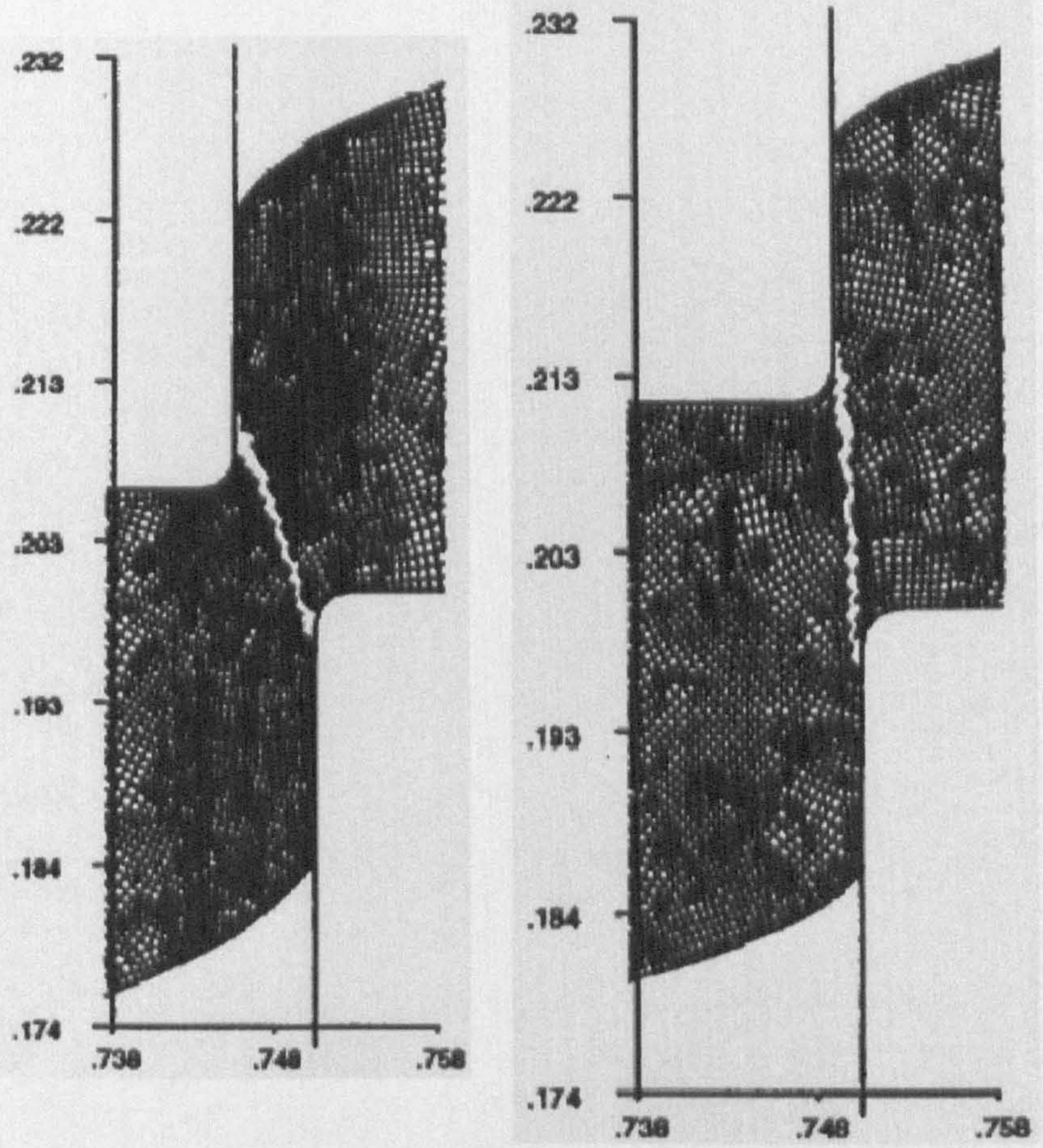

Fig. 1.28 Material separation (a) 15% clearance, sharp tool, low carbon steel; (b) 4.5% clearance, sharp tool, low carbon steel [64]

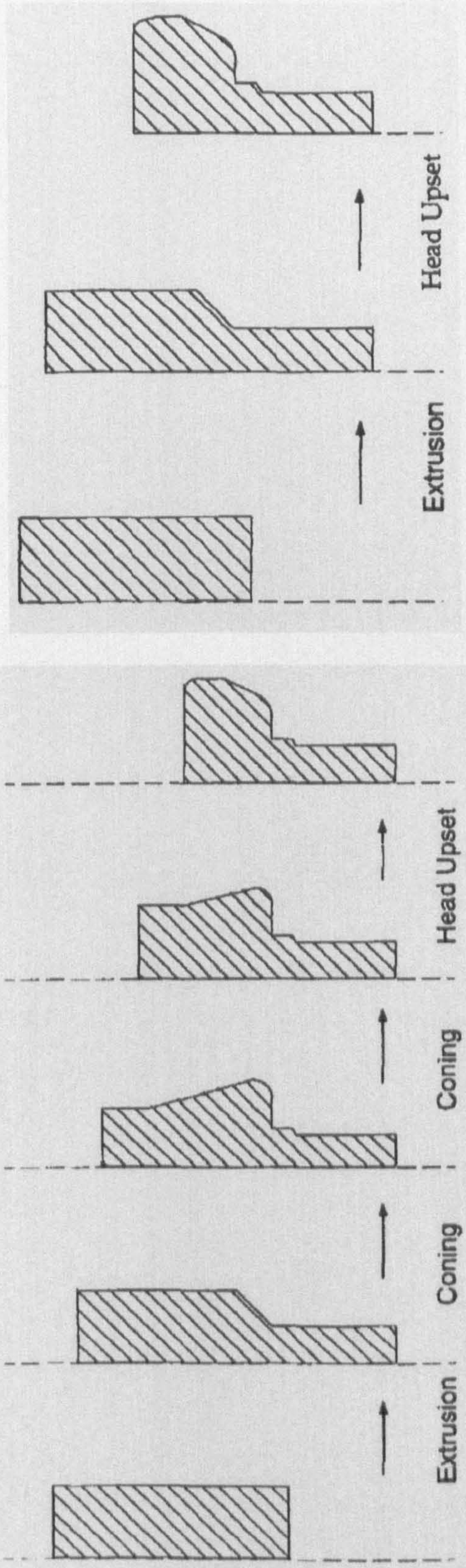

(b)

(a)

Fig. 1.29 Optimized processes (a)and original processes (b) [66]

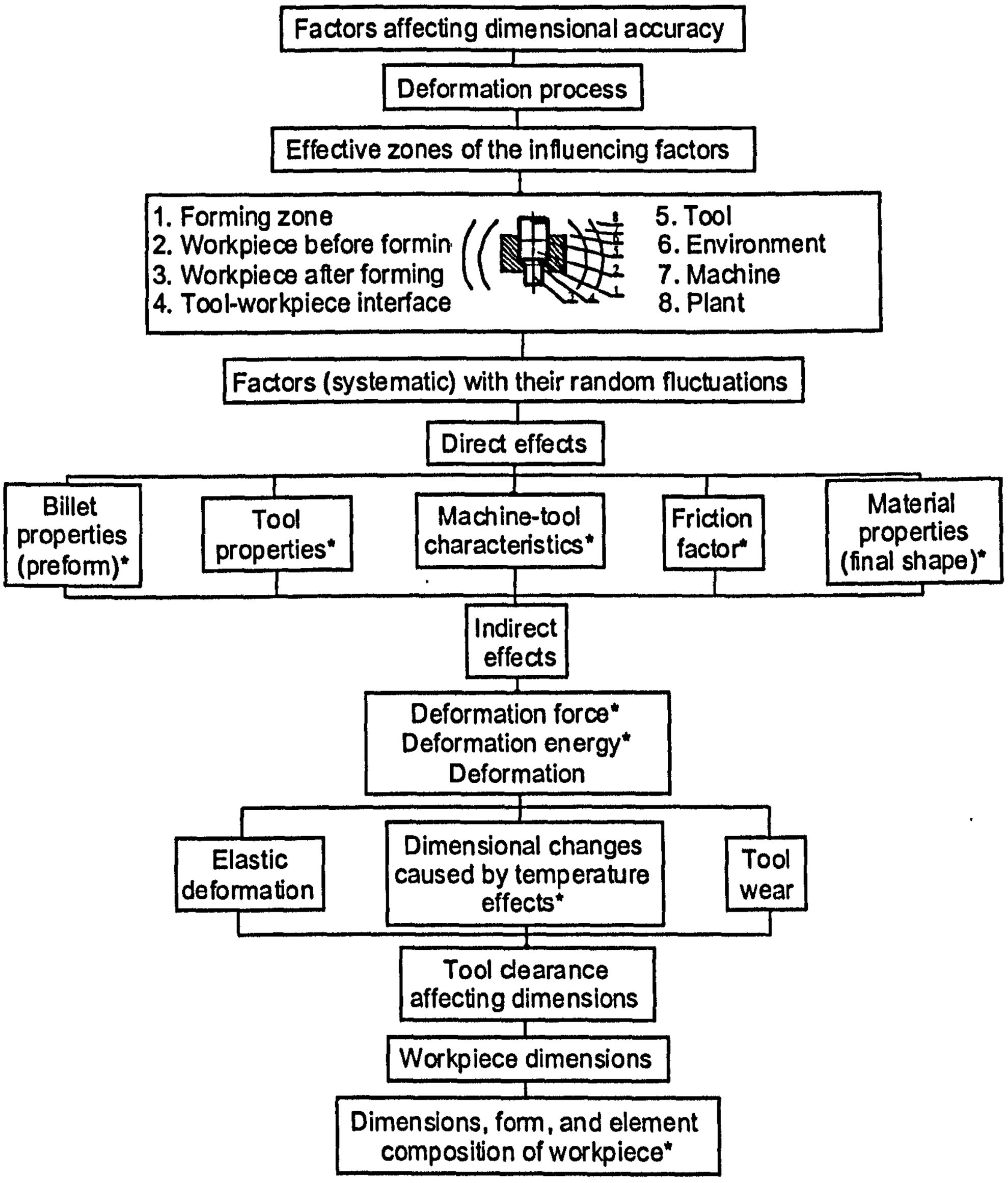

*Factors and values aimed at with natural deviations

Fig. 1.30 Schematic of the factors affecting dimensional accuracy in deformation processes [67]

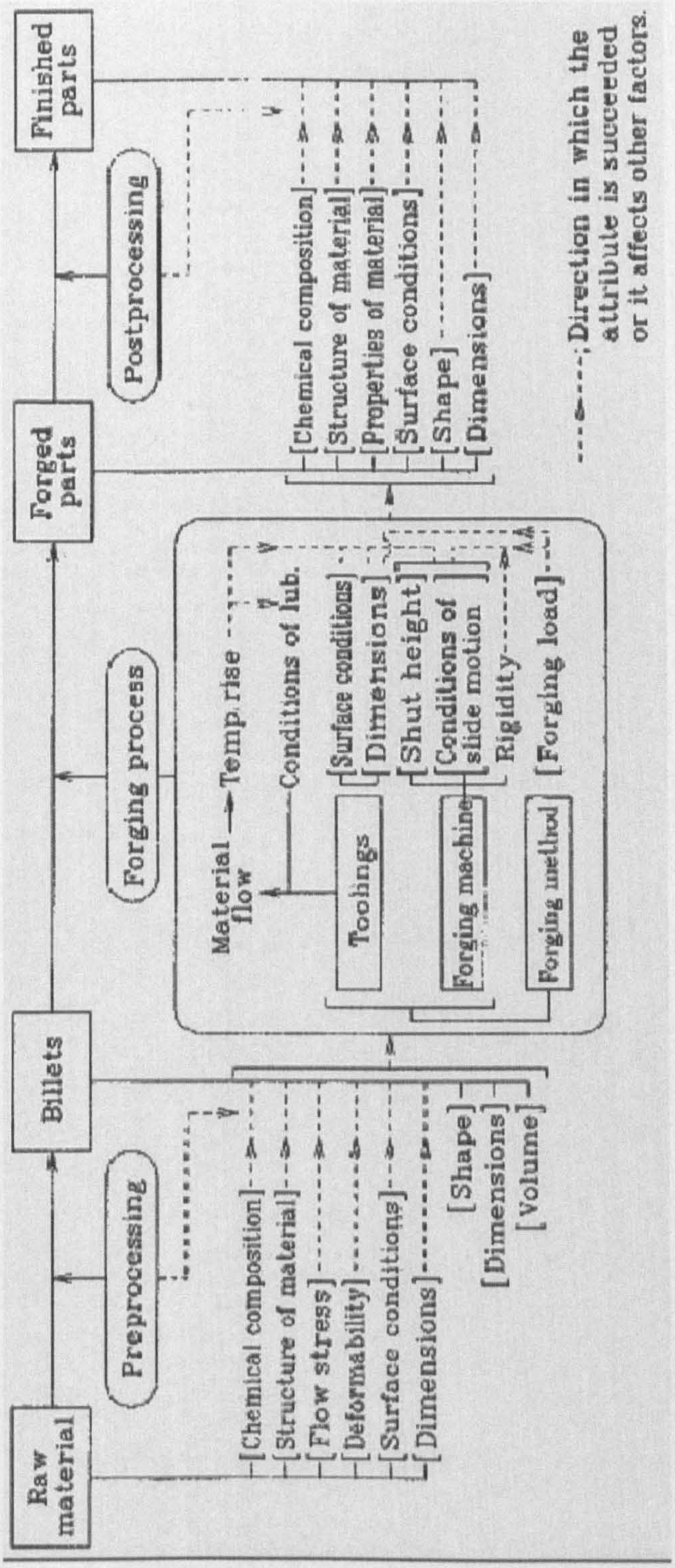

Fig. 1.31 Accuracy of forged parts vs. characteristics of mechanical press [25]

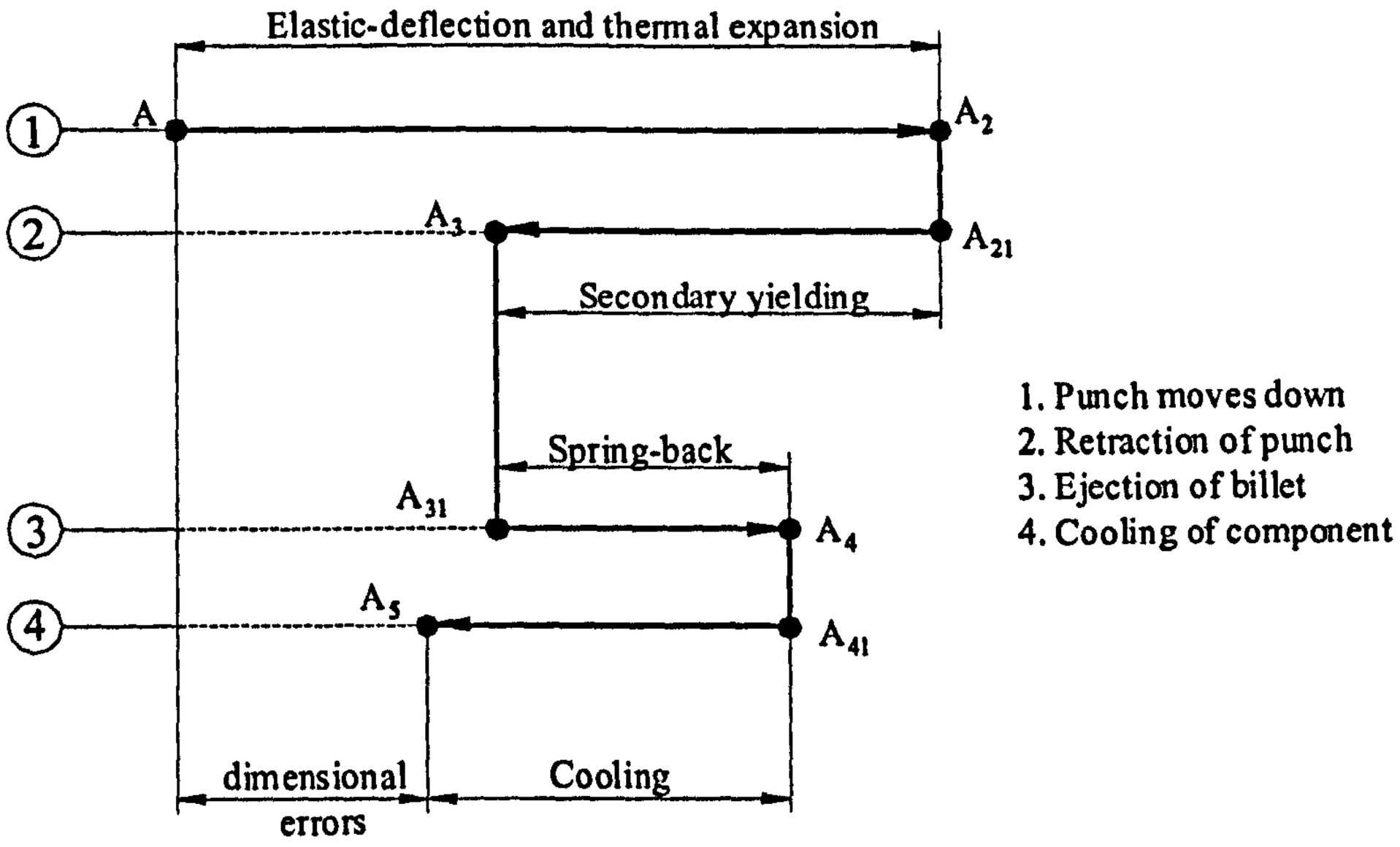

(a) Component-form error cumulation

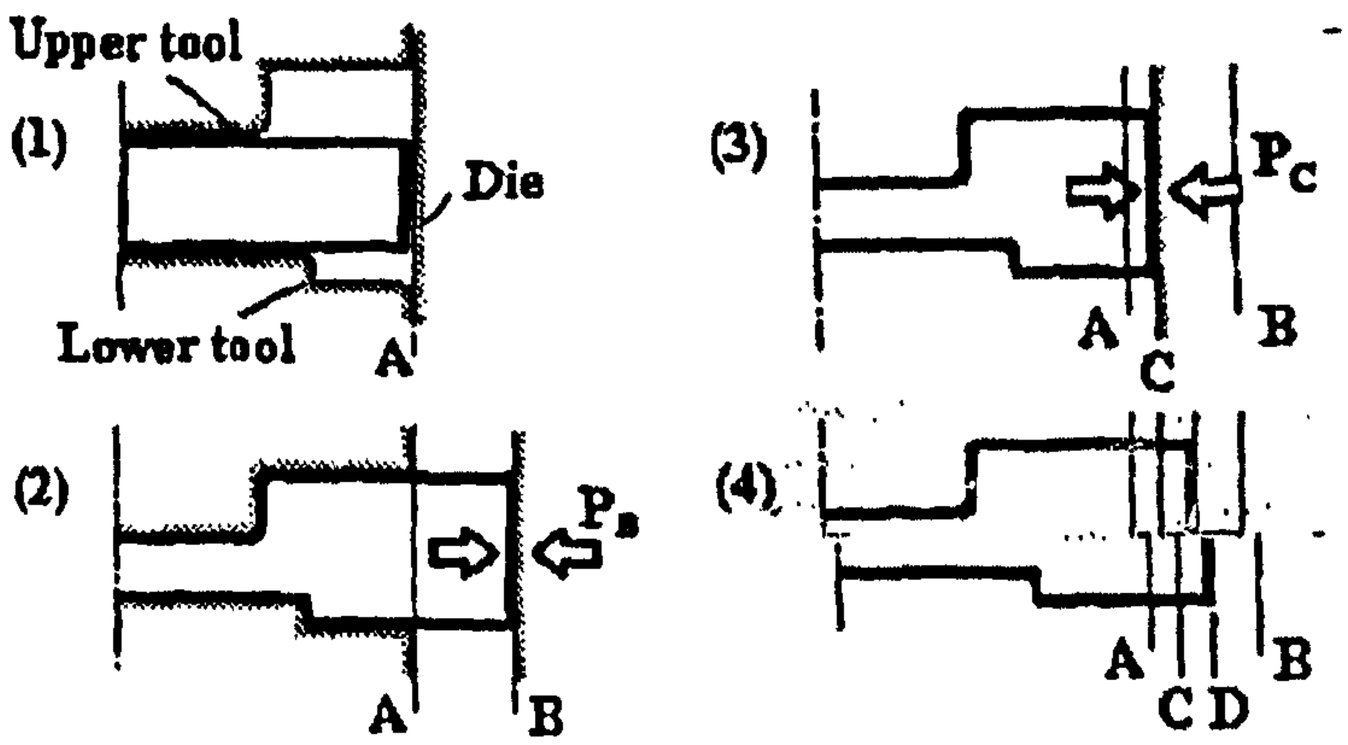

Fig. 1.32 Component-form error cumulation in closed- die-forging

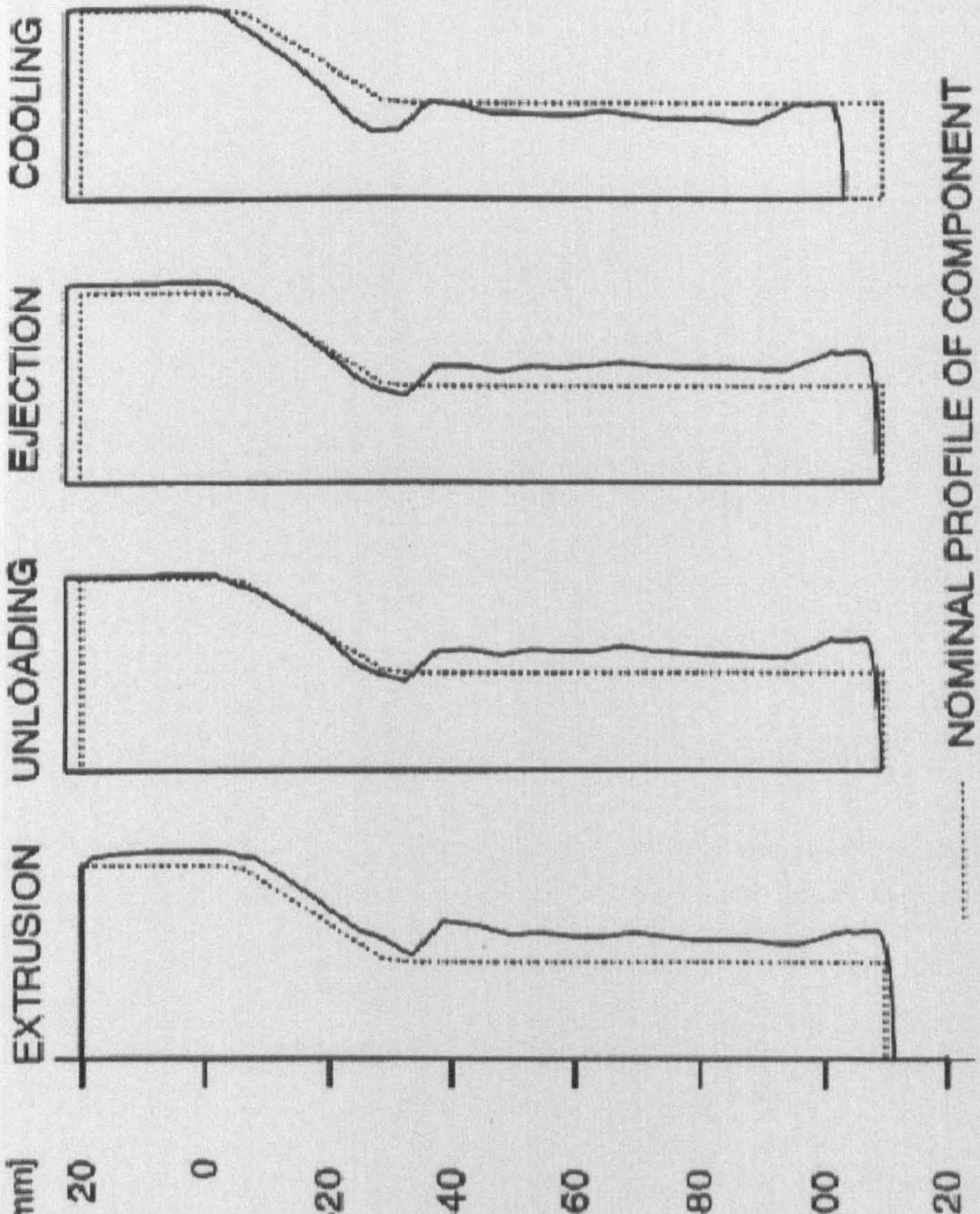

Fig. 1.33 Component-form errors at different forming stage [22]

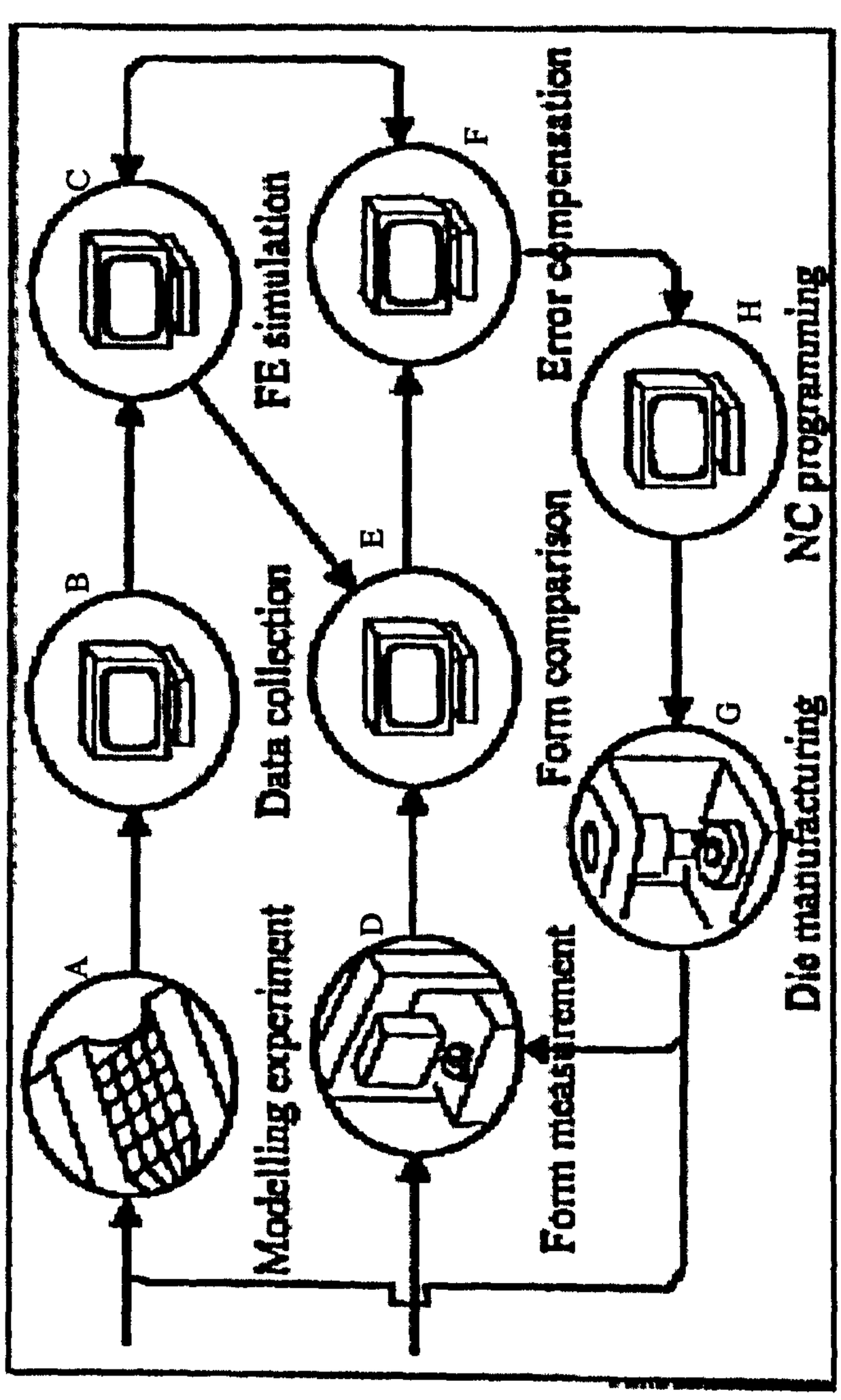

Fig. 1.34 Die elasticity error compensation procedures [24]

Diagrams for Chapter Two

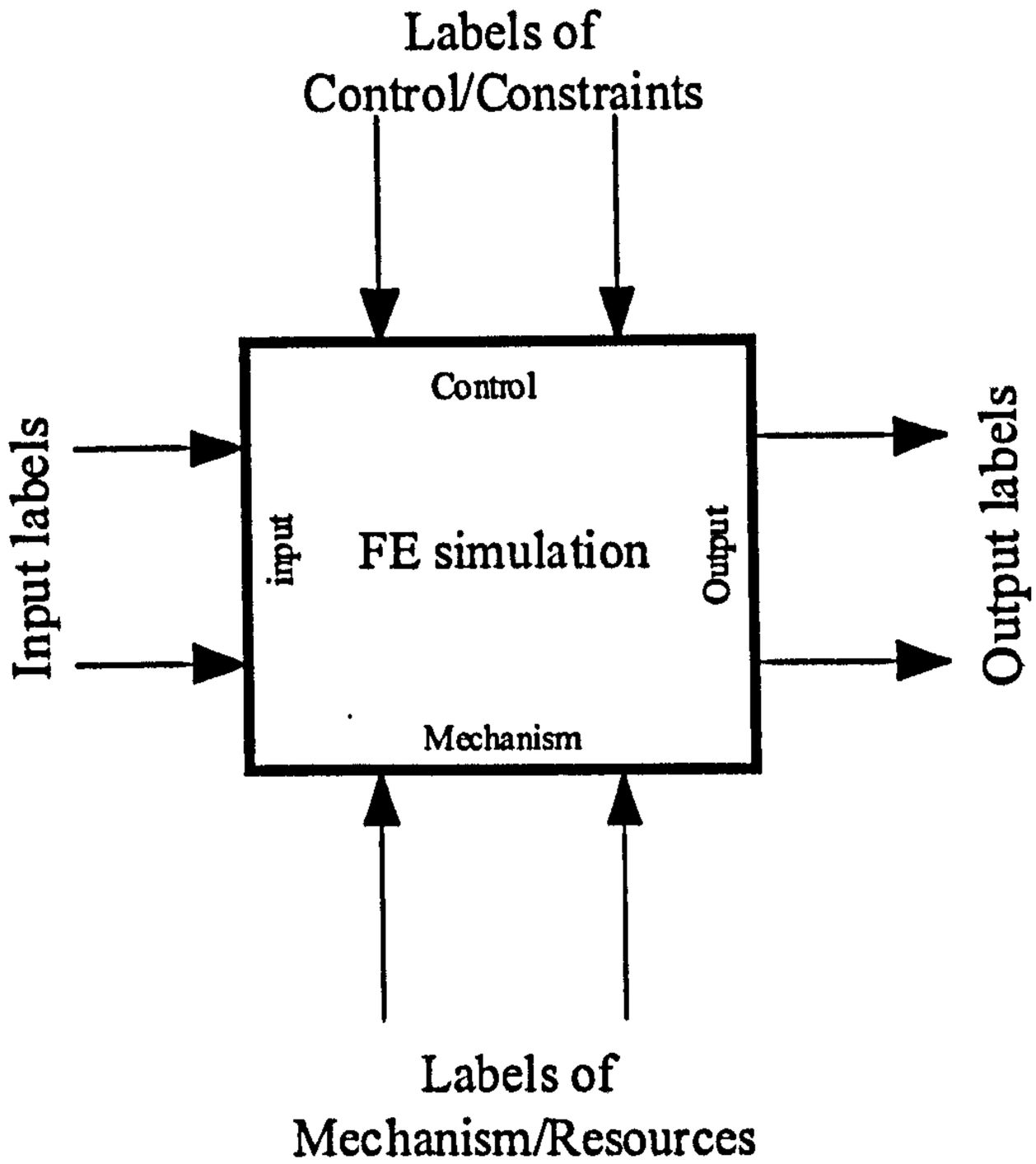

Fig. 2.1 Activity box and interfaces

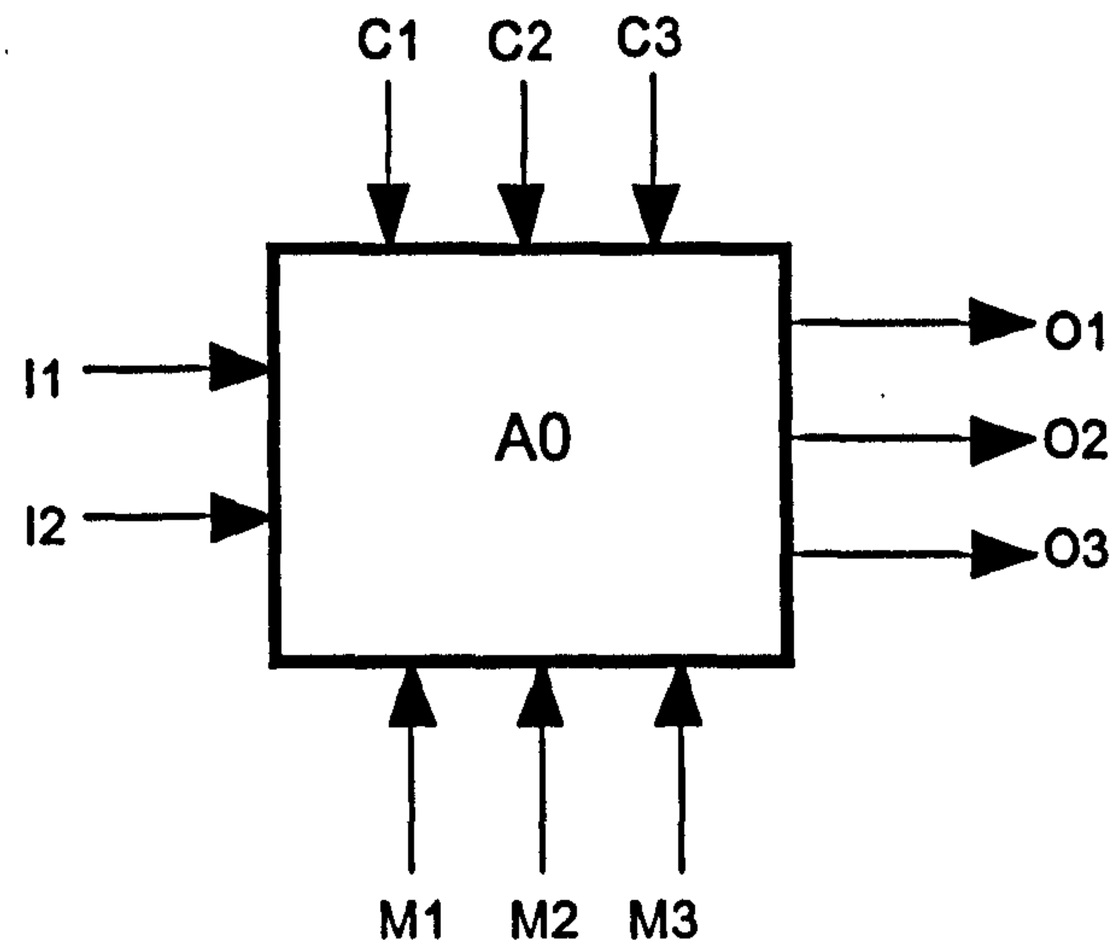

Fig. 2.2 Model of Activity A0

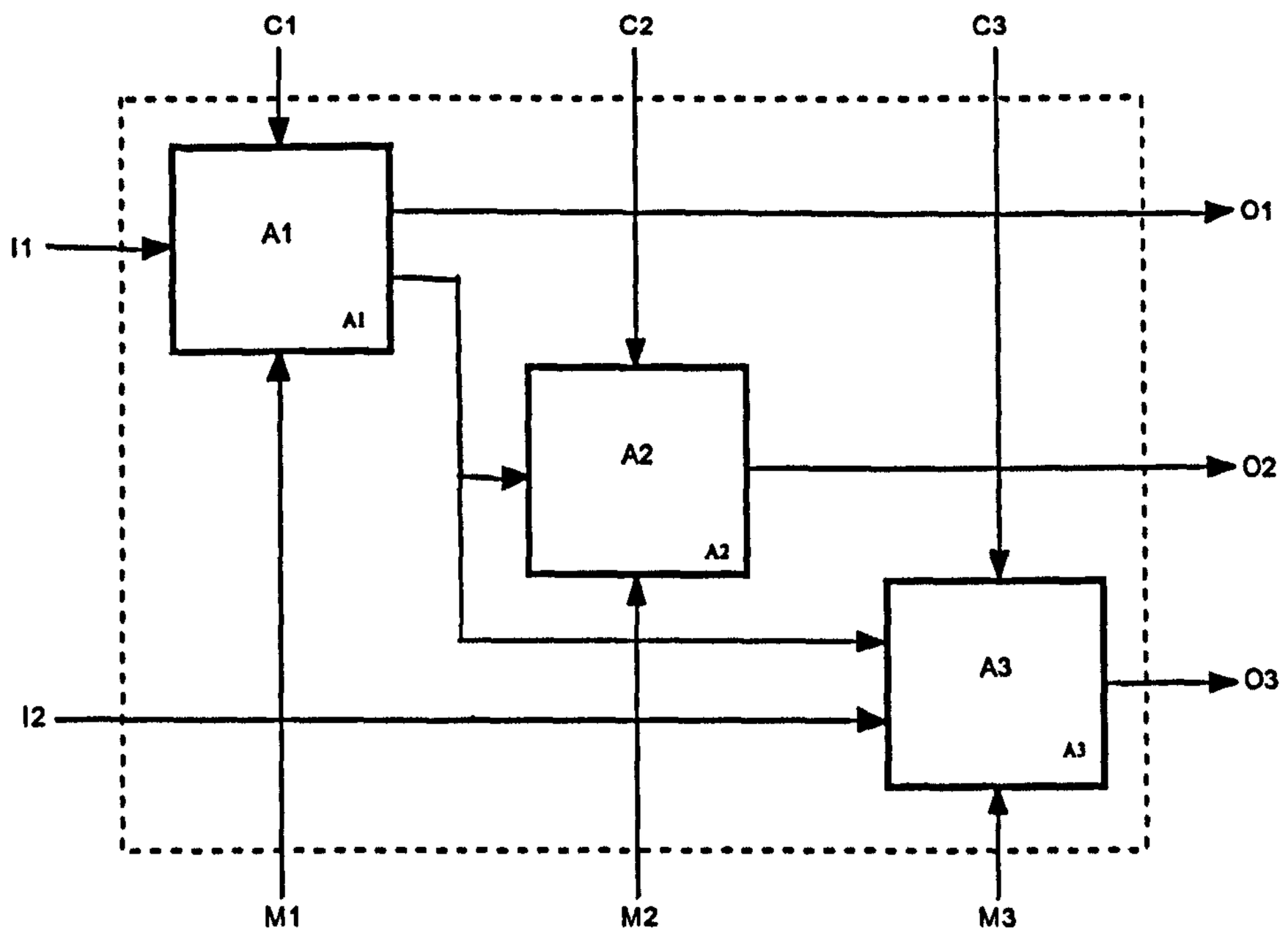

Fig. 2.3 Decomposition of activity A0

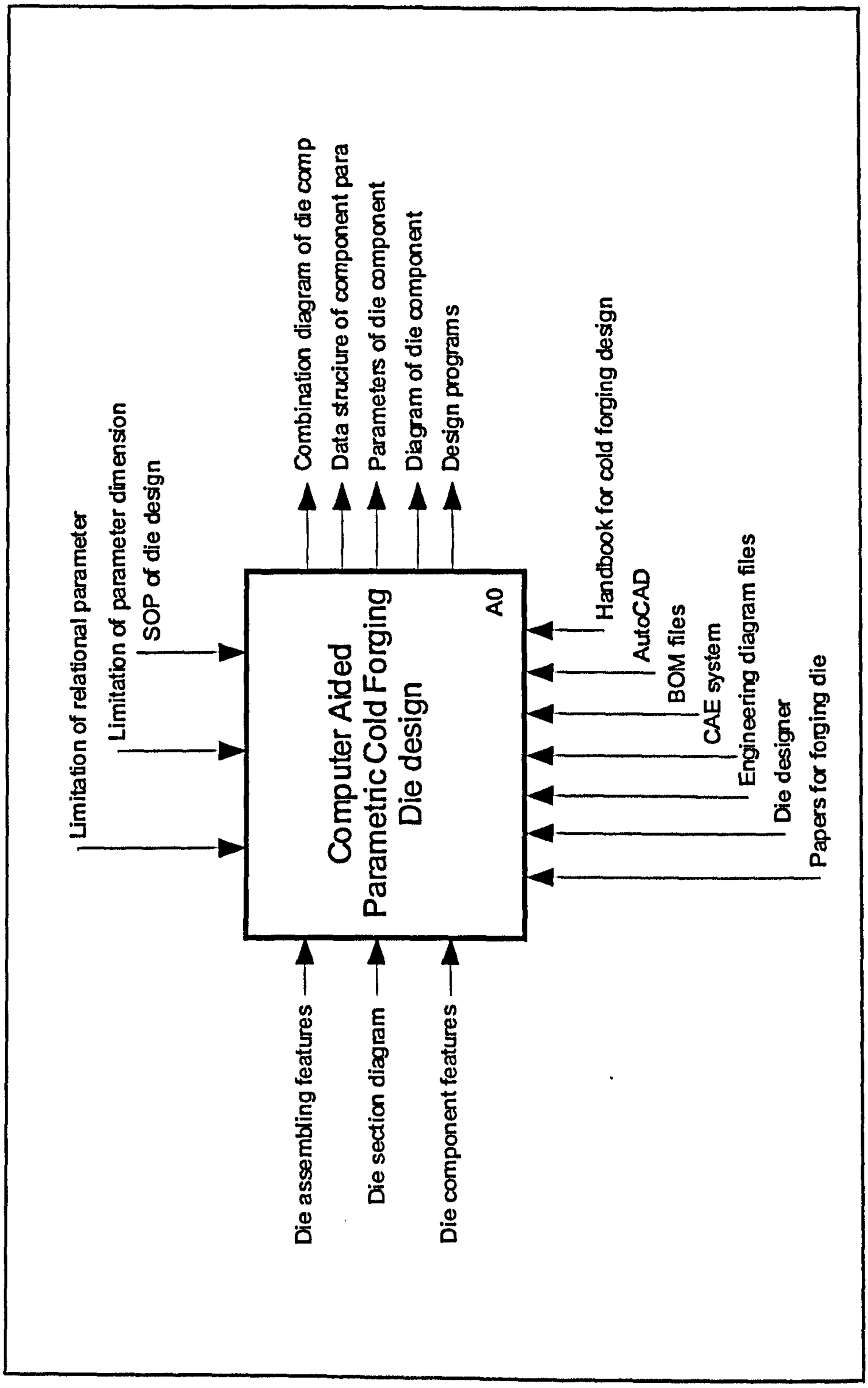

Fig. 2.4 The first layer of the parametric computer-aided die-design system (extracted from Ref [15])

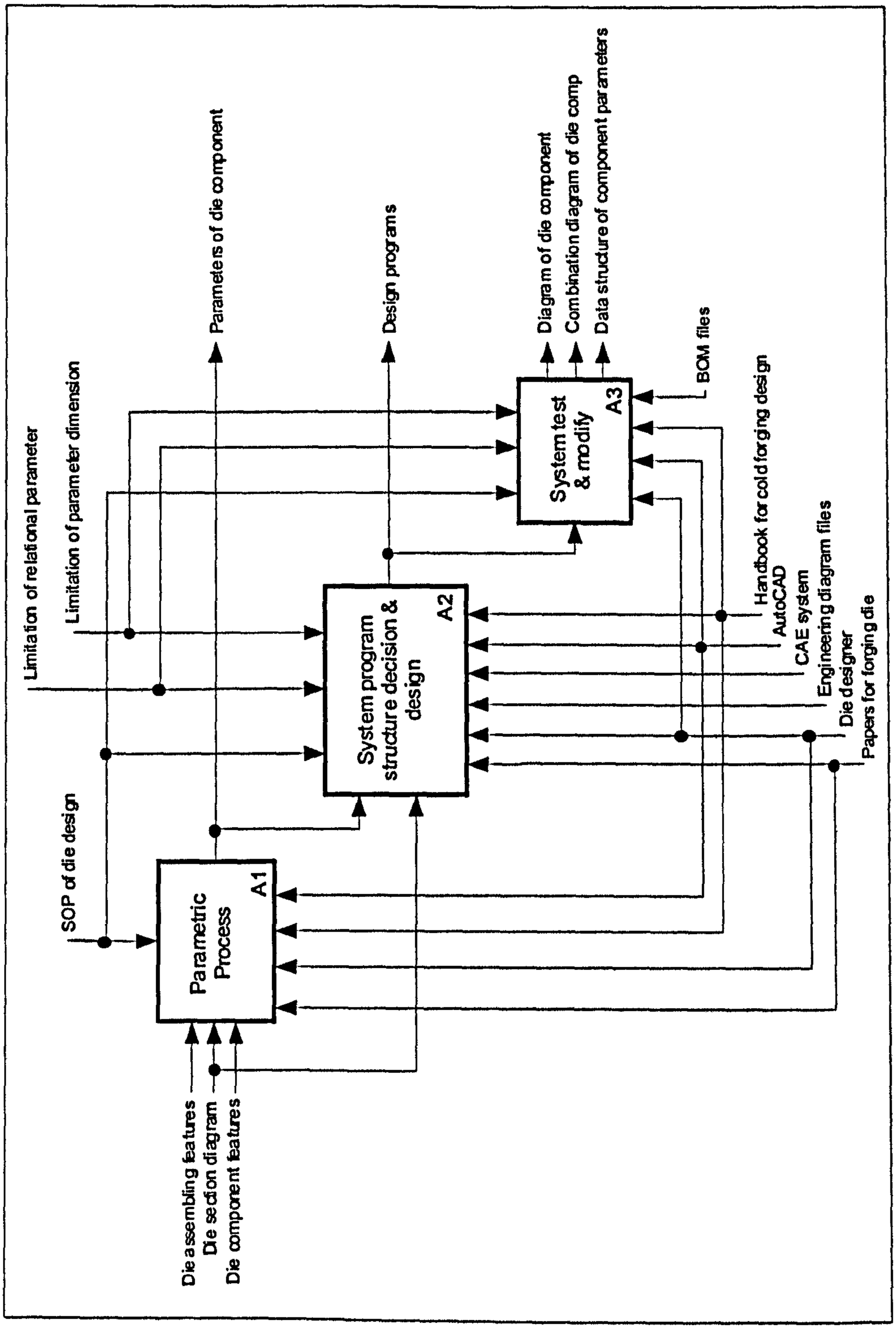

Fig. 2.5 Decomposing of cold-forging die design system (extracted from Ref [15])

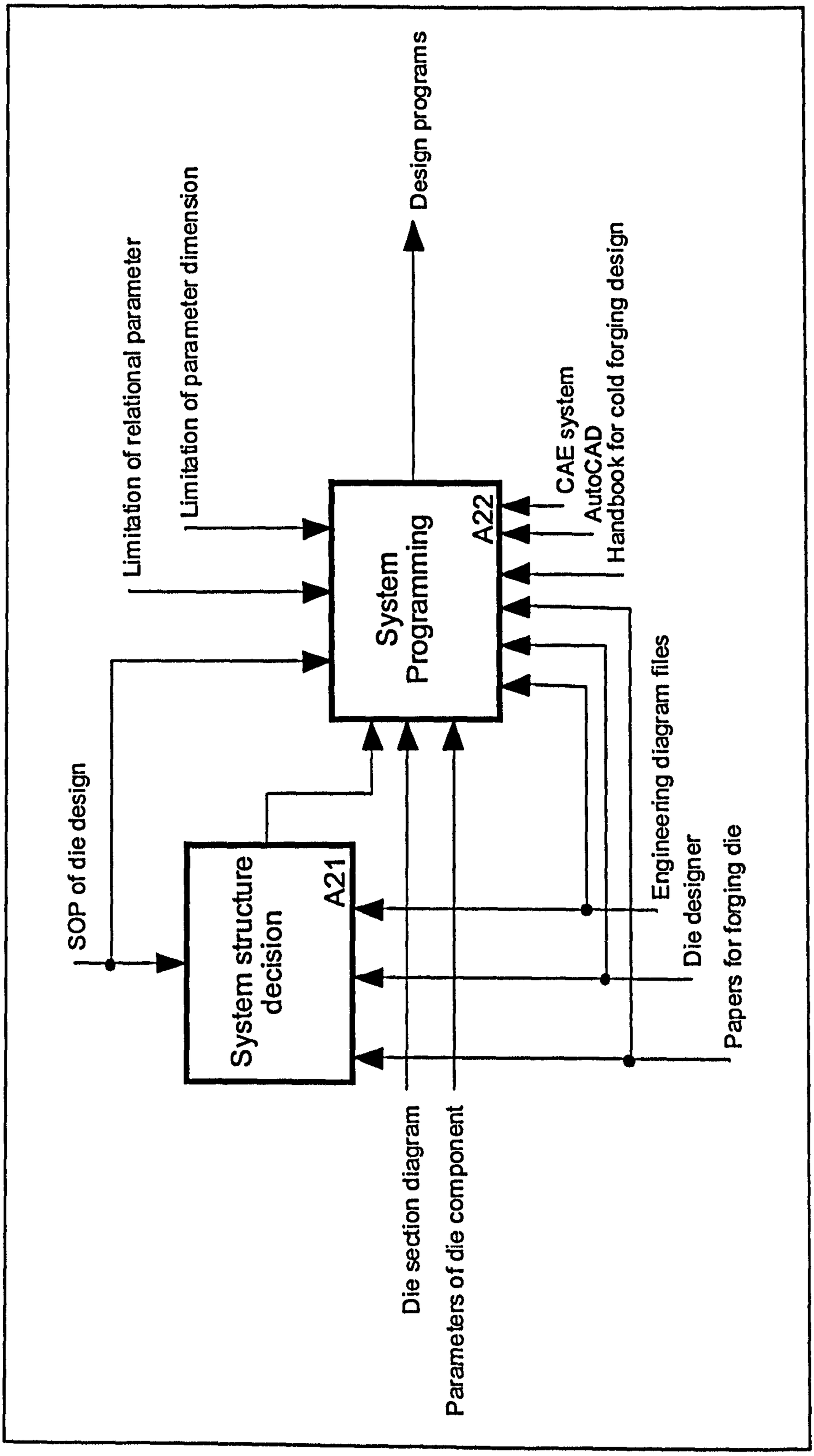

Fig. 2.6 The third layer of decomposition (extracted from Ref [15])

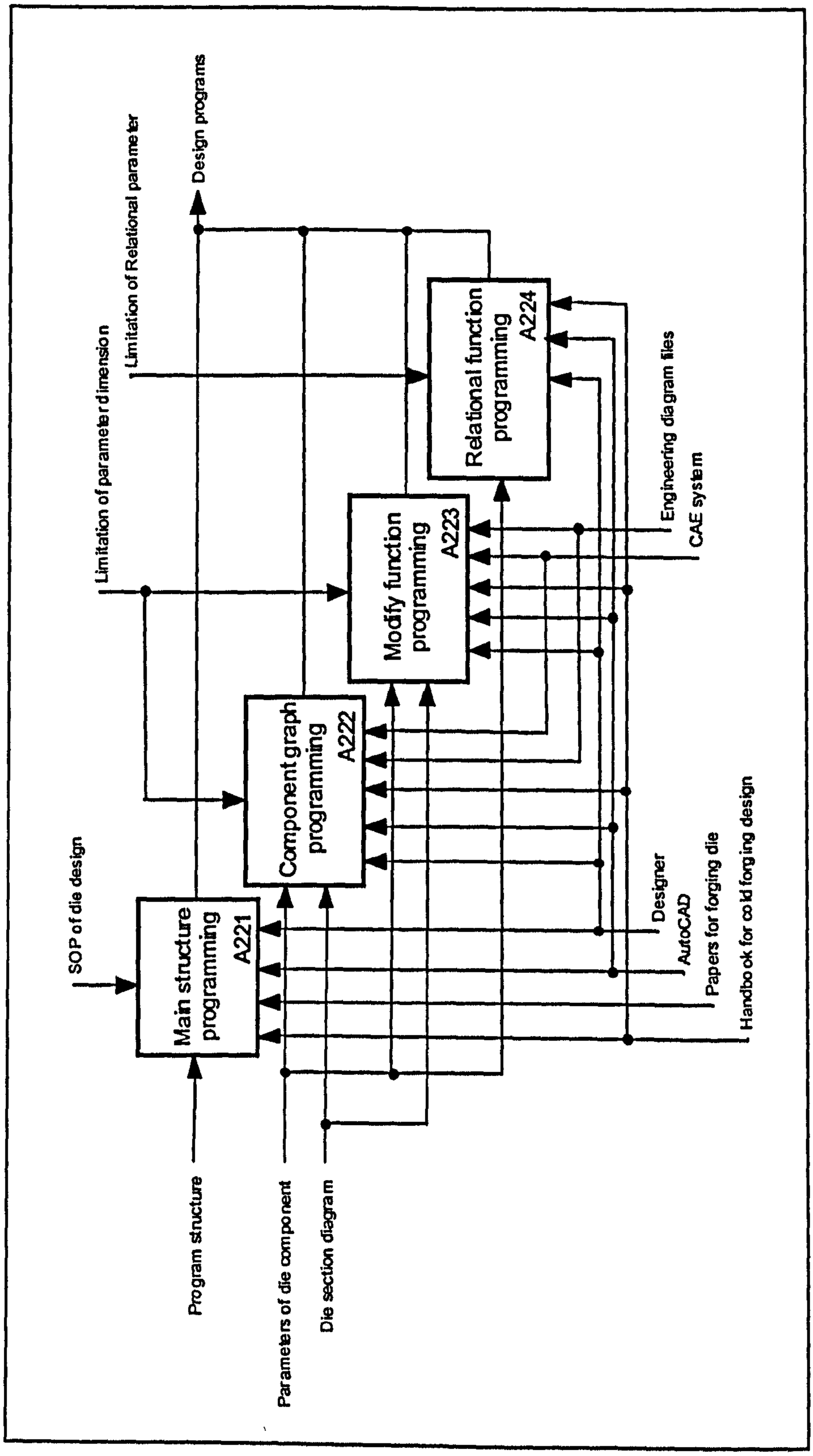

Fig. 2.7 The decomposition of activity A22
(extracted from Ref [15])

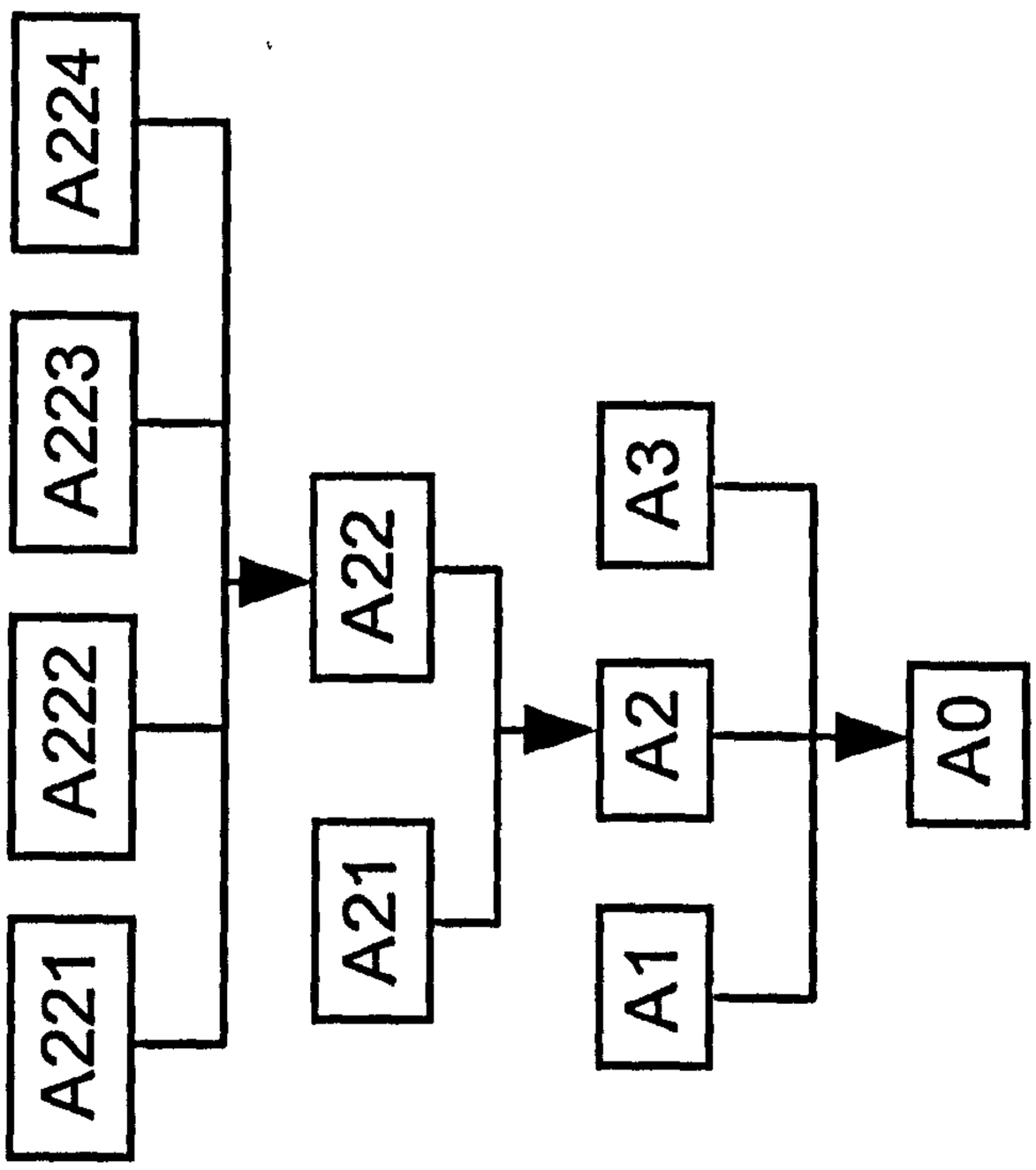

Fig. 2.8 Decision-tree of the computer-aided die design system (extracted from Ref [15])

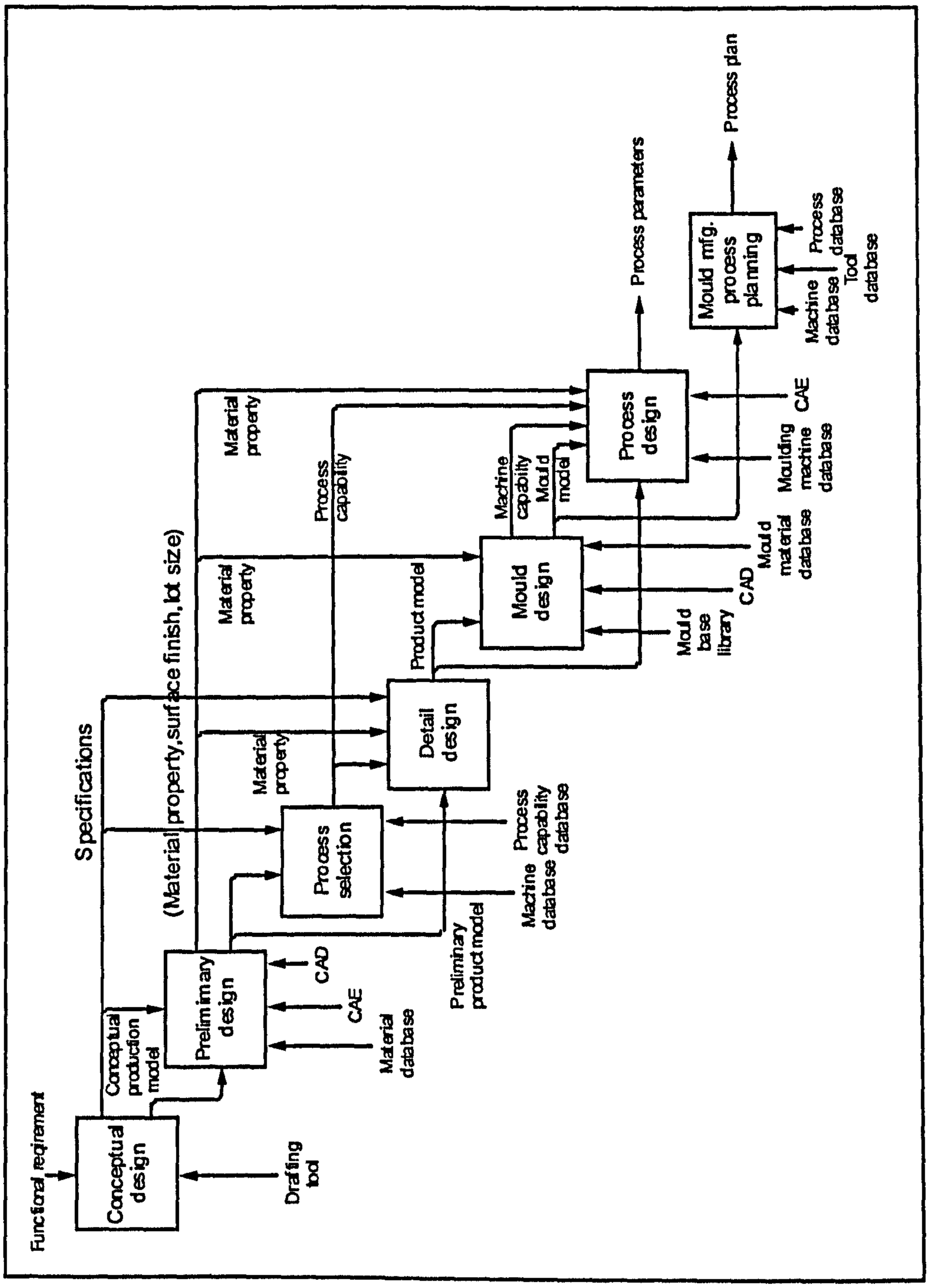

Fig. 2.9 IDEF0 modelling of nett shape casting process
(extracted from Ref [9])

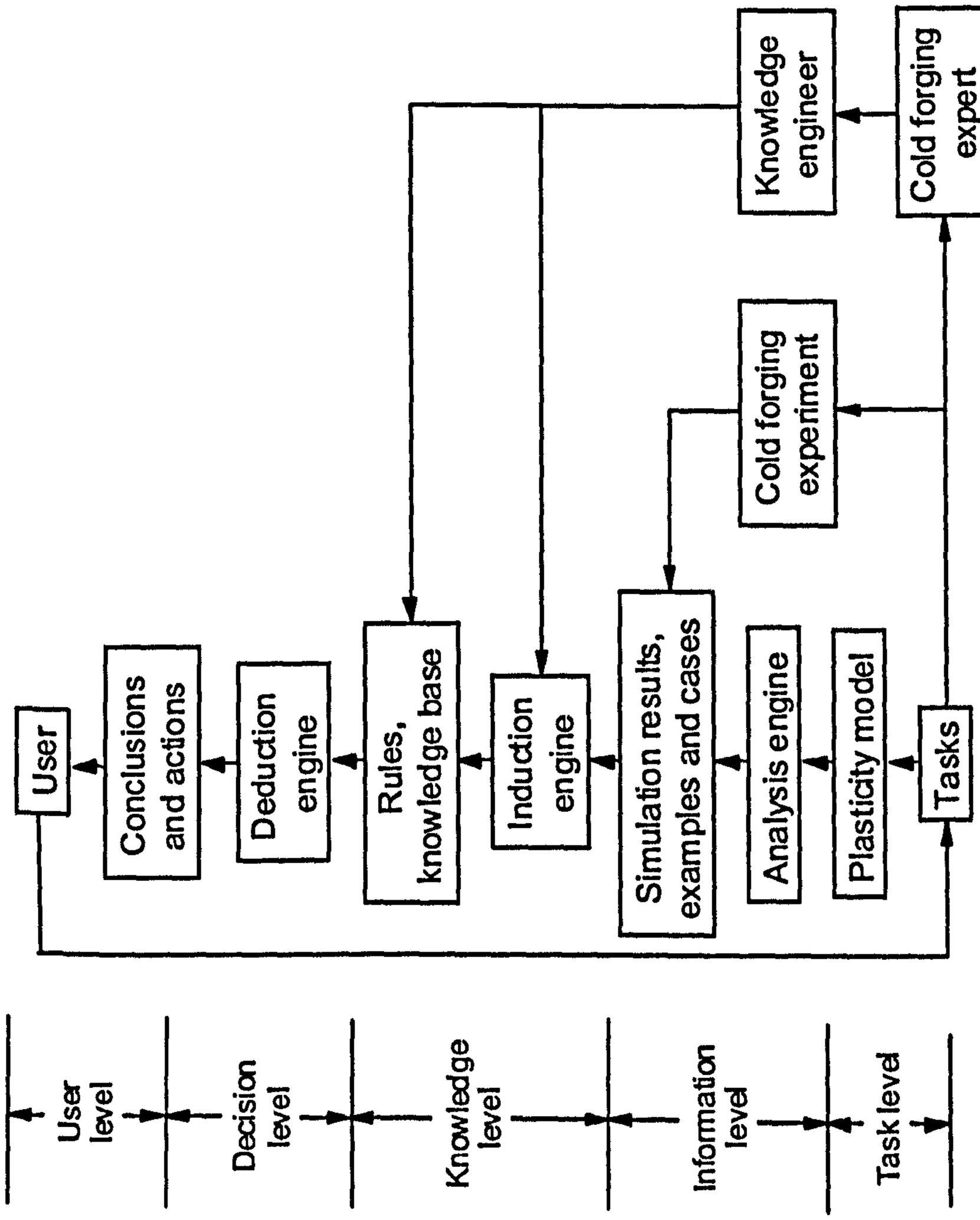

Fig. 2.10 Decision-making framework for intelligent cold forging (extracted from Ref [16])

USED AT:	AUTHOR:		DATE:	
	PROJECT:		PAGE:	
			LEVEL:	top

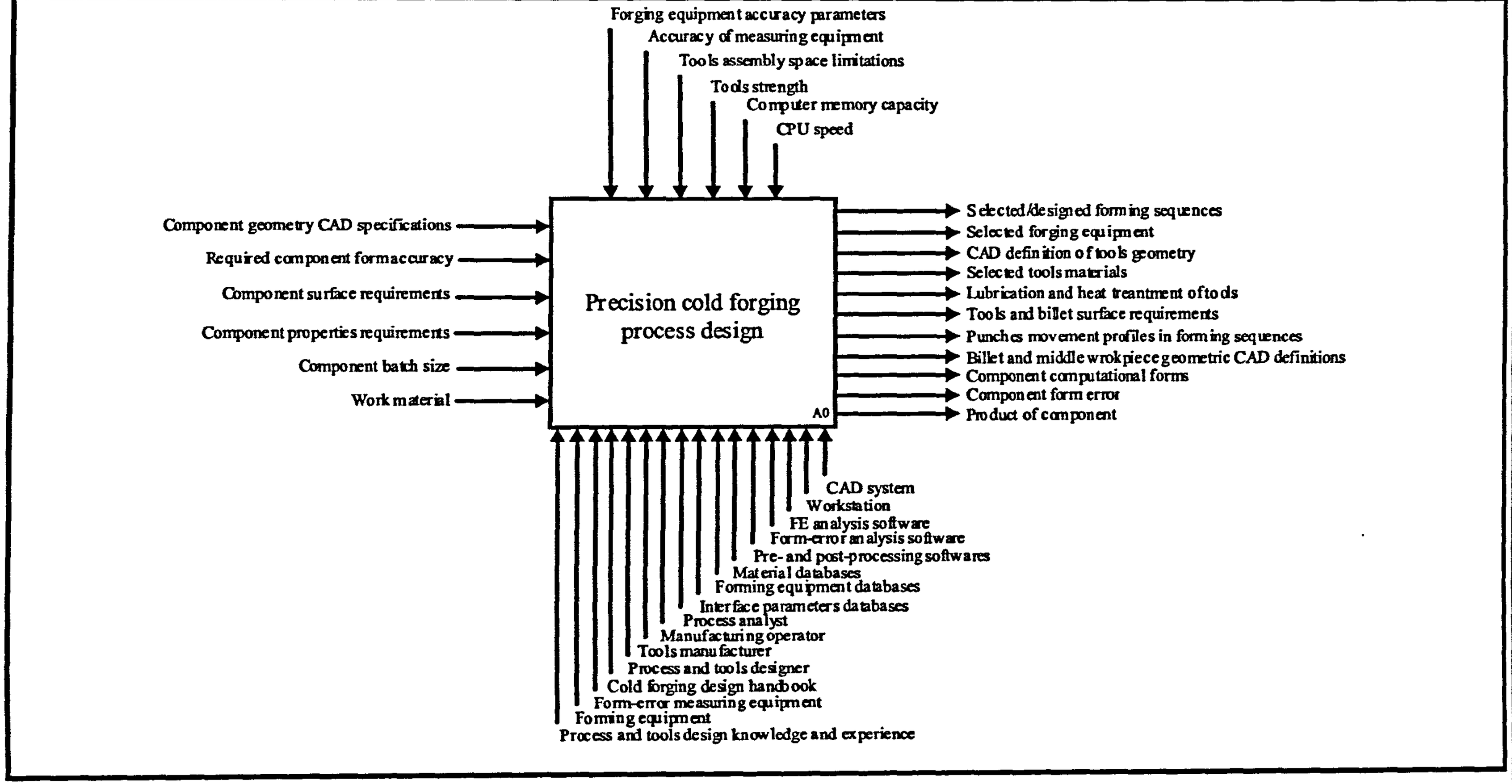

Fig. 2.11 Level zero of precision cold forming process design

USED AT:	AUTHOR:		DATE:	
	PROJECT:		PAGE:	
			LEVEL:	A0

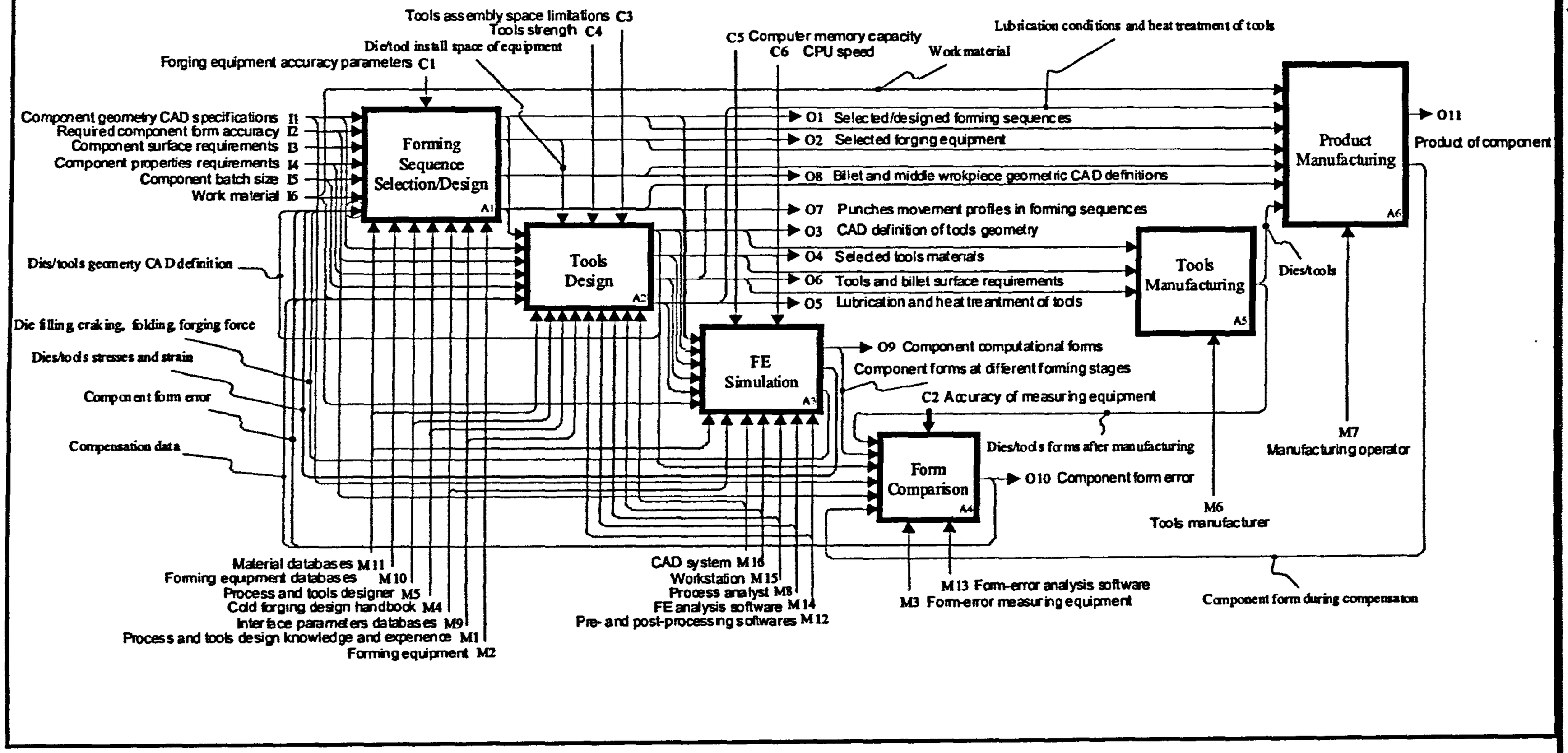

Fig. 2.12 The Sub-level of process modelling

USED AT:	AUTHOR:		DATE:	
	PROJECT:		PAGE:	
			LEVEL:	A2

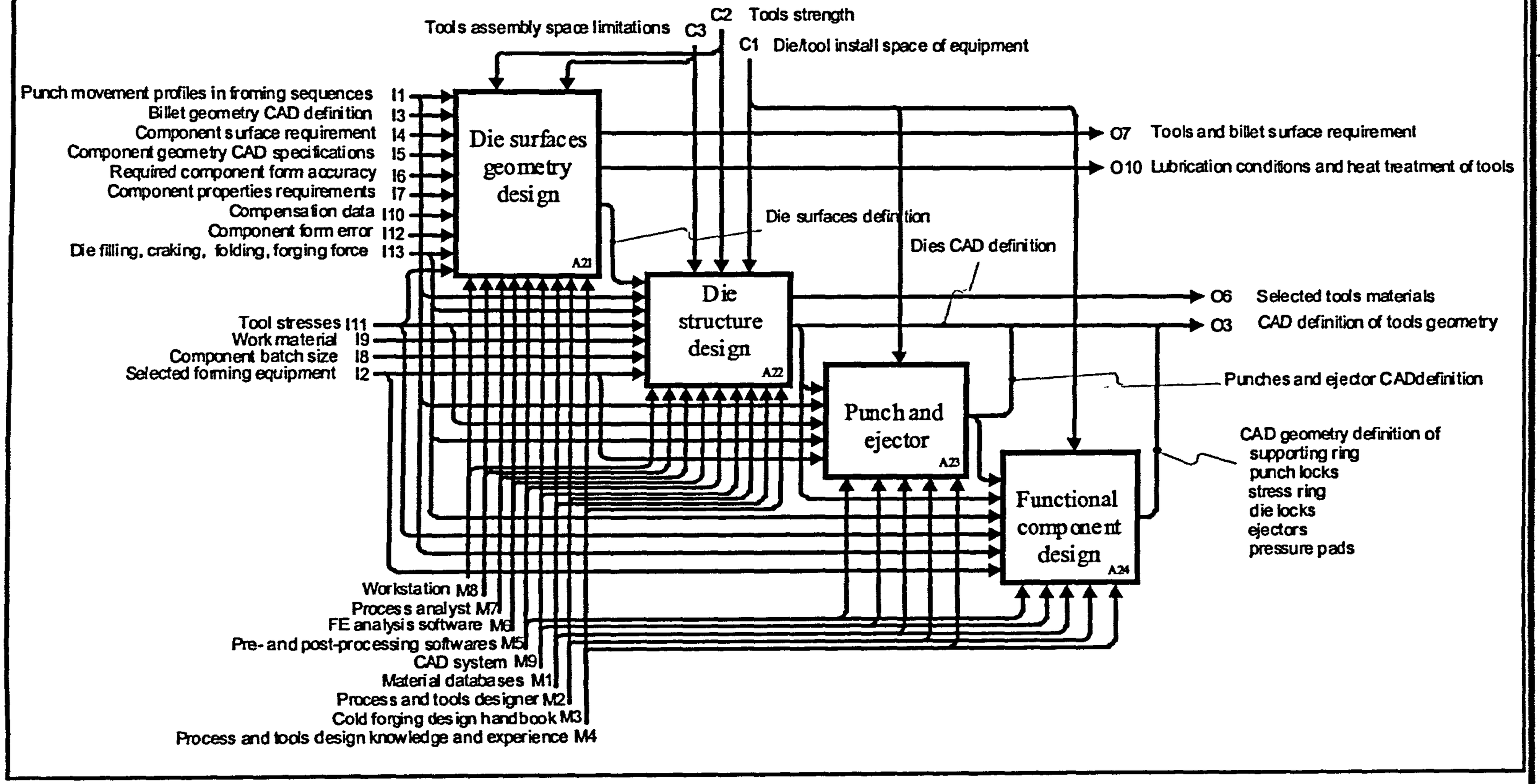

Fig. 2.13 Tool design modelling

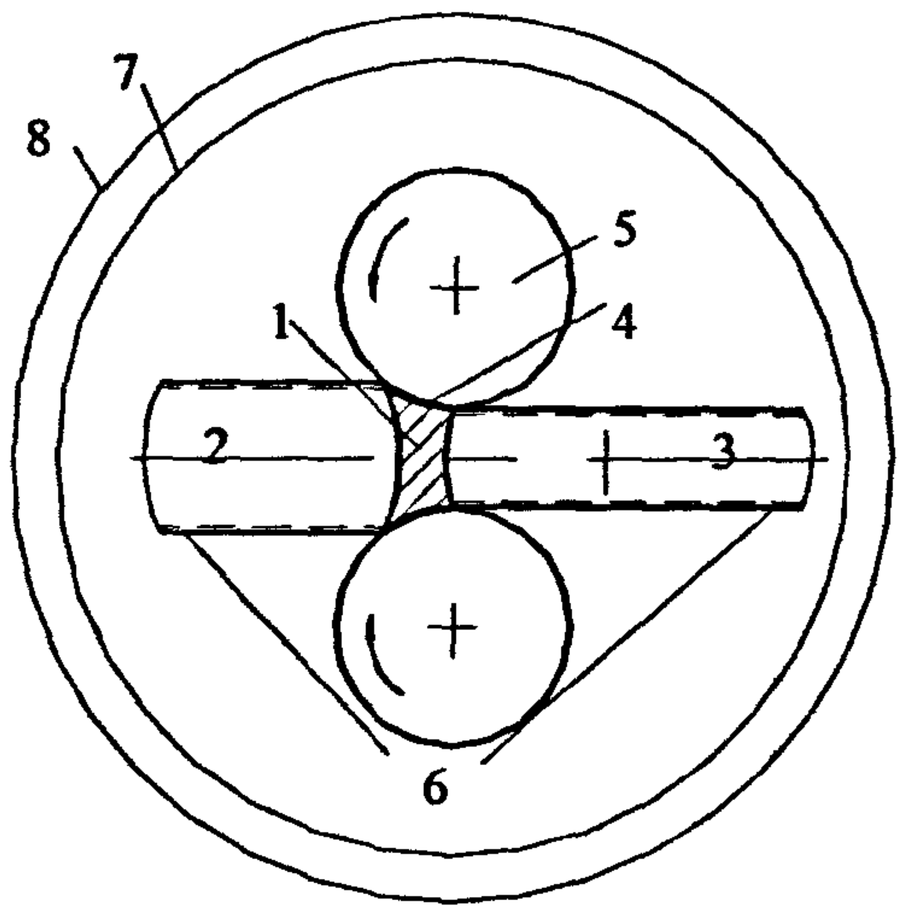

(a)

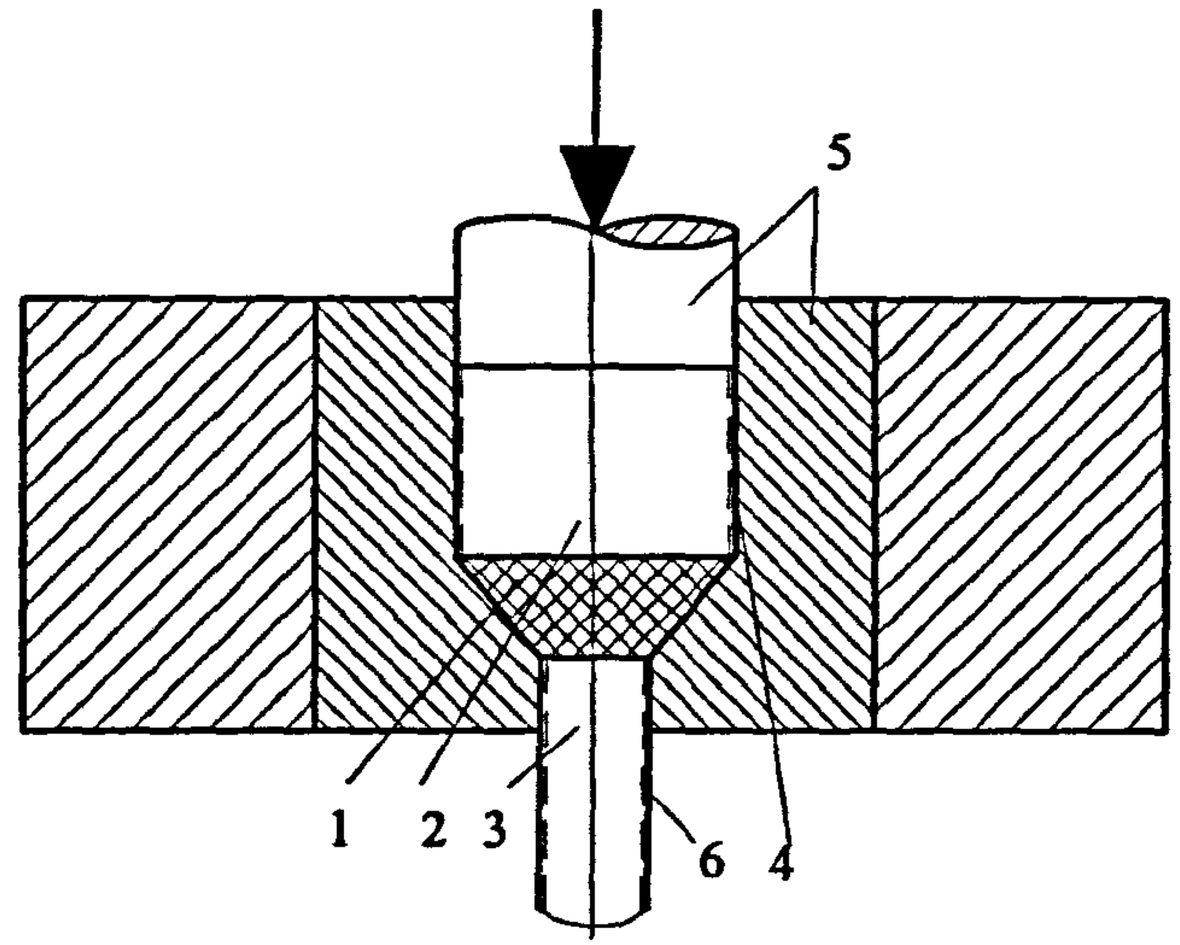

(b)

1. Plastic zone; 2. Stock material; 3. Component material;
4. Tool/work-material interface; 5. Tool; 6. Work- and component-material/environment interface;
7. Forming equipment; 8. External services

Fig. 2.14 System of approach to metal-forming problems
(extracted from Ref [18])

USED AT:	AUTHOR:		DATE:	
	PROJECT:		PAGE:	
			LEVEL:	A21

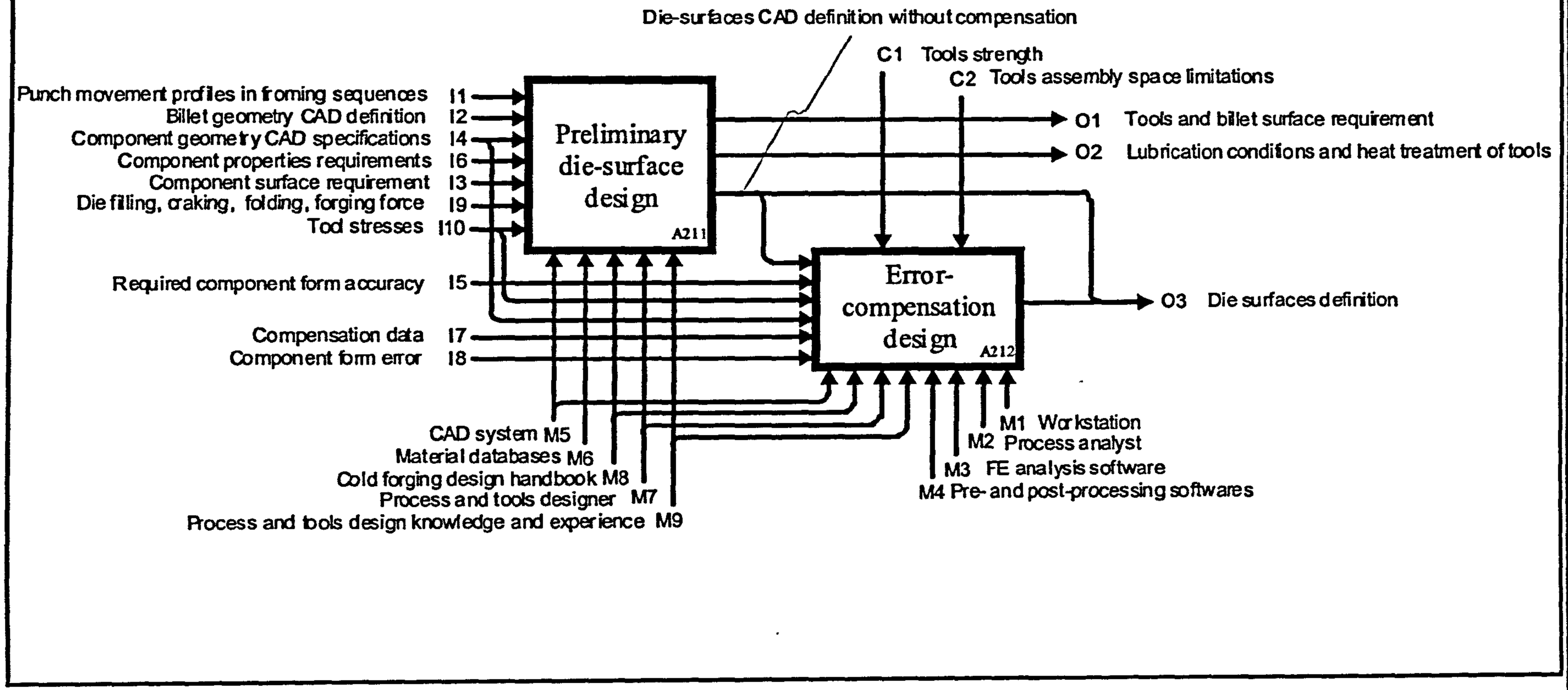

Fig. 2.15 Die surface geometry design modelling

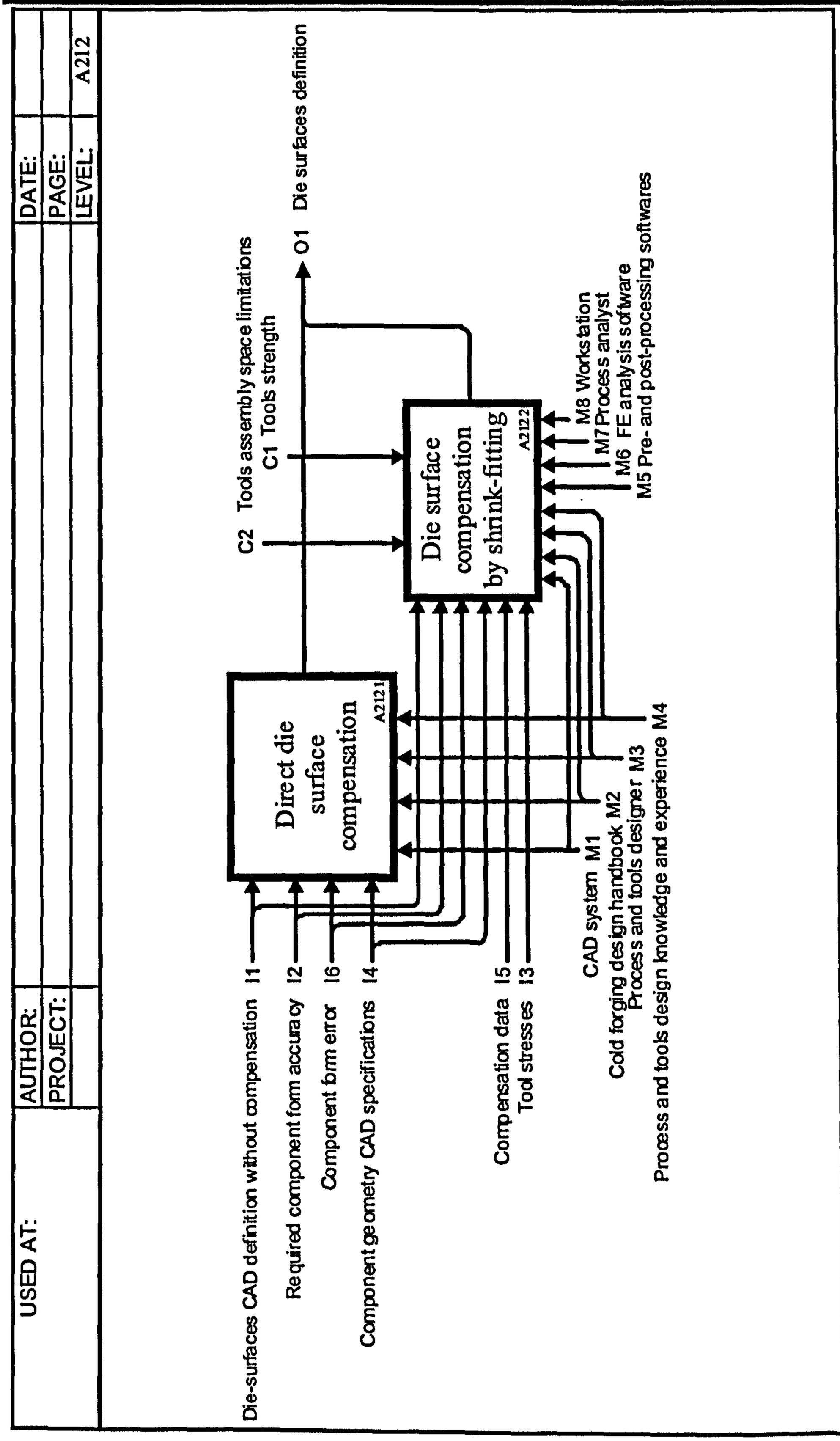

Fig. 2.16 Form-error compensation design

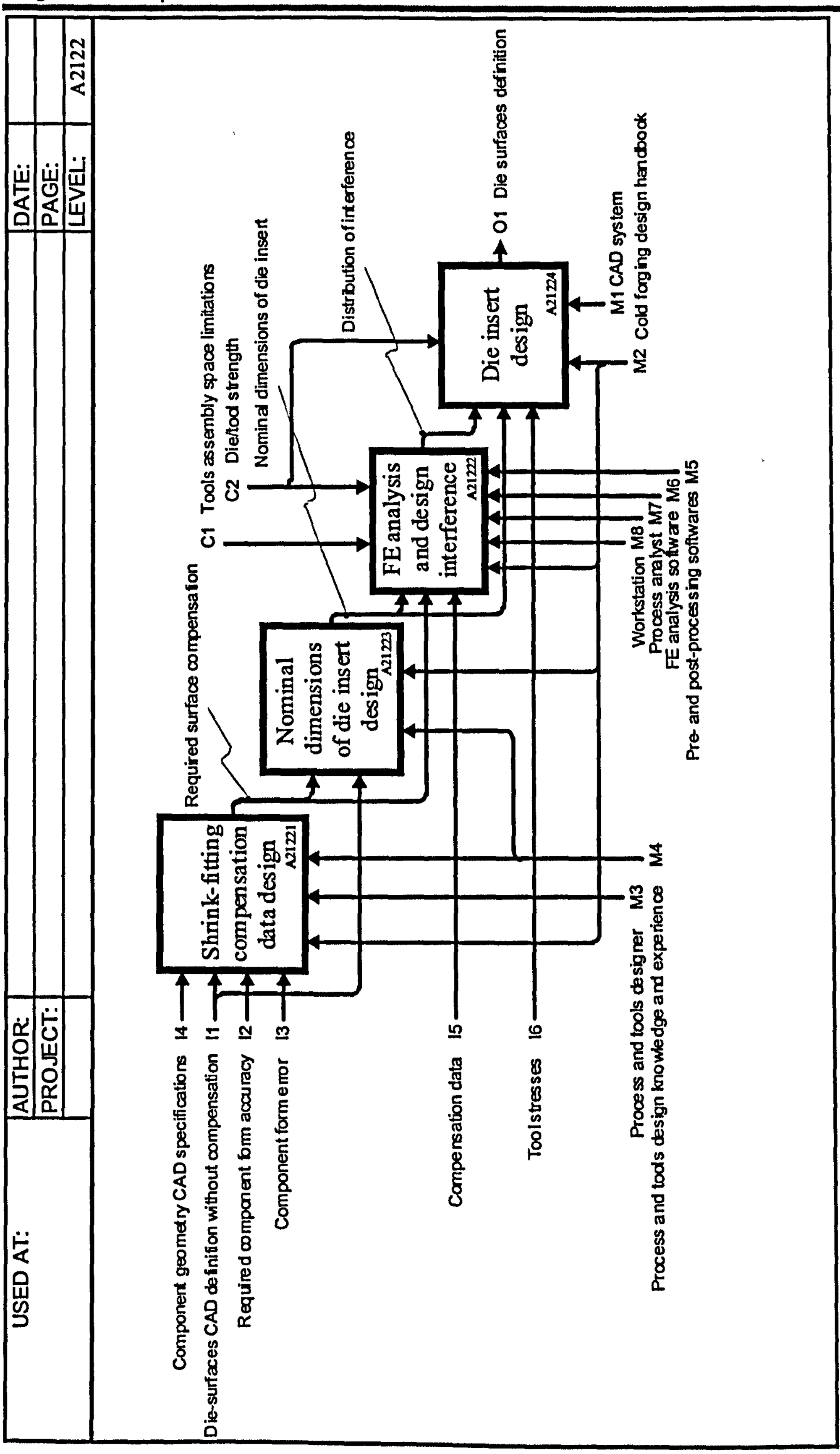

Fig. 2.17 Shrink-fitted die surface design modelling

USED AT:	AUTHOR:		DATE:	
	PROJECT:		PAGE:	
			LEVEL:	A3

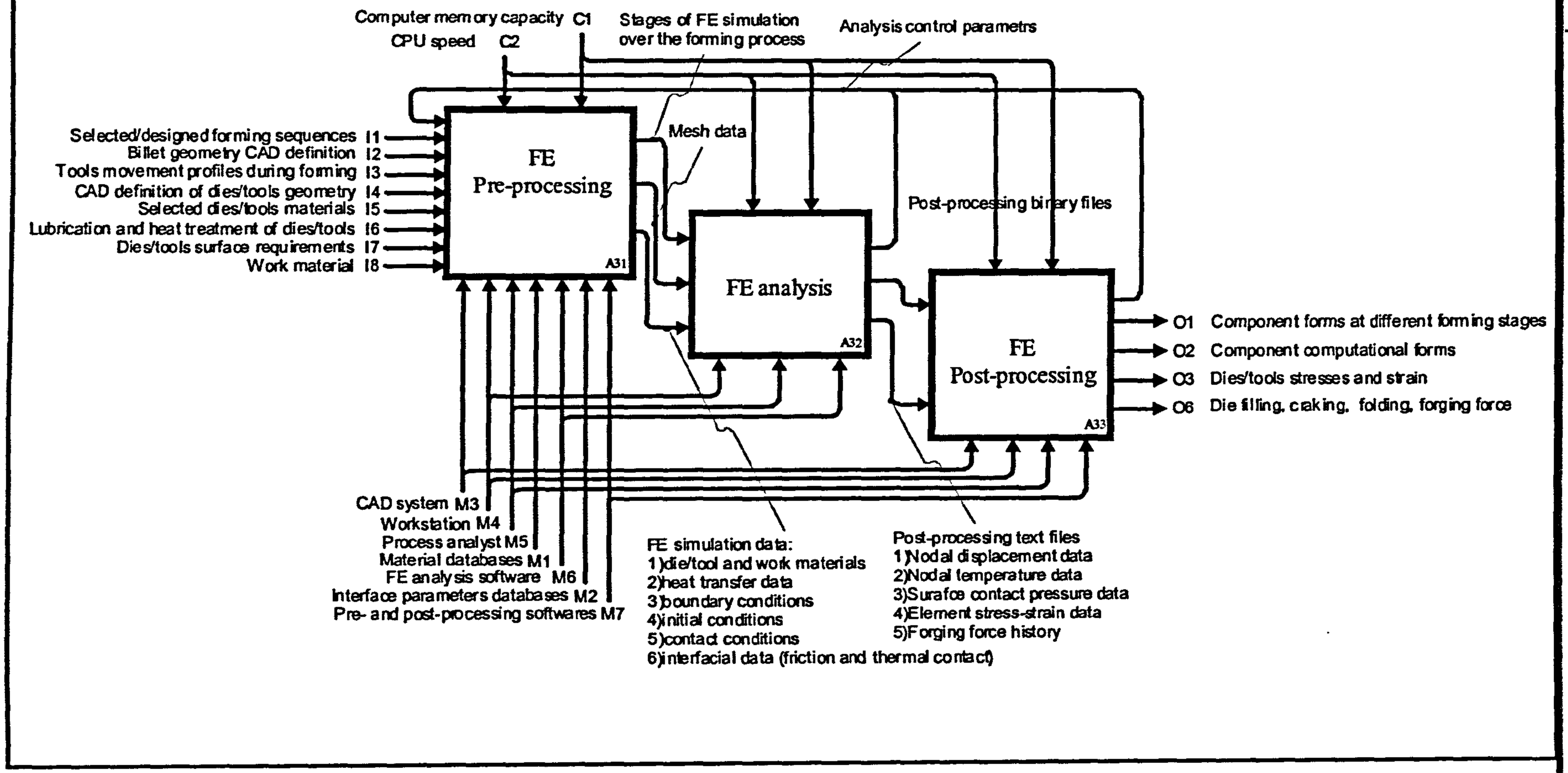

Fig. 2.18 FE simulation process modelling

USED AT:	AUTHOR:		DATE:	
	PROJECT:		PAGE:	
			LEVEL:	A4

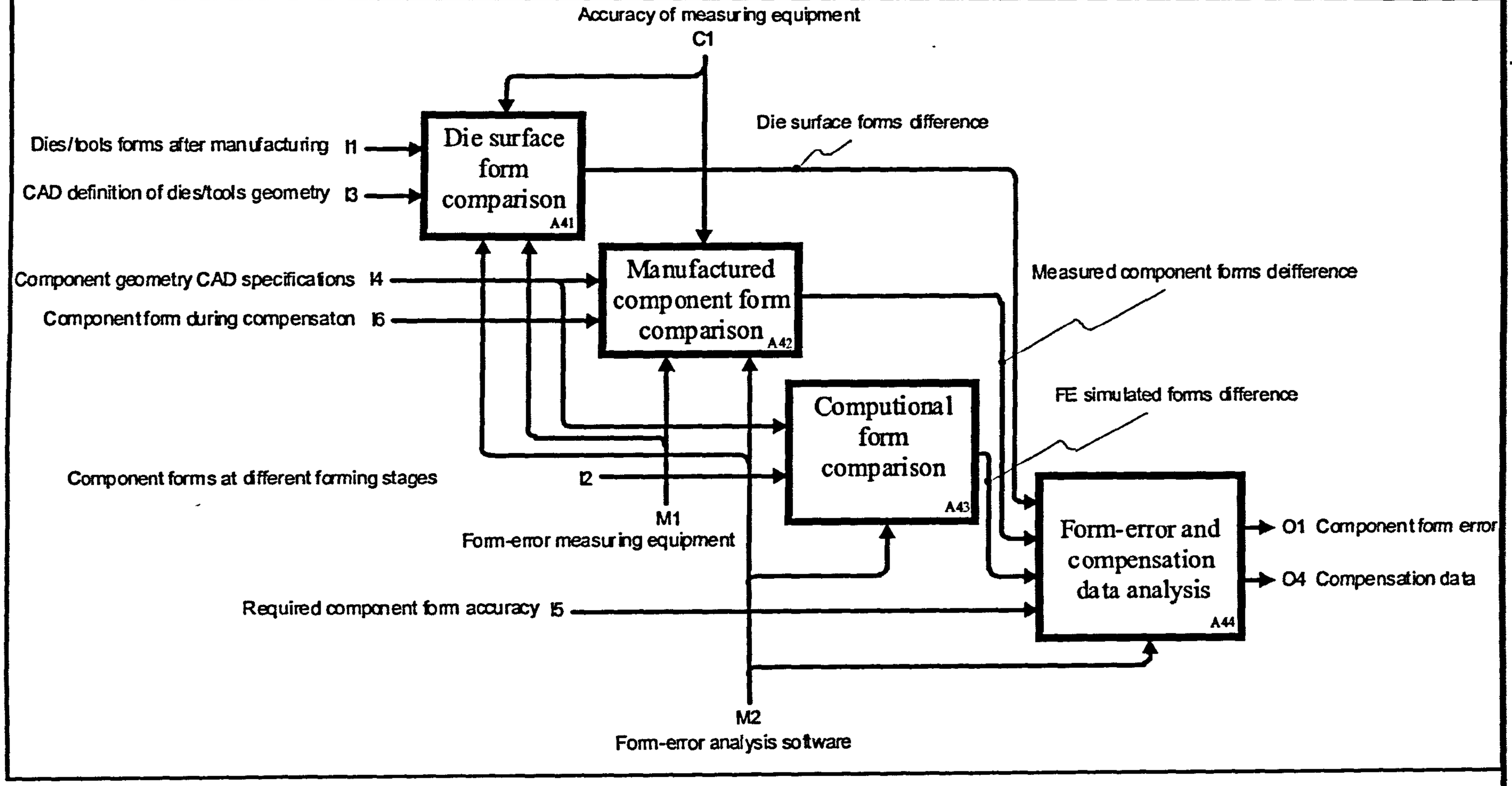

Fig. 2.19 Forms comparison decomposition

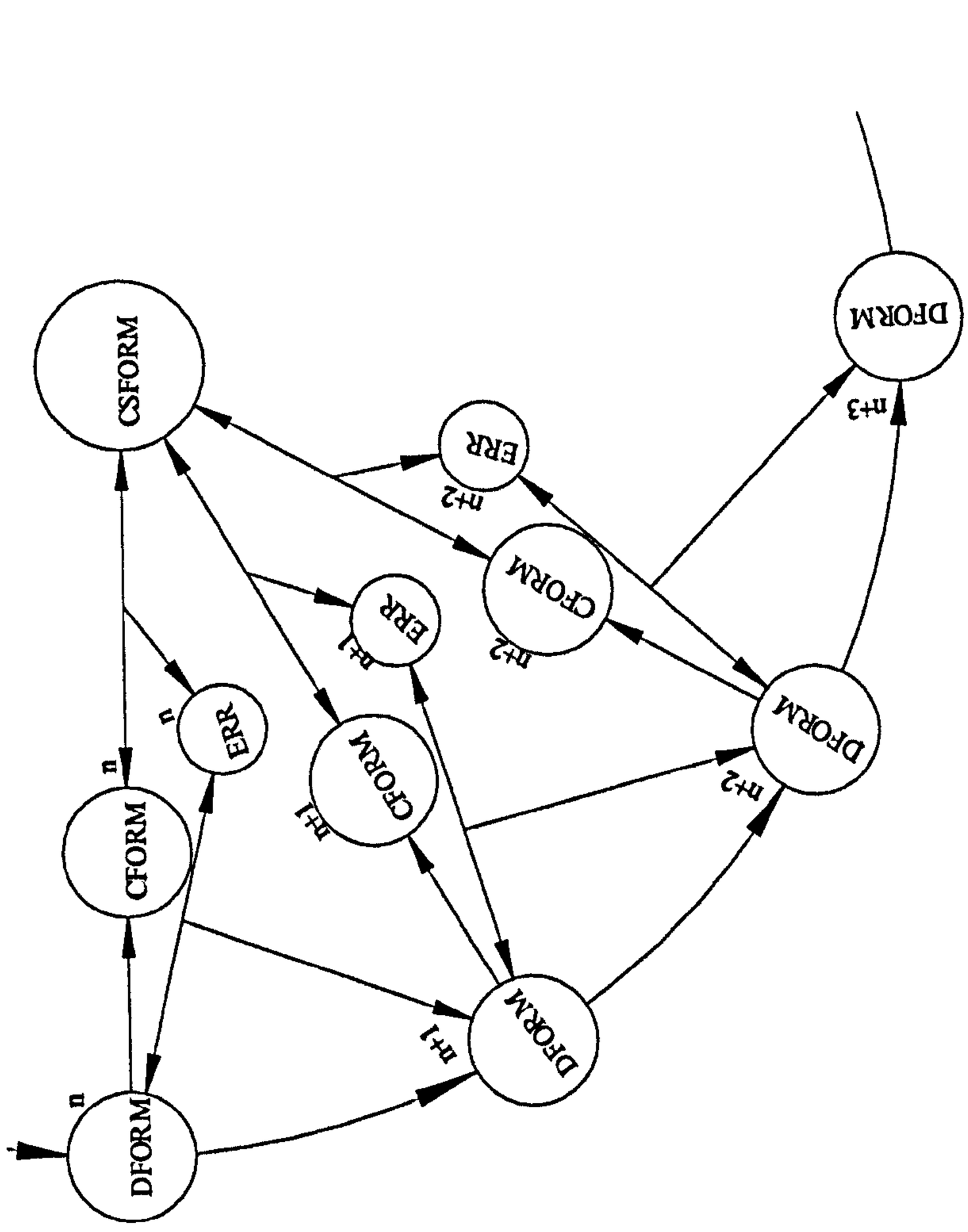

Fig. 2.20 The iteration process of component form-error compensation proce

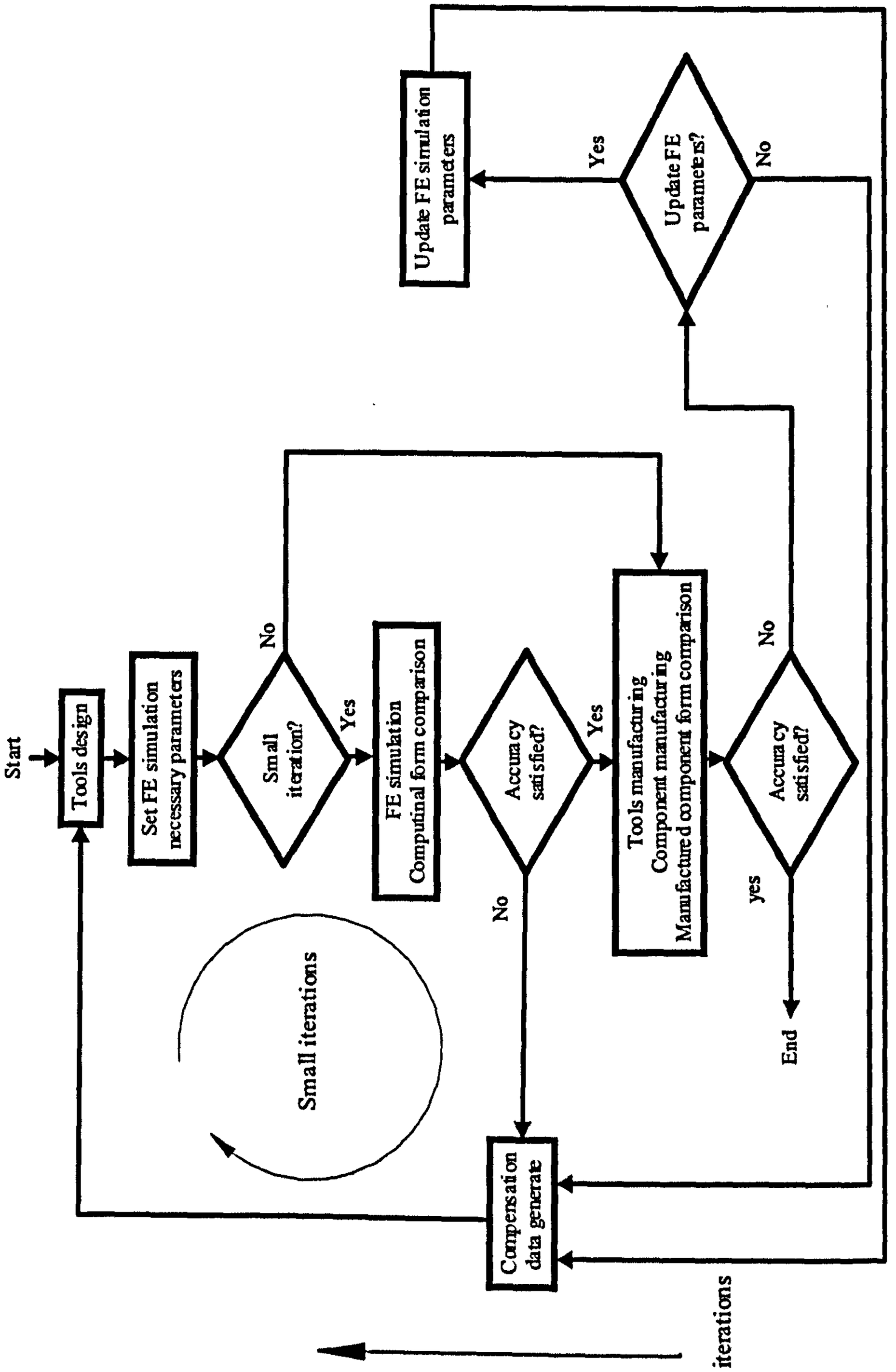

Fig. 2.21 Big and small iterations for precision cold forming design

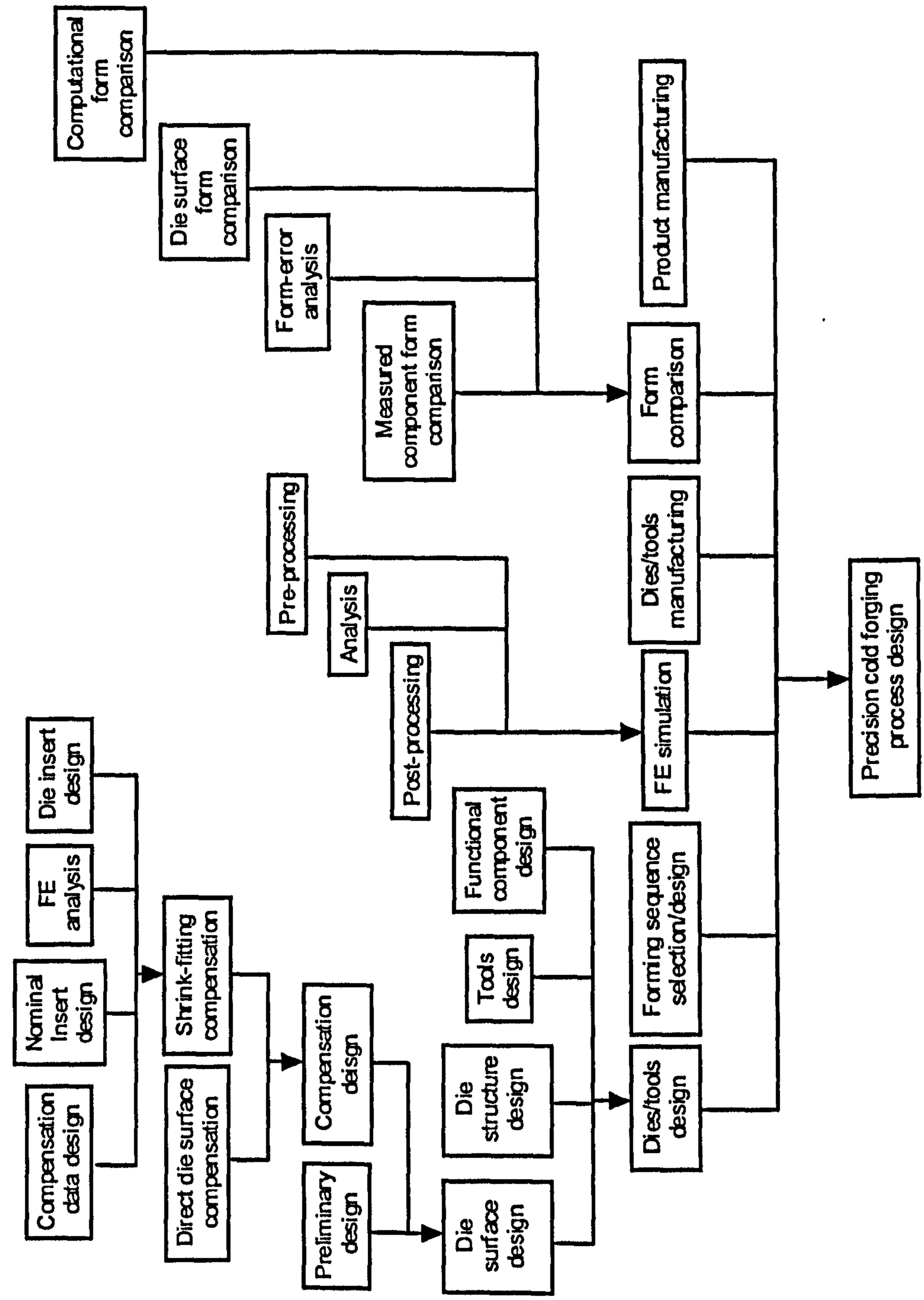

Fig. 2.22 Decision-tree of precision cold forming process design

Diagrams for Chapter Three

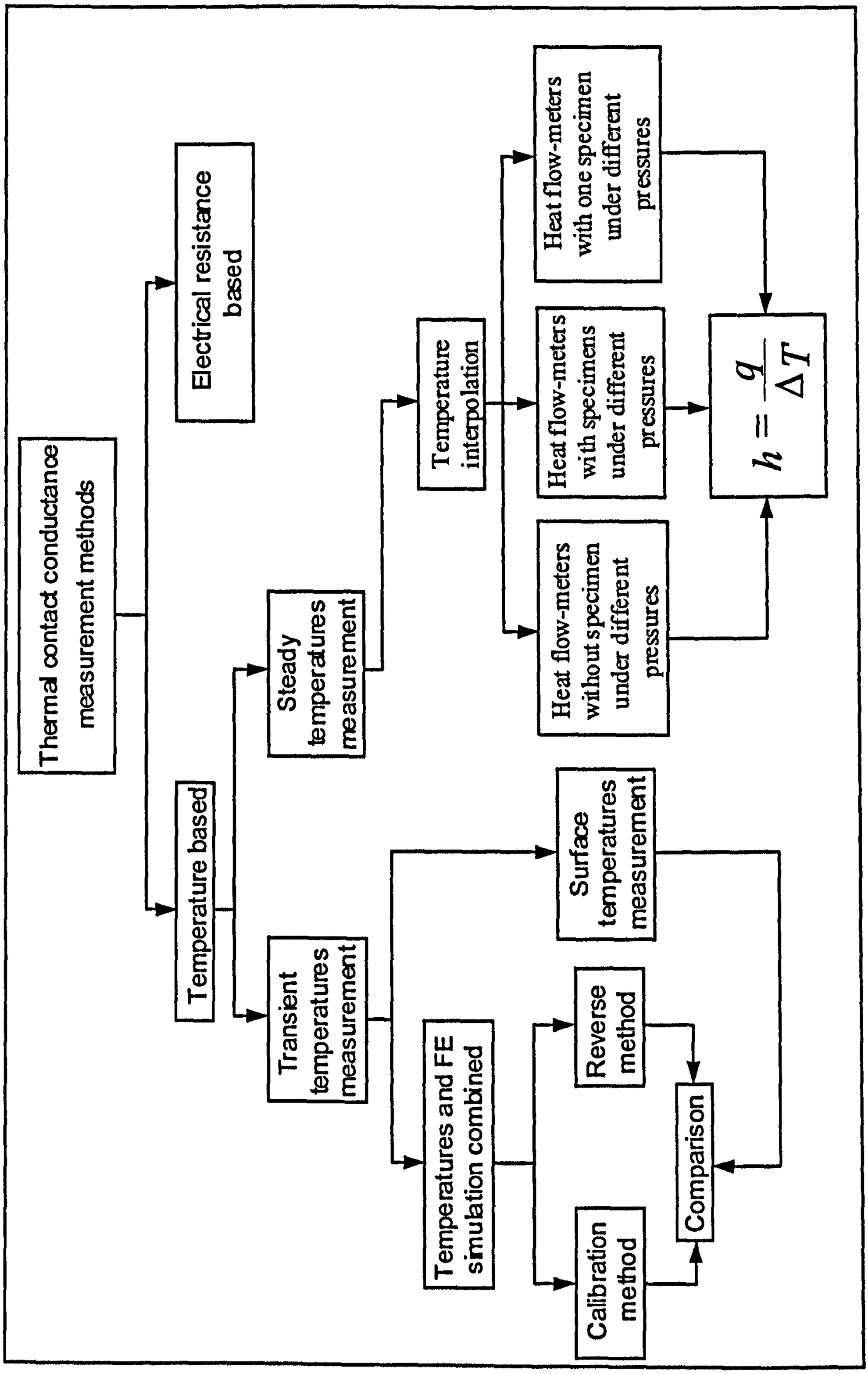

Fig. 3.1 Approaches for measuring thermal contact conductance

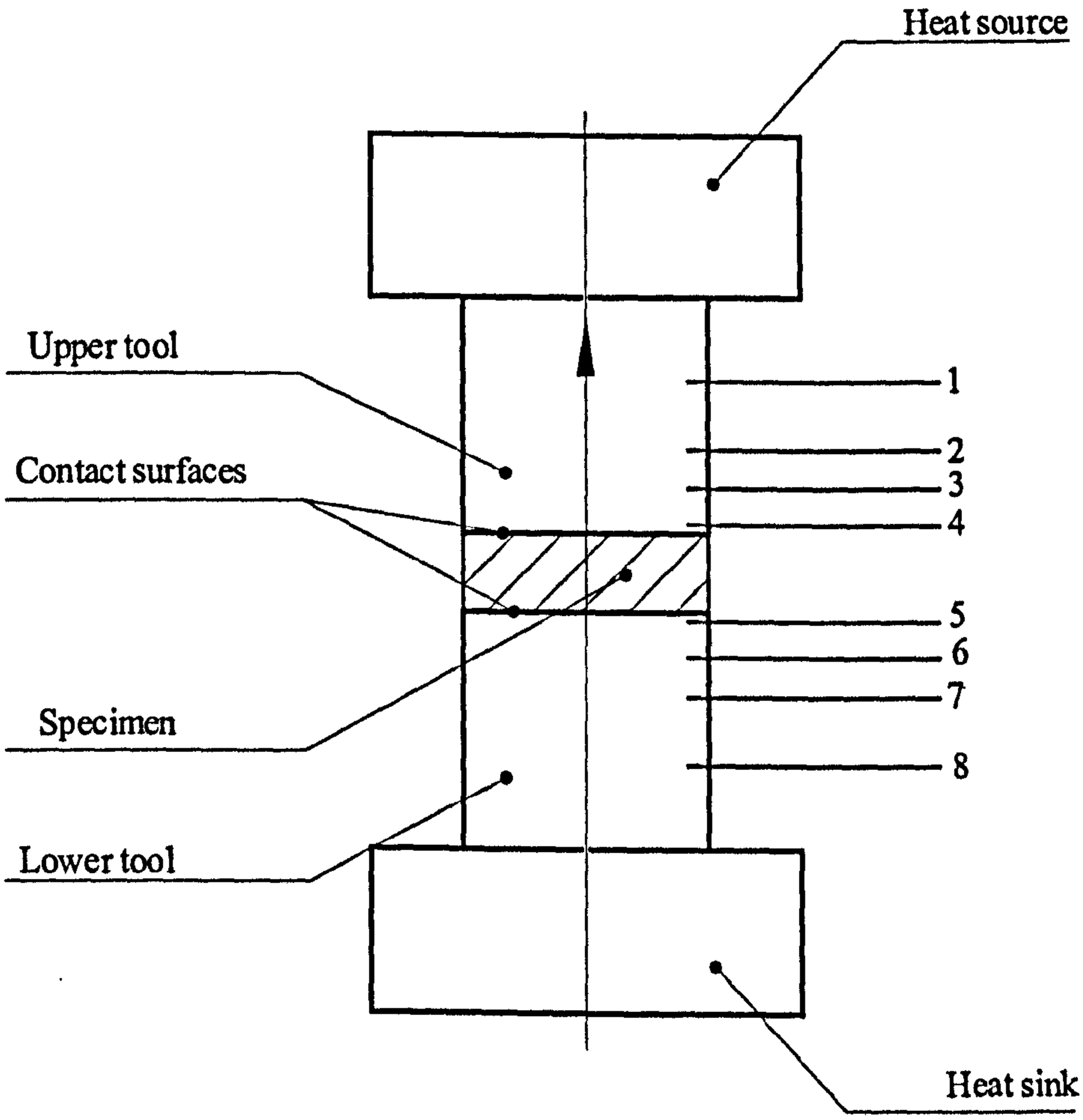

Fig. 3.2 Temperature based method

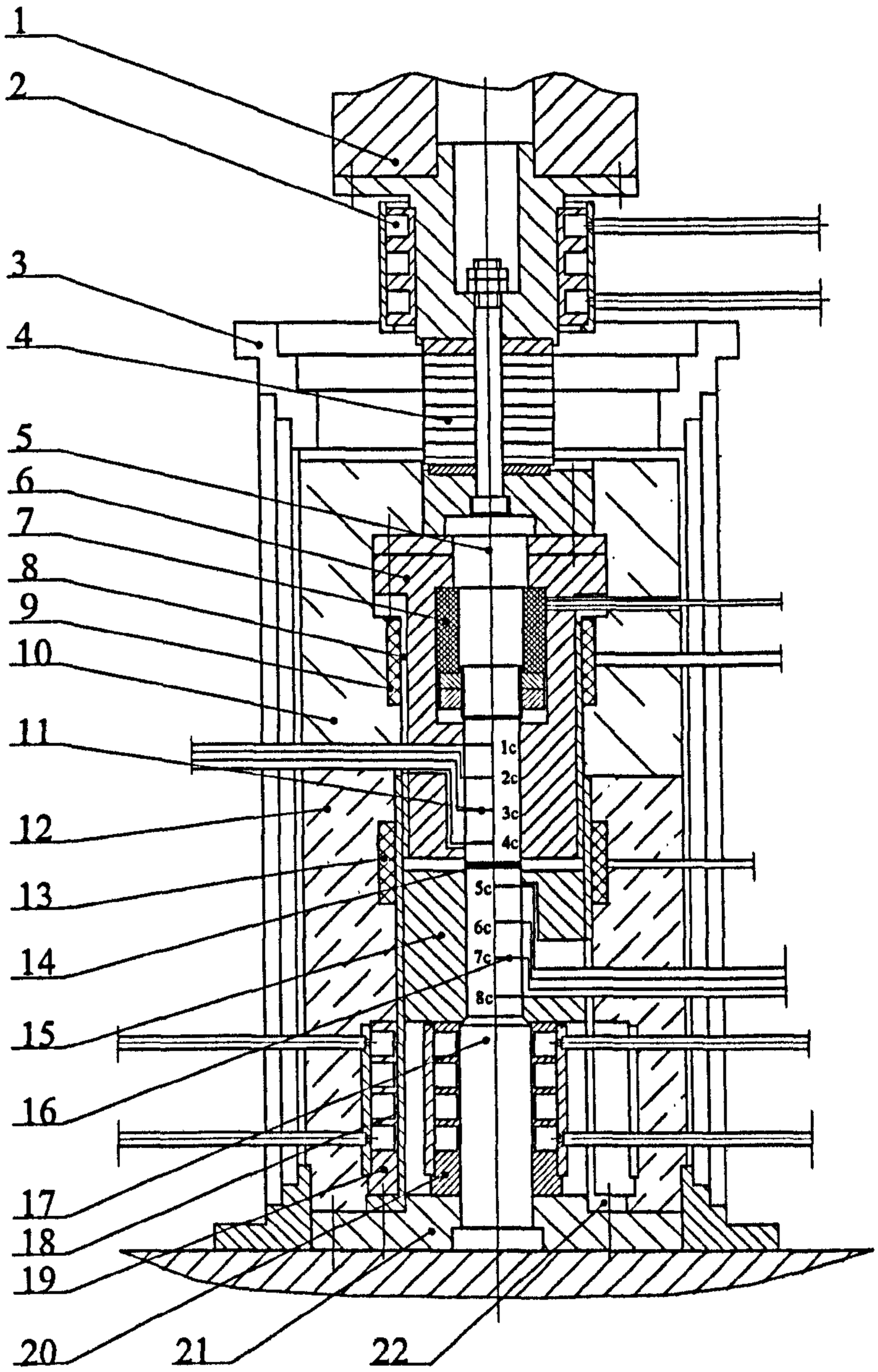

1. Loadcell;
2. Upper-cooler;
3. Radiation shield;
4. Insulator;
5. Upper-tool;
6. Upper insulator;
7. Main heater;
8. Upper frame;
9. Upper compensation heater;
10. Insulator;
11. Thermocouples in upper tool;
12. Insulator;
13. Lower compensation heater;
14. Specimen;
15. Insulator;
16. Thermocouples in lower tool;
17. Lower tool;
18. Lower frame;
19. Outer cooler;
20. Inner cooler;
21. Seat;
22. Connector

Fig. 3.3 Experimental equipment

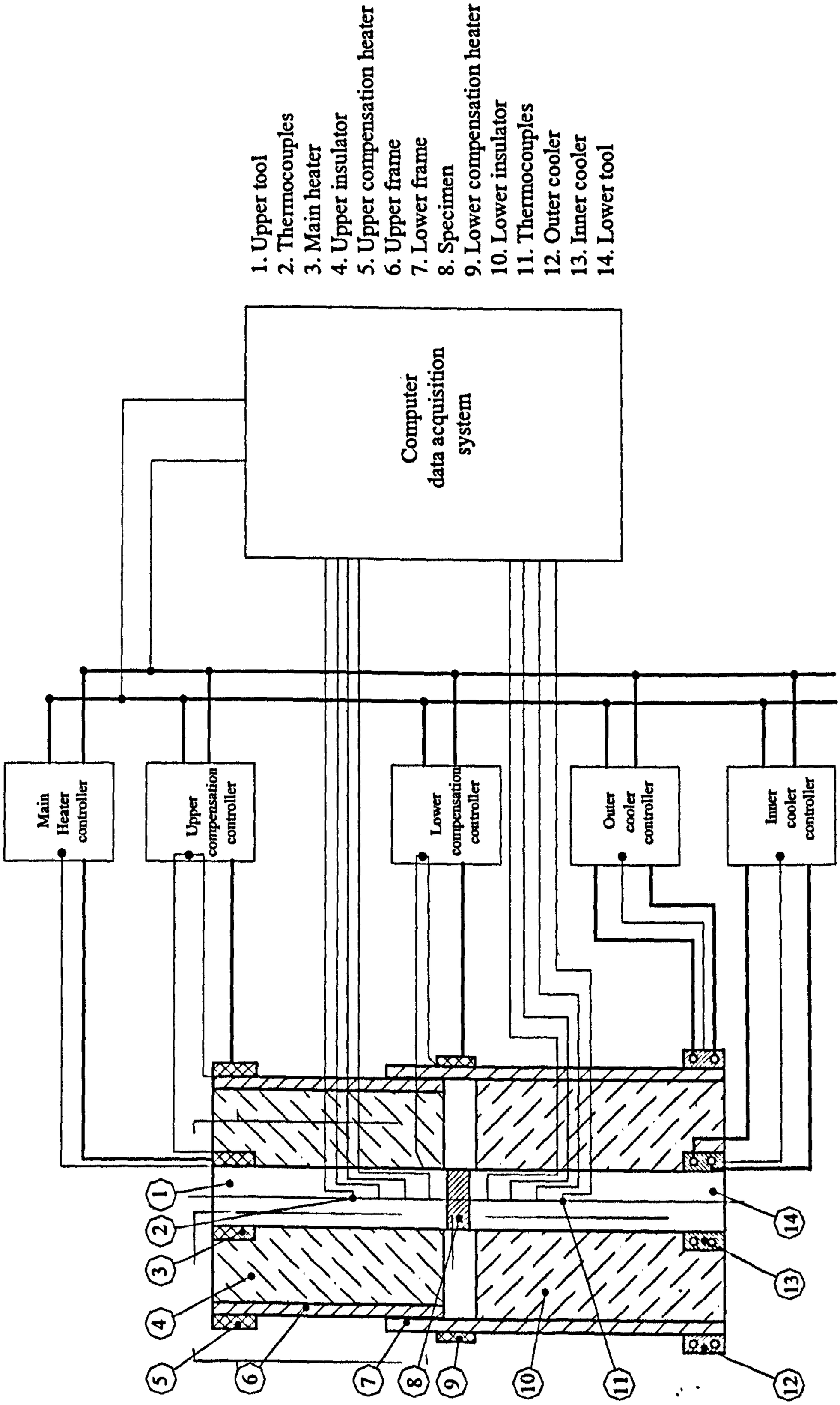

Fig. 3.4 Controlling system of experimental equipment

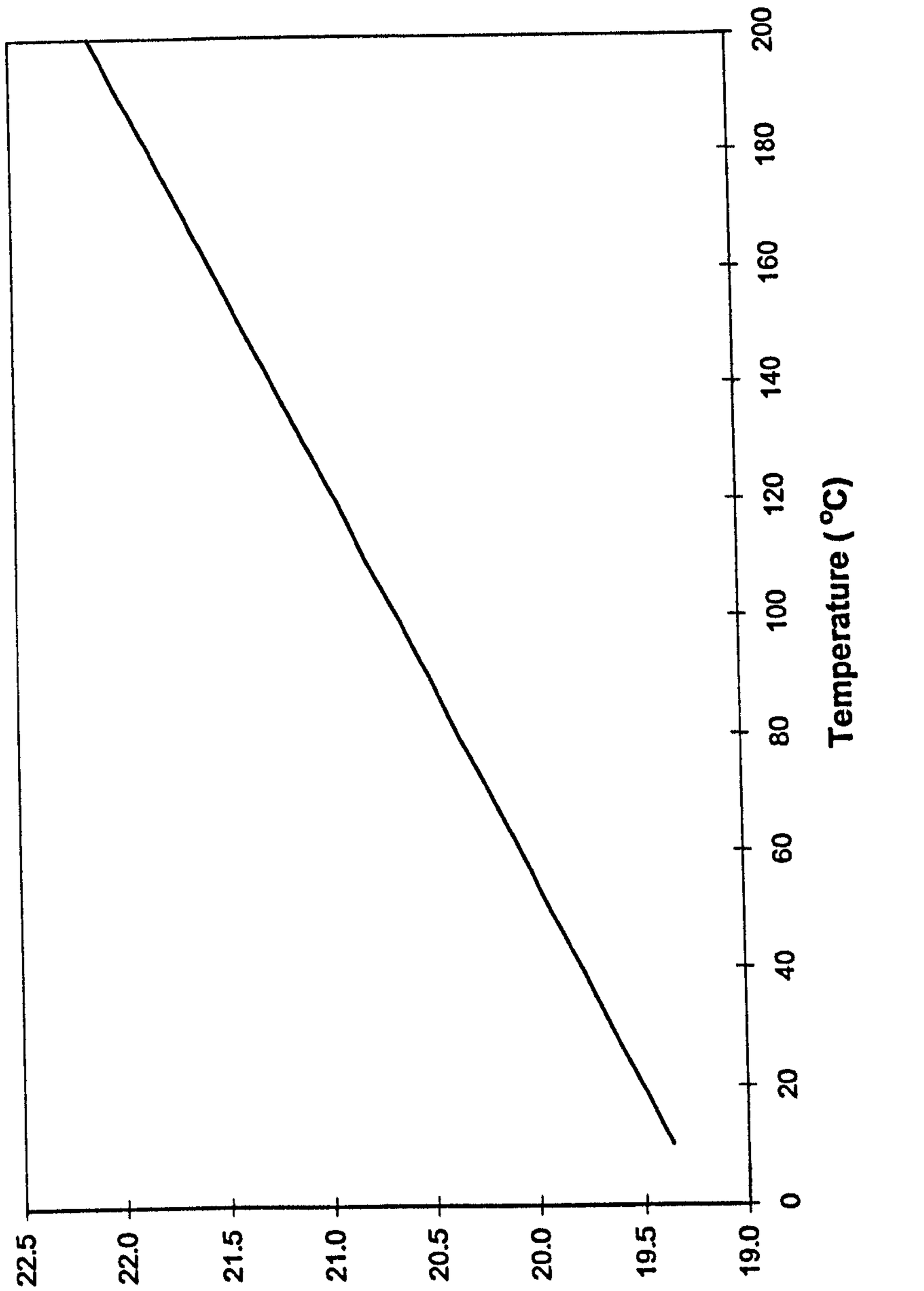

Fig. 3.5 The variation of thermal conductivity of N910 with temperature

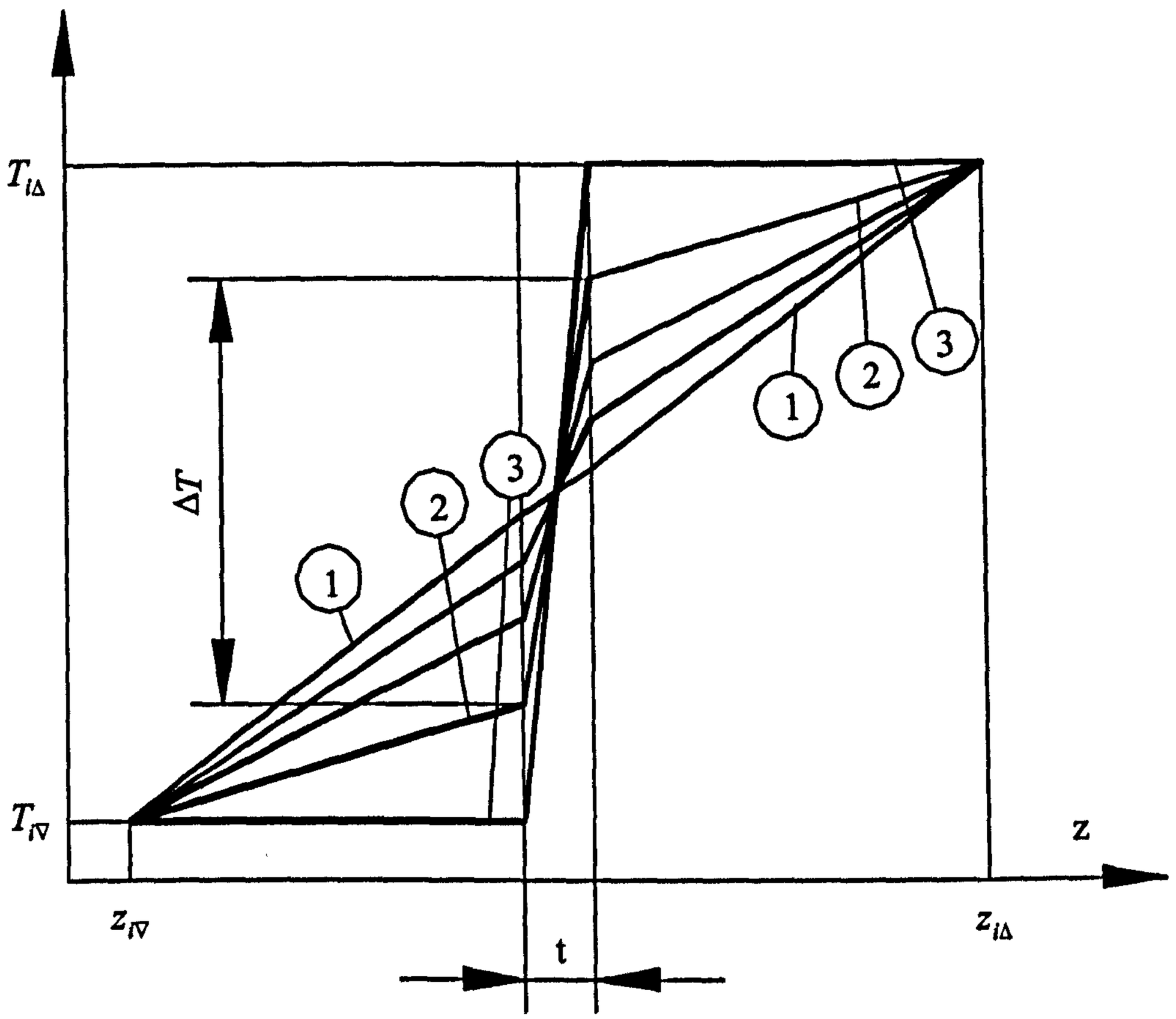

Fig. 3.6 Possible distribution of temperature

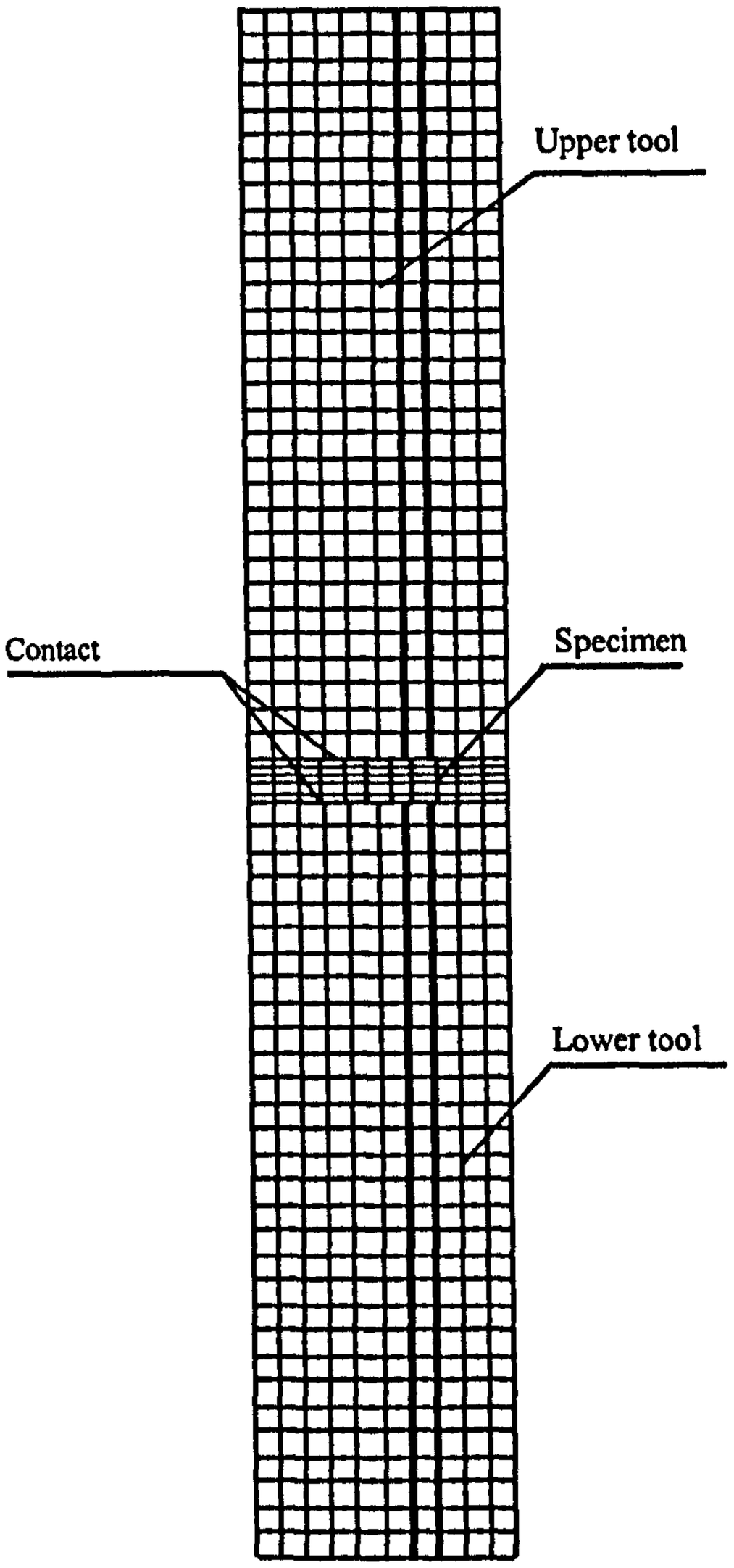

Fig. 3.7 The FE geometric model of heat transfer

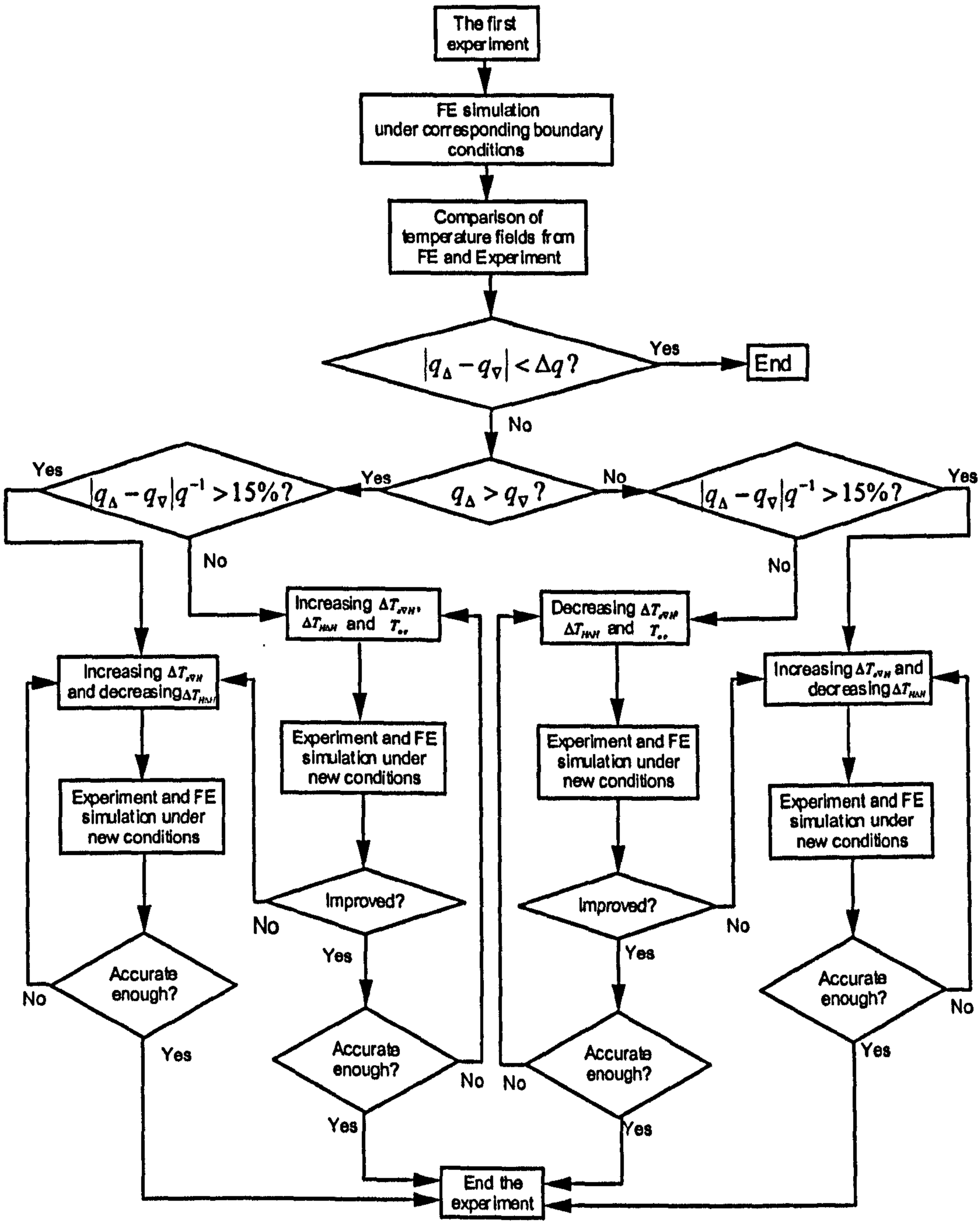

T_{oc} : Outer cooler temperature

$\Delta T_{H\Delta H}$: Upper compensation heater control temperature difference

$\Delta T_{\nabla H}$: Lower compensation heater control temperature difference

Fig. 3.8 Flowchart for control parameters setting

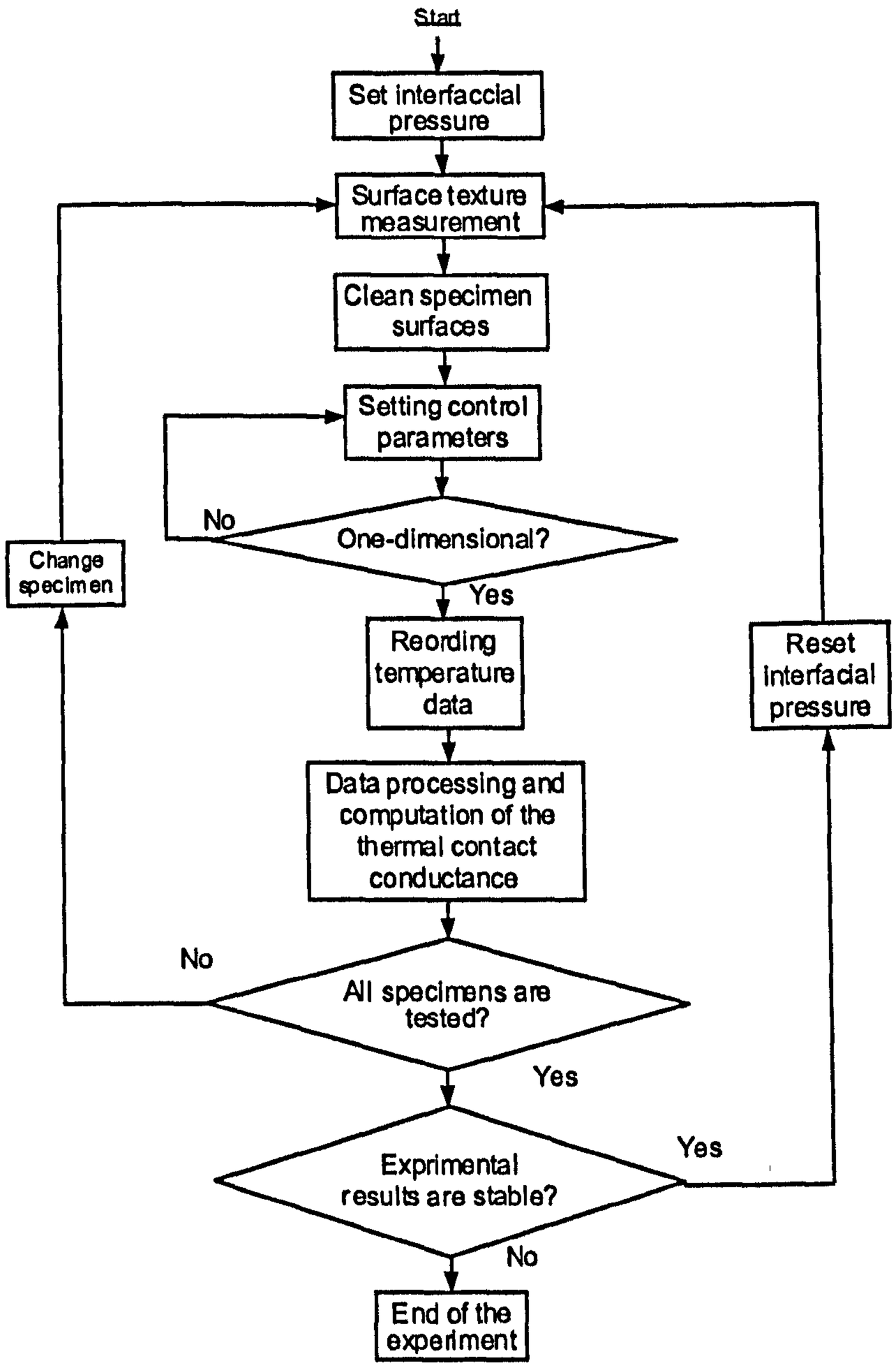

Fig. 3.9 Flow-chart of experiment procedure

Tool-transverse

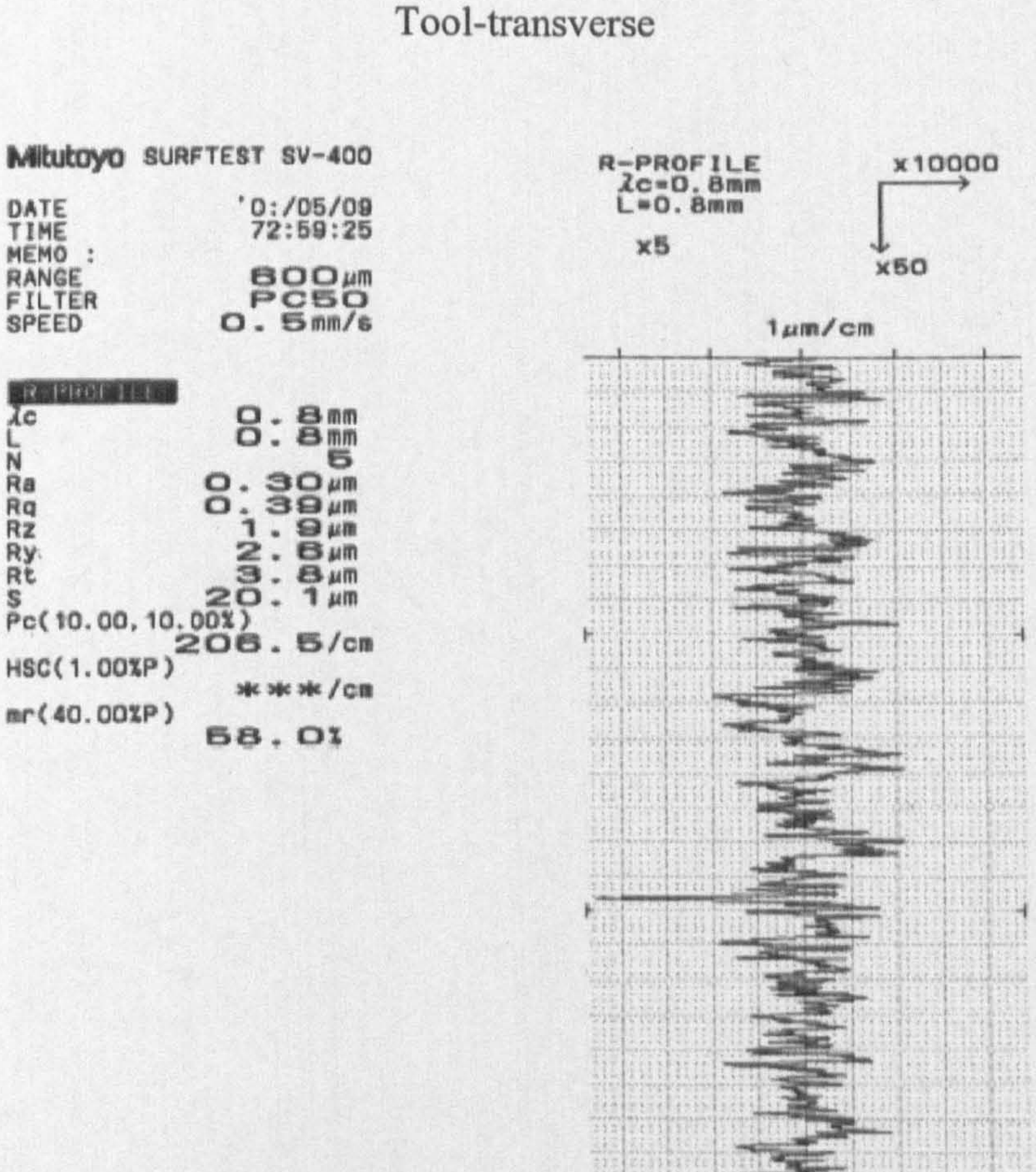

Fig. 3.10 Upper tool surface texture along direction transverse to grinding direction

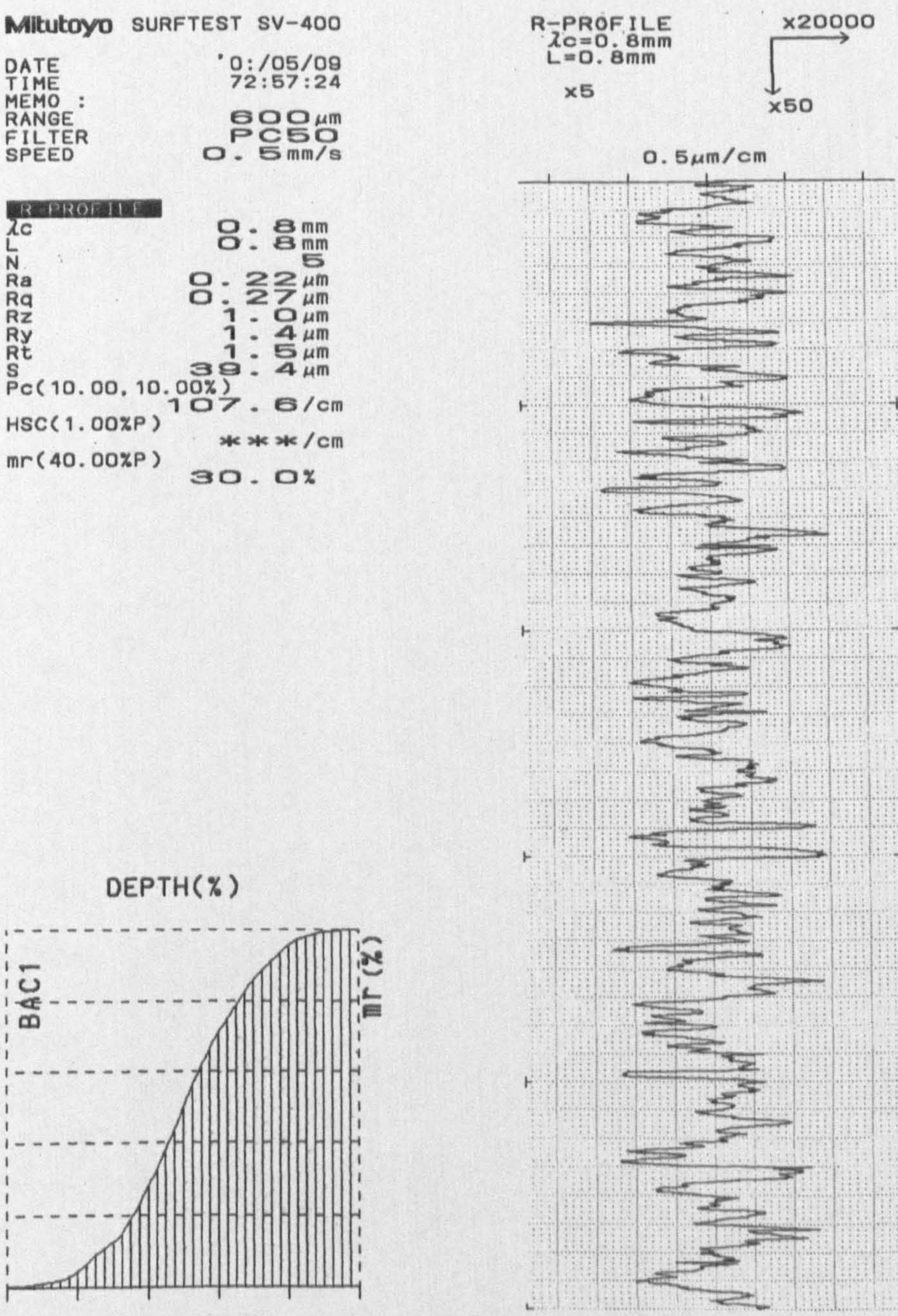

Fig.3.11 Upper tool surface texture along direction parallel to grinding direction

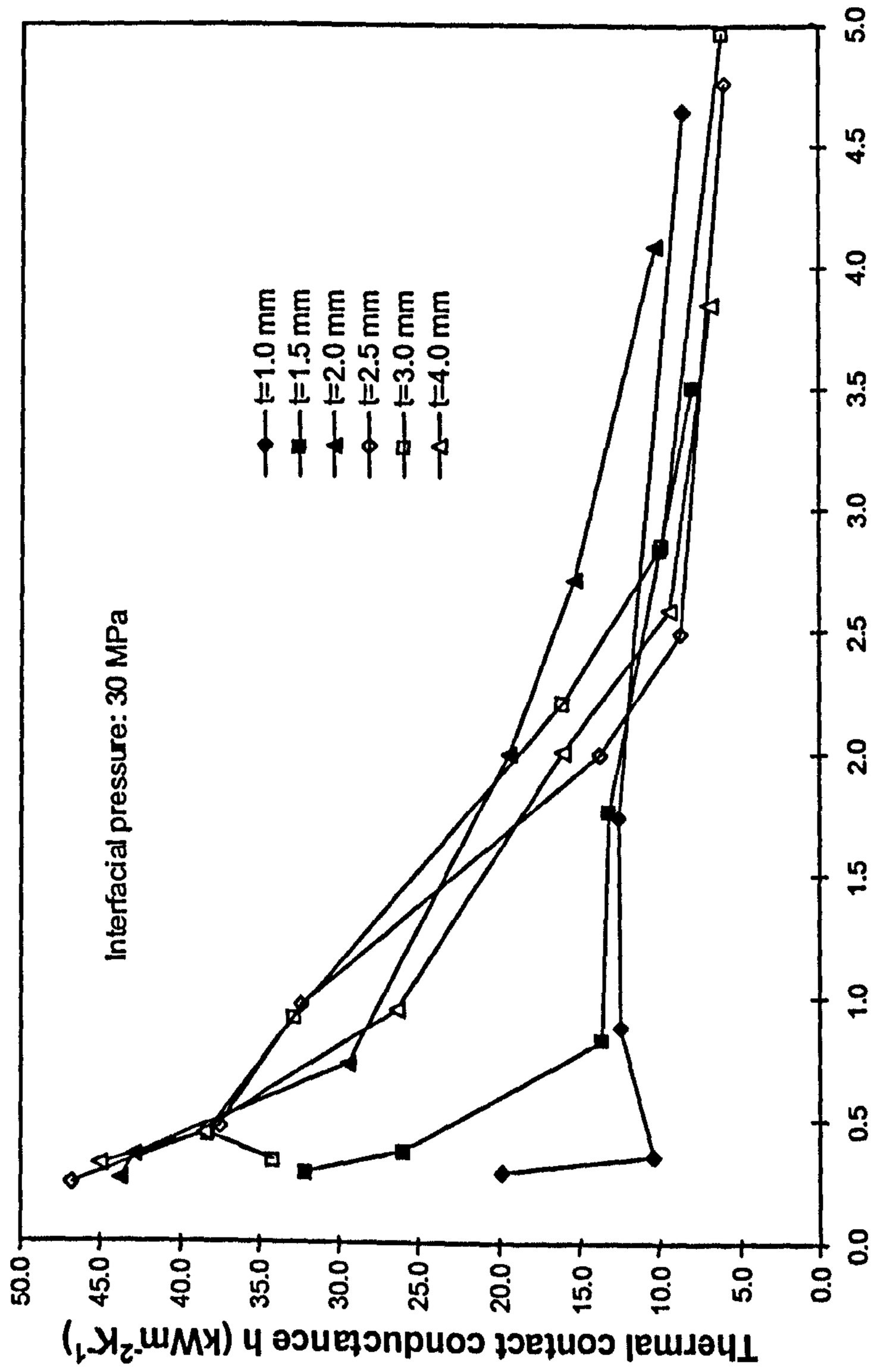

Fig. 3.12 Thermal contact conductance under interfacial pressure of 30 MPa

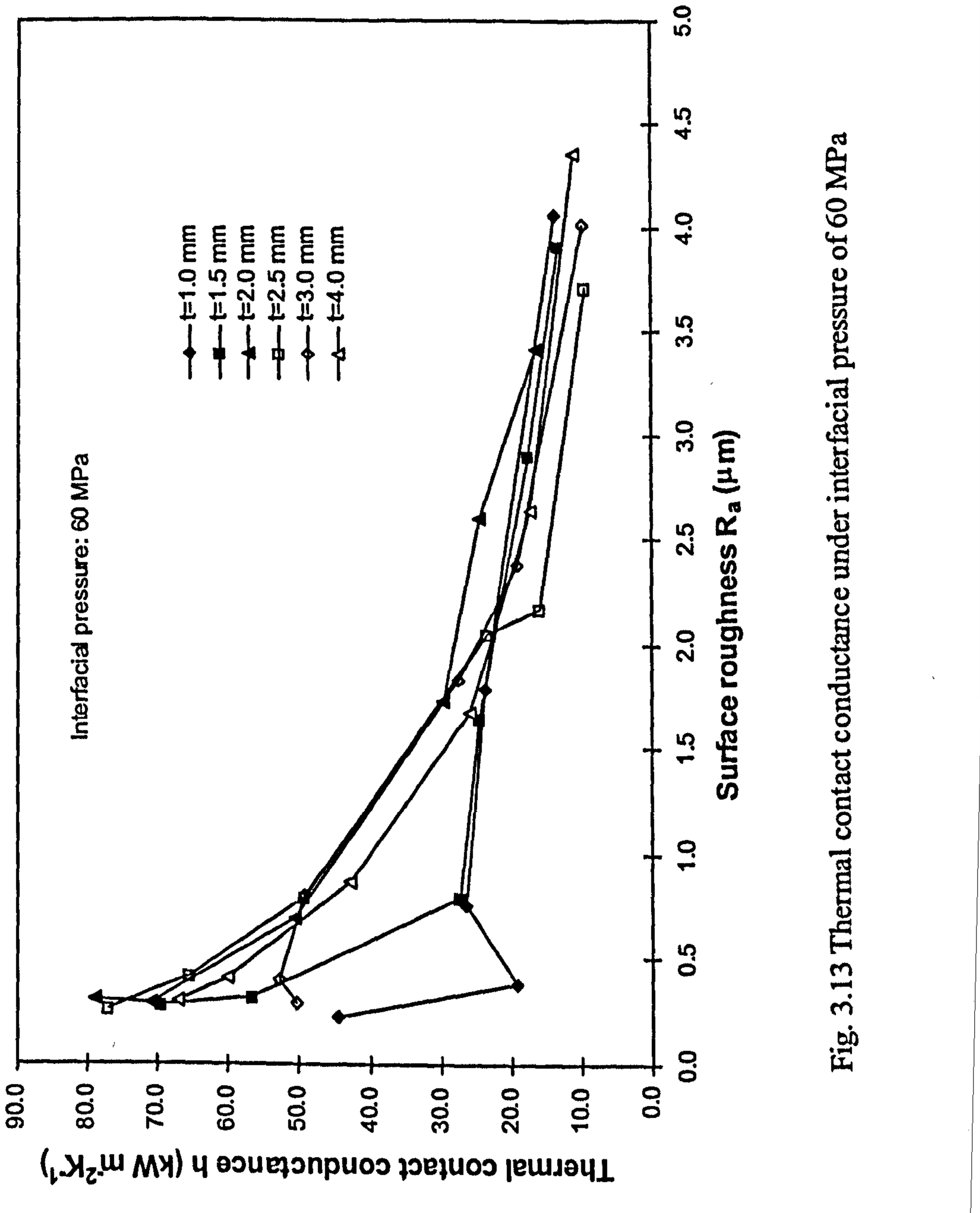

Fig. 3.13 Thermal contact conductance under interfacial pressure of 60 MPa

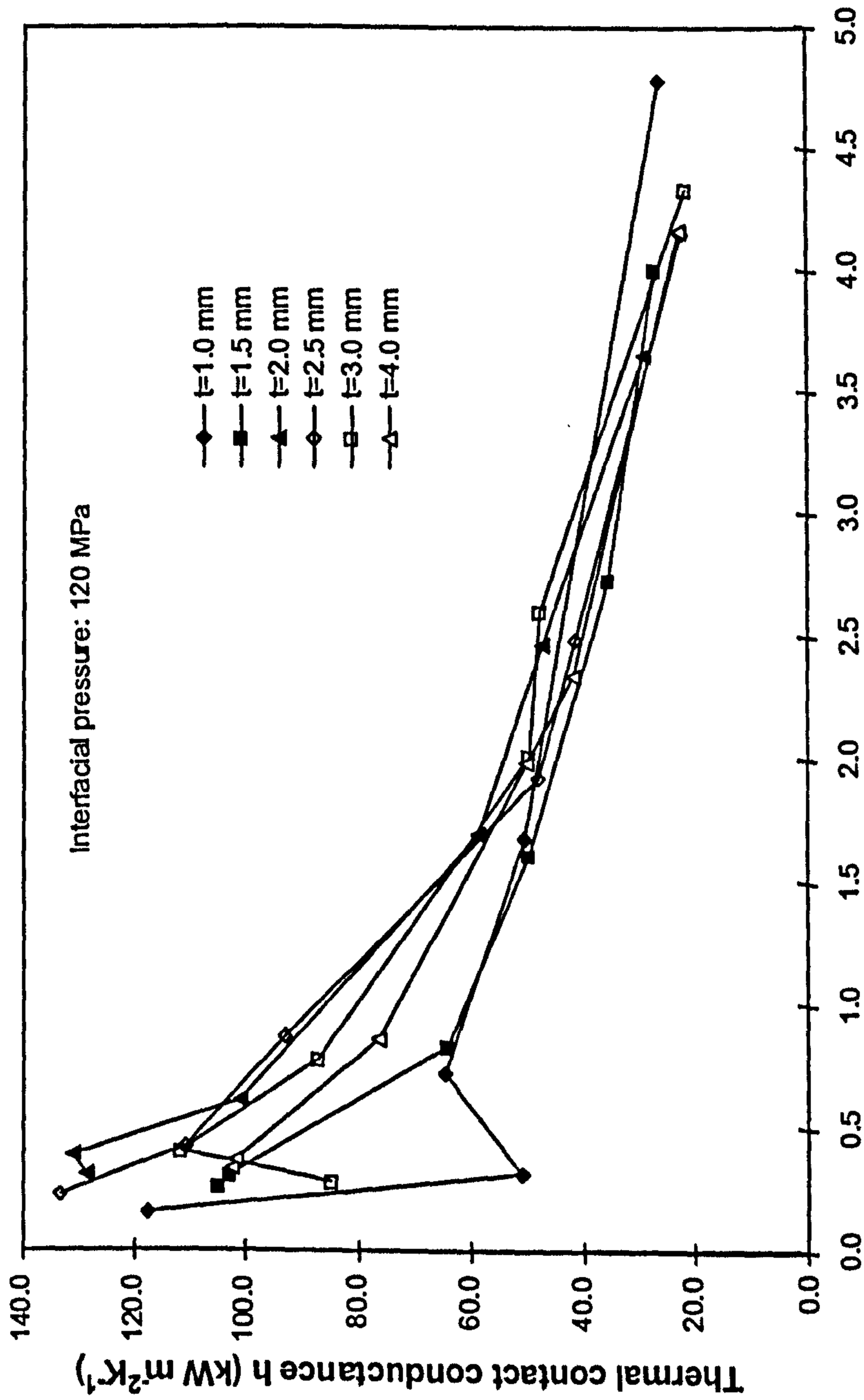

Fig. 3.14 Thermal contact conductance under interfacial pressure of 120 MPa

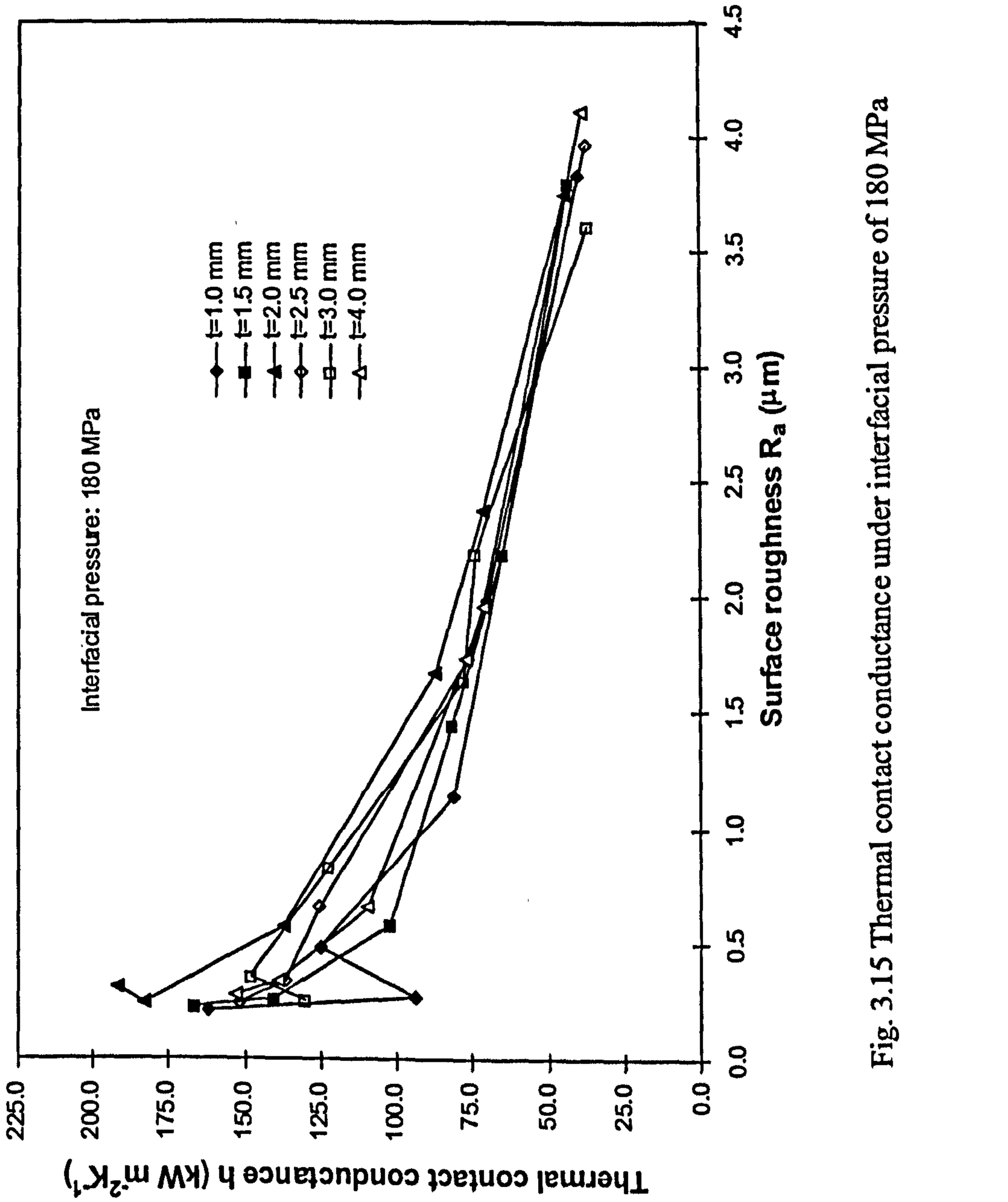

Fig. 3.15 Thermal contact conductance under interfacial pressure of 180 MPa

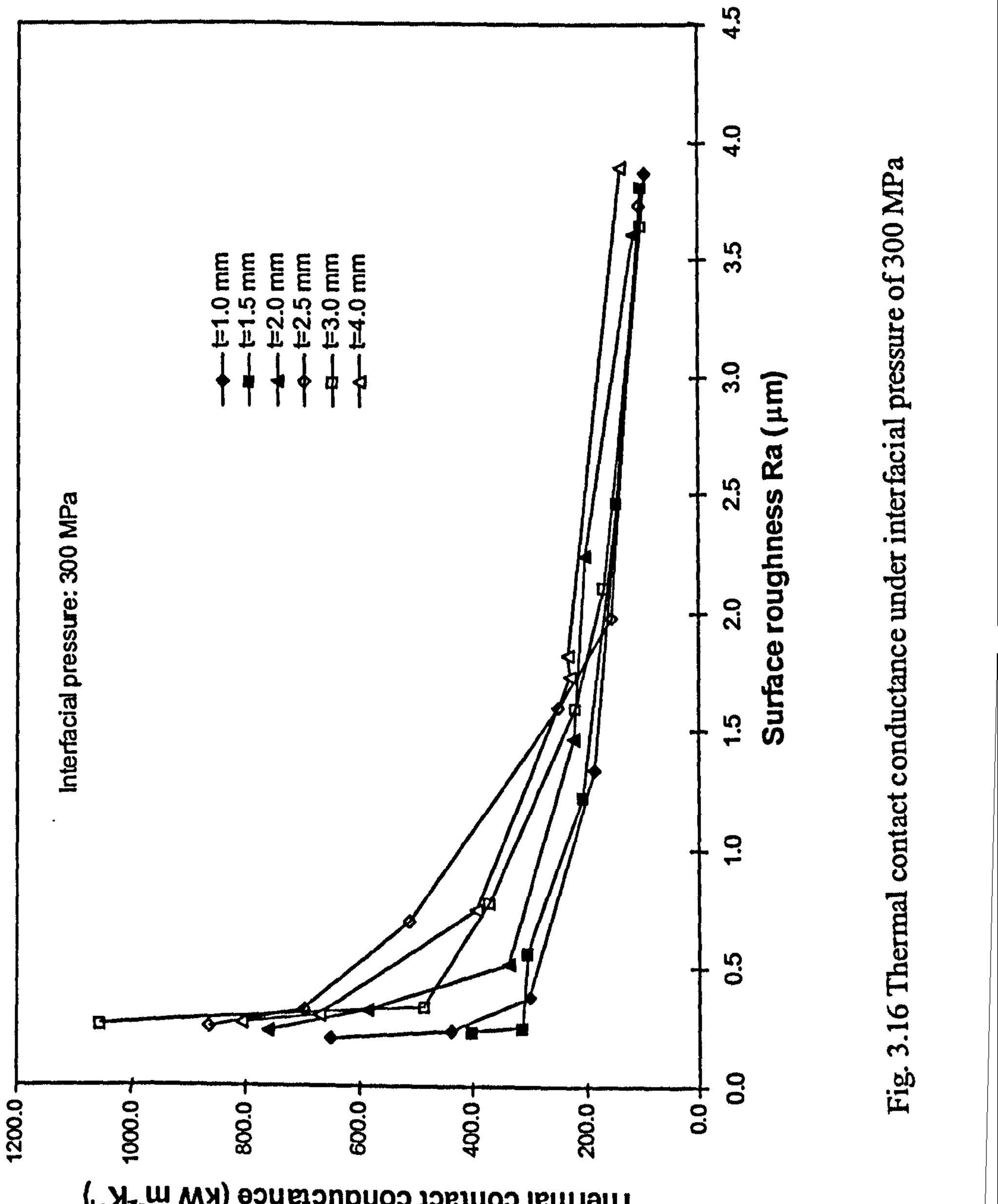

Fig. 3.16 Thermal contact conductance under interfacial pressure of 300 MPa

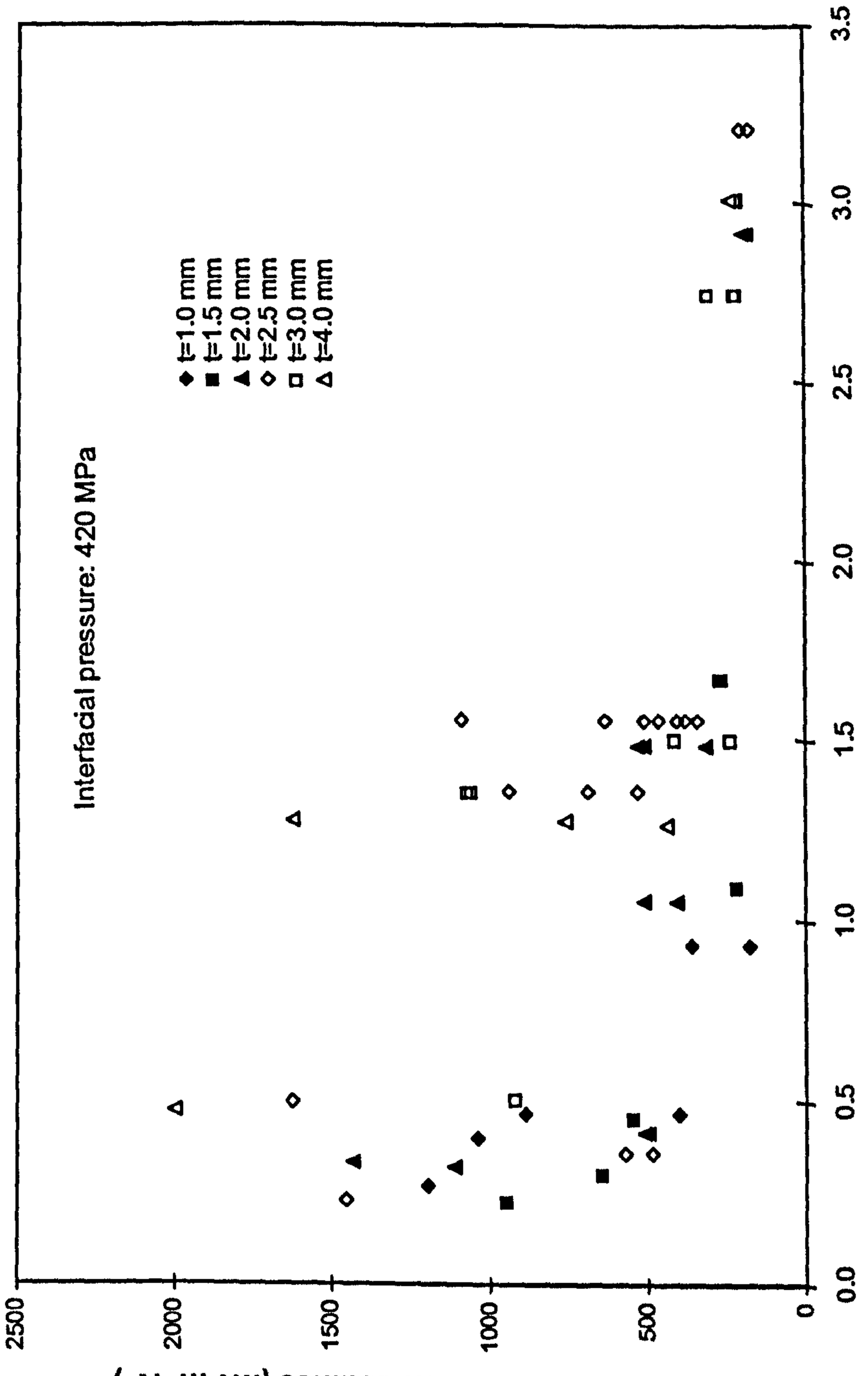

Fig. 3.17 Thermal contact conductance under interfacial pressure of 420 MPa

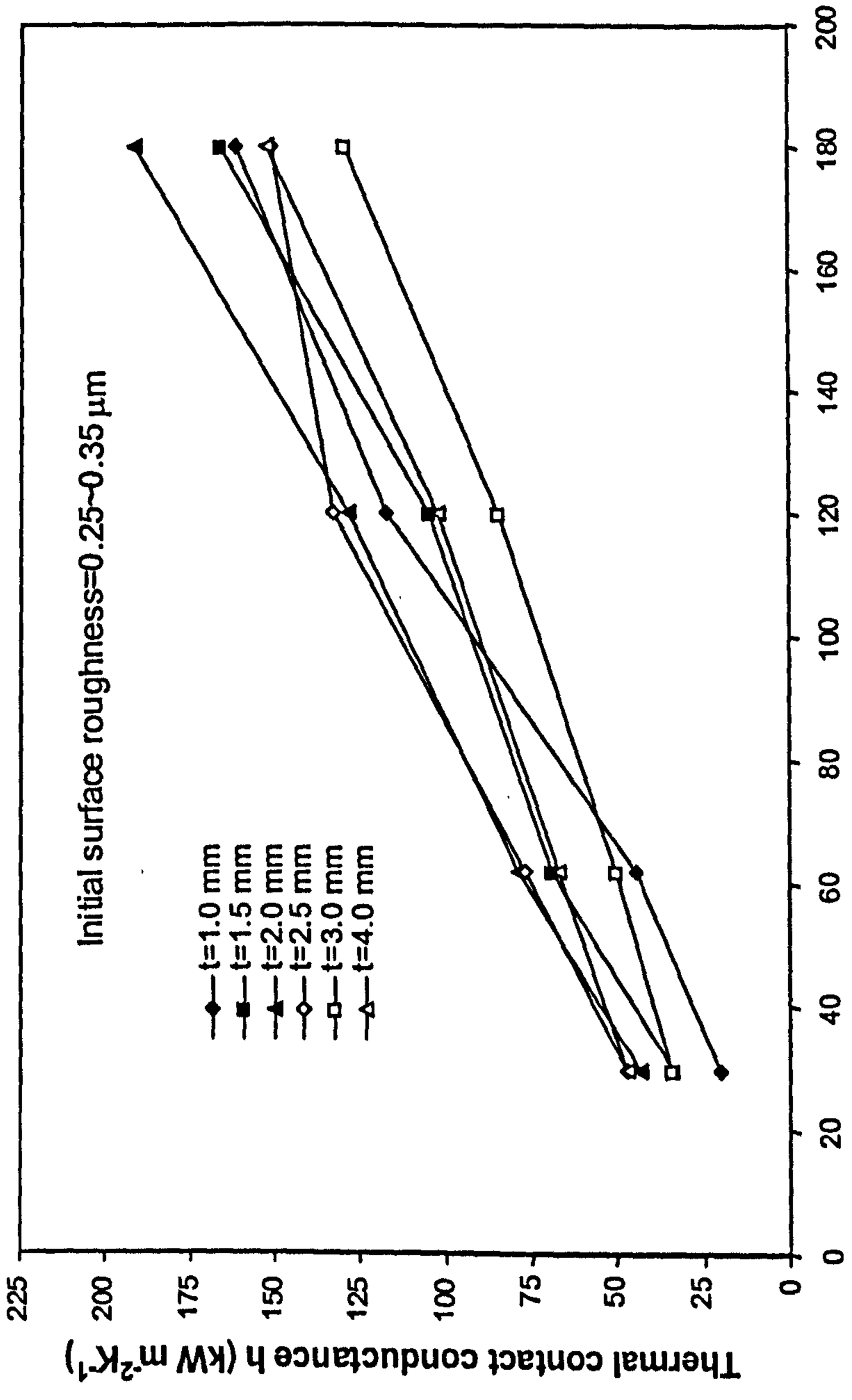

Fig. 3.18 Thermal contact conductance as a function of contact pressure for specimens with initial surface roughness 0.25~0.35 μm

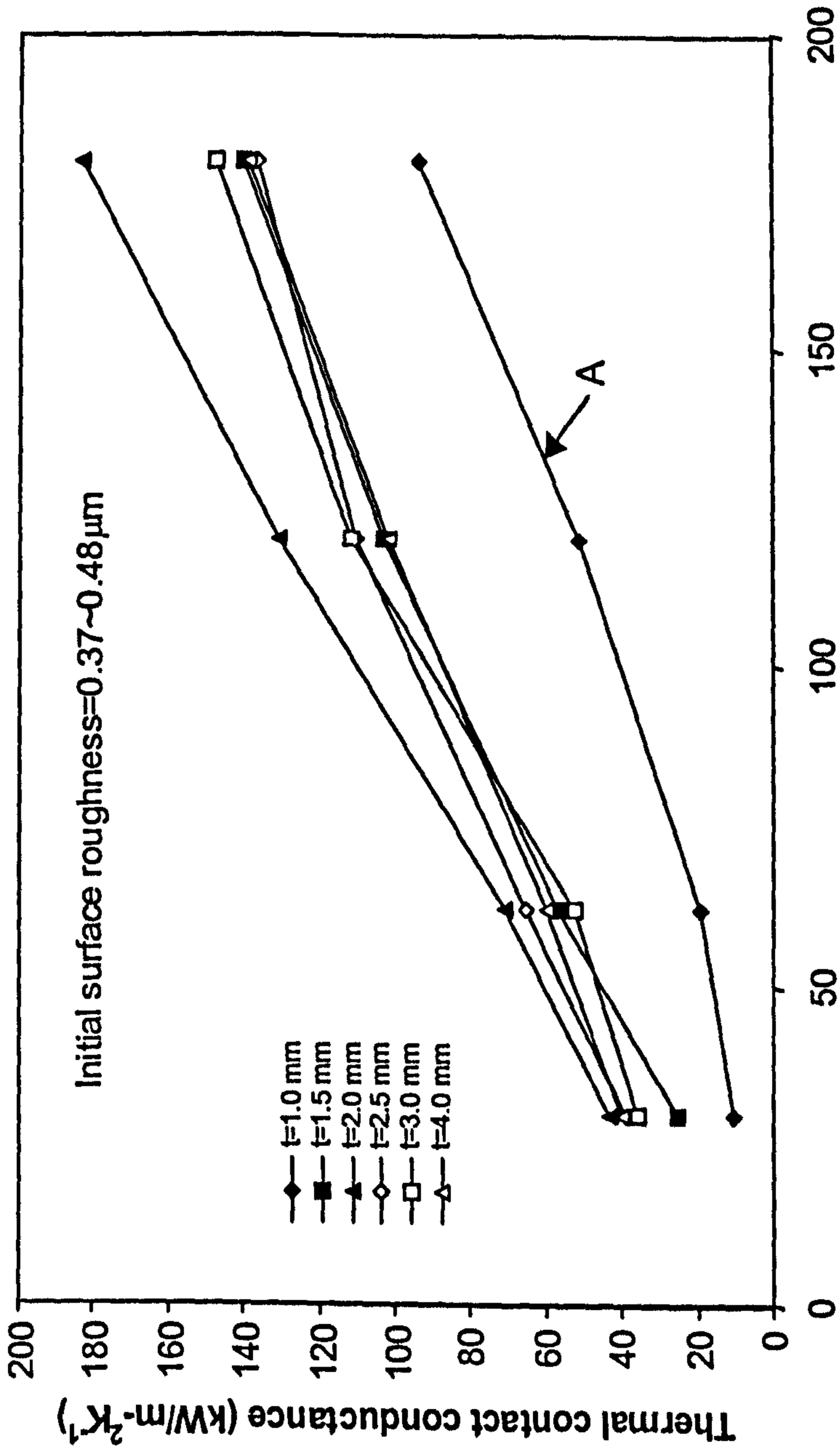

Fig. 3.19 Thermal contact conductance as a function of contact pressure for specimens with initial surface roughness 0.37~0.48 μm

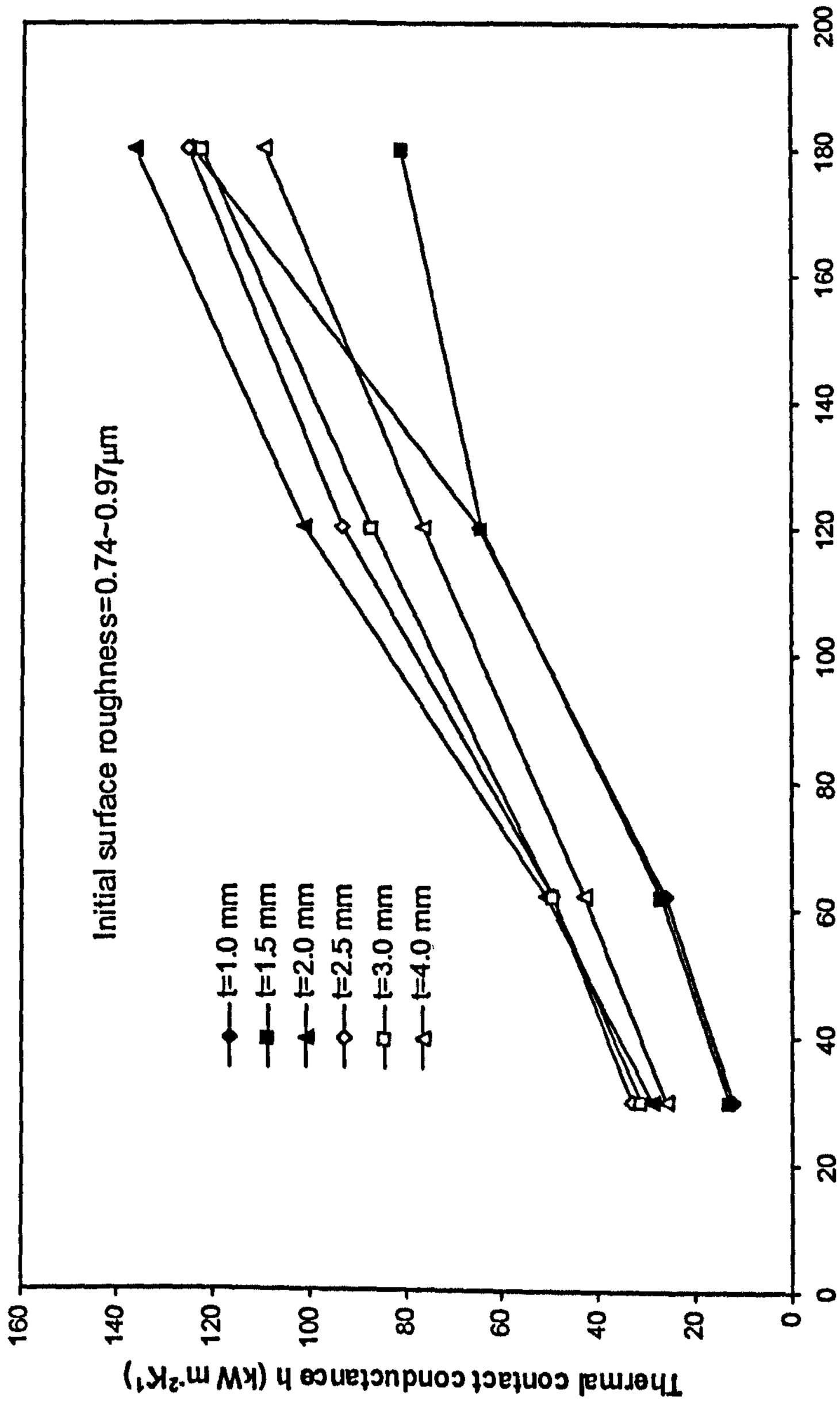

Fig. 3.20 Thermal contact conductance as a function of contact pressure for specimens with initial surface roughness 0.74~0.97 μm

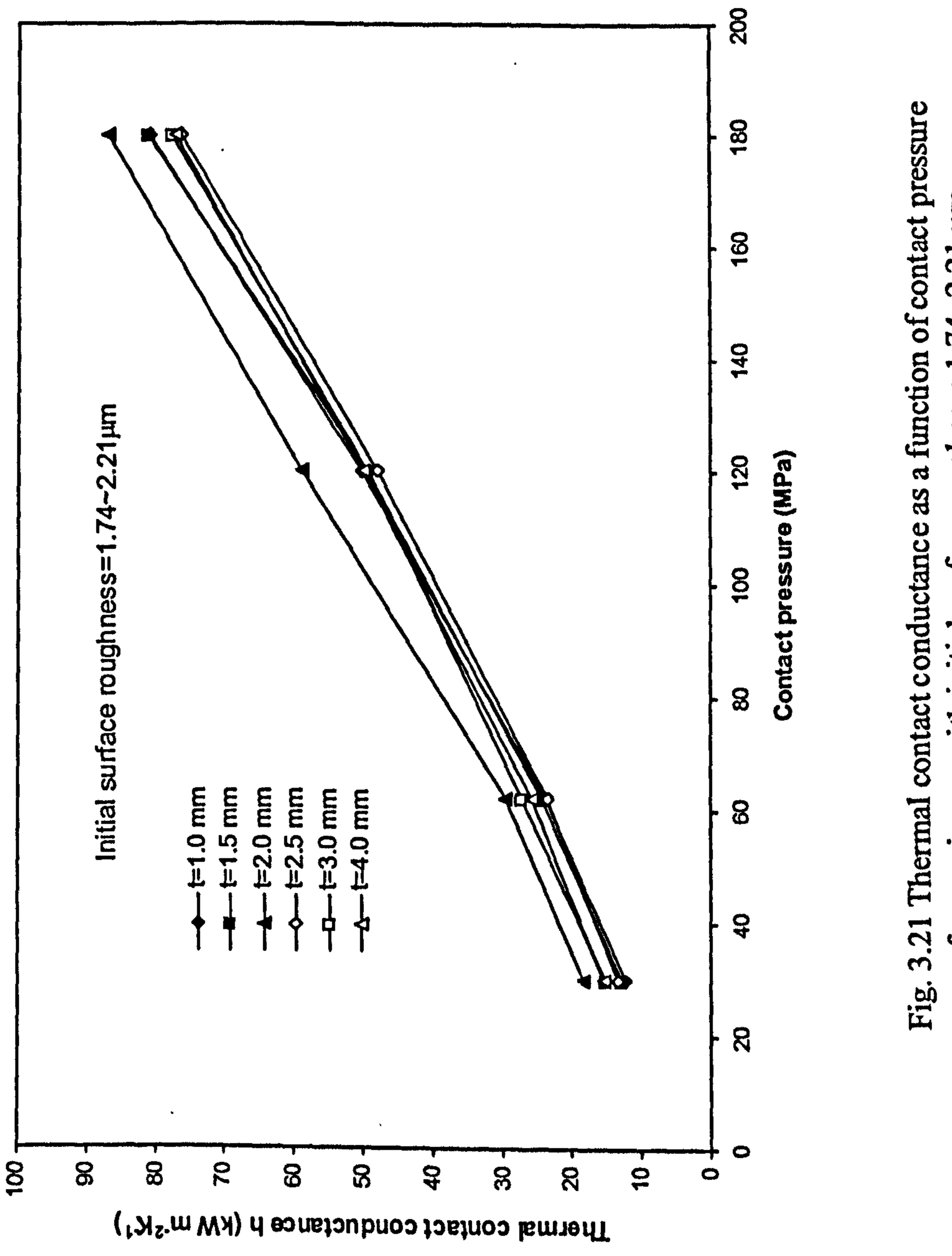

Fig. 3.21 Thermal contact conductance as a function of contact pressure for specimens with initial surface roughness 1.74~2.21 μm

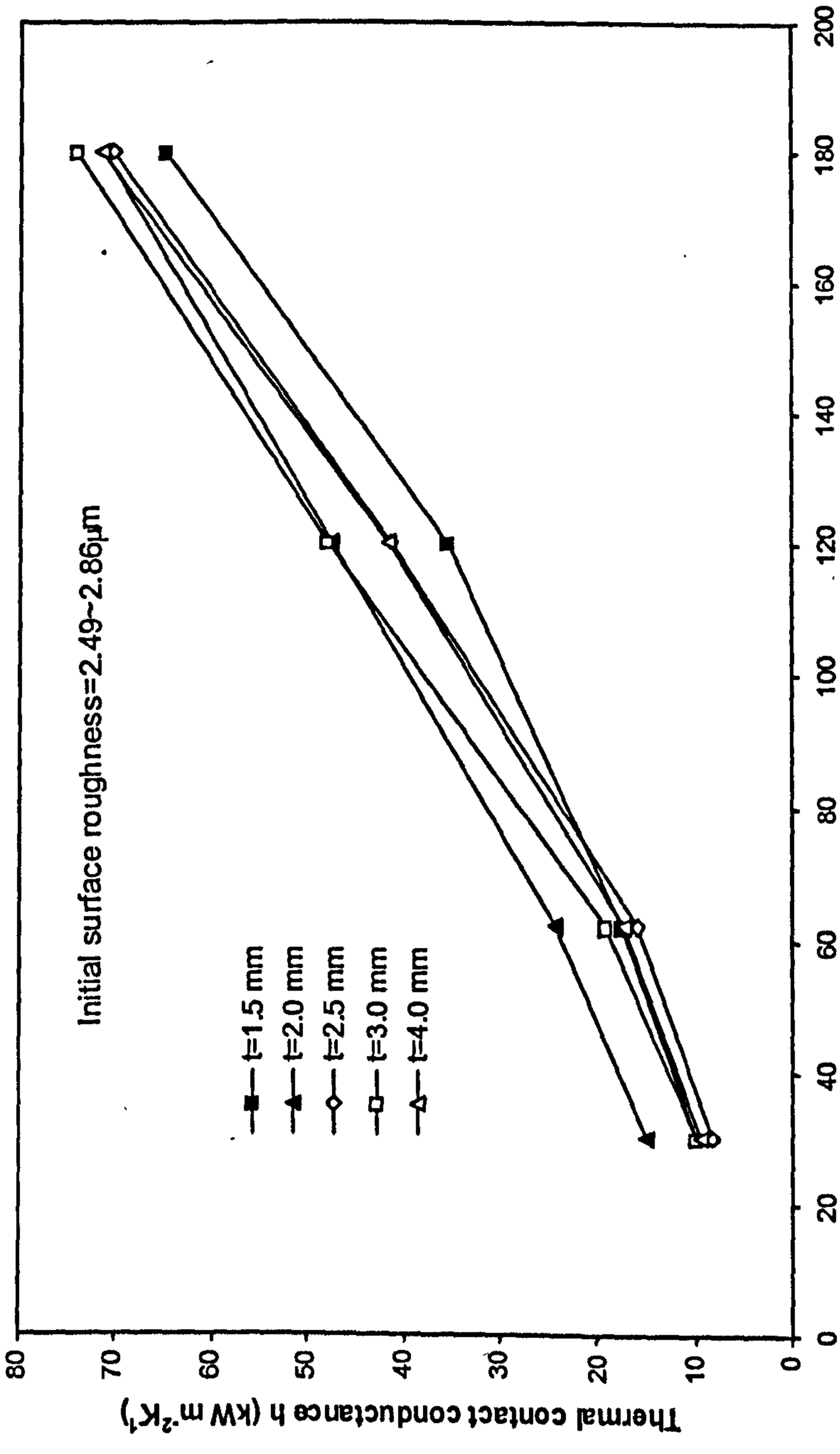

Fig. 3.22 Thermal contact conductance as a function of contact pressure for specimens with initial surface roughness 2.49~2.86 μm

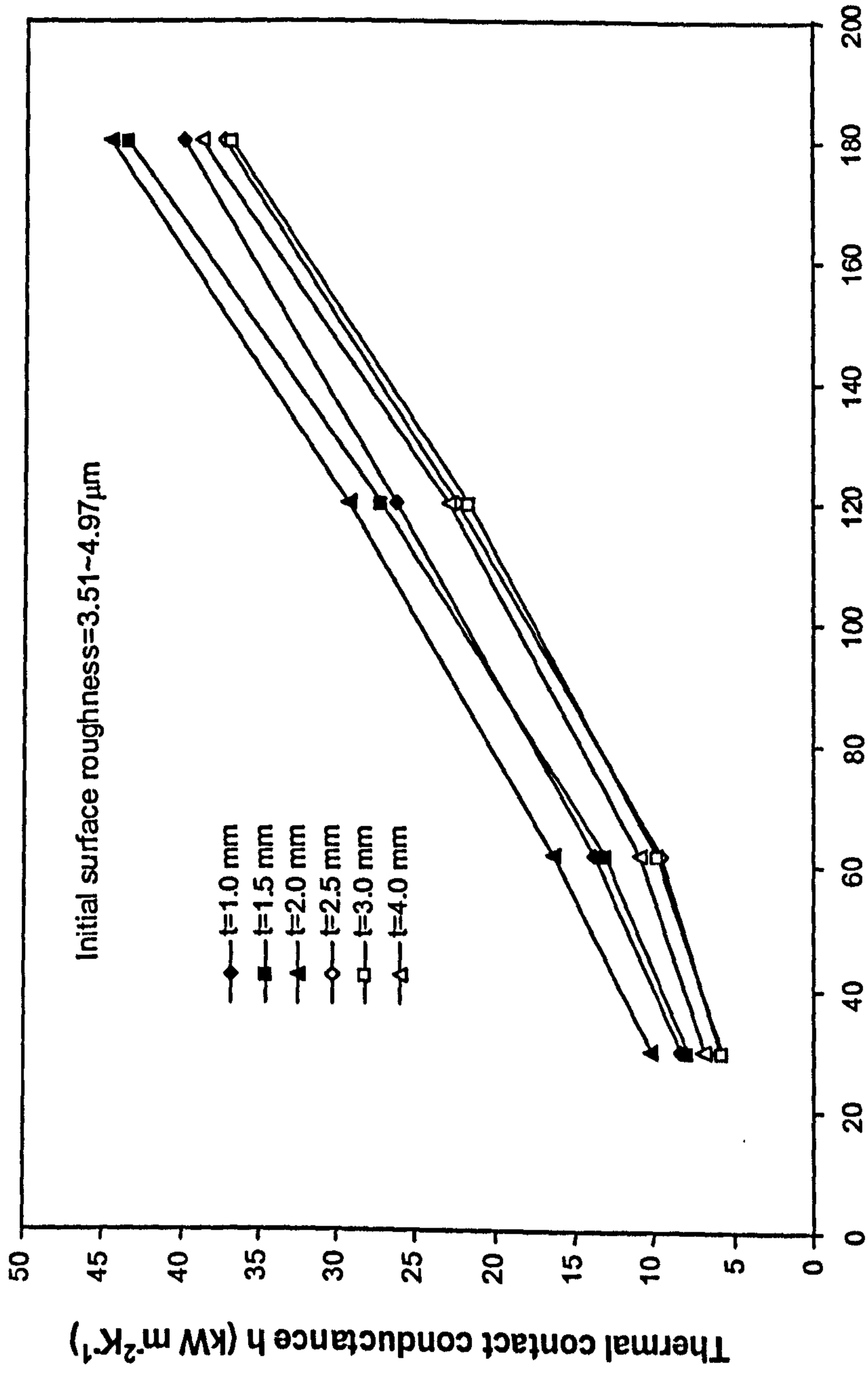

Fig. 3.23 Thermal contact conductance as a function of contact pressure for specimens with initial surface roughness 3.51~4.97 μm

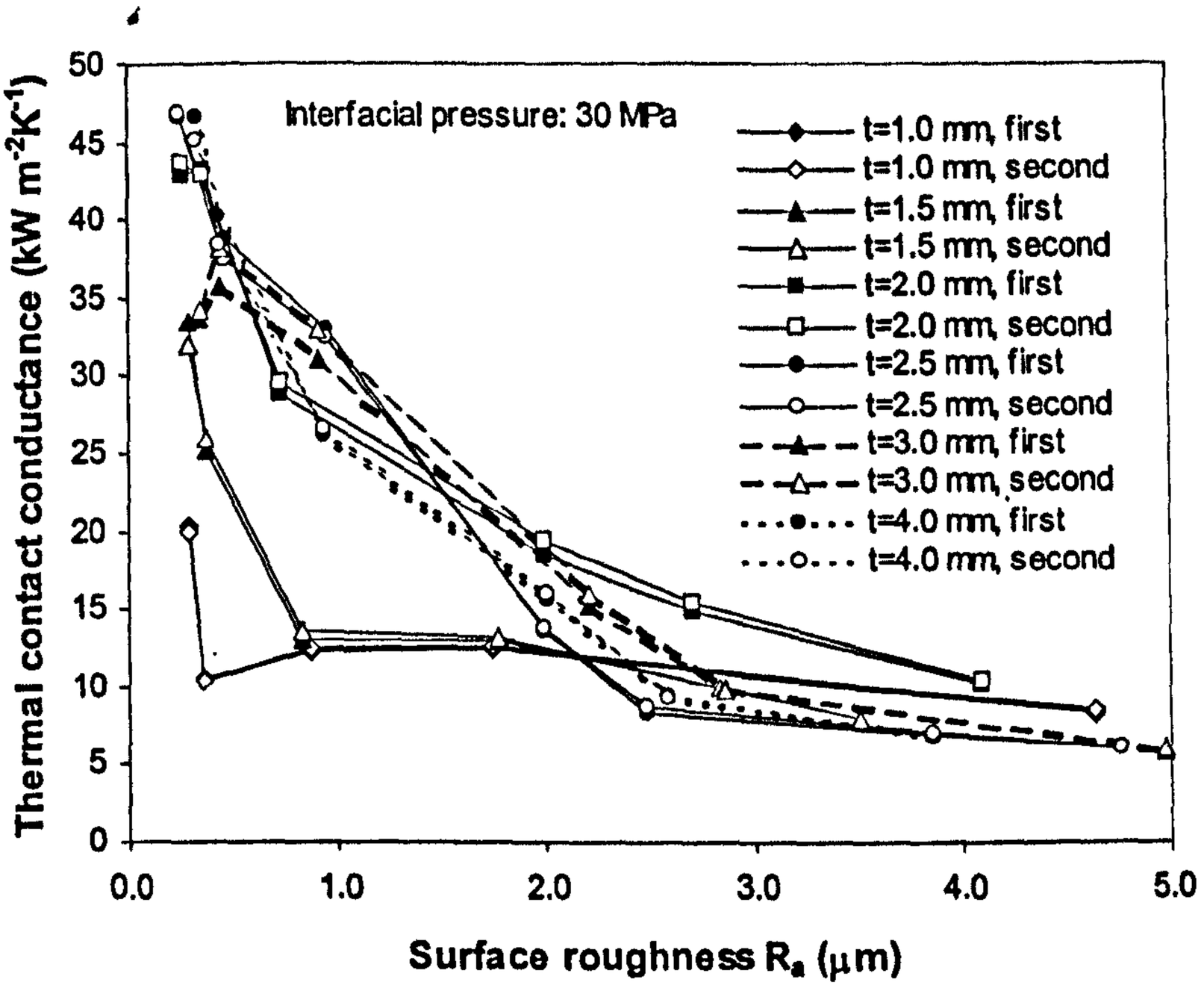

(a) Repeated experiments

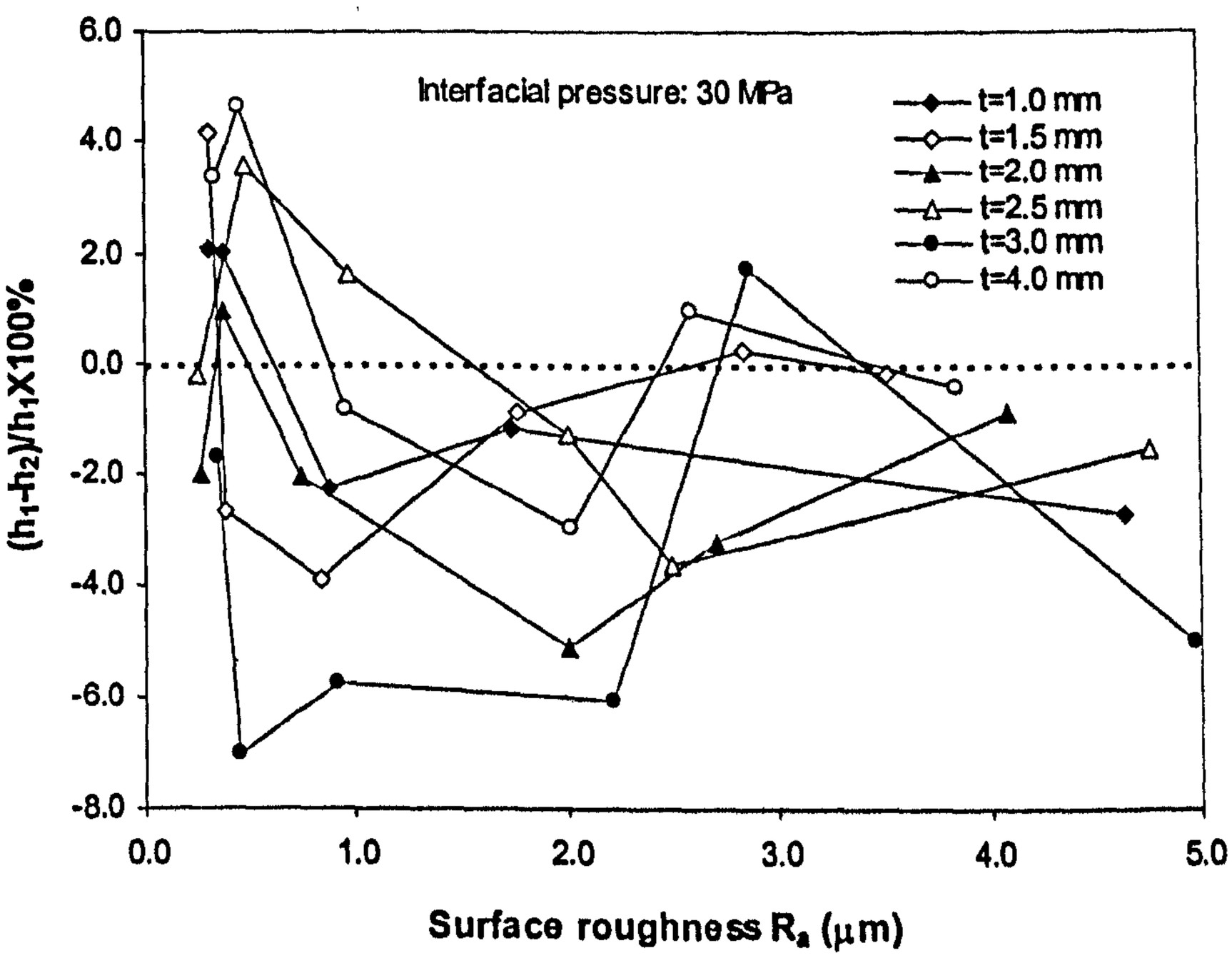

(b) Relative difference of h-value in repeated experiments

Fig. 3.24 Uncertainties in evaluation of h-values
under interfacial pressure of 30 MPa

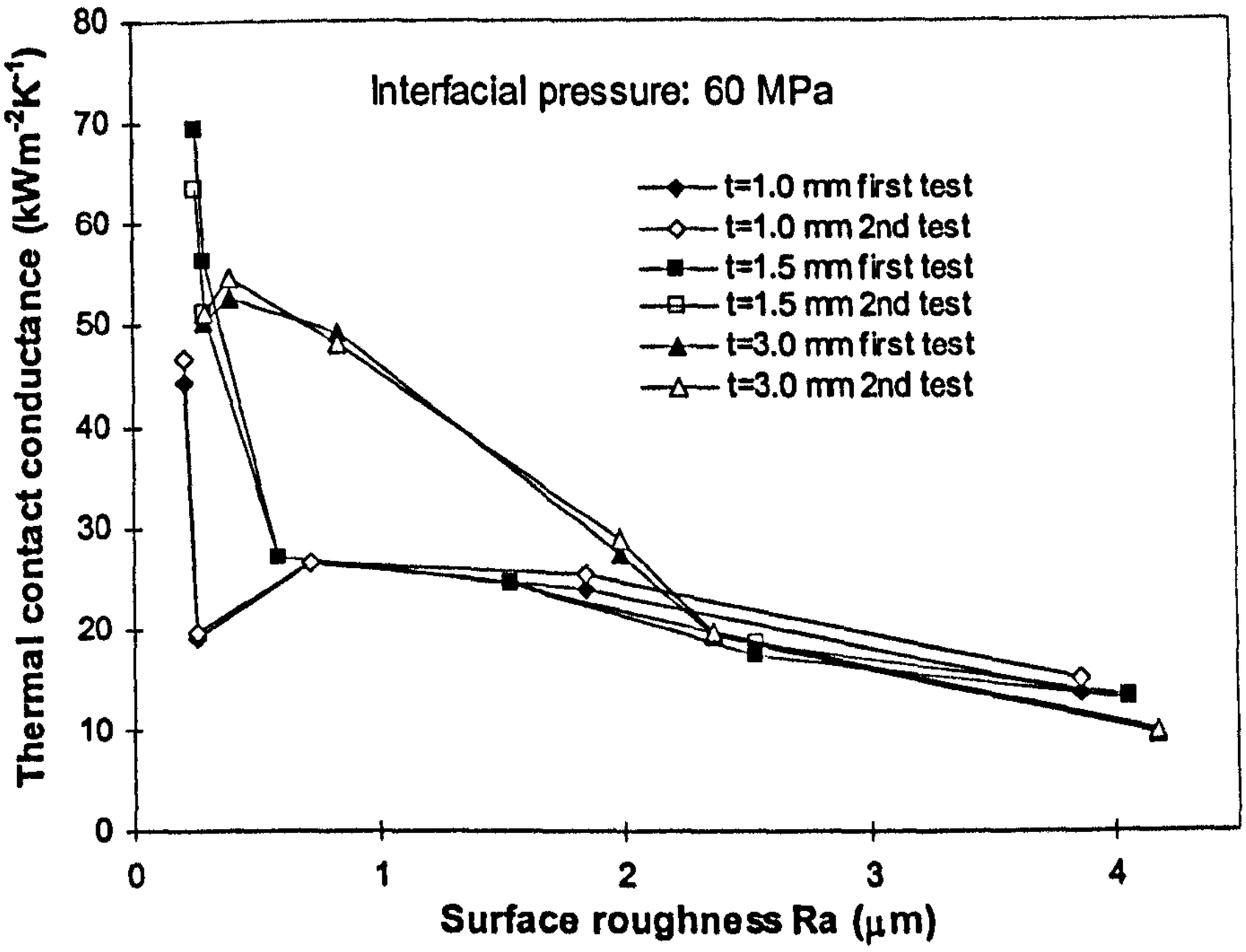

(a) Repeated experiments

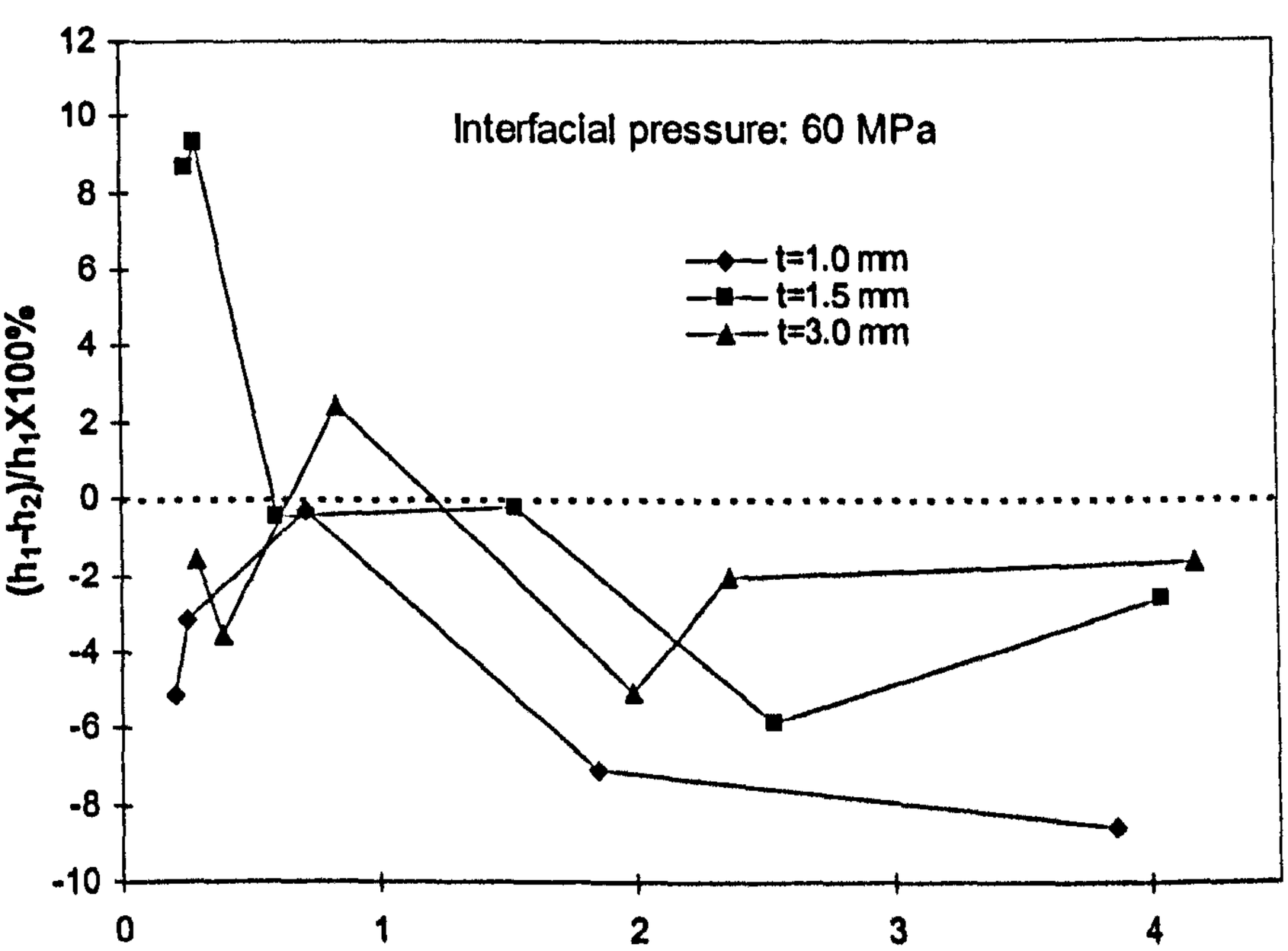

(b) Relative difference of h-value in repeated experiments

Fig.3.25 Uncertainties in computation of h-values
under interfacial pressure of 60 MPa

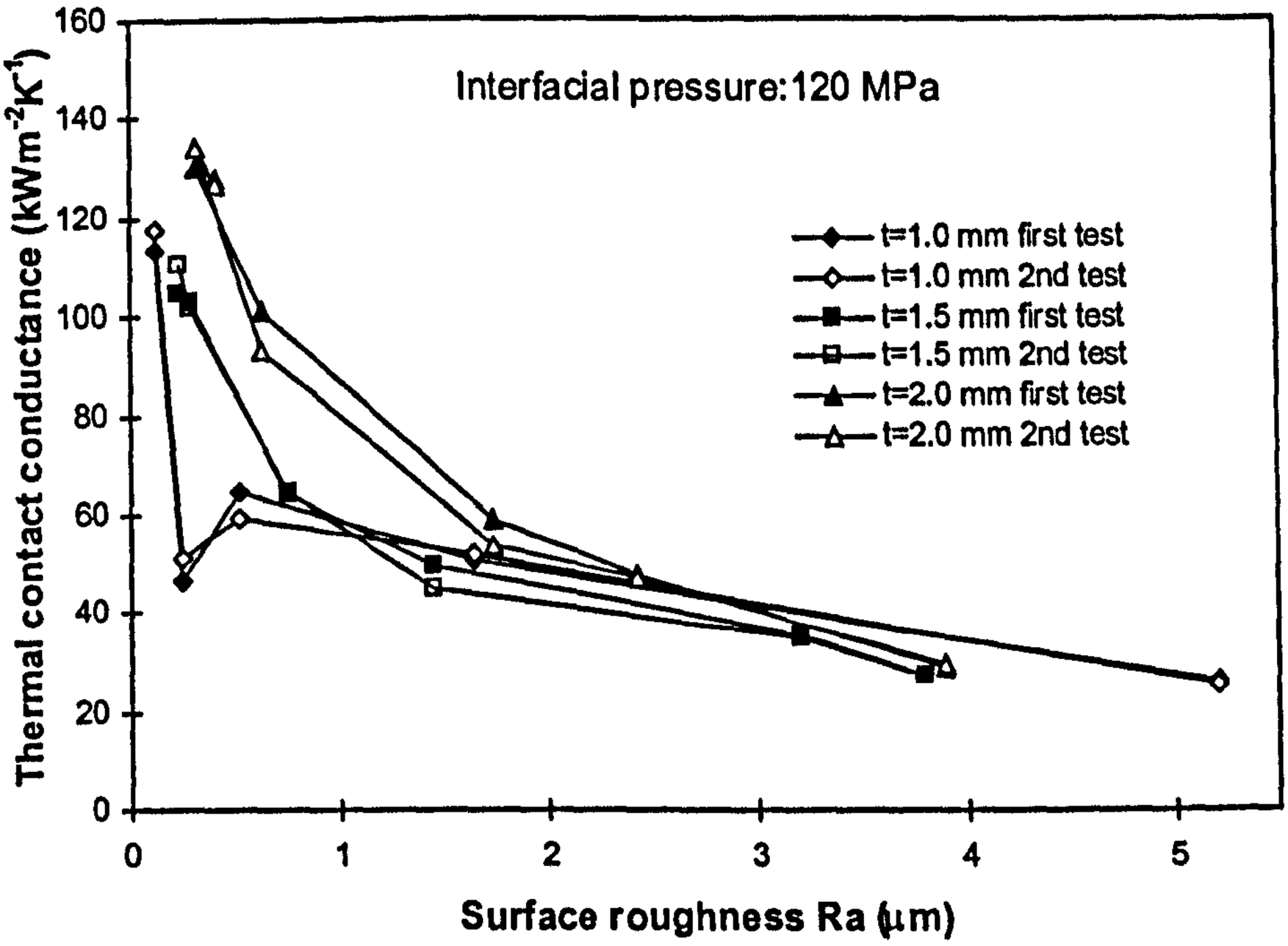

(a) Repeated experiments

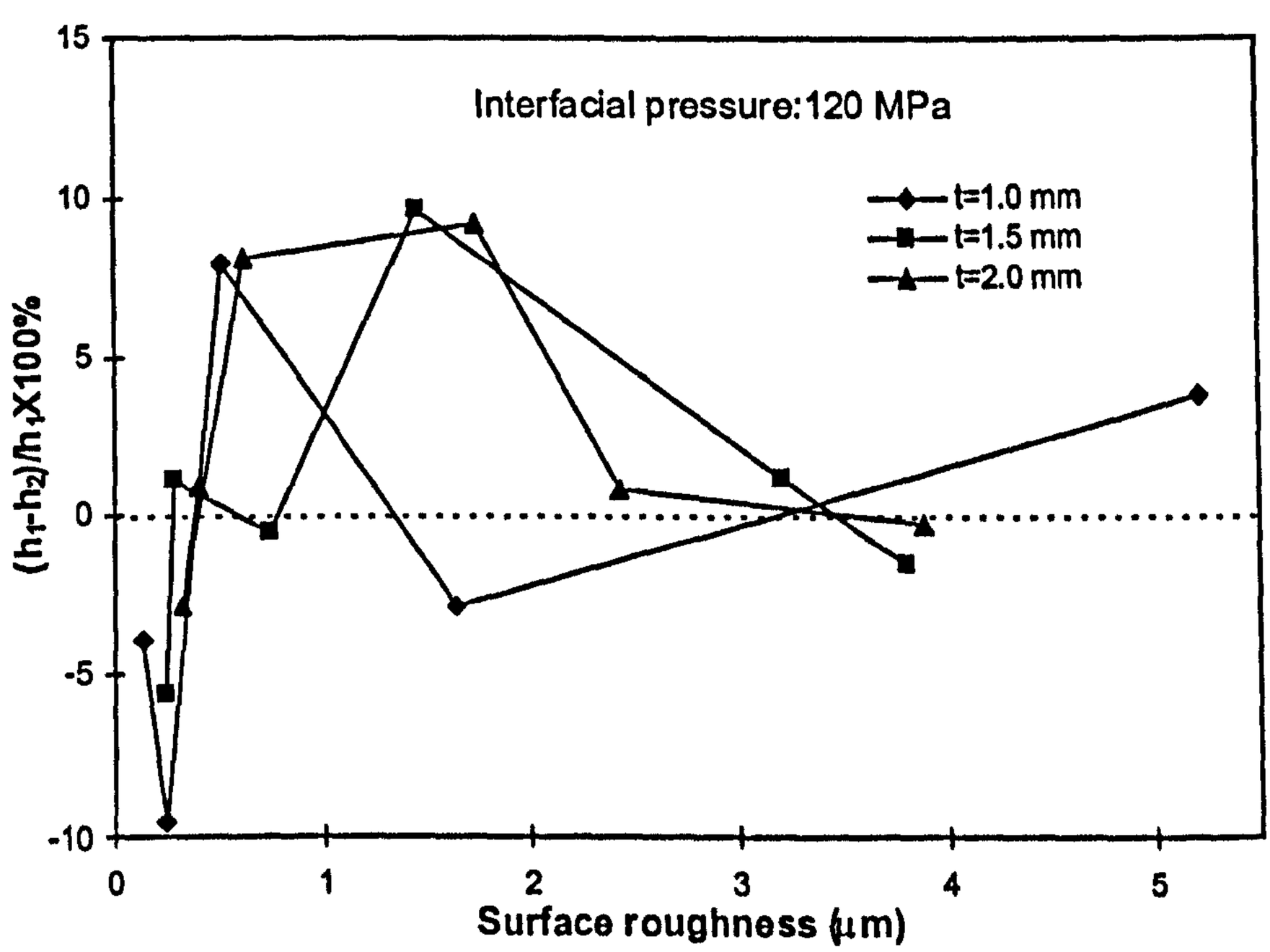

(b) Relative difference of h-value in repeated experiments

Fig.3.26 Uncertainties in computation of h-values under interfacial pressure of 120 MPa

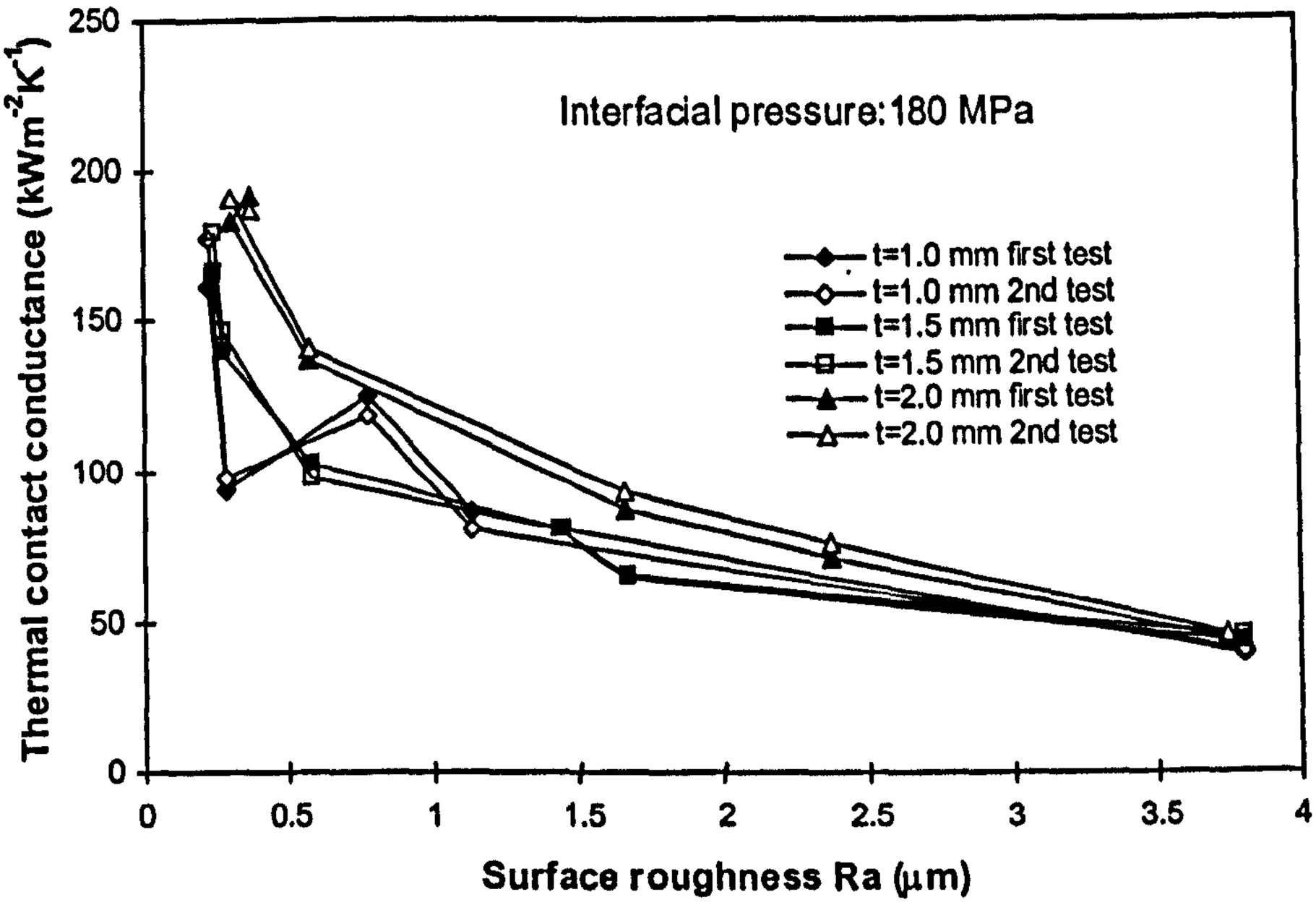

(a) Repeated experiments

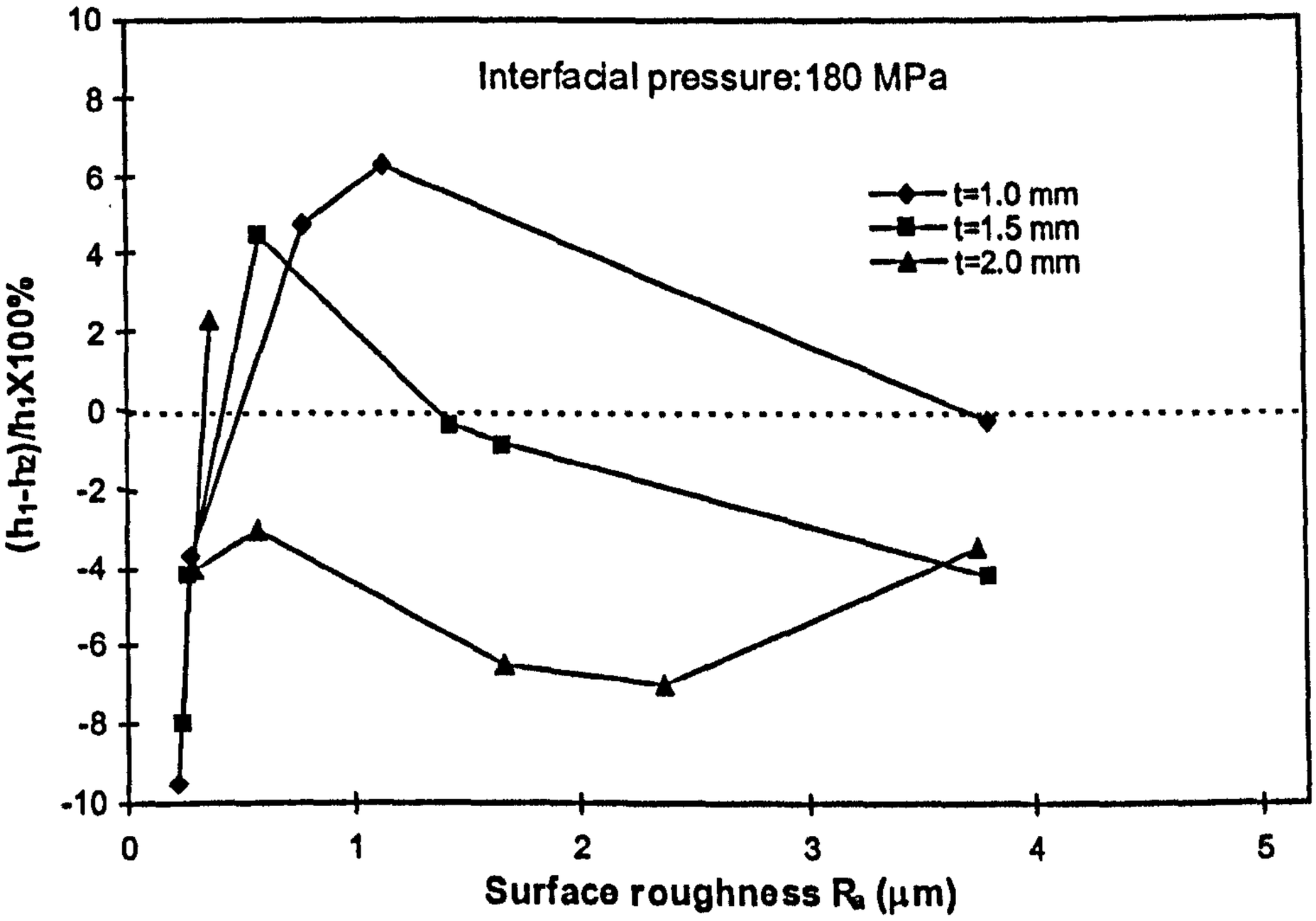

(b) Relative difference of h-value in repeated experiments

Fig. 3.27 Uncertainties in computation of h-values
under interfacial pressure of 180 MPa

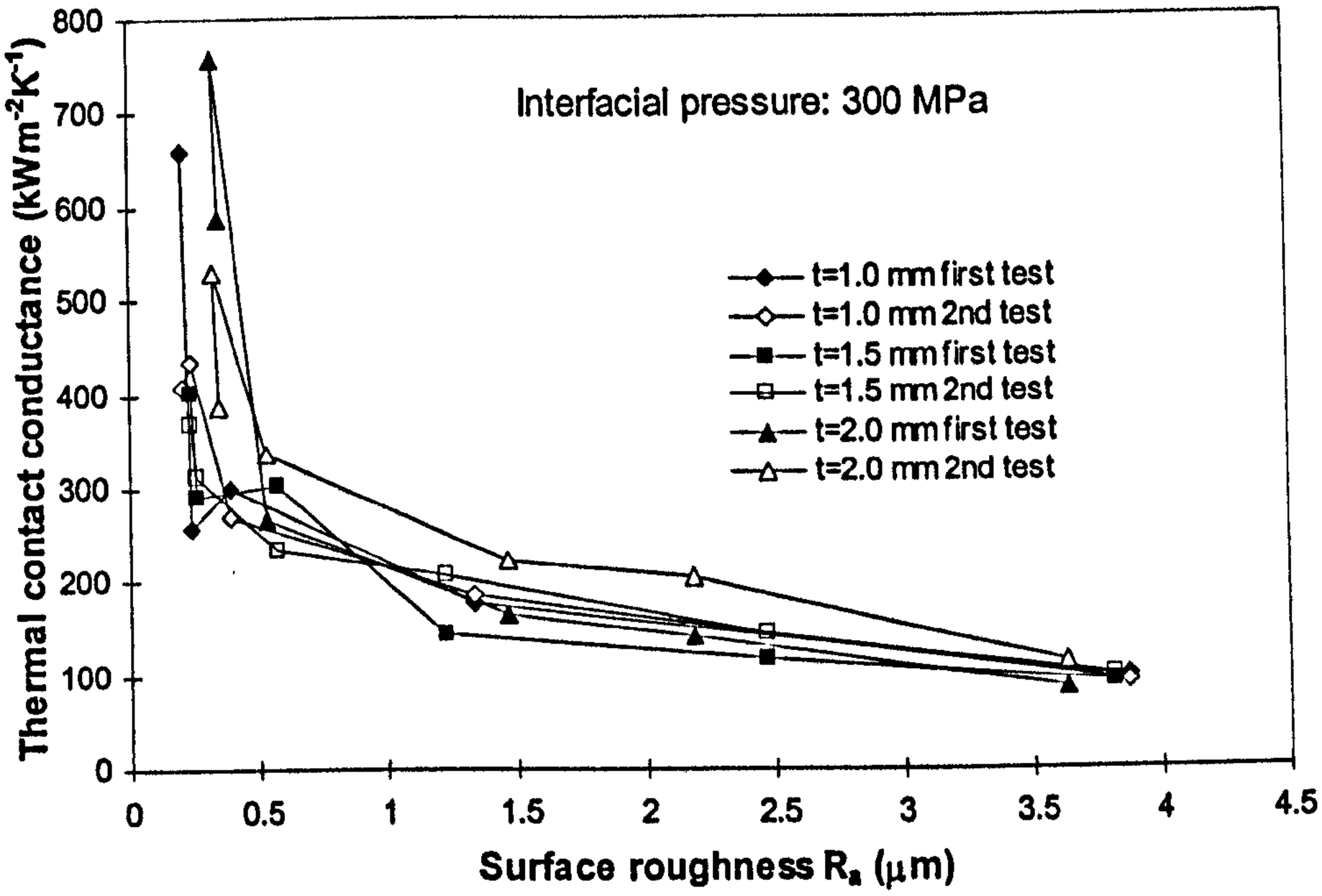

(a) Repeated experiments

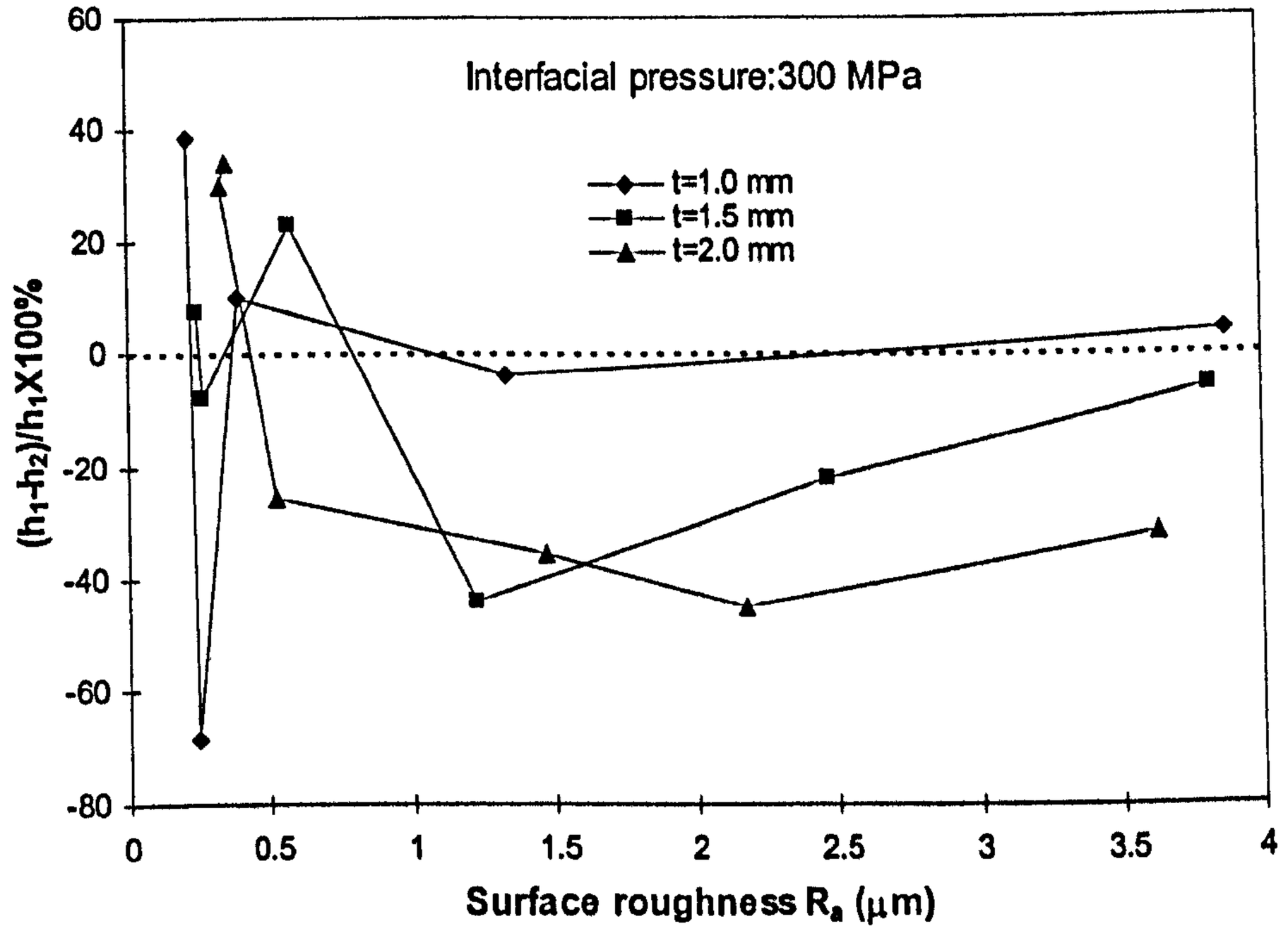

(b) Relative difference of h-value in repeated experiments

Fig. 3.28 Uncertainties in computation of h-values
under interfacial pressure of 300 MPa

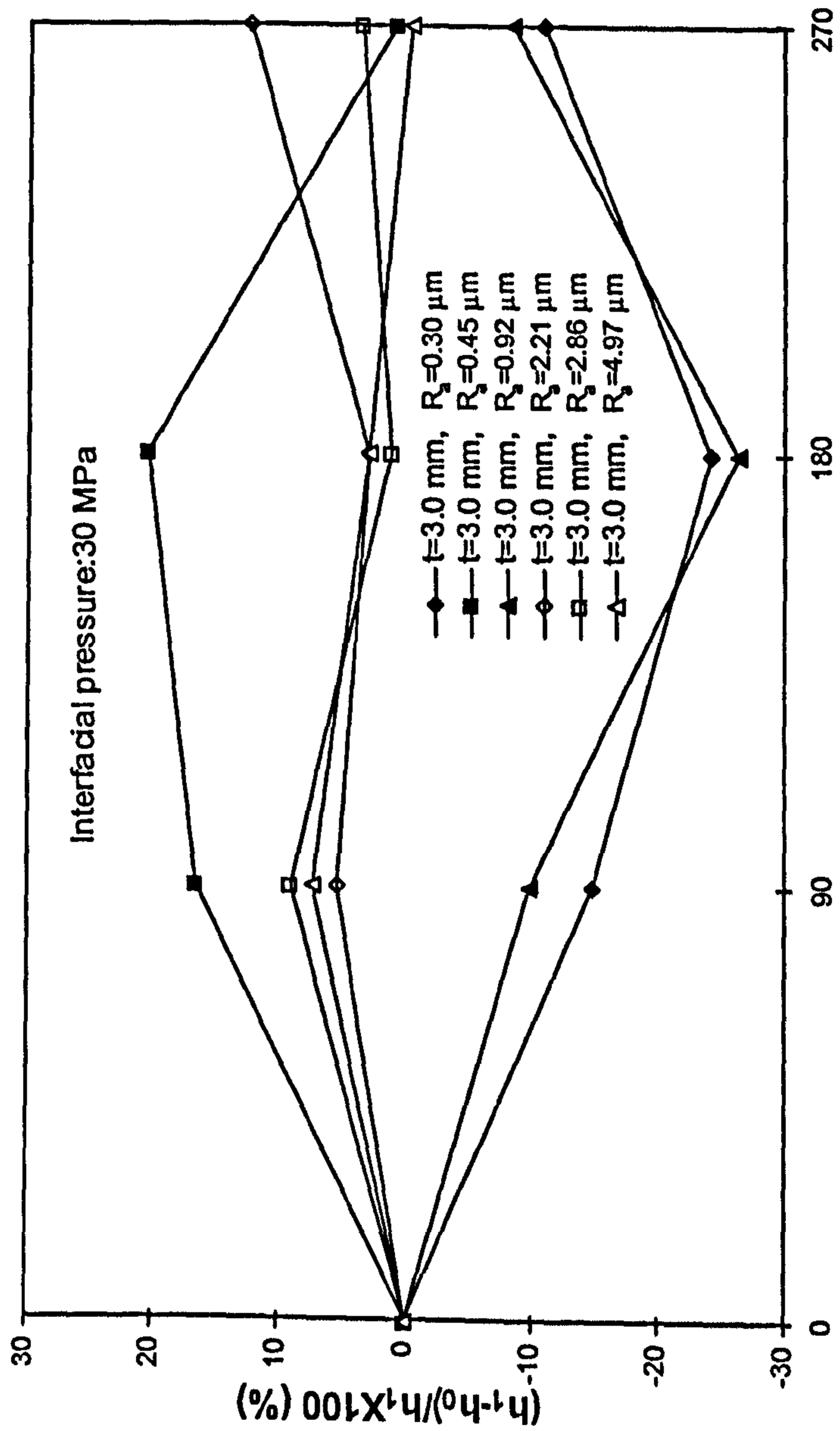

Fig. 3.29 Evaluation of h-values for different orientations of test specimens

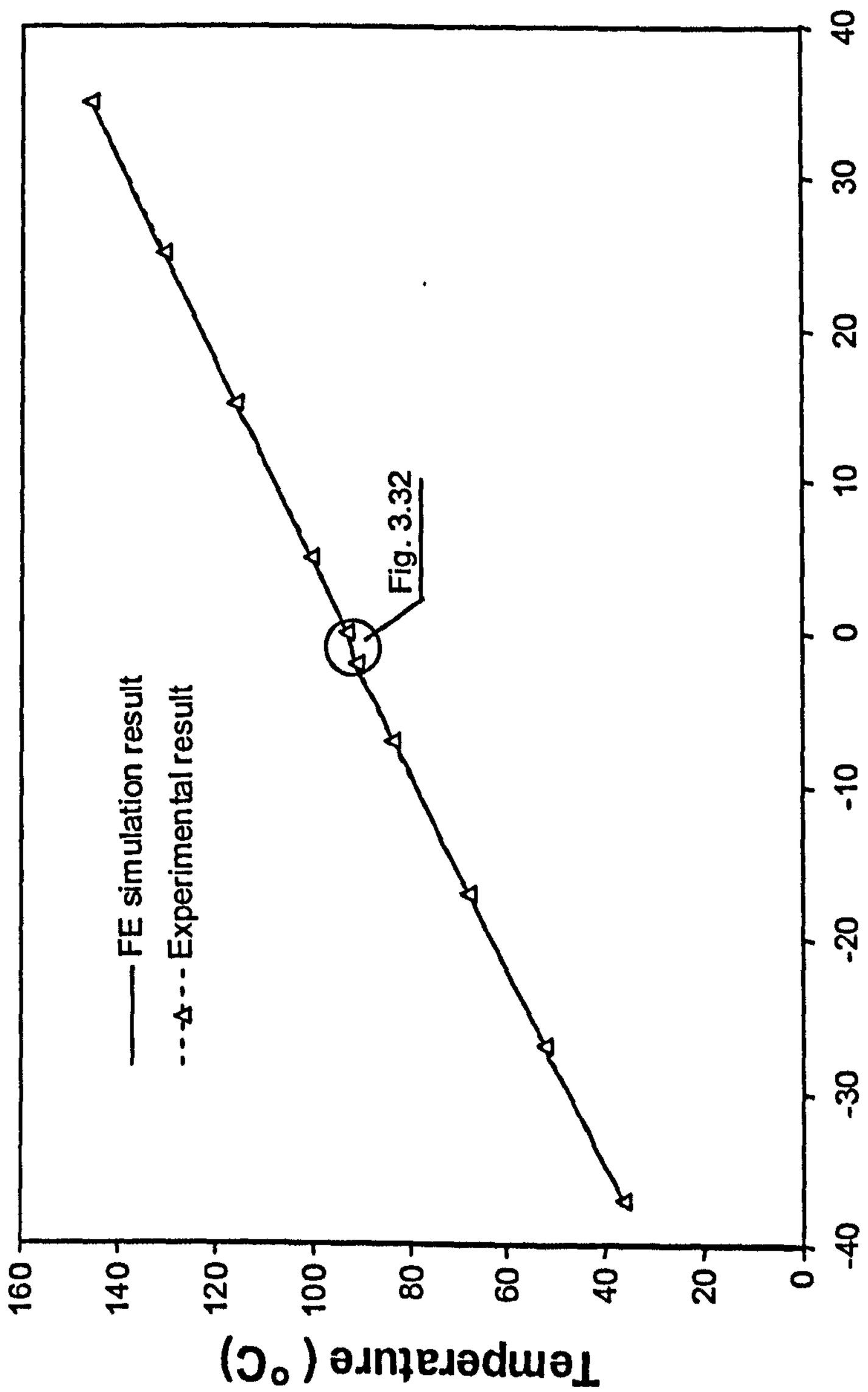

Fig. 3.30 The temperature comparison between FE simulation and experiment

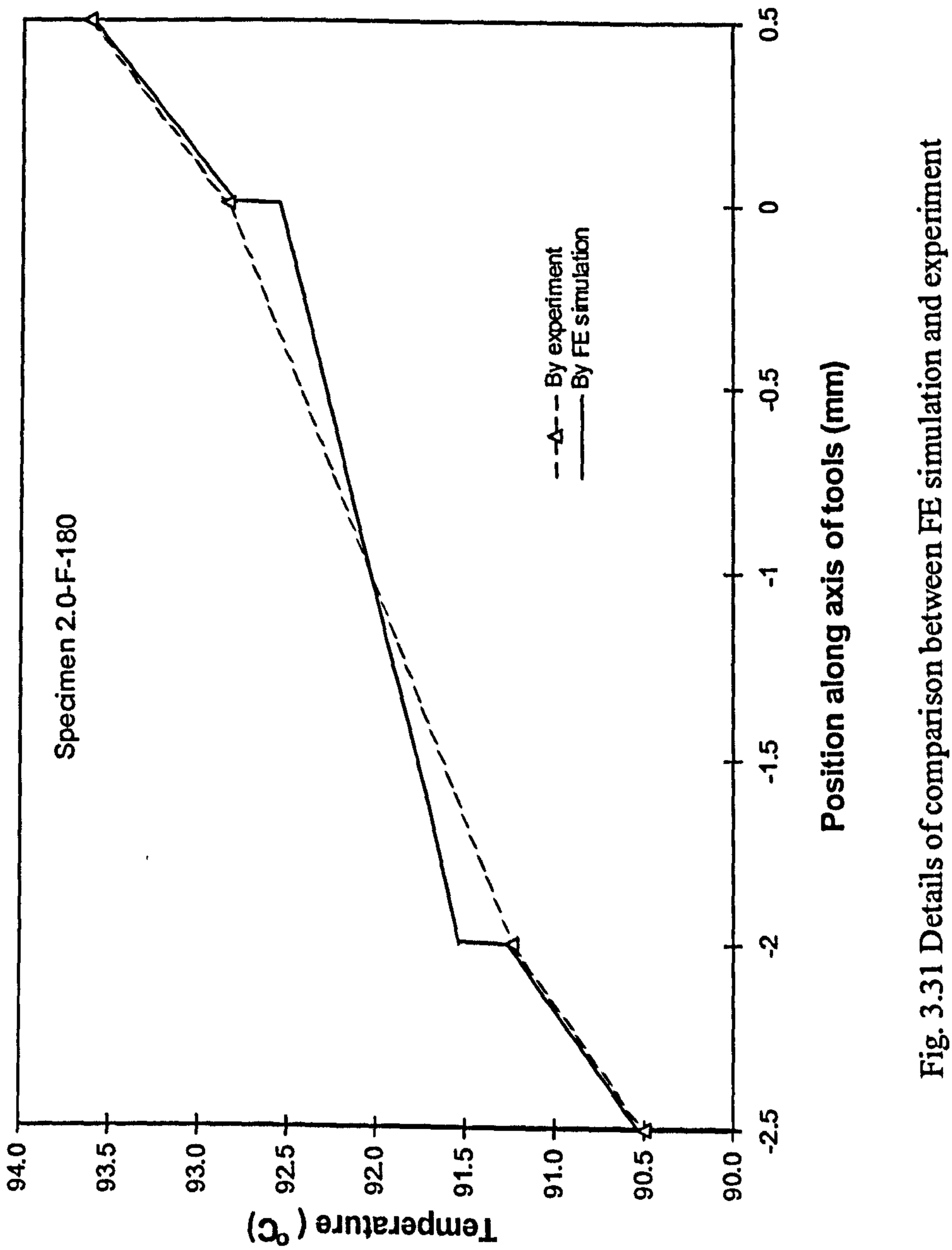

Fig. 3.31 Details of comparison between FE simulation and experiment

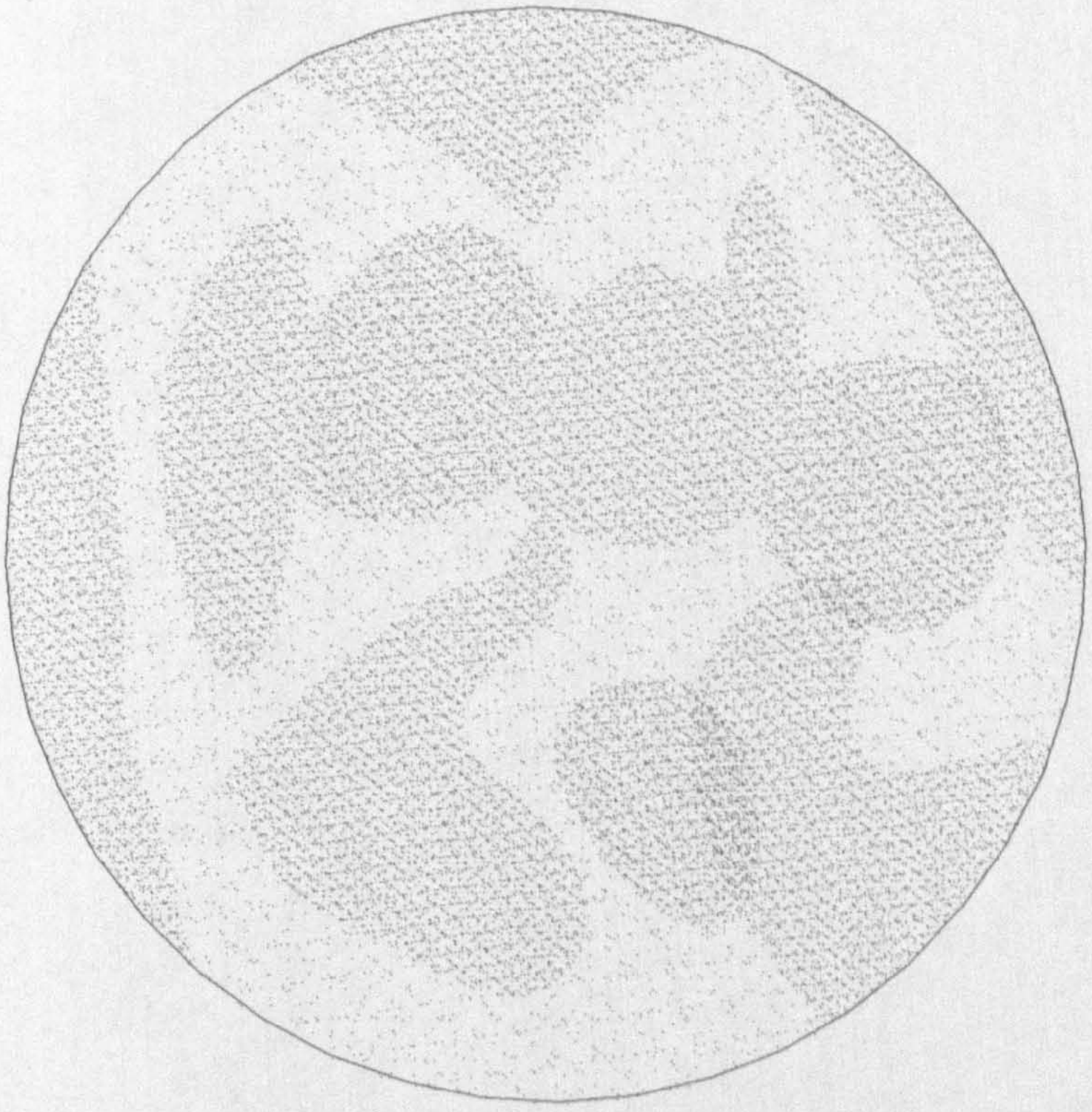

Darken areas are in contact

Fig. 3.32 Tool-specimen contact profile

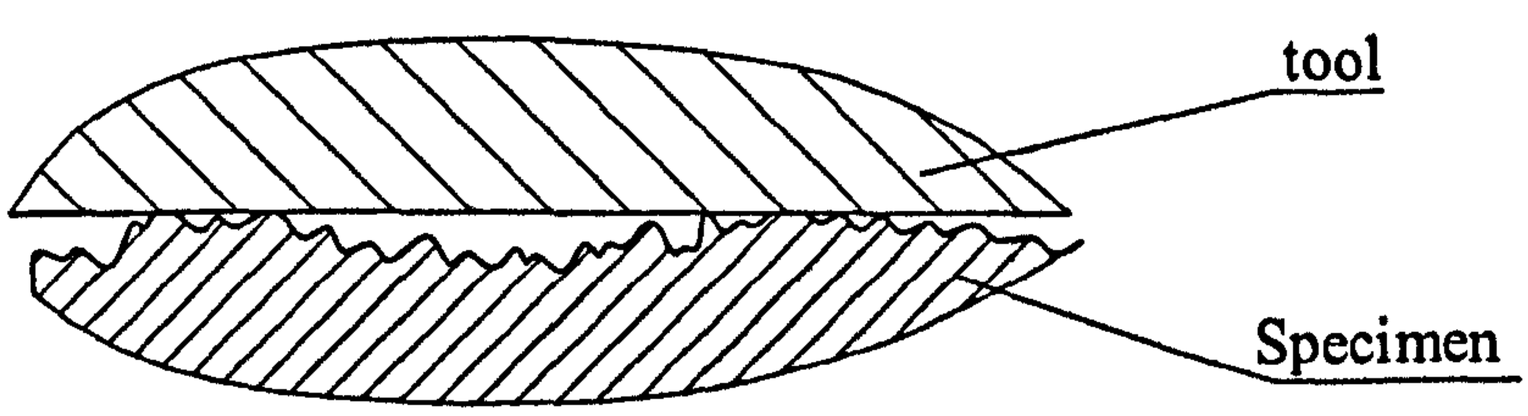

(a) Specimen surface with surface macro-irregularities

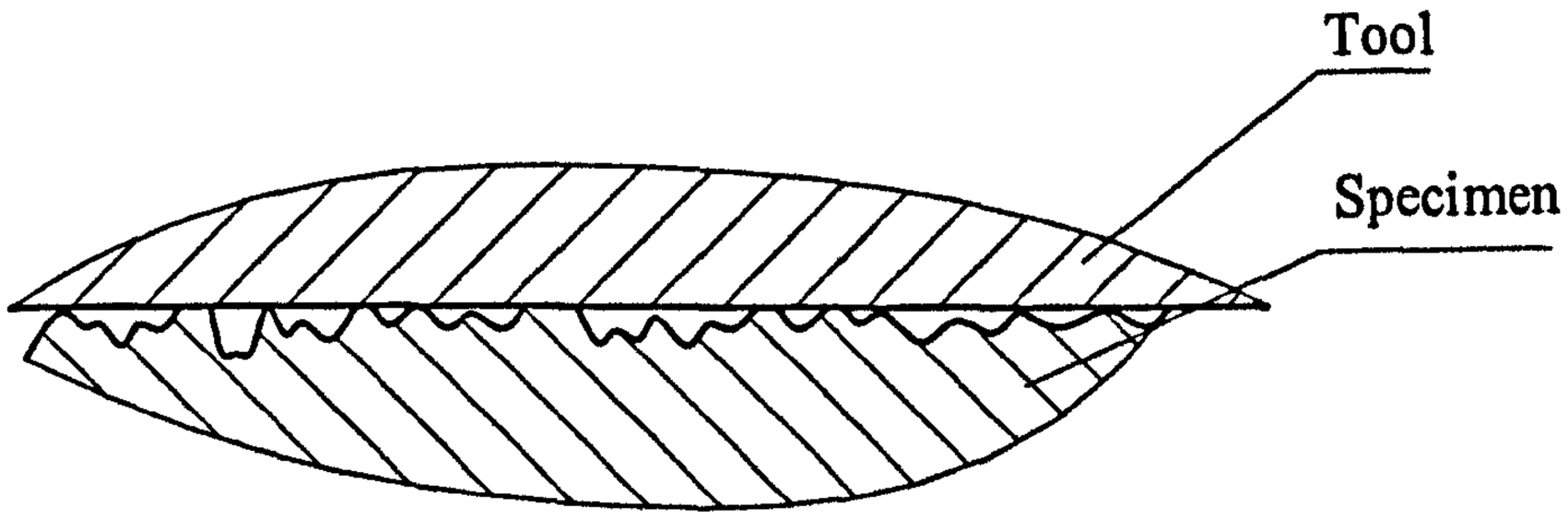

(b) Specimen surface without surface macro-irregularities

Fig. 3.33 Interface contact situations
with and without surface macro-irregularities

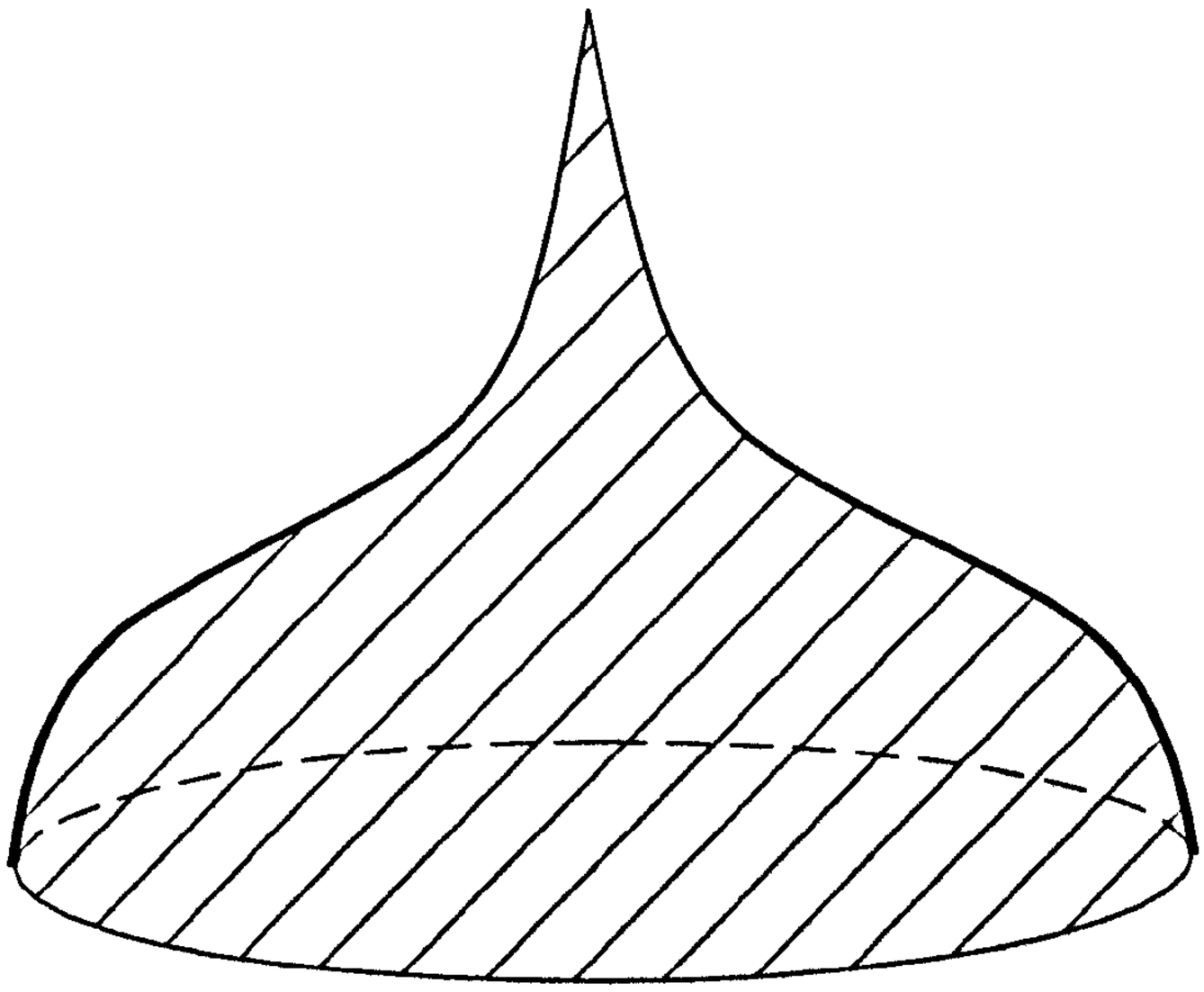

(a) Representative asperity

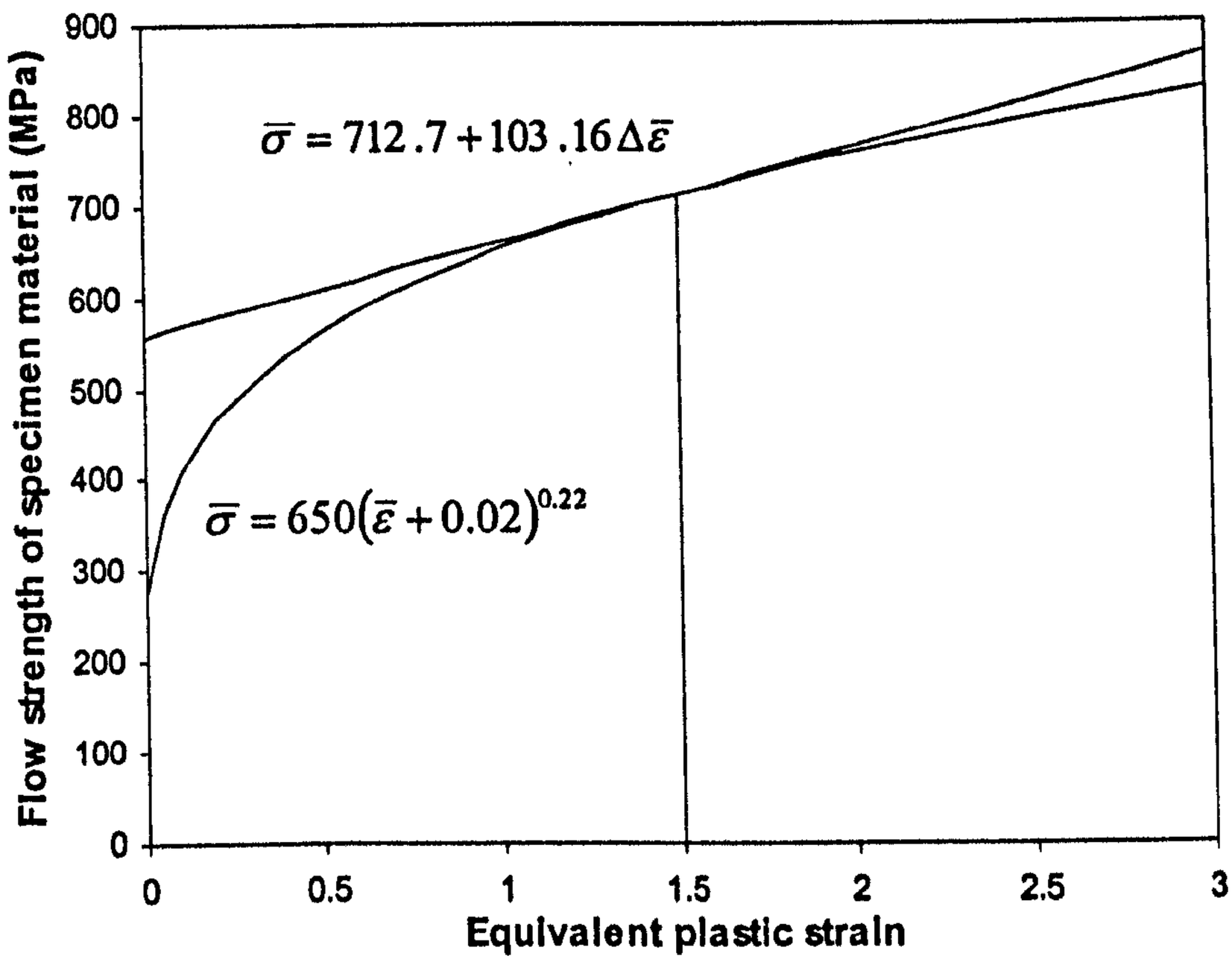

(b) Assumed stress-strain relation

Fig. 3.34 Representative asperity and its assumed stress-strain relationship

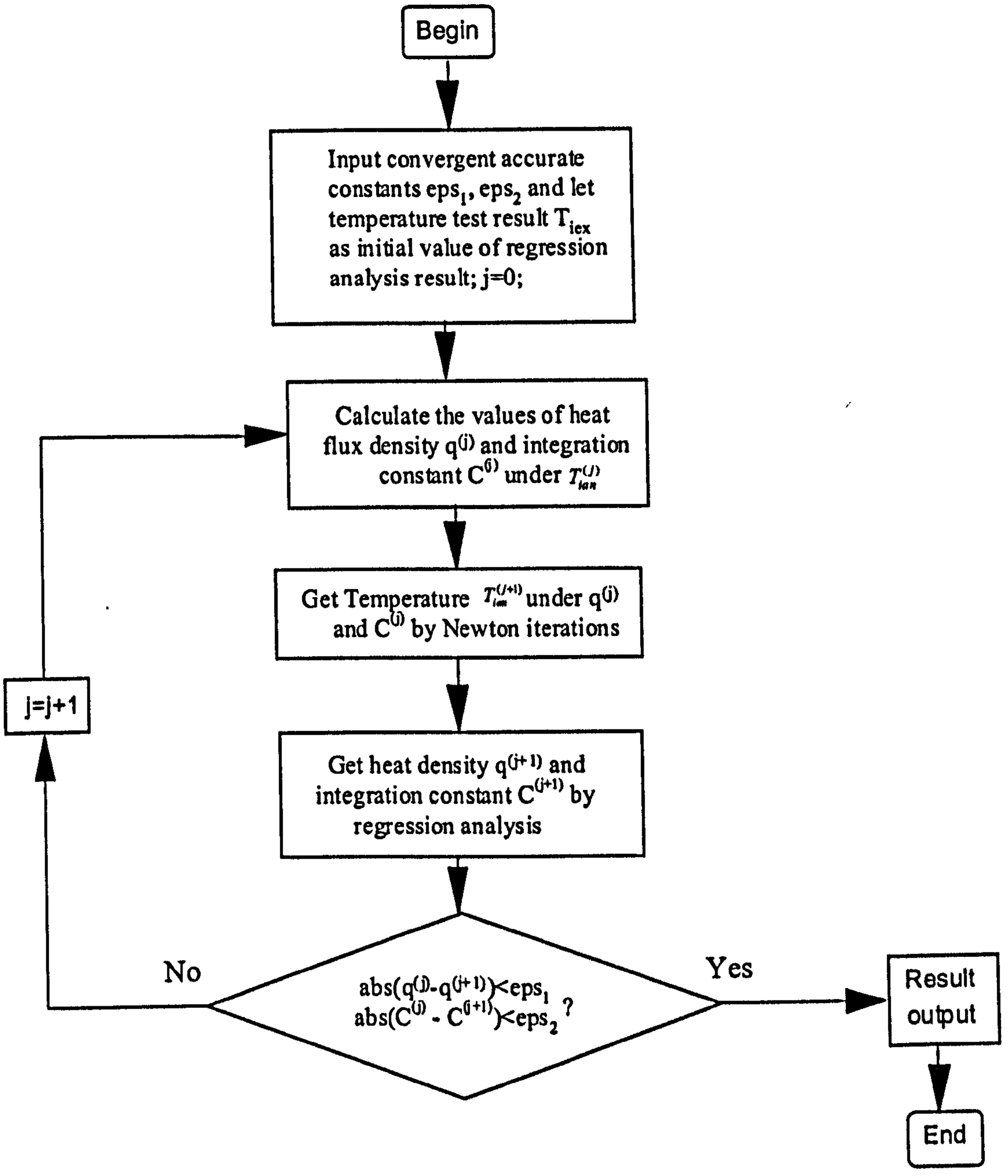

Fig. 3.1.1 Iterative process with variable conductivity

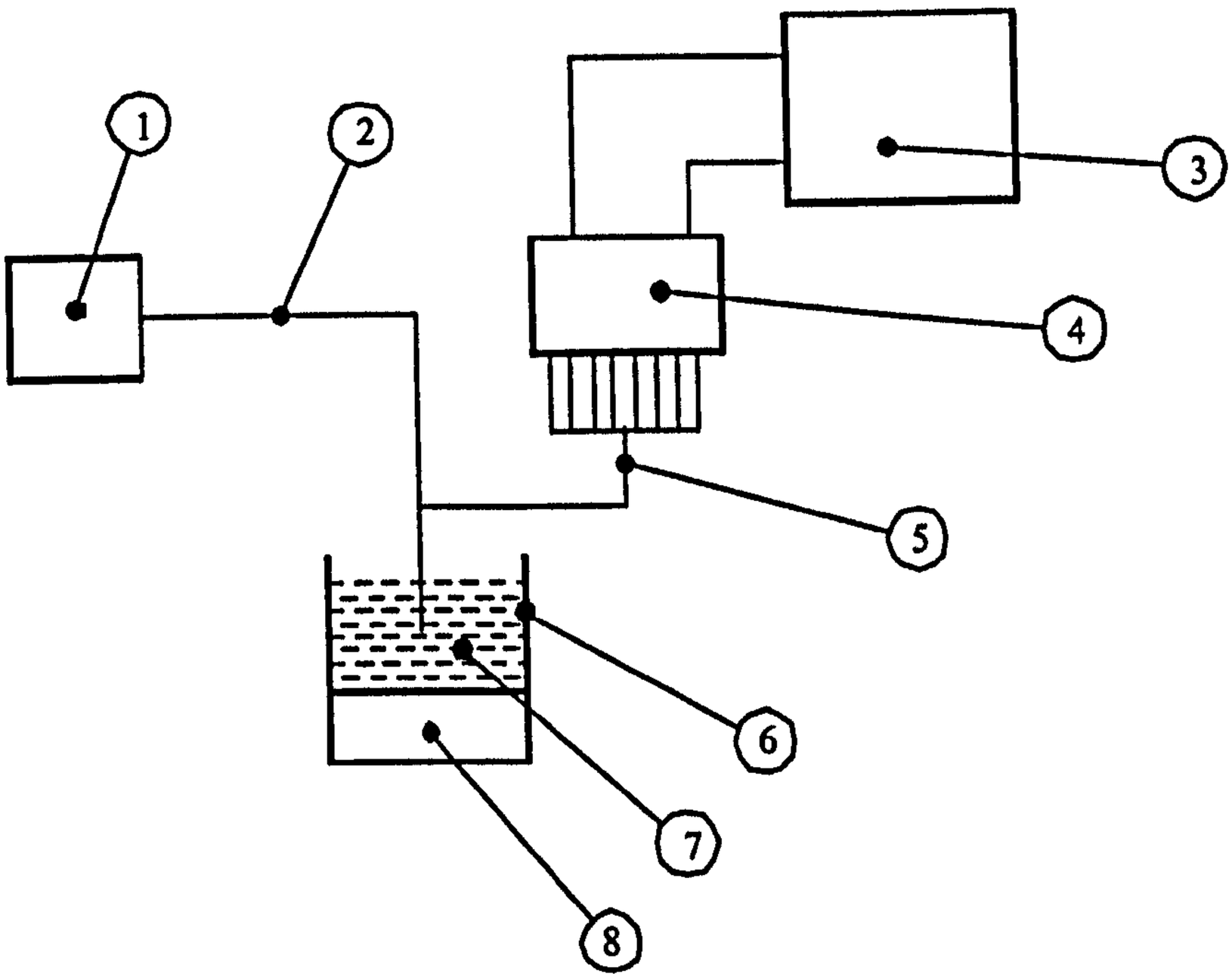

1. Reference Instrument for temperature measurement
2. Calibrated Reference thermocouple
3. Computer monitor system
4. Amplifier and data acquisitive system
5. Eight thermocouples used in the experimental equipment
6. Heat transfer oil tank
7. Heat transfer oil
8. Adjustable electric heater

Fig. 3.2.1 Schematic diagram of thermocouple calibration

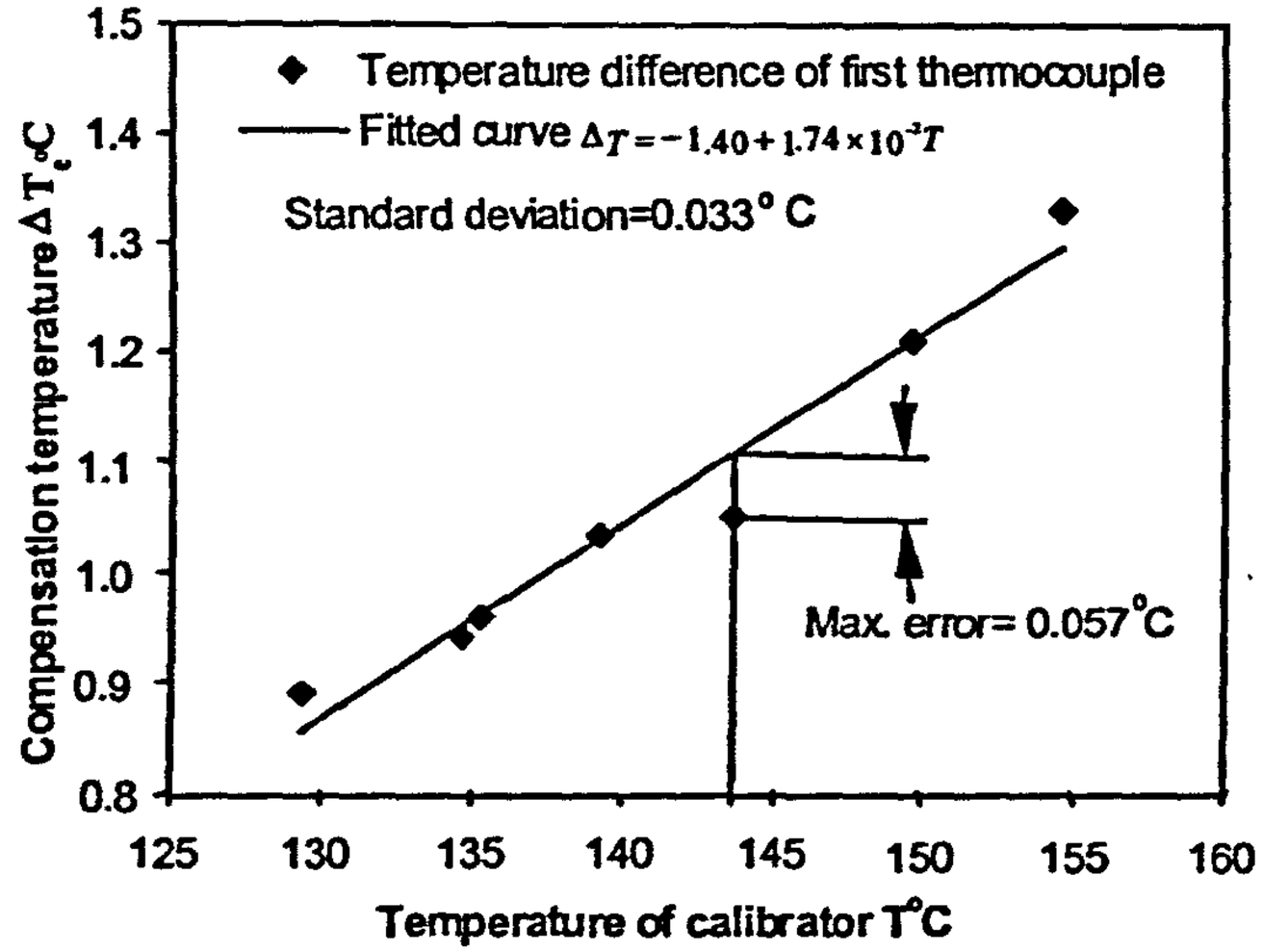

(b)

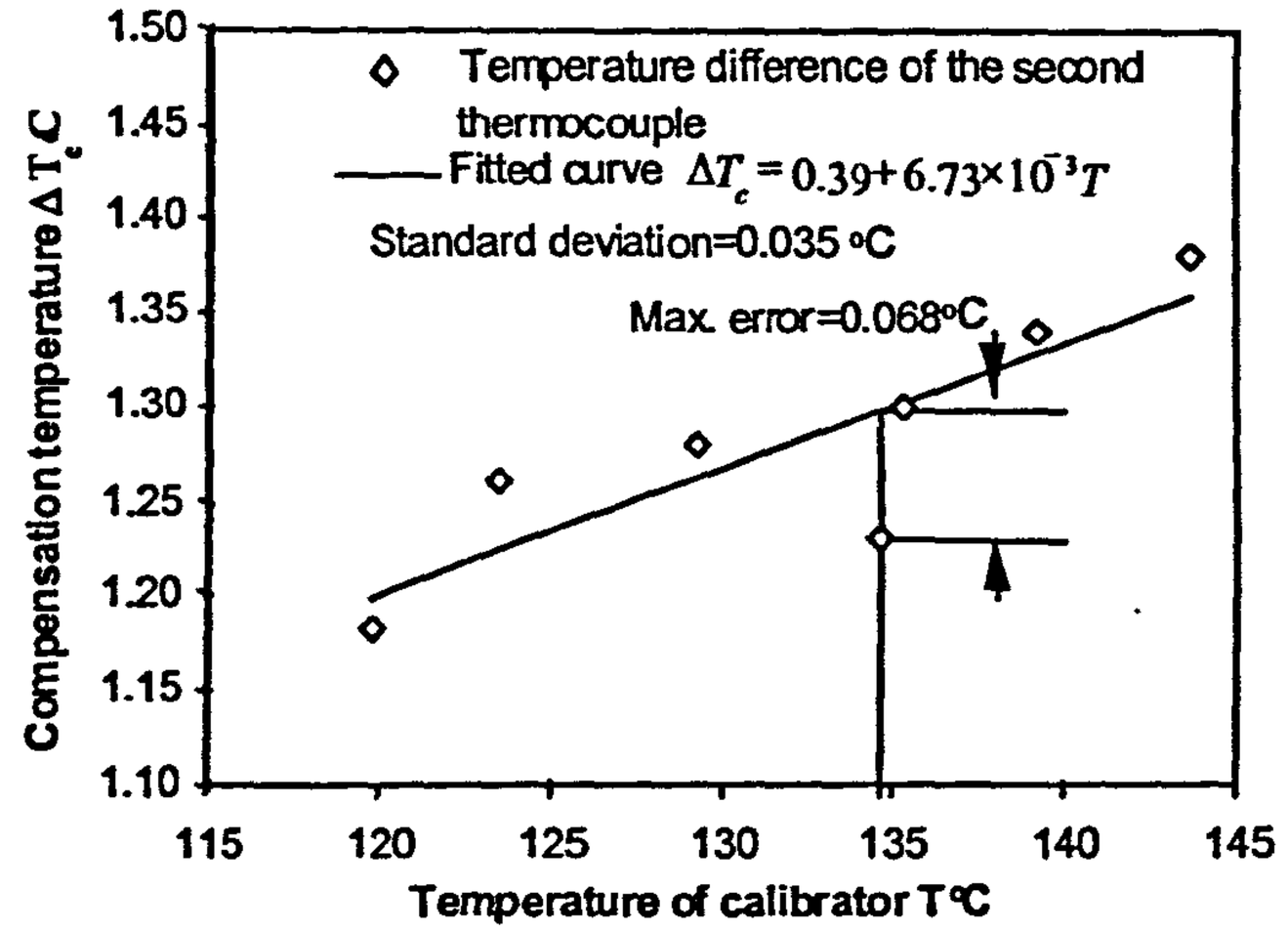

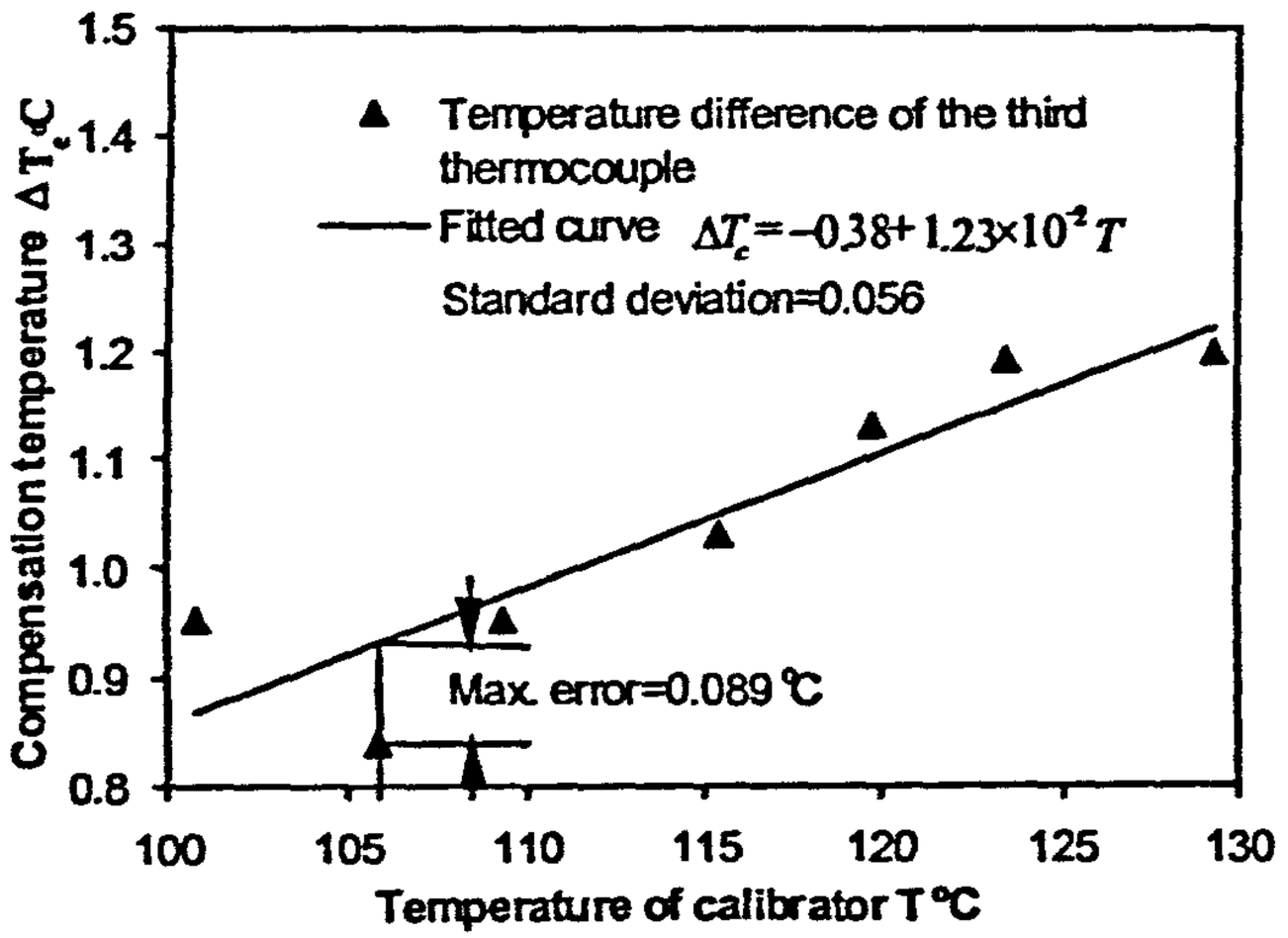

(d)

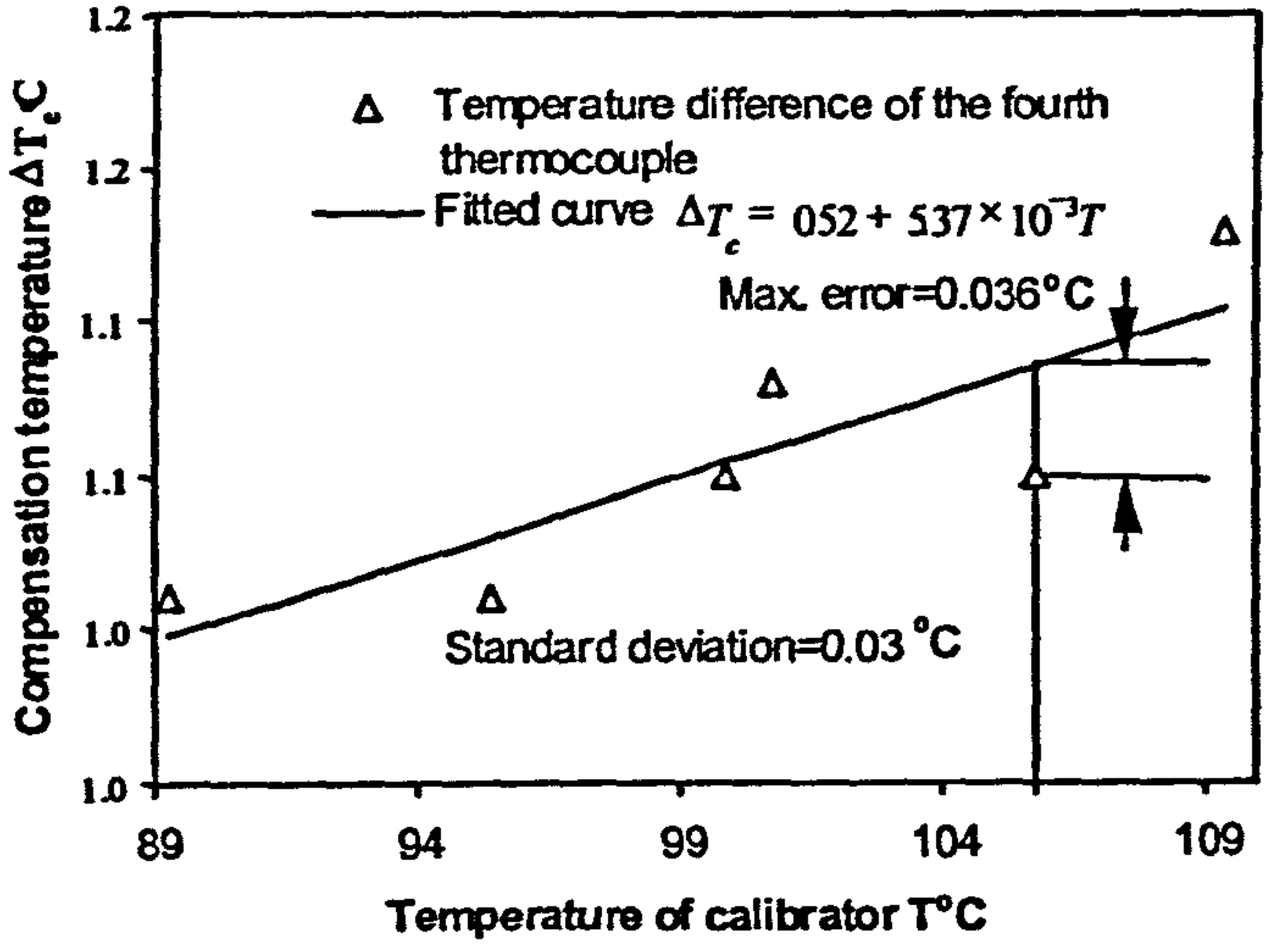

Fig. 3.2.2 Upper tool thermocouple calibration results

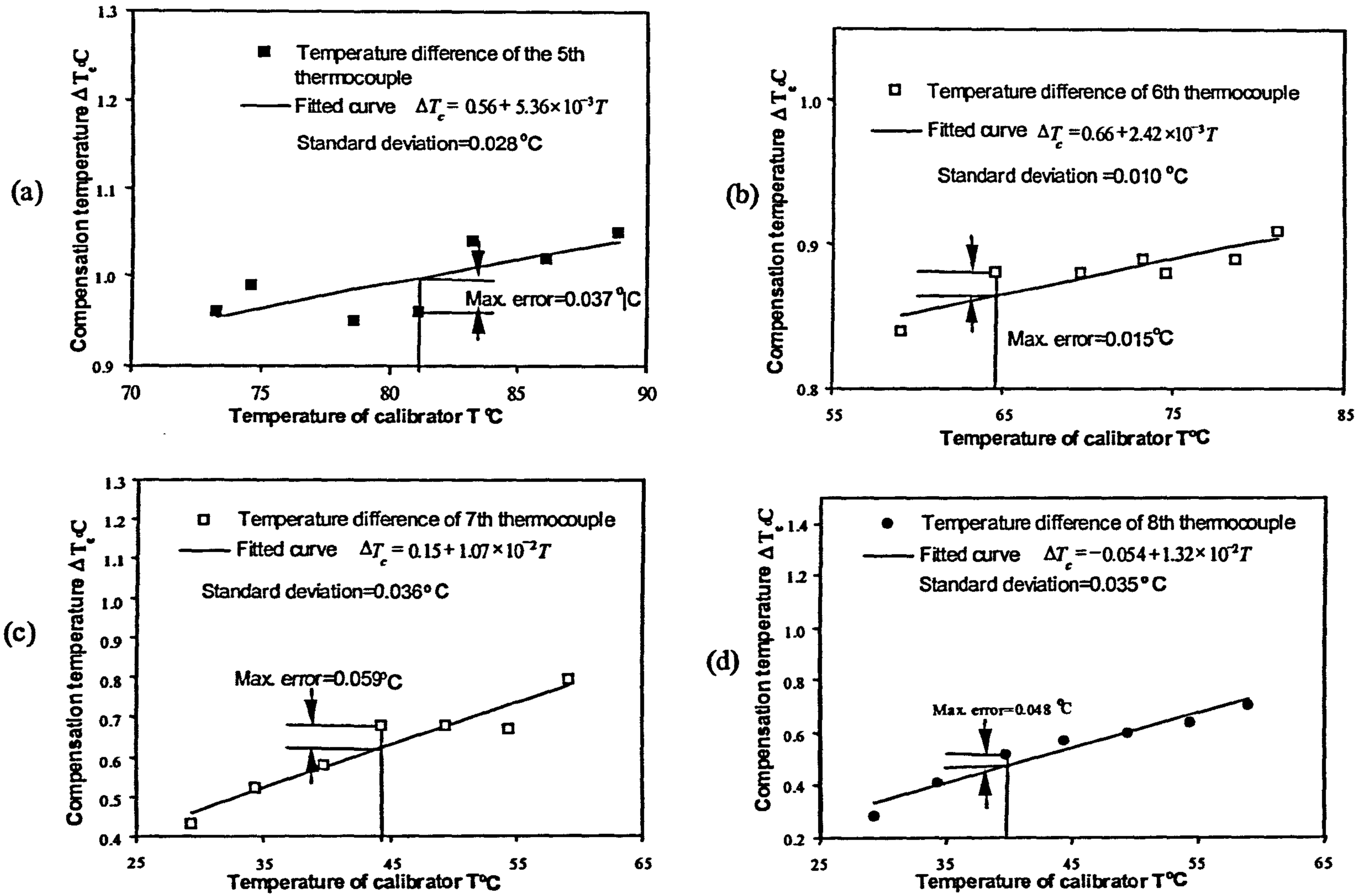

Fig. 3.2.3 Lower tool thermocouple calibration results

4.0-E-000

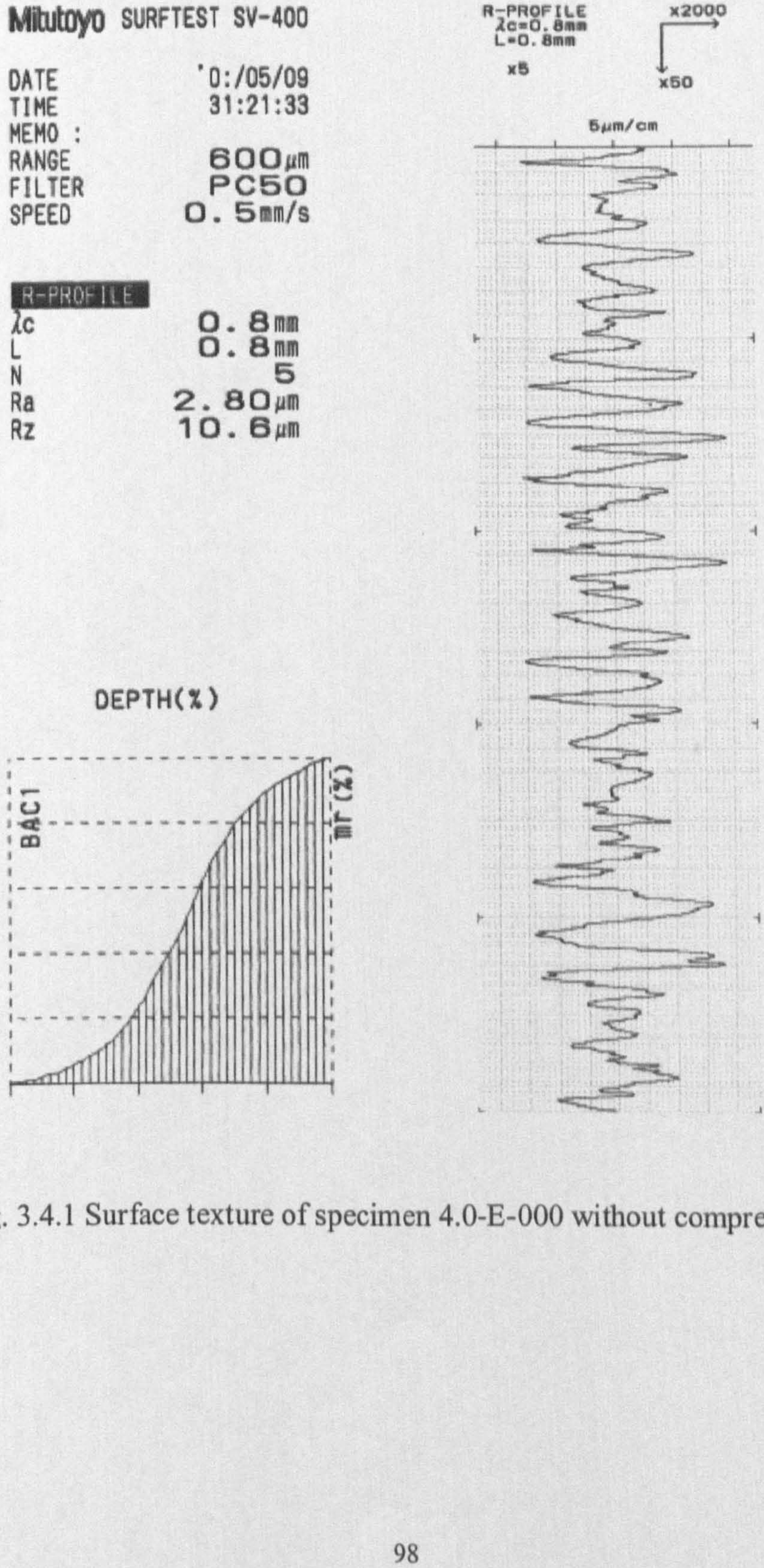

Fig. 3.4.1 Surface texture of specimen 4.0-E-000 without compression

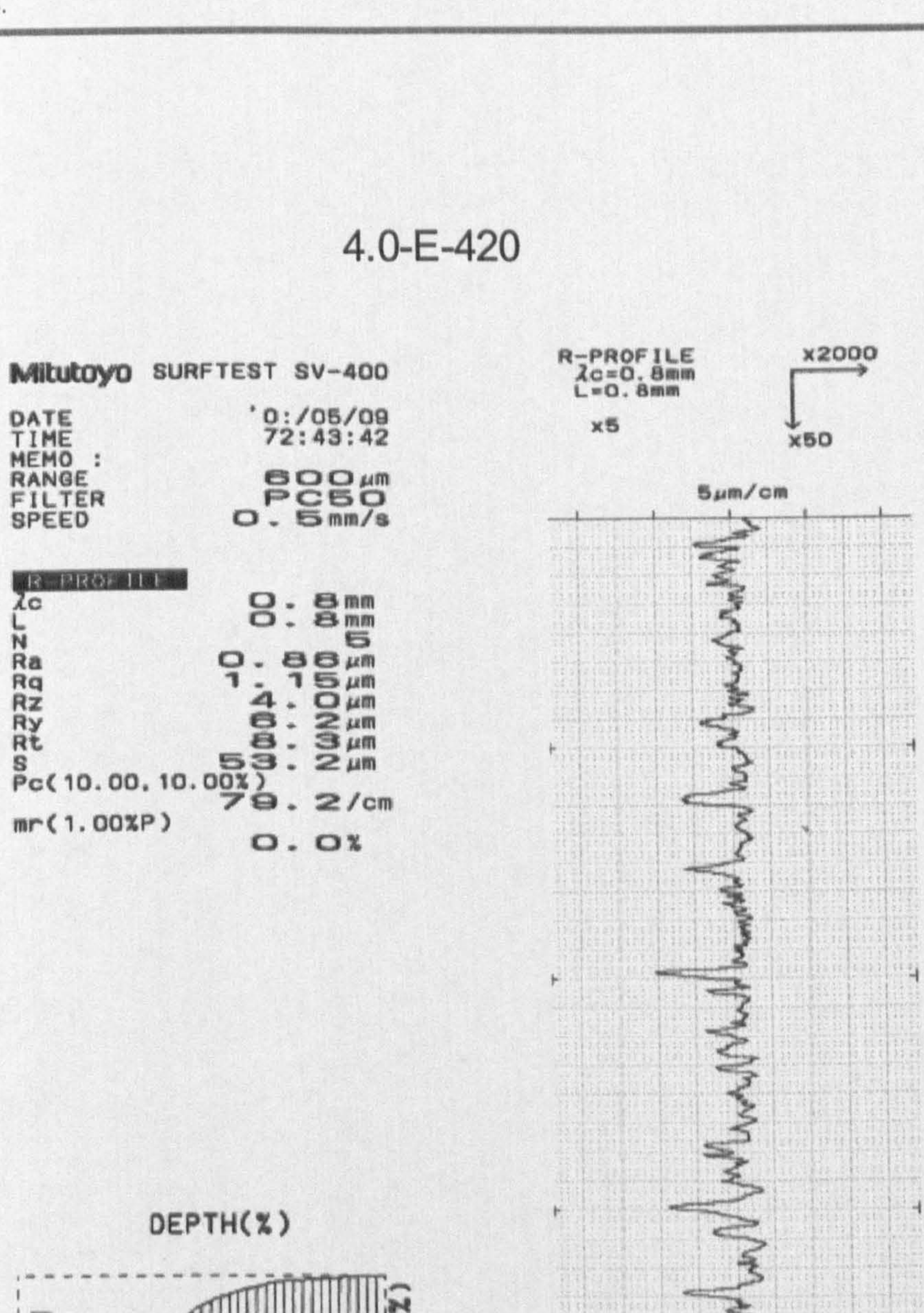

Fig. 3.4.2 Surface texture of specimen 4.0-E-420 after compression under pressure 420 MPa

1.0-A-000

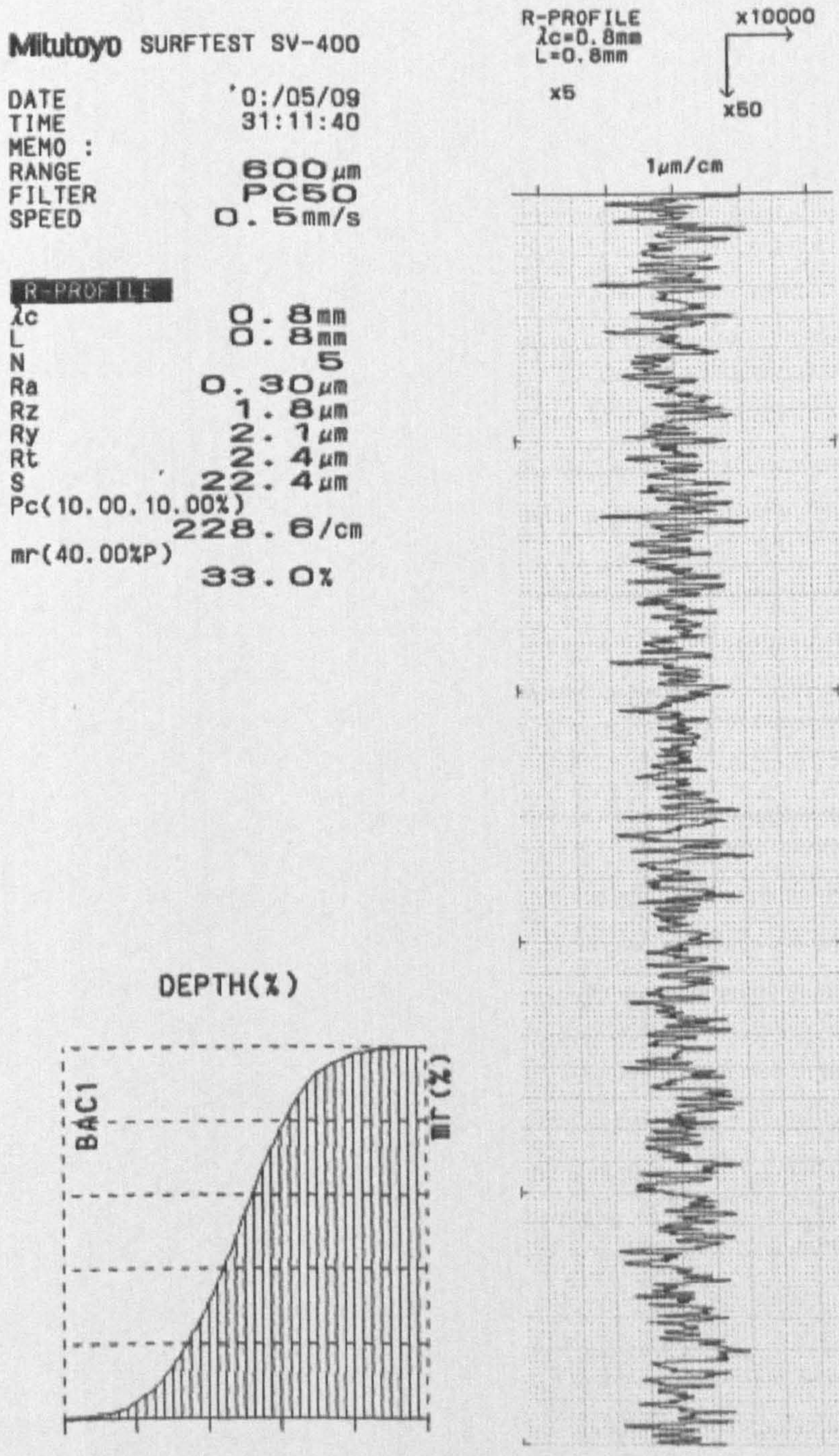

Fig. 3.4.3 Surface texture of specimen 1.0-A-000 without pressure

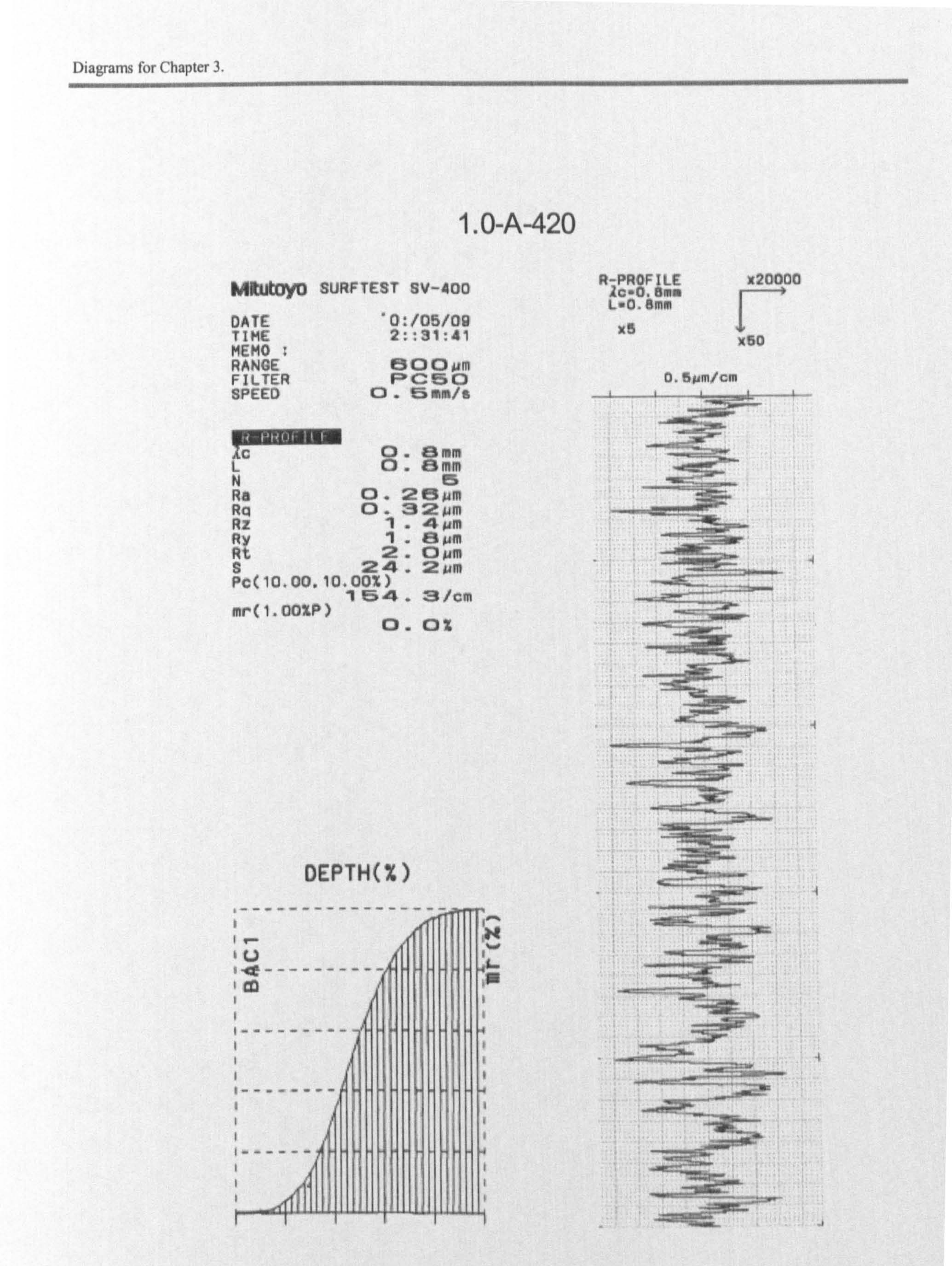

Fig. 3.4.4 Surface texture of specimen 1.0-A-420 with pressure420 MPa

2.5-C-000

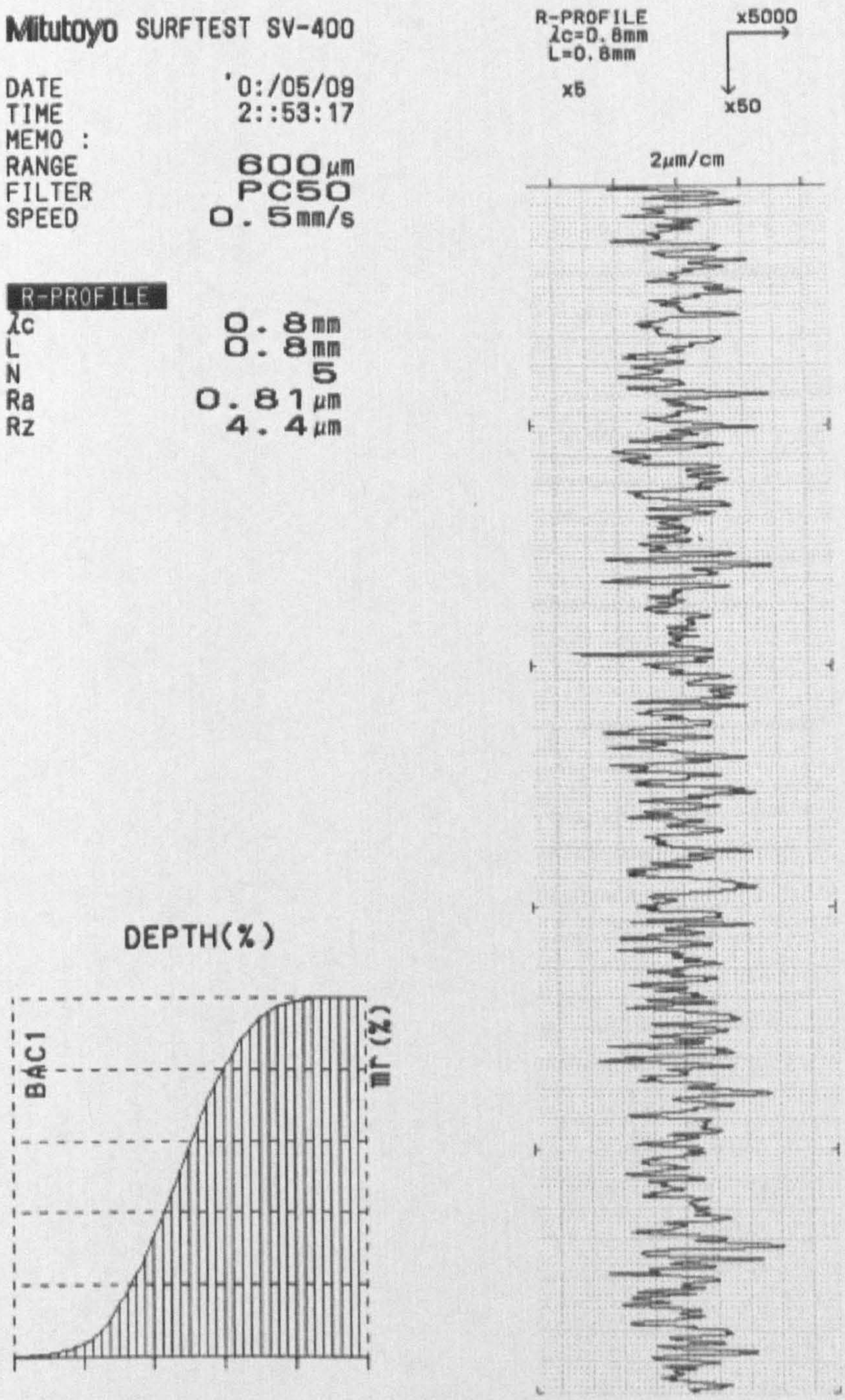

Fig. 3.4.5 Surface texture of specimen 2.5-C-000 without compression

2.5-C-180

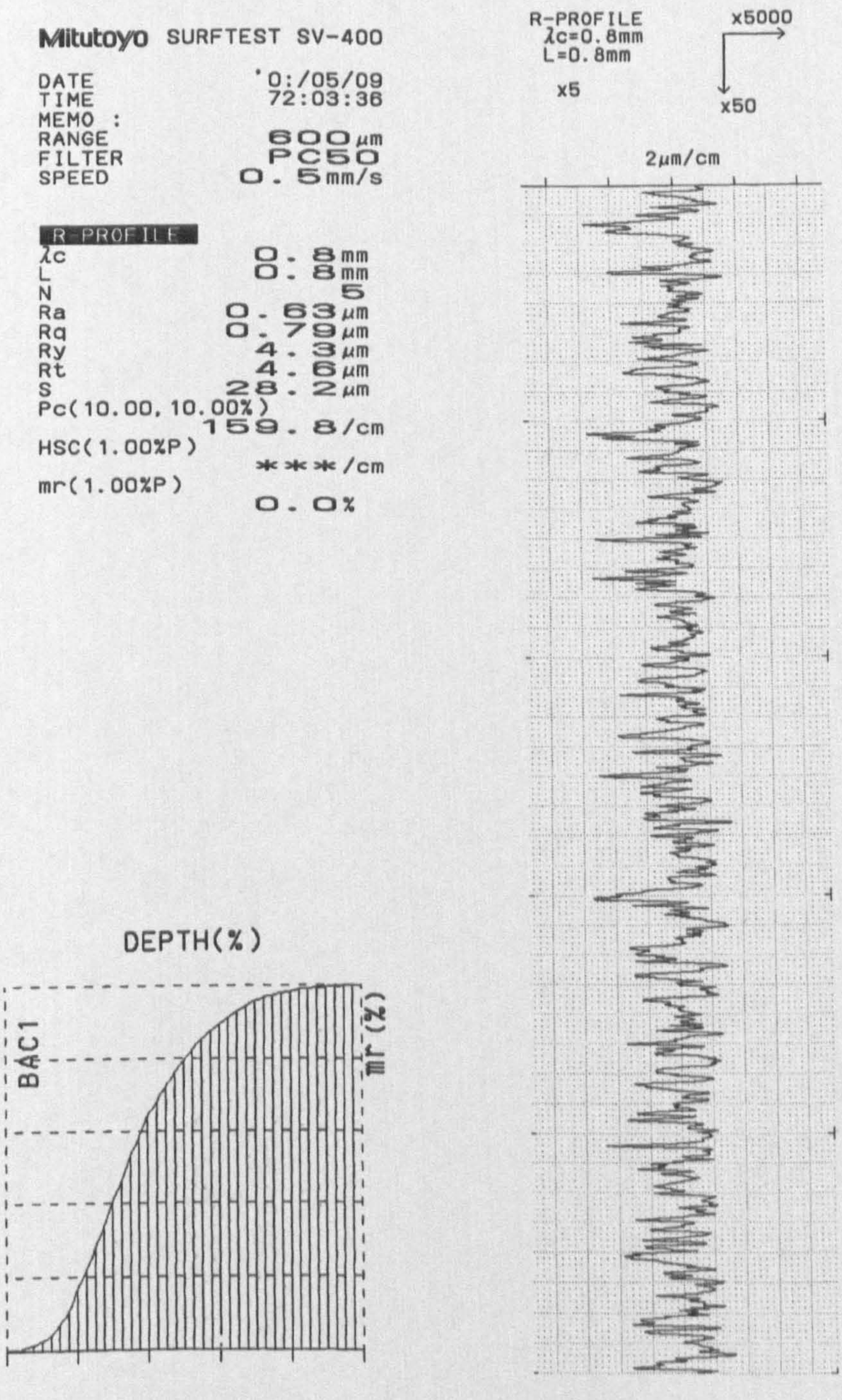

Fig. 3.4.6 Surface texture of specimen 2.5-C-180
after compression at pressure 180 MPa

2.5-C-420

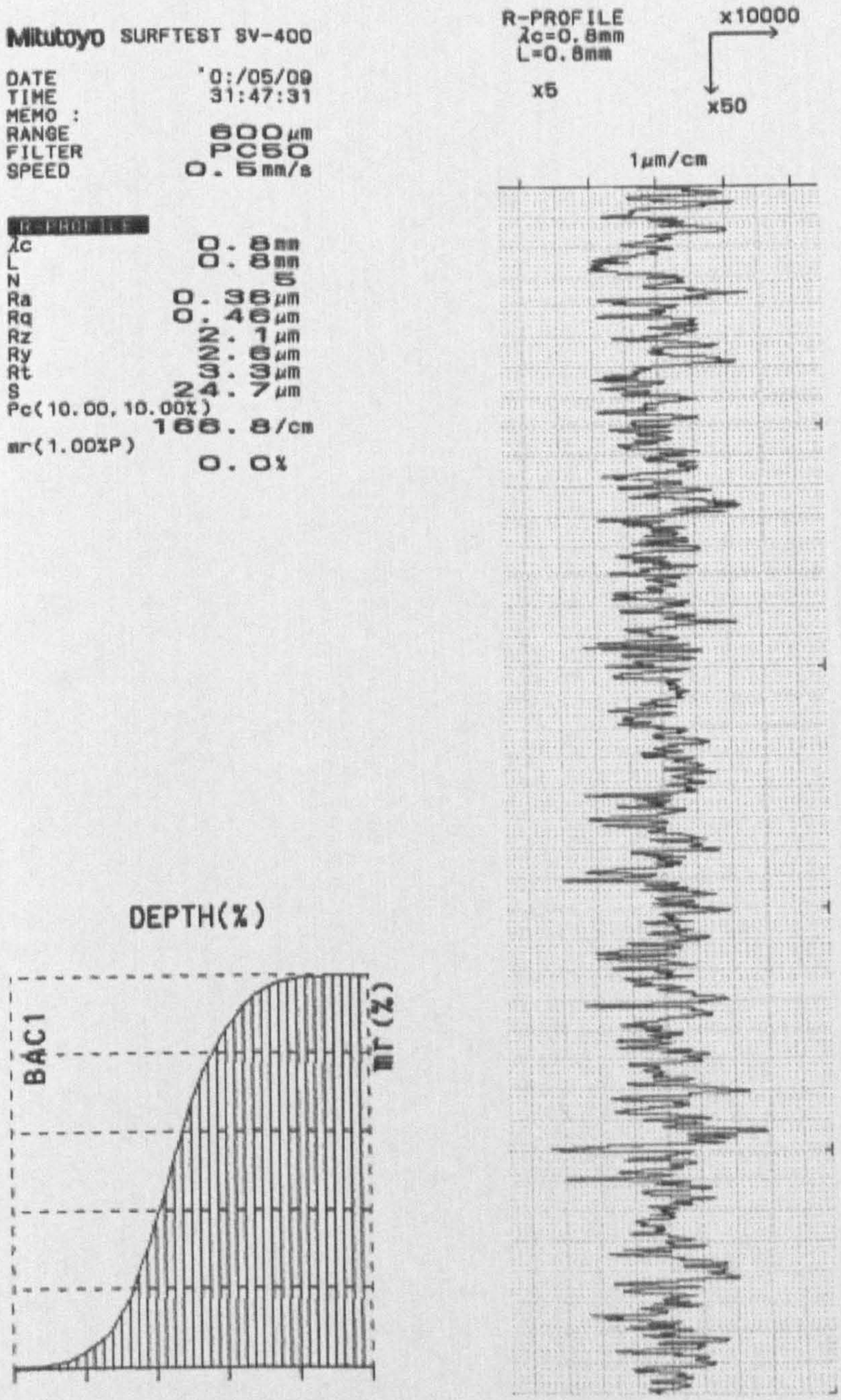

Fig. 3.4.7 Surface texture of specimen 2.5-C-420
after compression under pressure 420 MPa

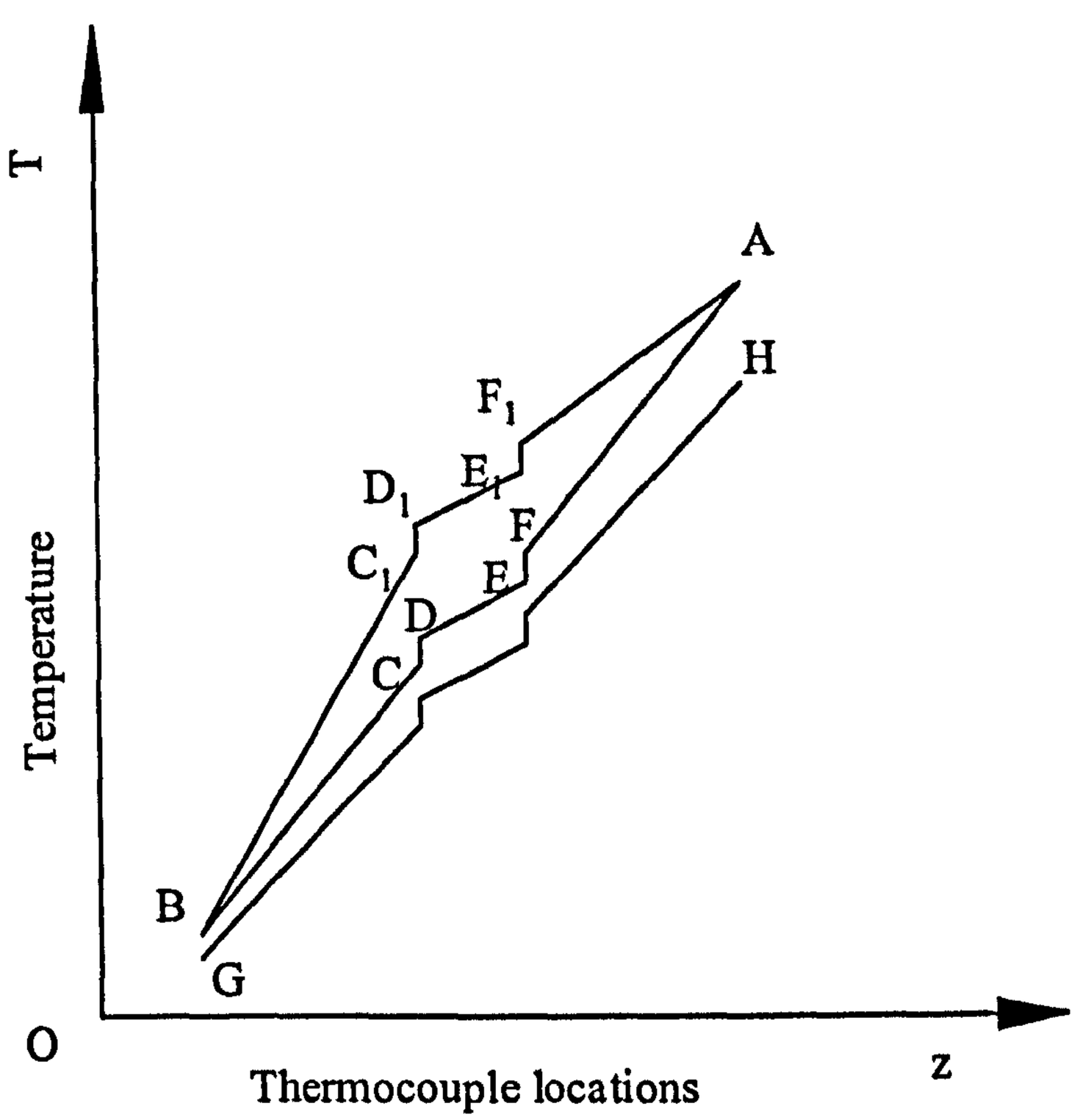

Fig. 3.5.1 Influence of transverse heat flow upon temperature distribution.

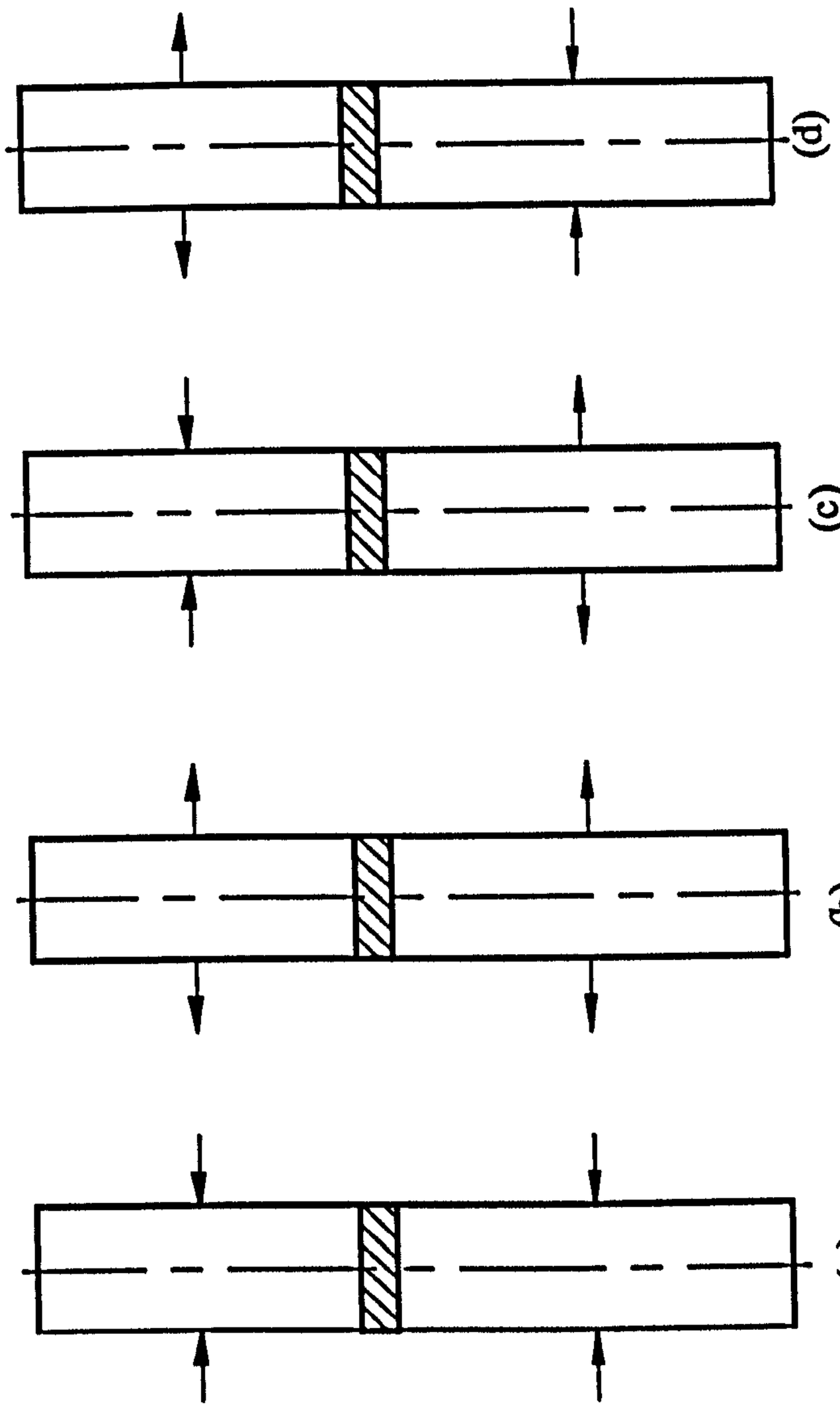

Fig.3.5.2 The possible heat exchange cases

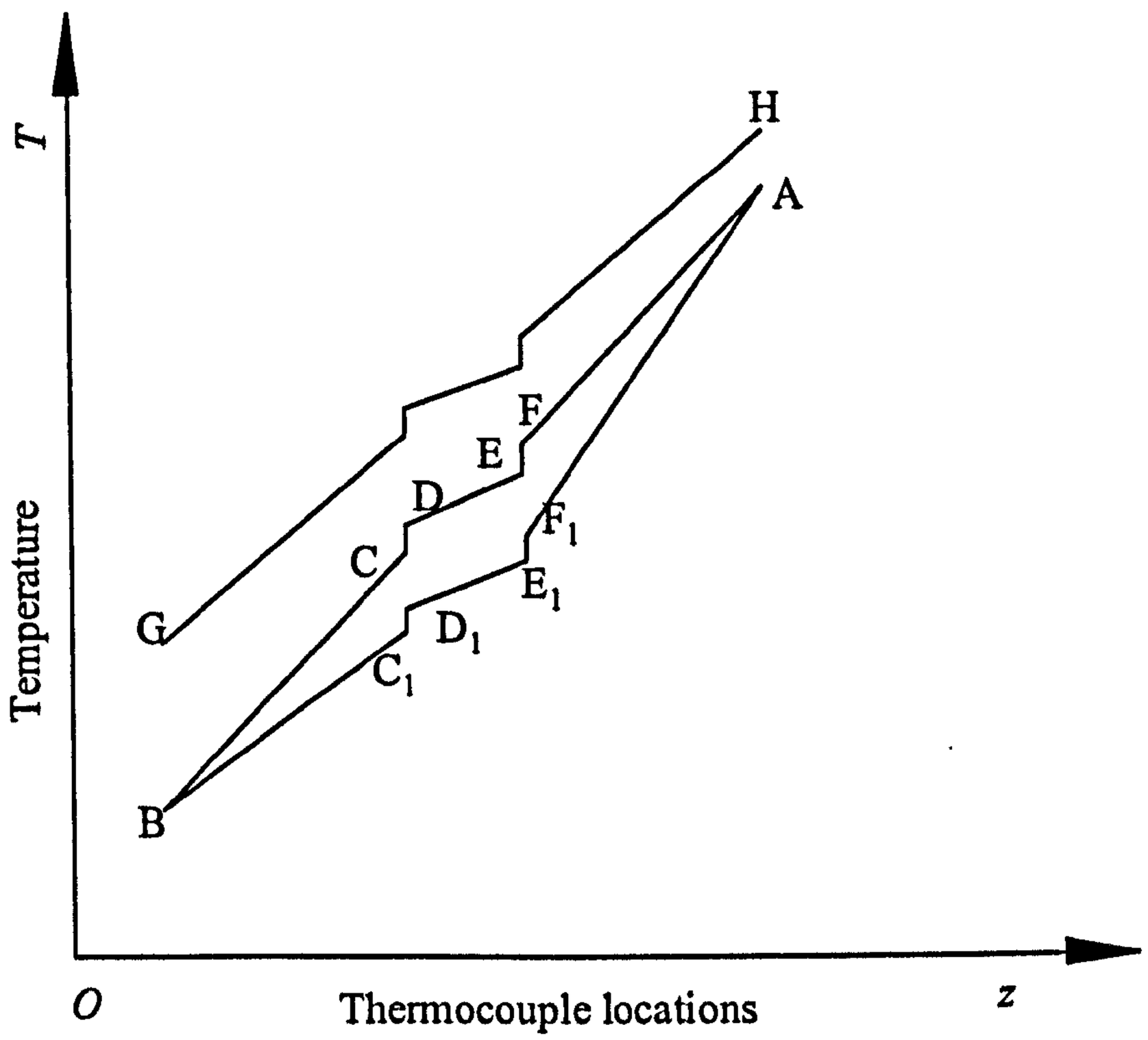

Fig. 3.5.3 Case of $q_{t\Delta} > q_{t\nabla}$

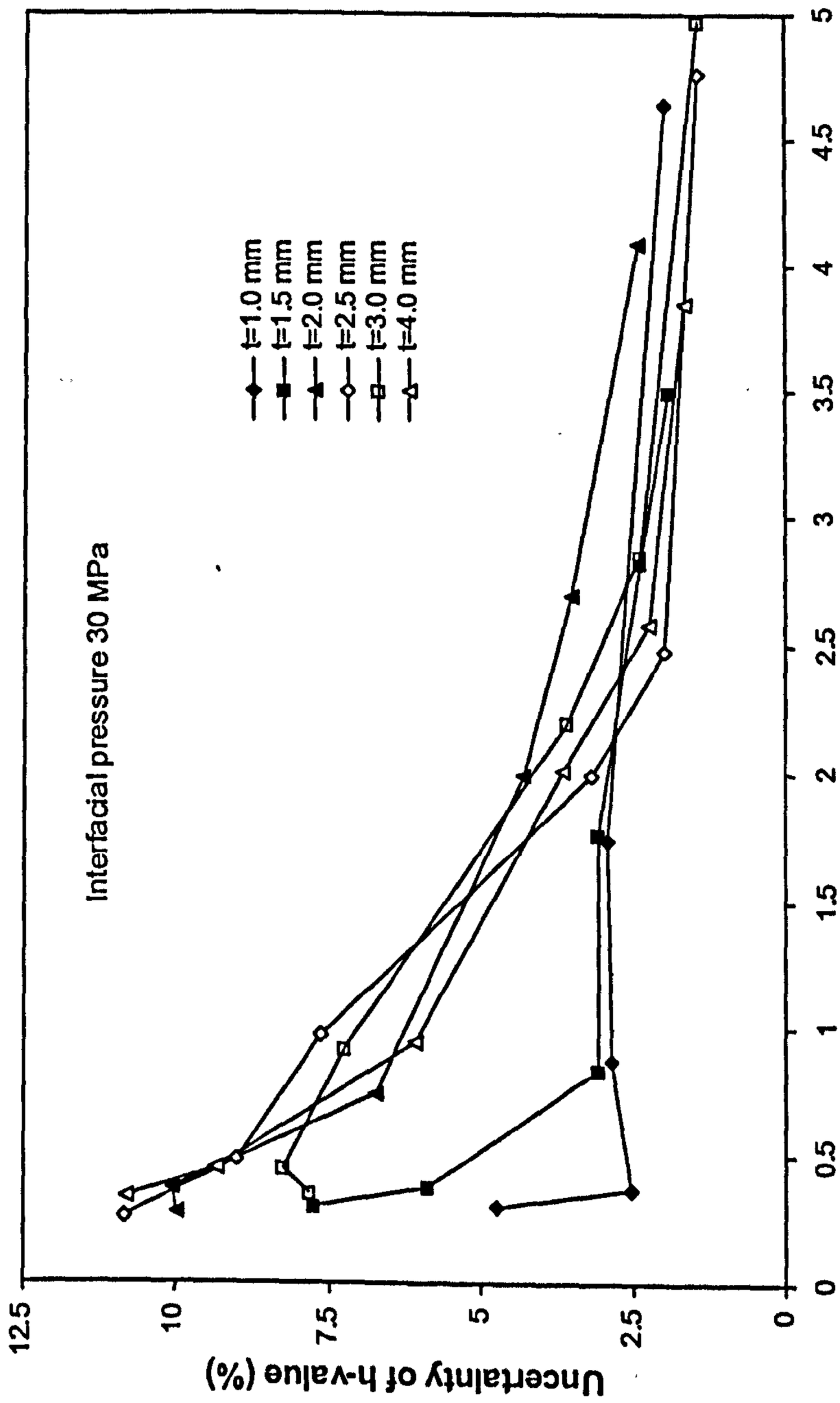

Fig. 3.6.1 Uncertainty of h-value at interfacial pressure 30 MPa

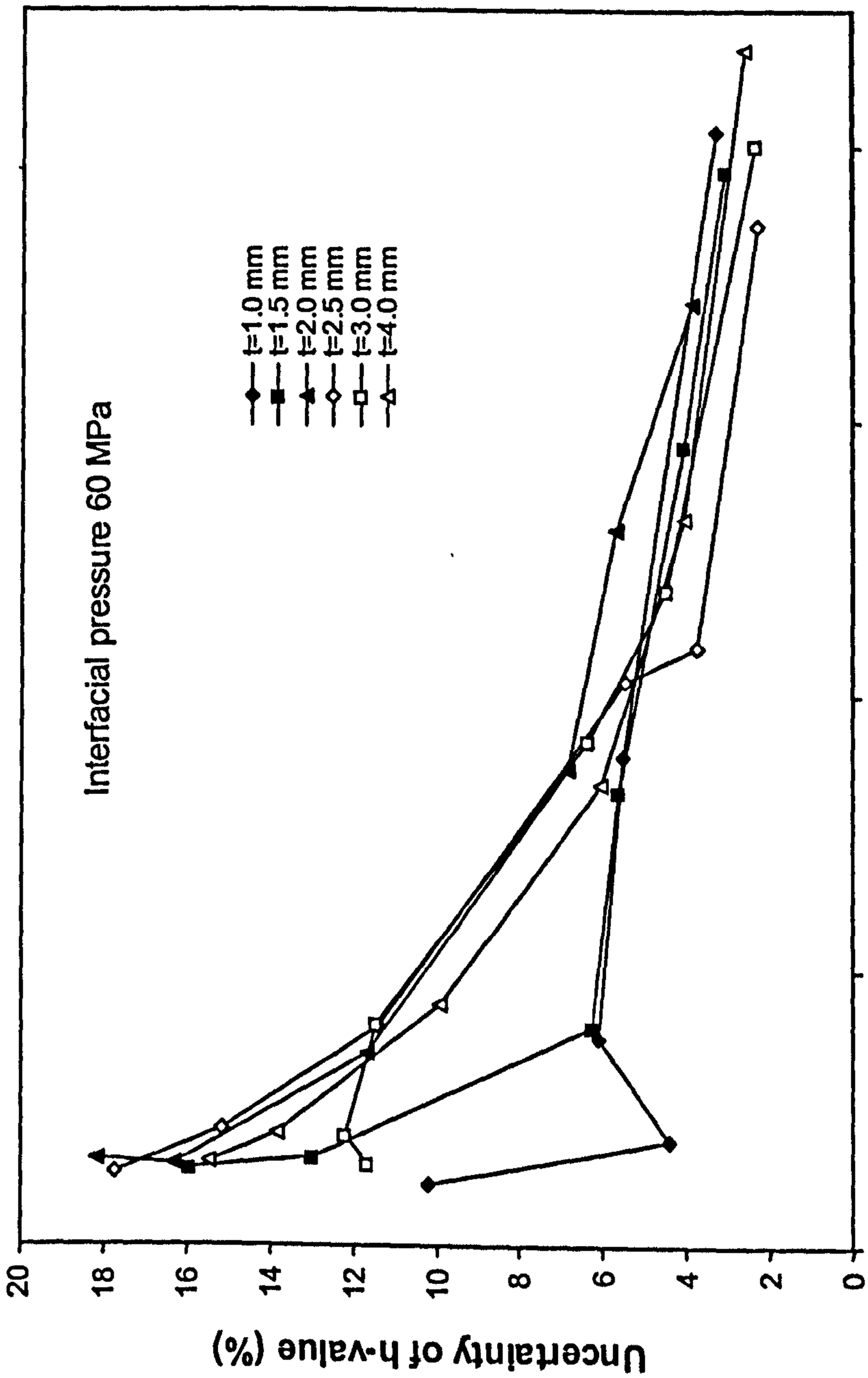

Fig. 3.6.2 Uncertainty of h-value at interfacial pressure 60 MPa

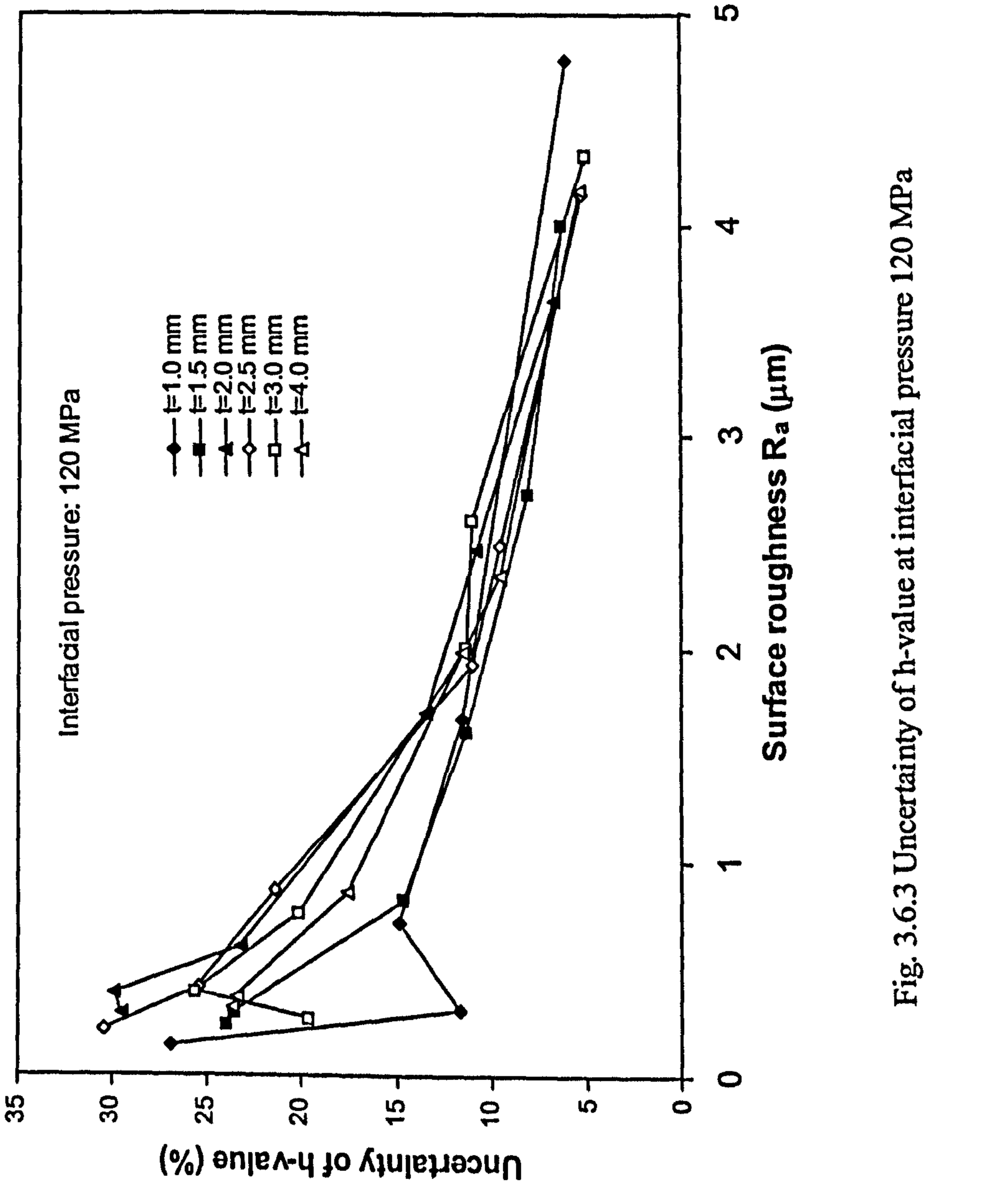

Fig. 3.6.3 Uncertainty of h-value at interfacial pressure 120 MPa

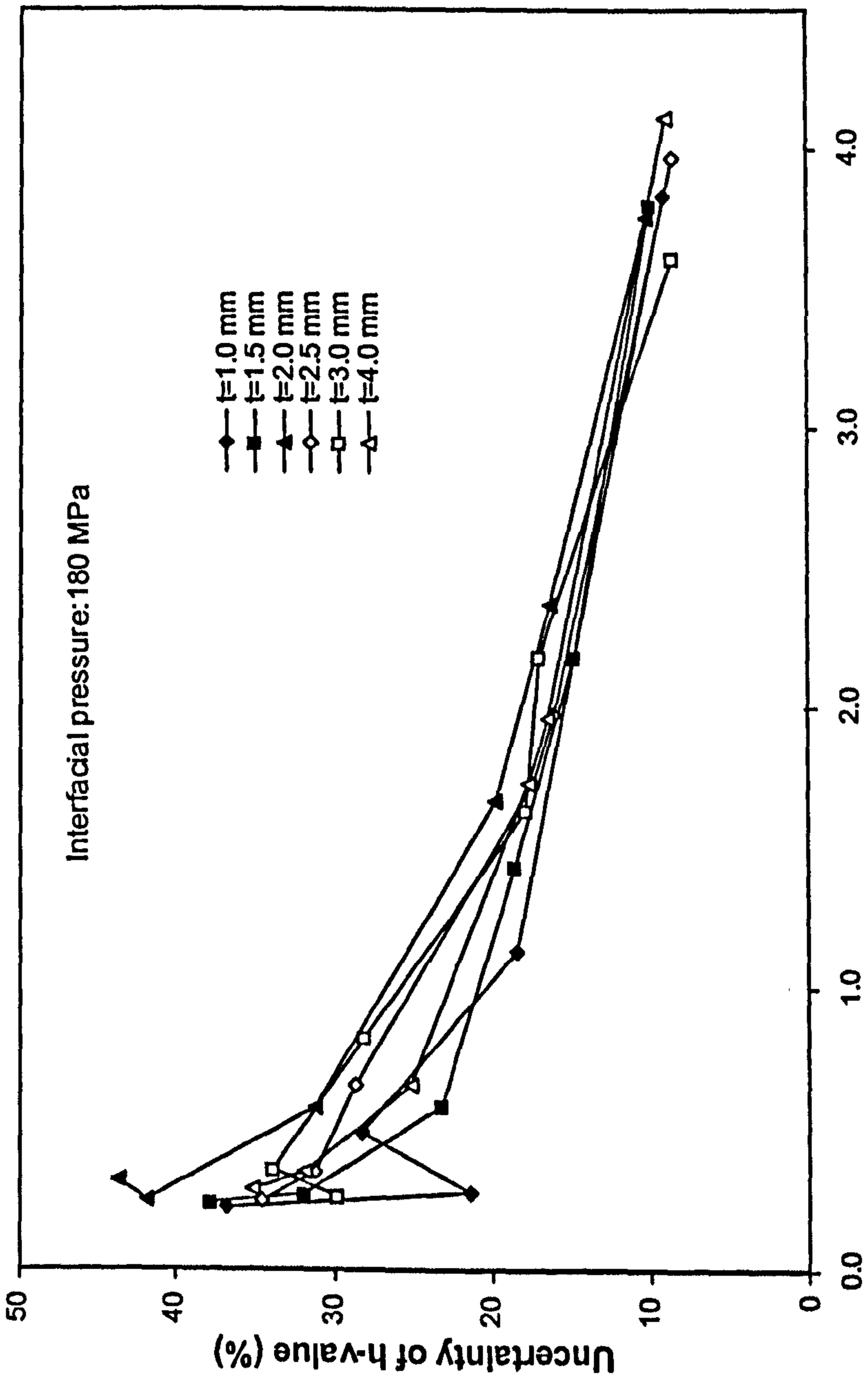

Fig. 3.6.4 Uncertainty of h-value at interfacial pressure 180 MPa

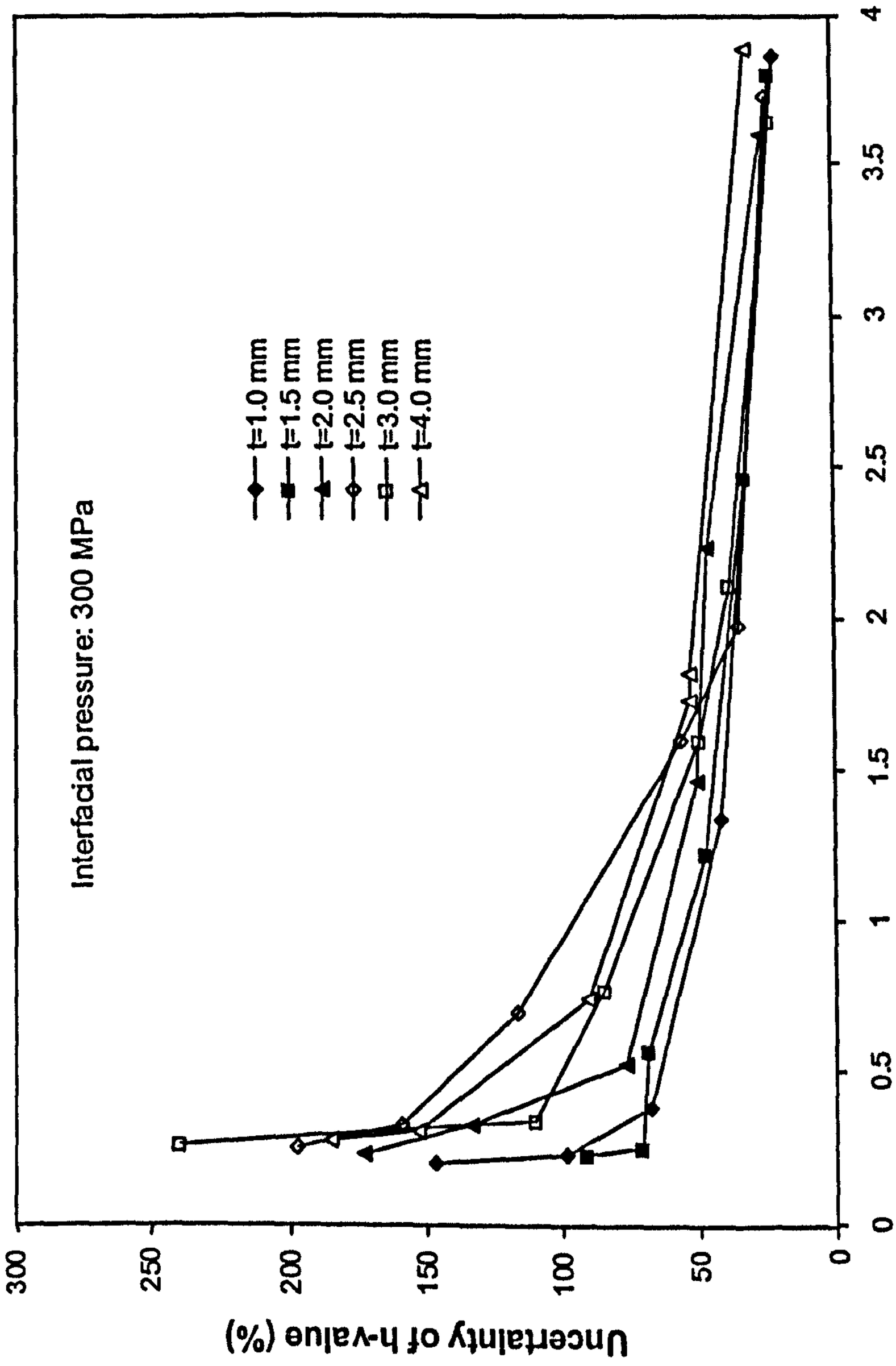

Fig. 3.6.5 Uncertainty of h-value at interfacial pressure 300 MPa

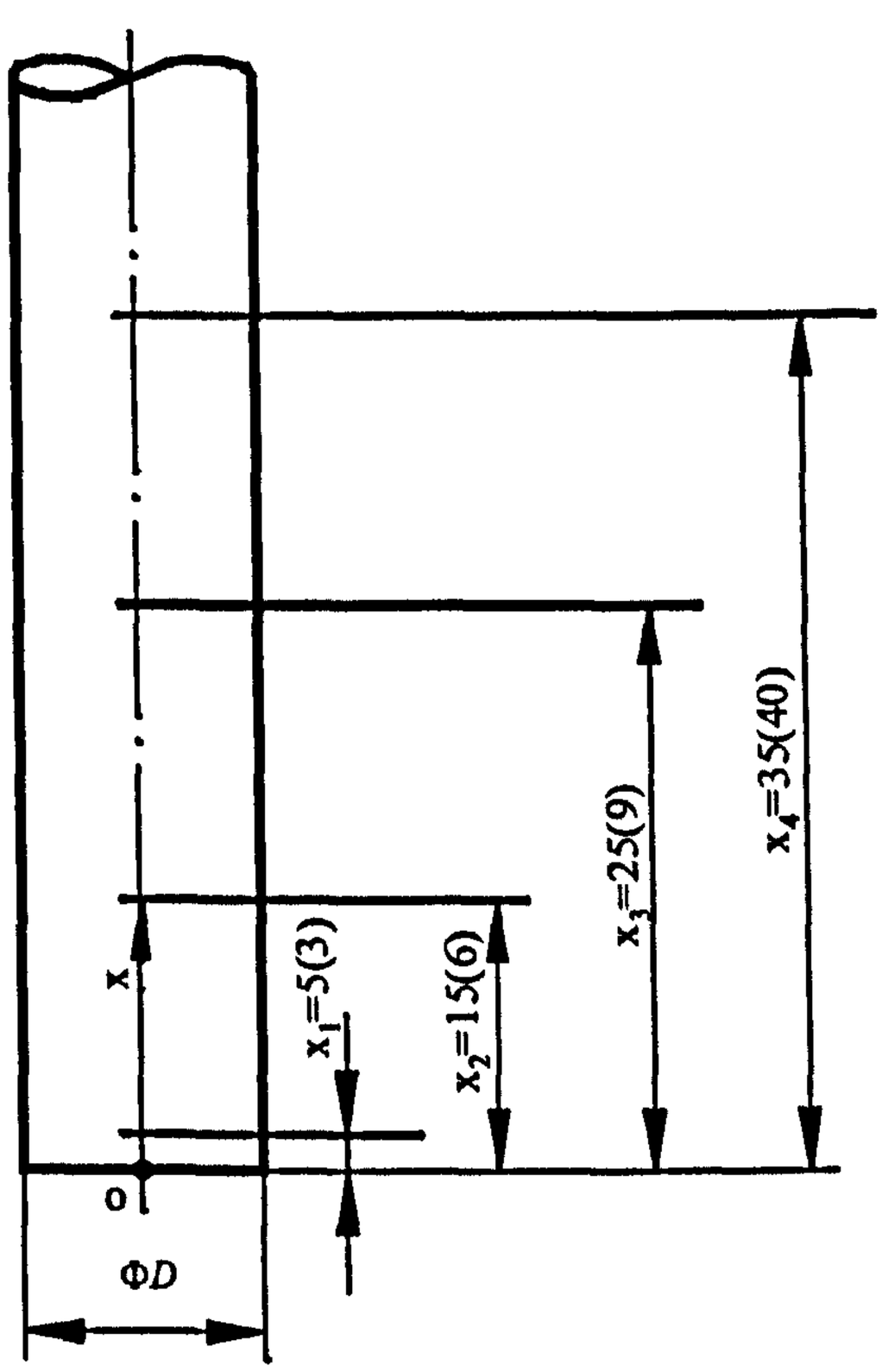

In brackets are the possible optimal dimensional values

Fig. 3.6.2.1 Positioning thermocouples

Diagrams for Chapter Four

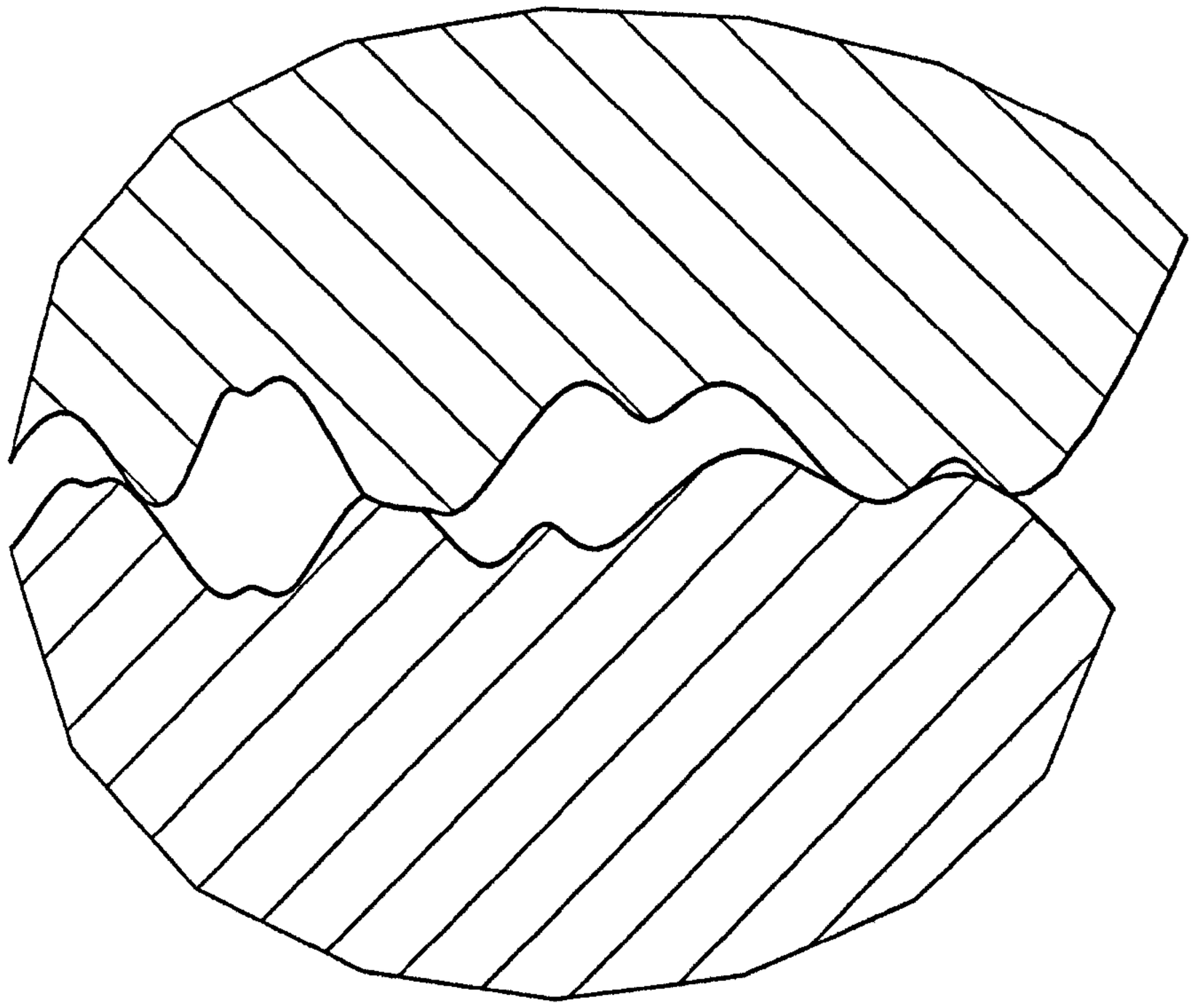

Fig.4.1 Mechanical contact between rough surfaces

Fig.4.2 GW surface contact model

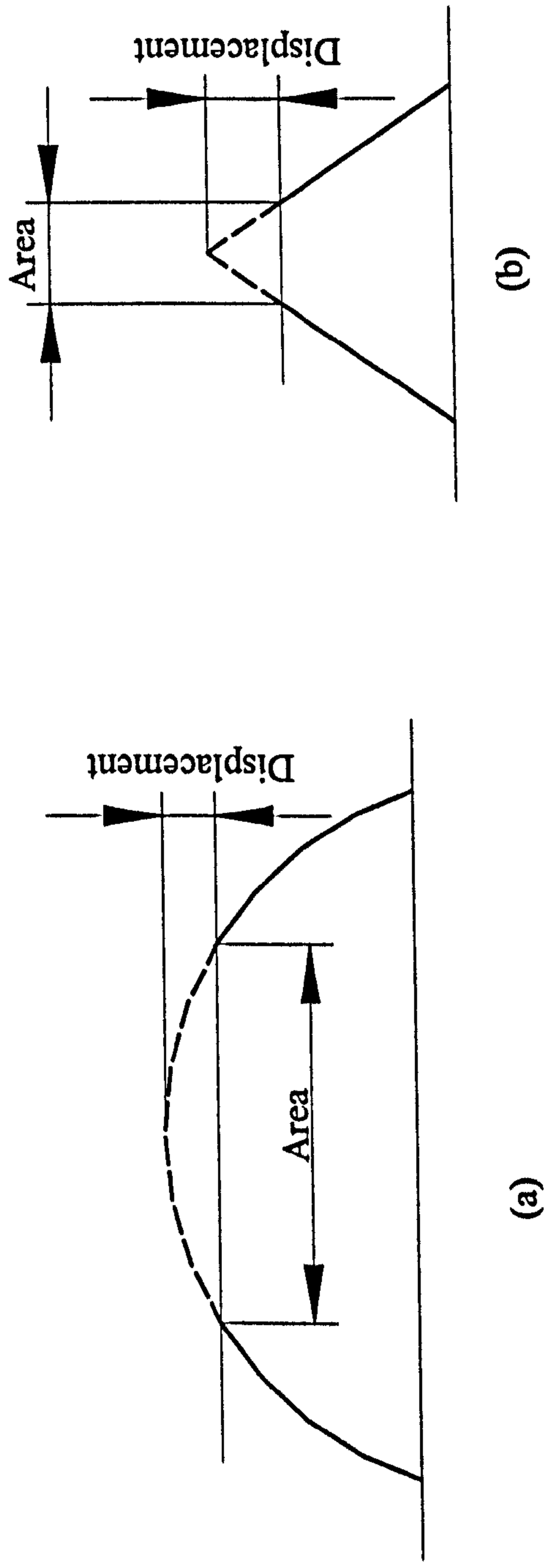

Fig.4.3 Classic plastic deformation models

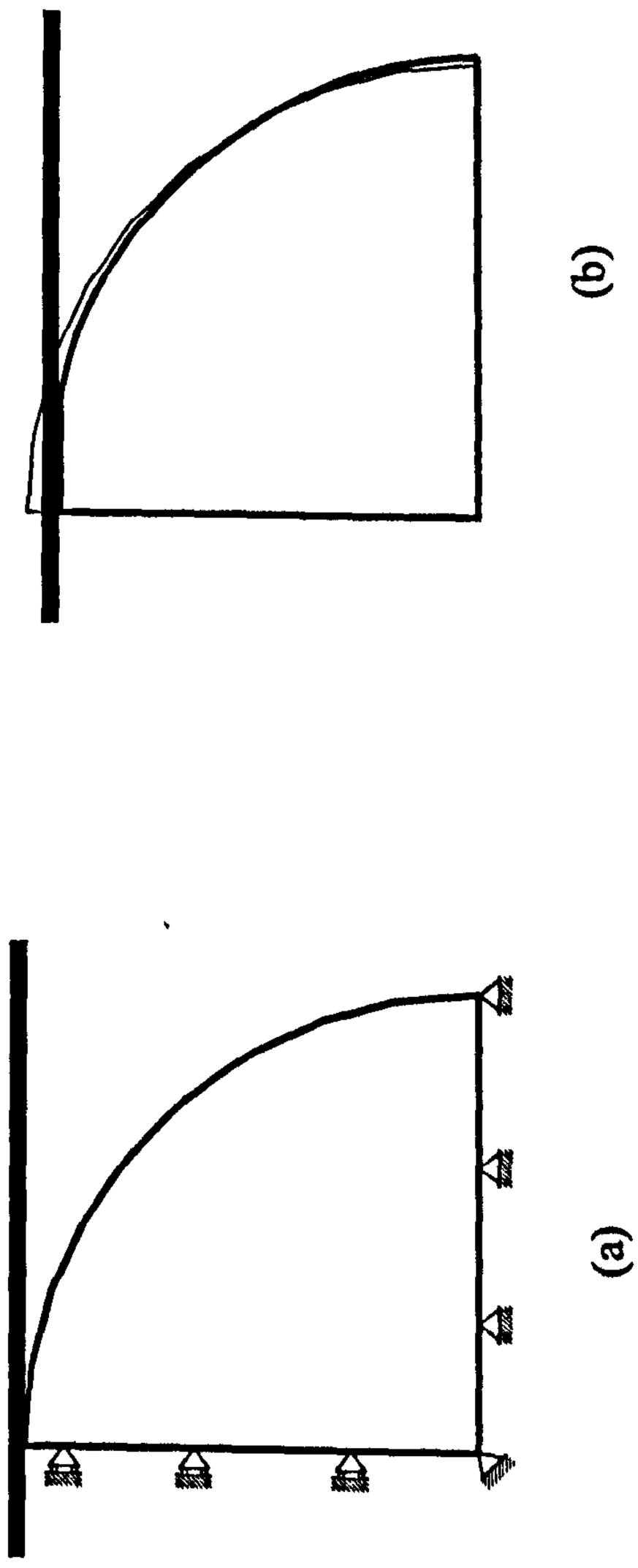

(b)

(a)

Fig.4.4 Finite element model of surface deformation

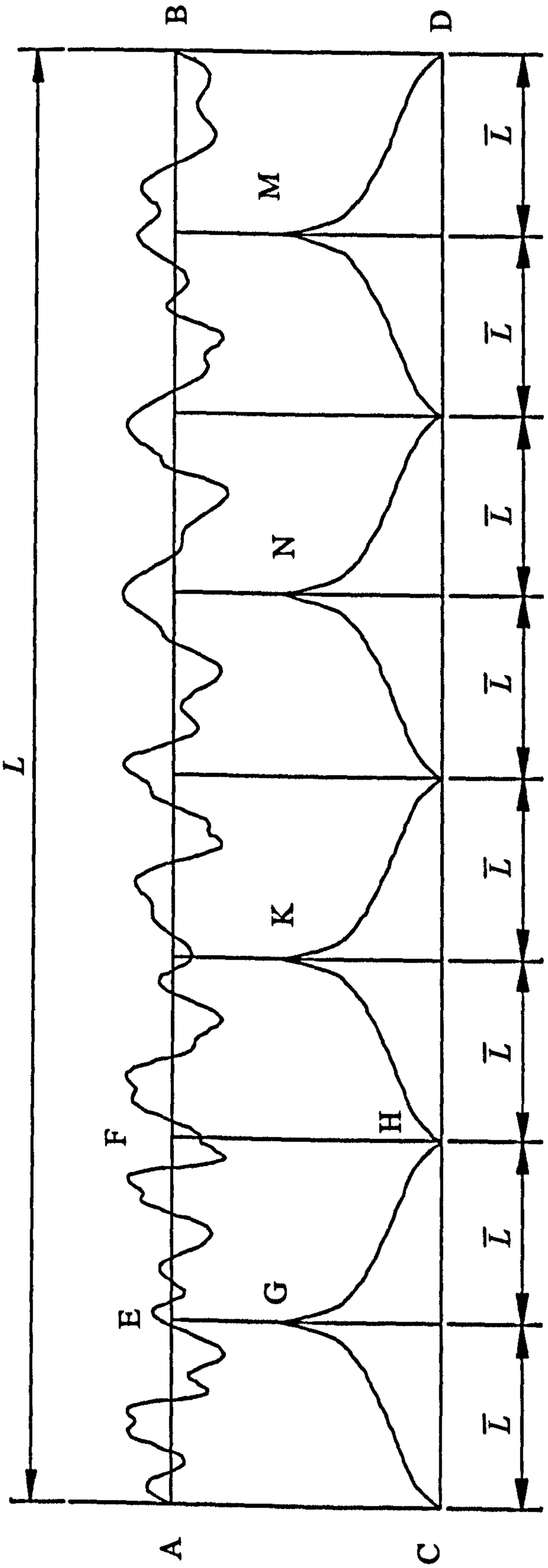

Fig. 4.5 Surface profile, expanded bearing ratio curves and equivalent asperity

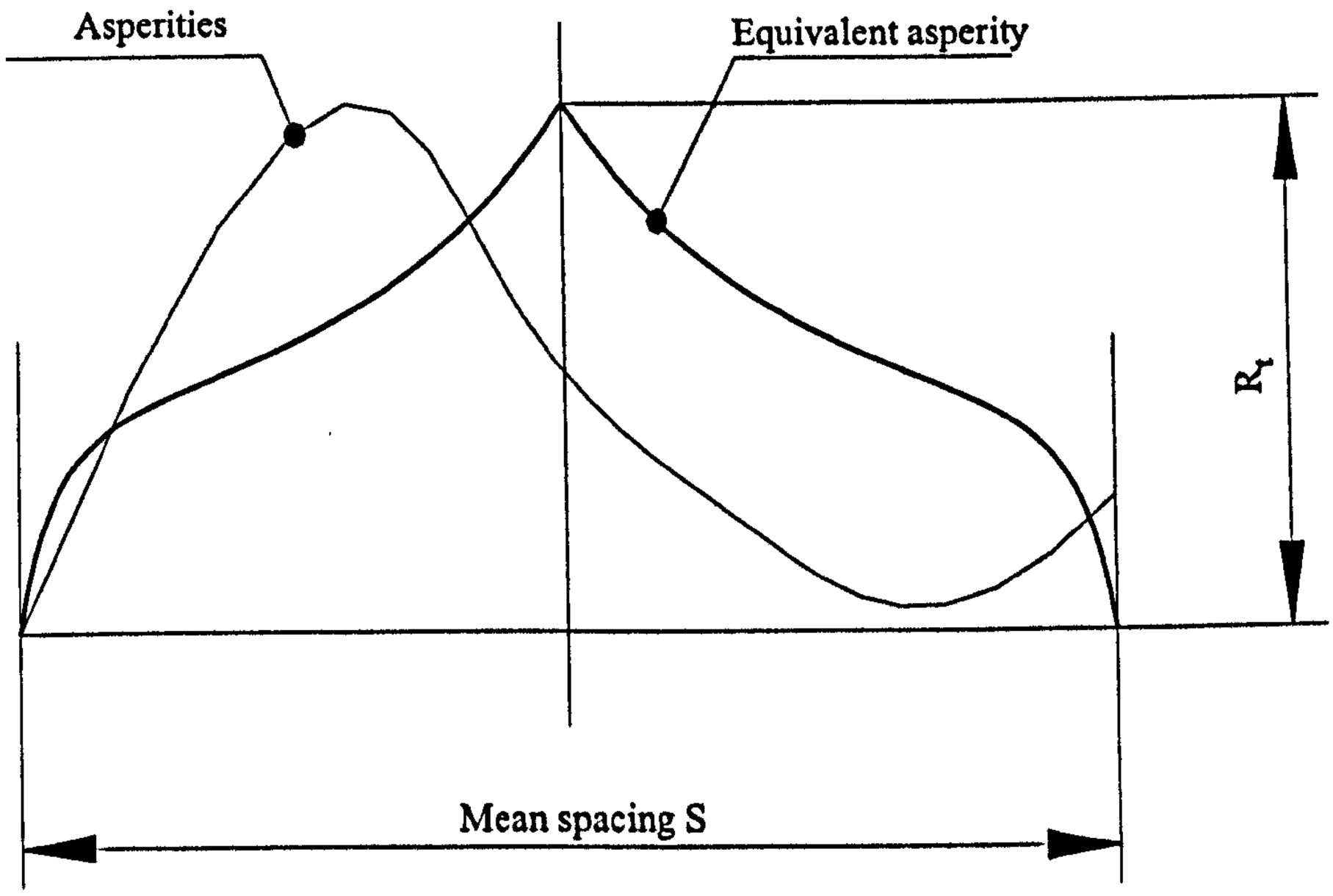

Fig.4.6 Equivalent asperity

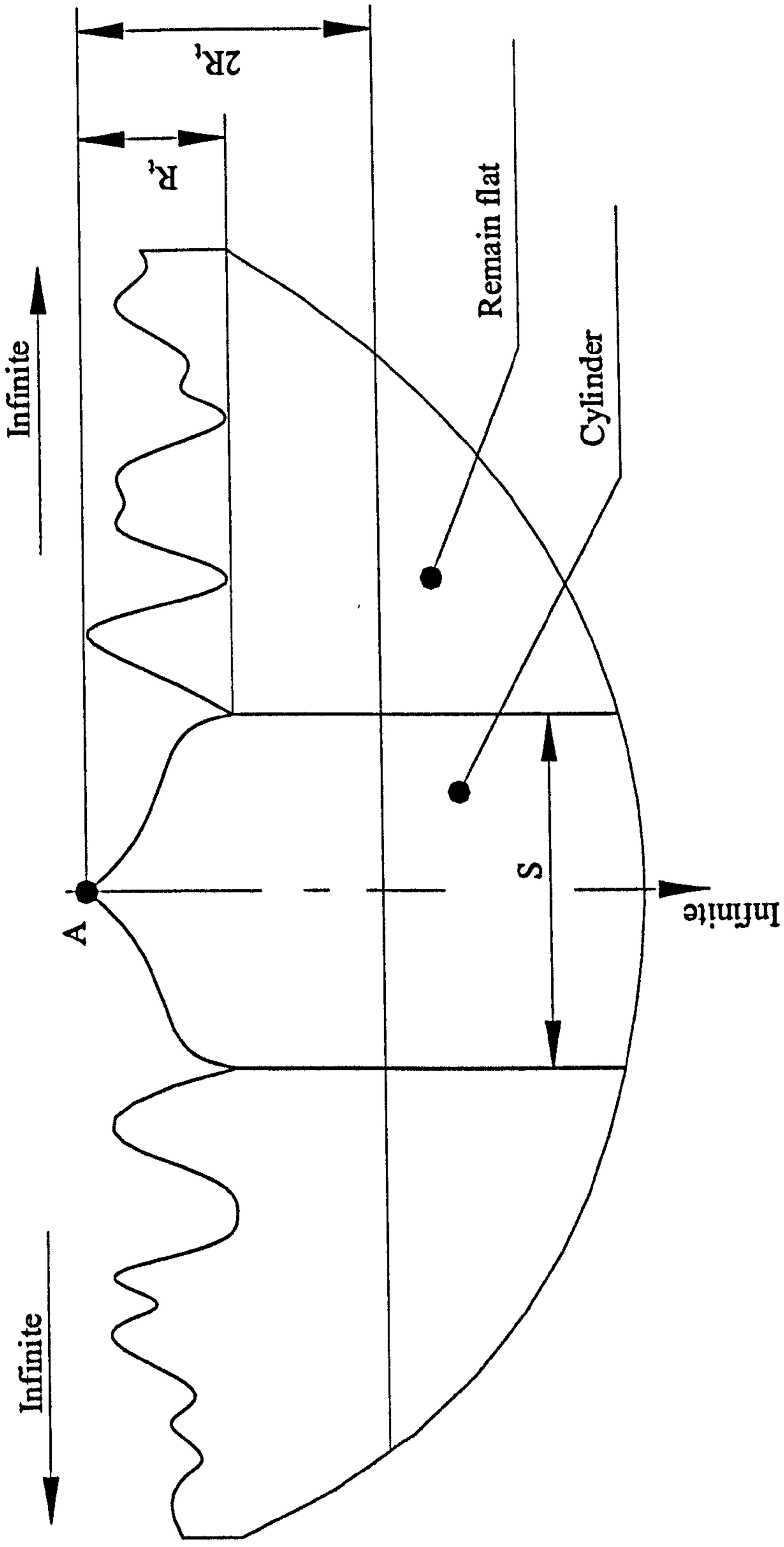

Fig.4.7 Basis of FE simulation model

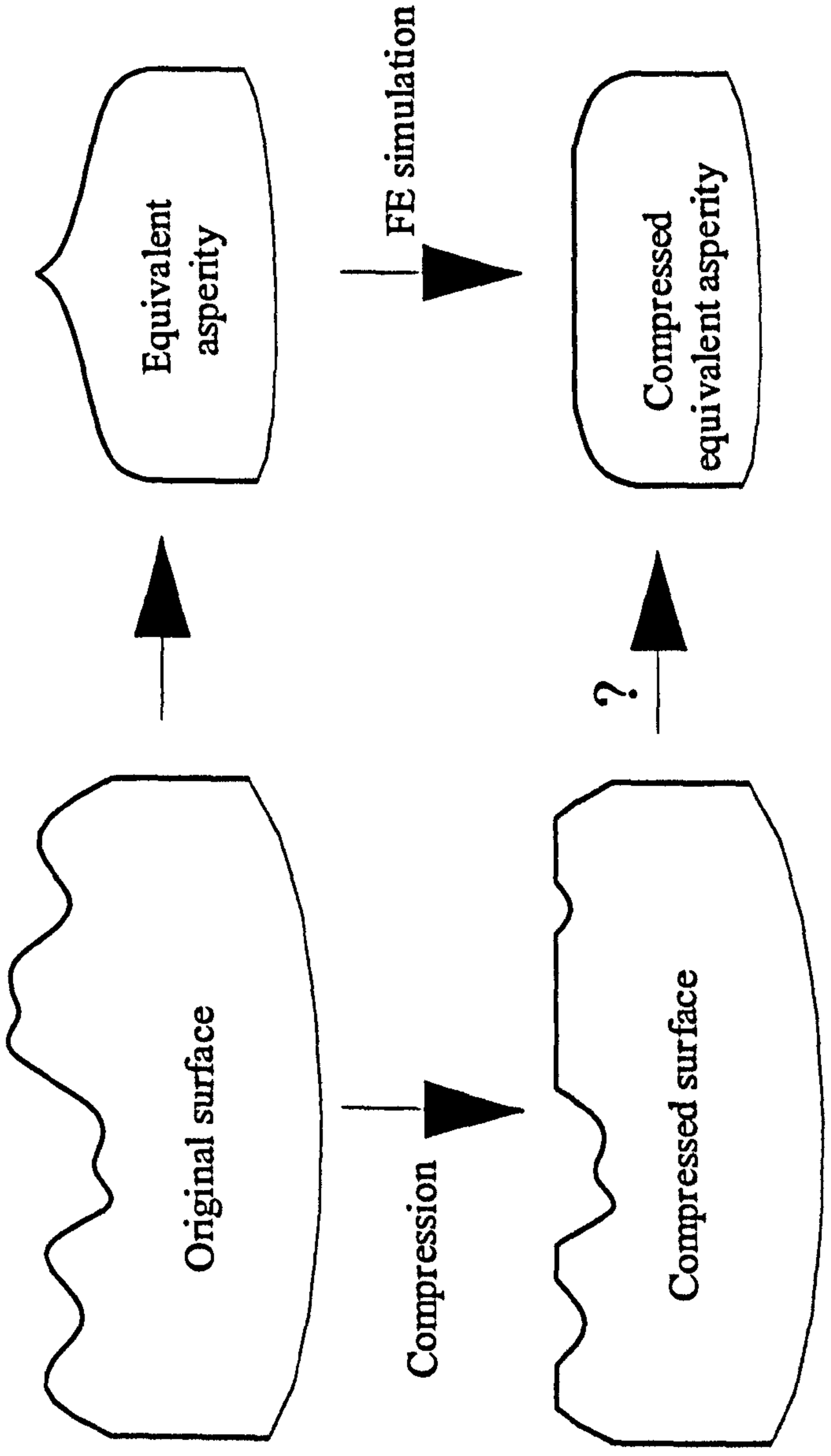

Fig. 4.8 Assumption on equi

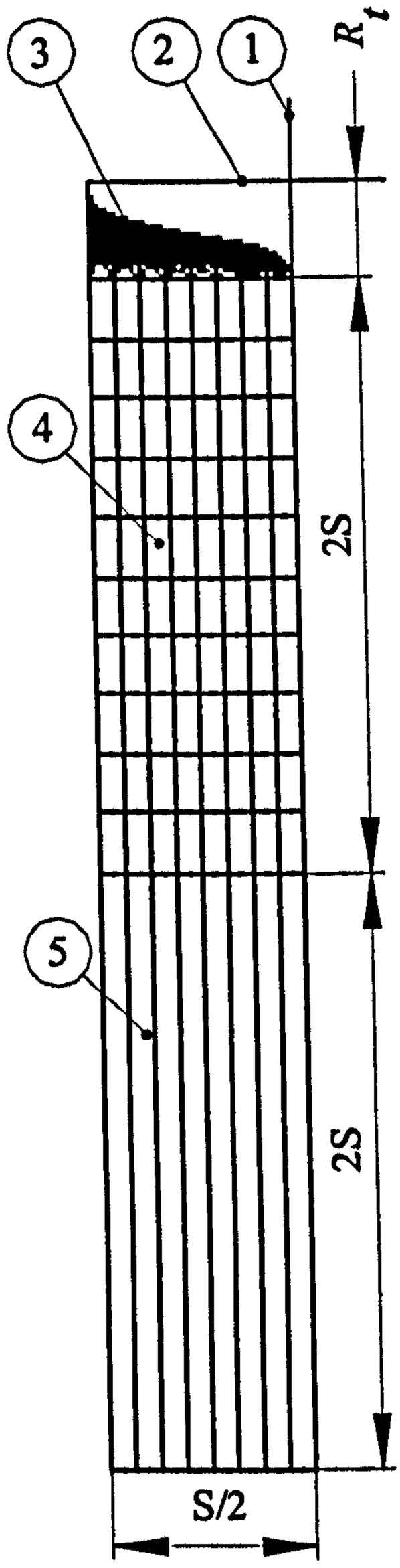

1. Virtual rigid cylinder
2. Rigid tool
3. Equivalent asperity mesh with element CAX4
4. Substrate mesh with CAX4
5. Mesh with infinite element CINAX4

Fig. 4.9 Geometric mesh model for surface deformation simulation

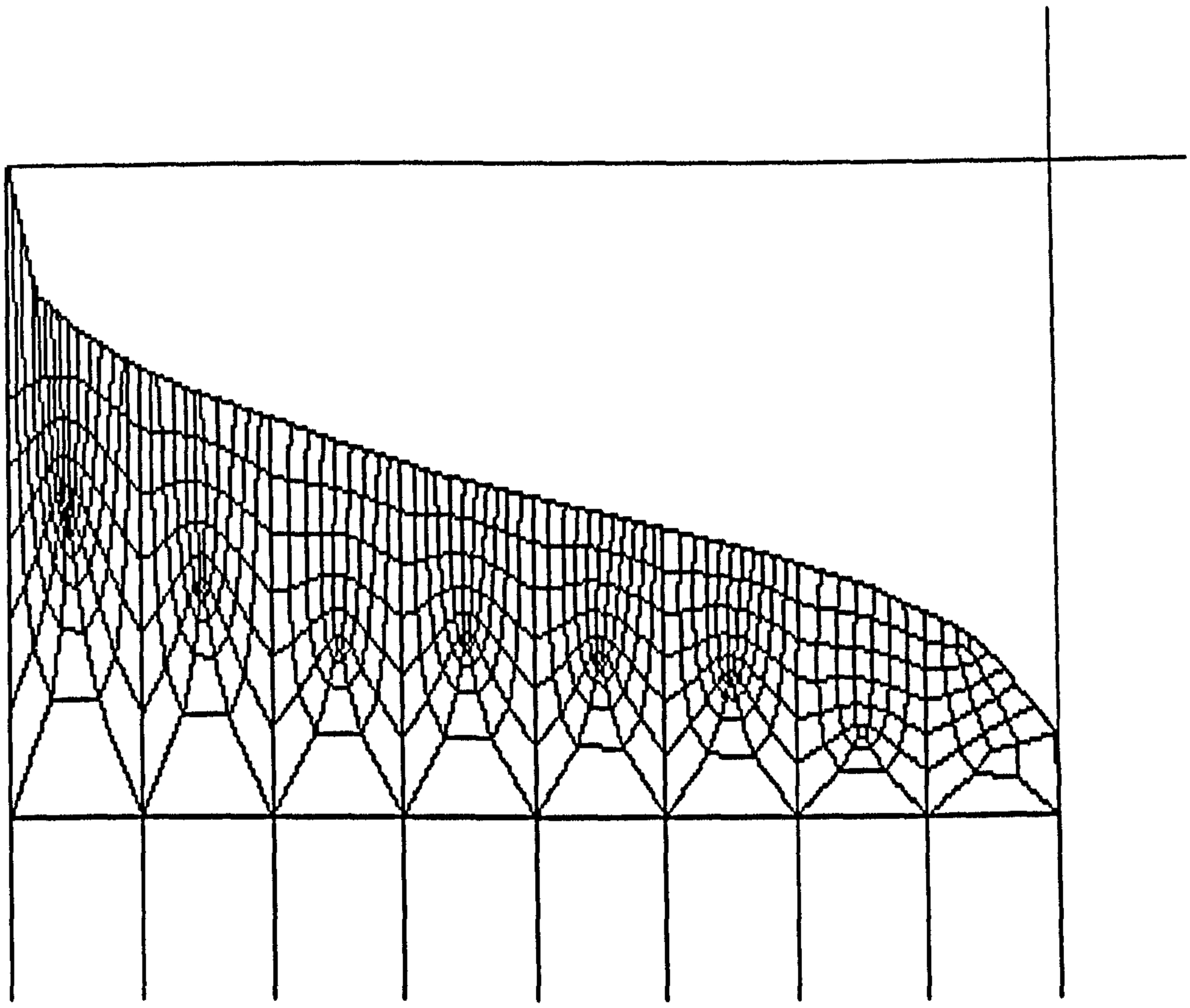

Fig.4.10 Mesh of equivalent asperity for specimen 3.0-D-000

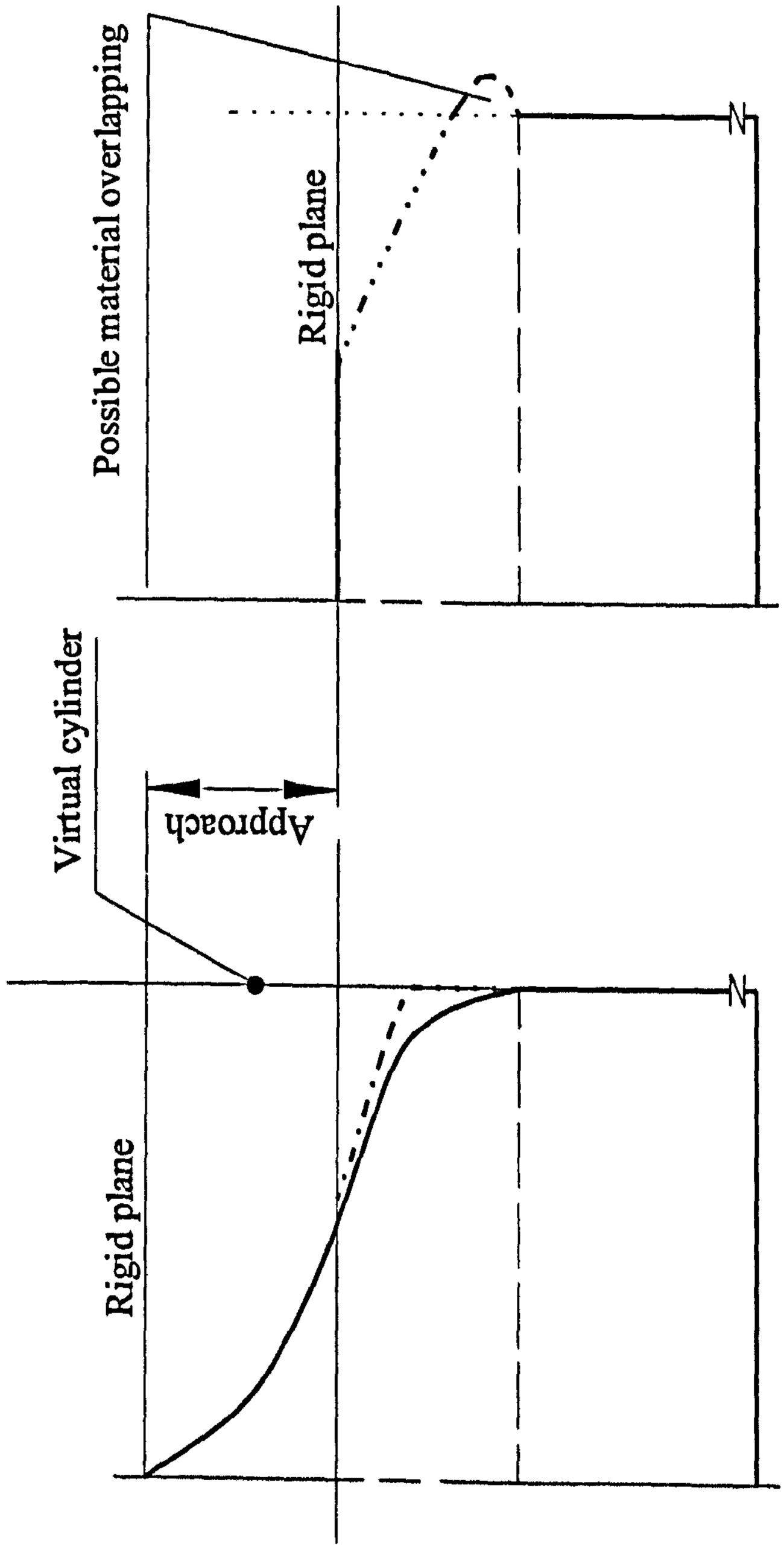

Fig. 4.11 Interaction between asperities and virtual rigid cylinder

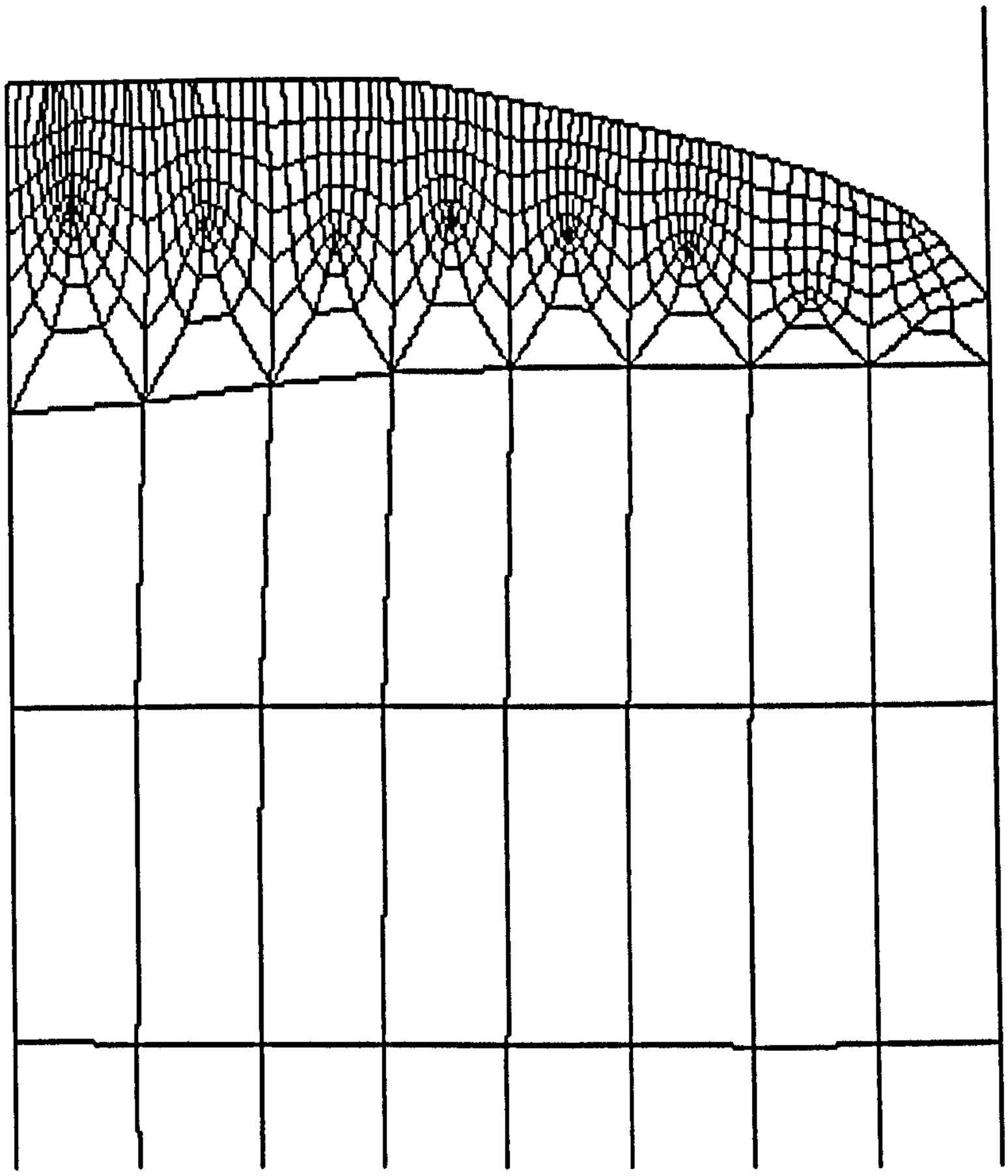

Fig. 4.12 Deformed mesh of specimen 3.0-D-420

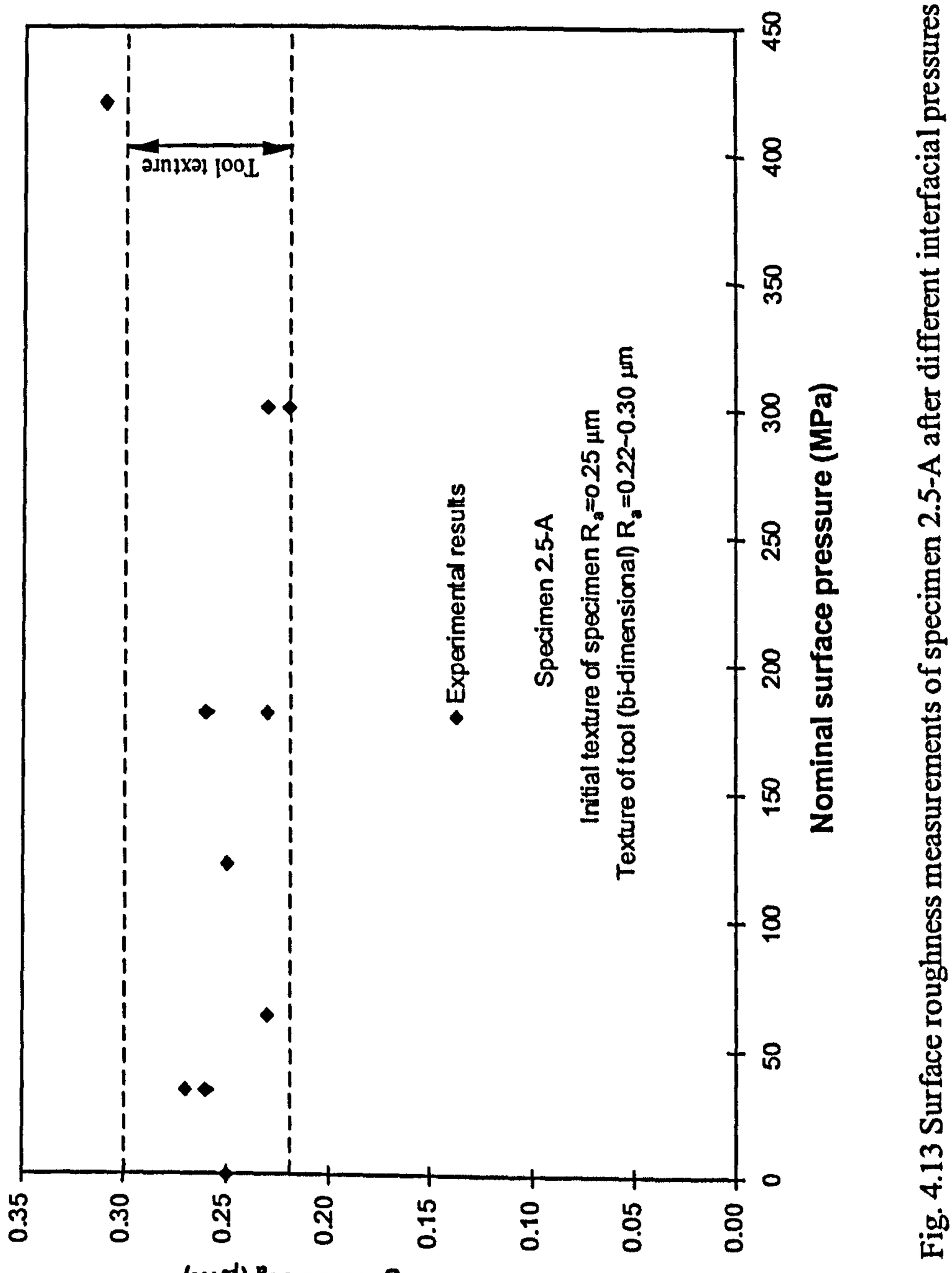

Fig. 4.13 Surface roughness measurements of specimen 2.5-A after different interfacial pressures

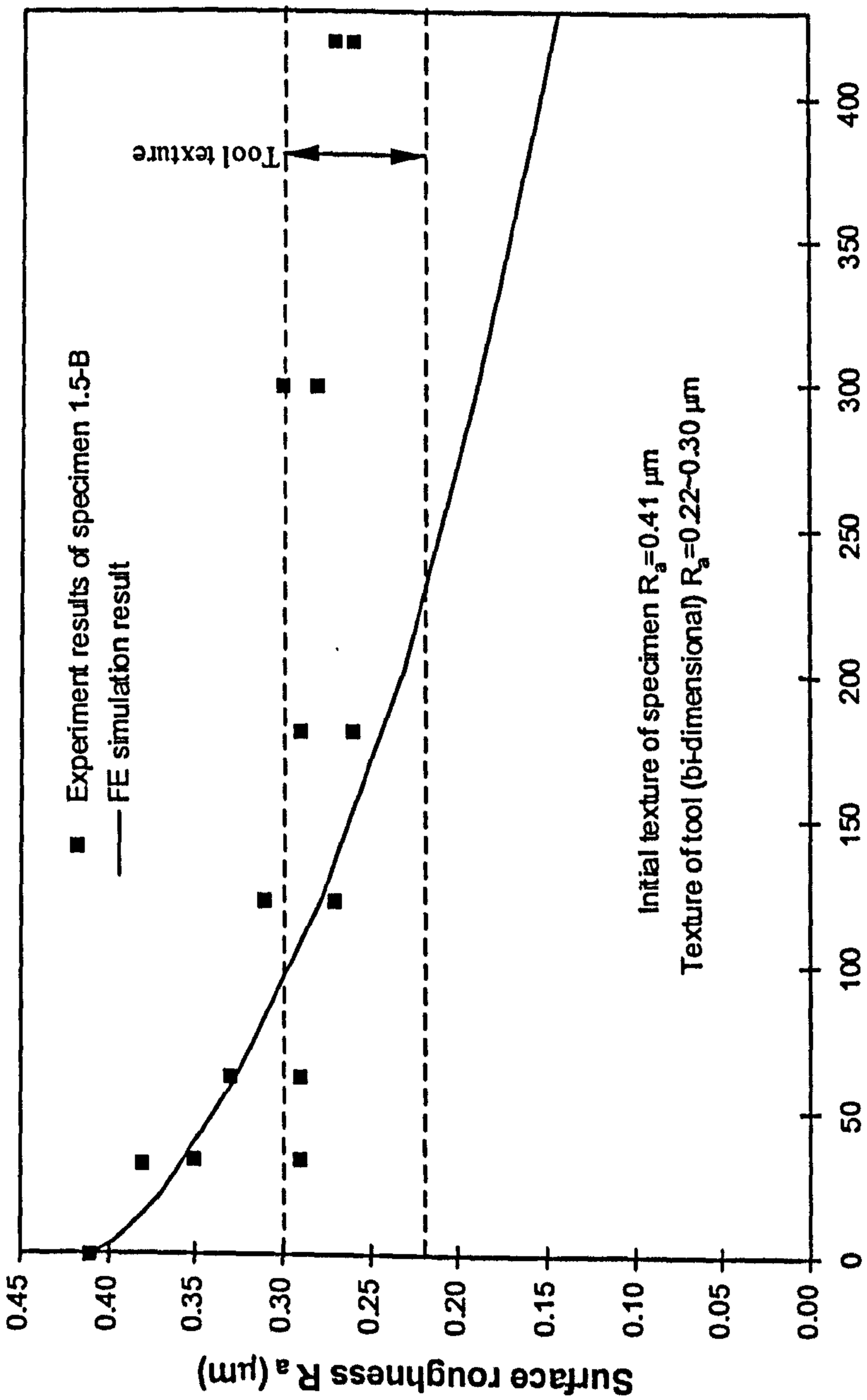

Fig. 4.14 Surface roughness measurements and FE simulation result of specimen 1.5-B after deformation under different interfacial pressures

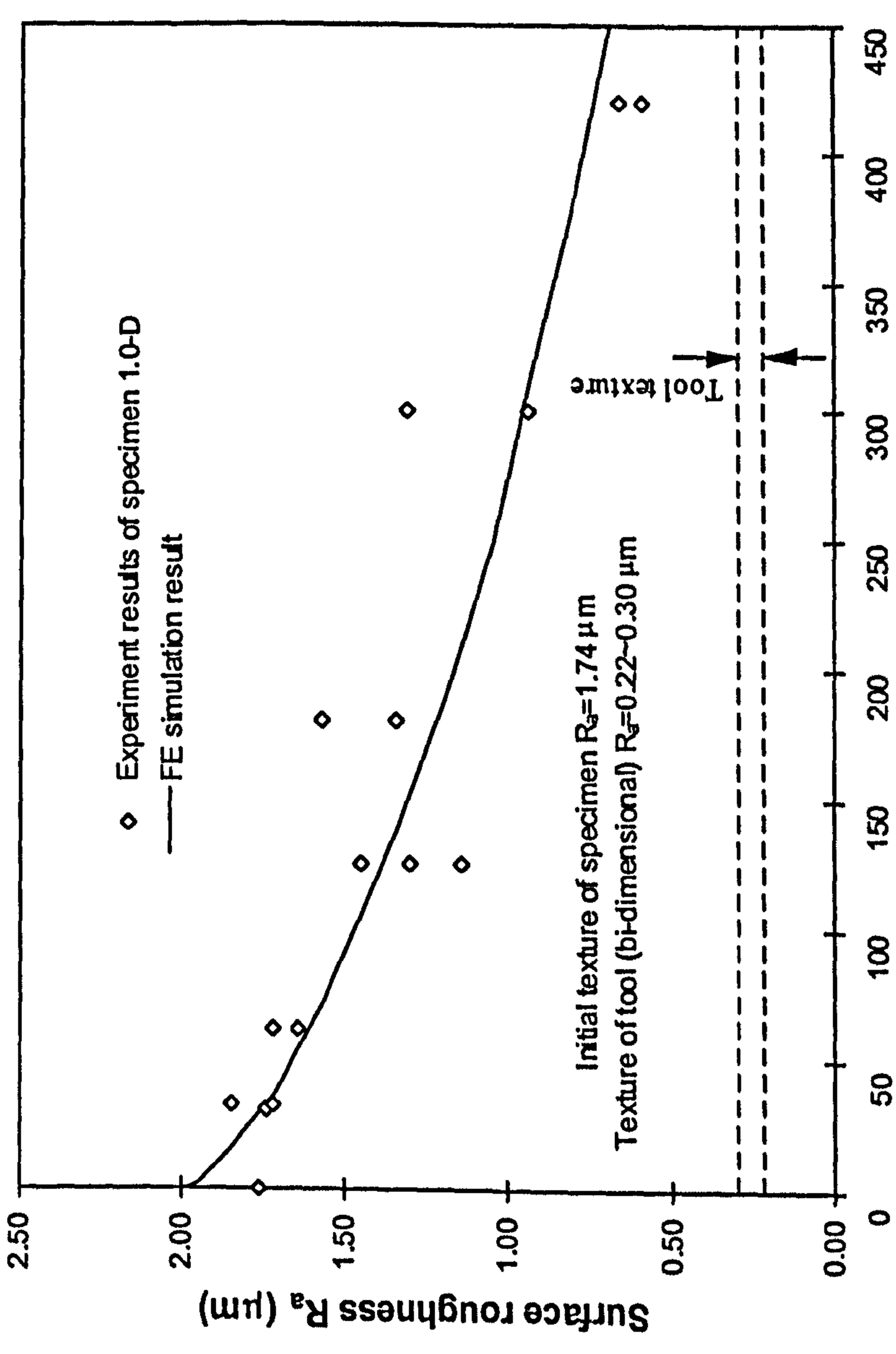

Fig. 4.15 Surface roughness measurements and FE simulation result of specimen 1.0-D after different interfacial pressures

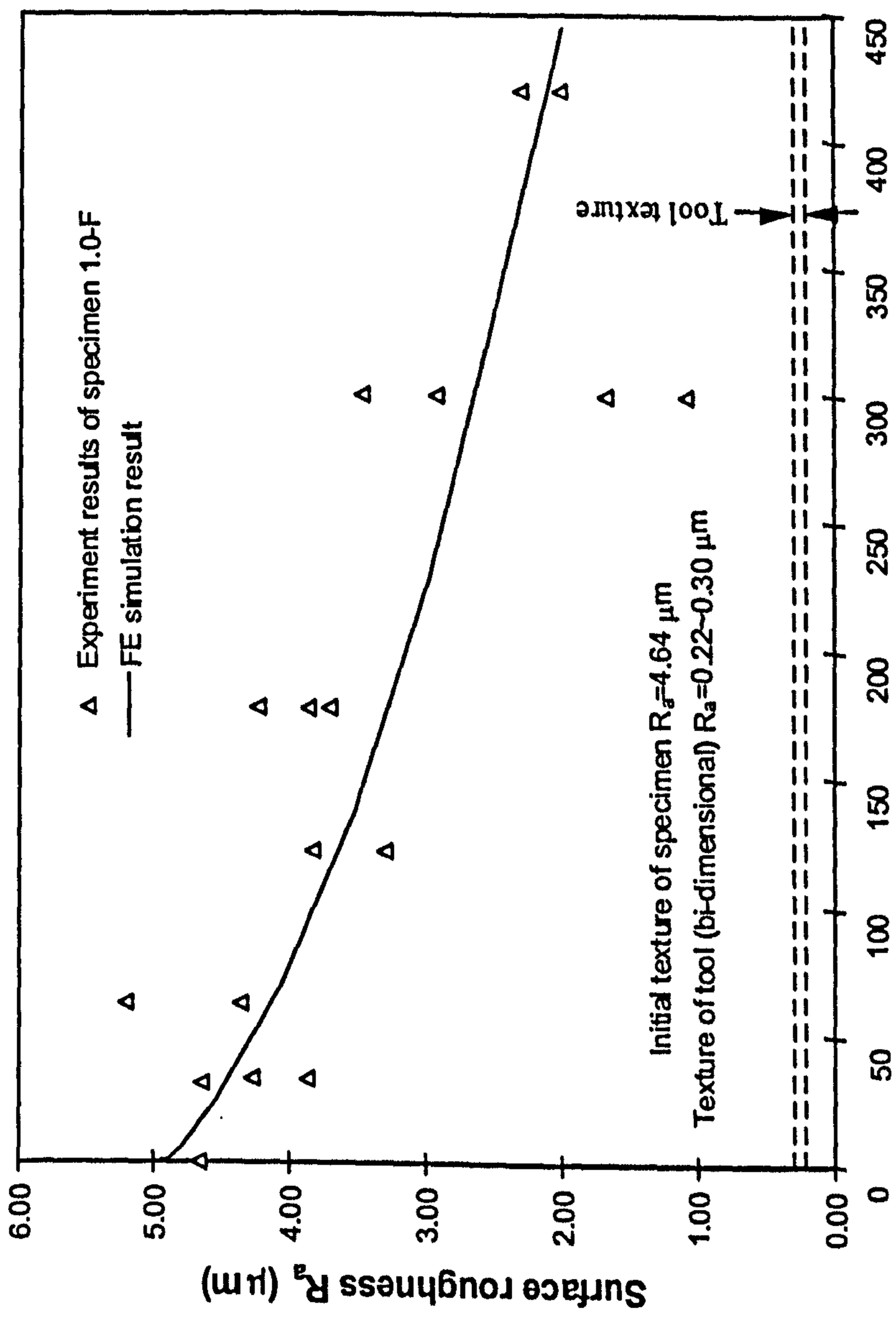

Fig. 4.16 Surface roughness measurements and FE simulation result of specimen 1.0-F after different interfacial pressures

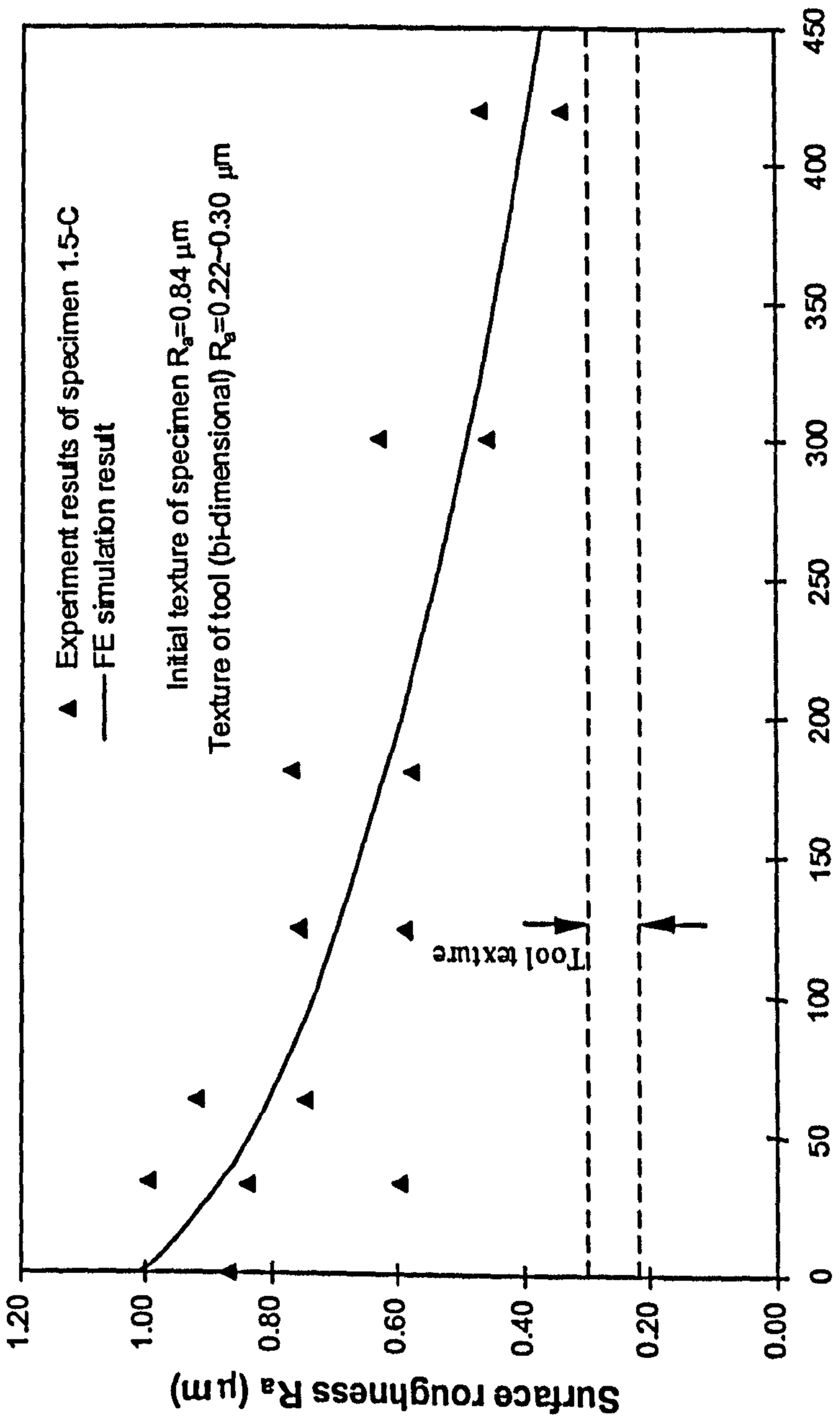

Fig. 4.17 Surface roughness measurements and FE simulation result of specimen 1.5-C after different interfacial pressures

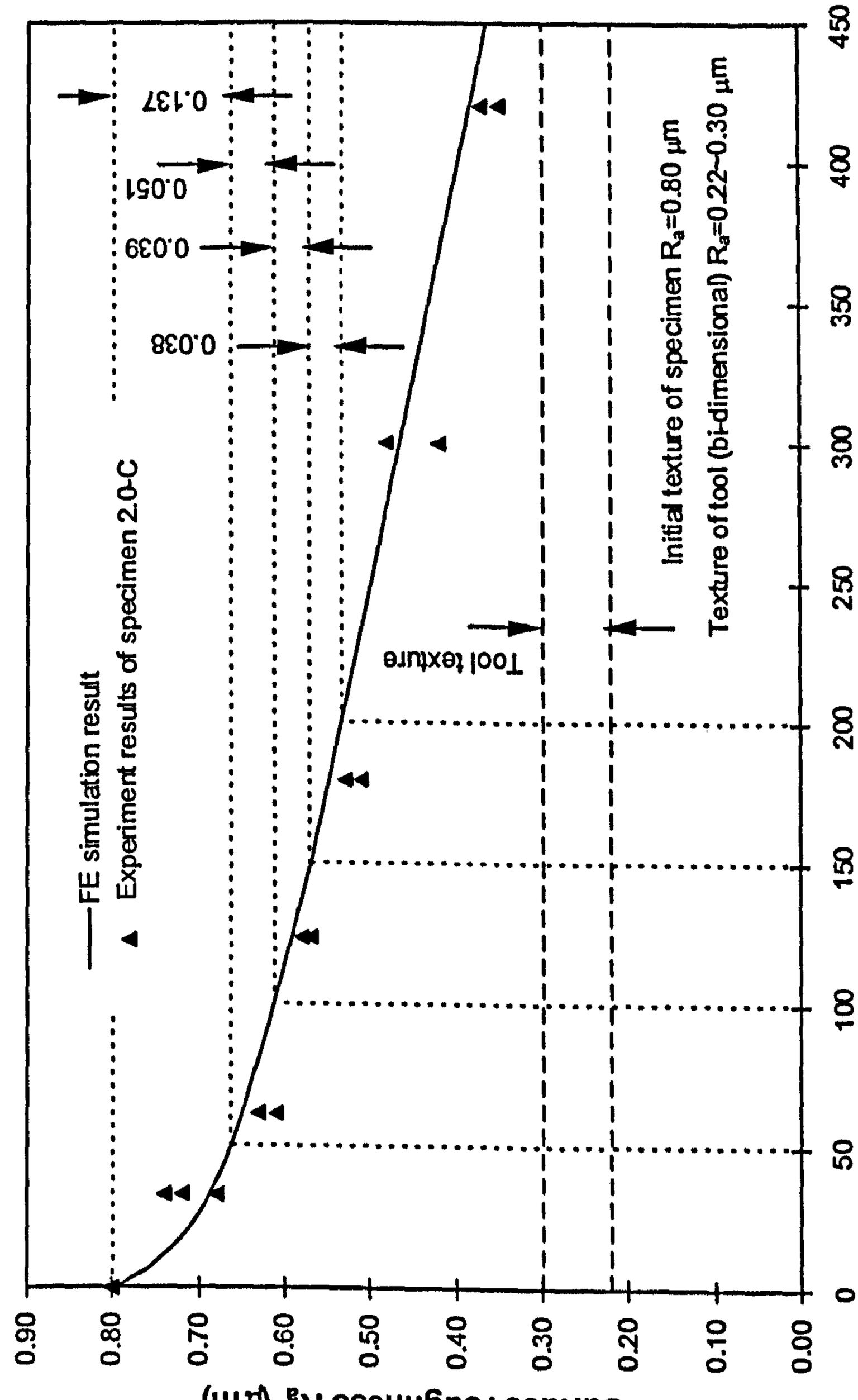

Fig. 4.18 Surface roughness measurements and FE simulation result of specimen 2.0-C after different interfacial pressures

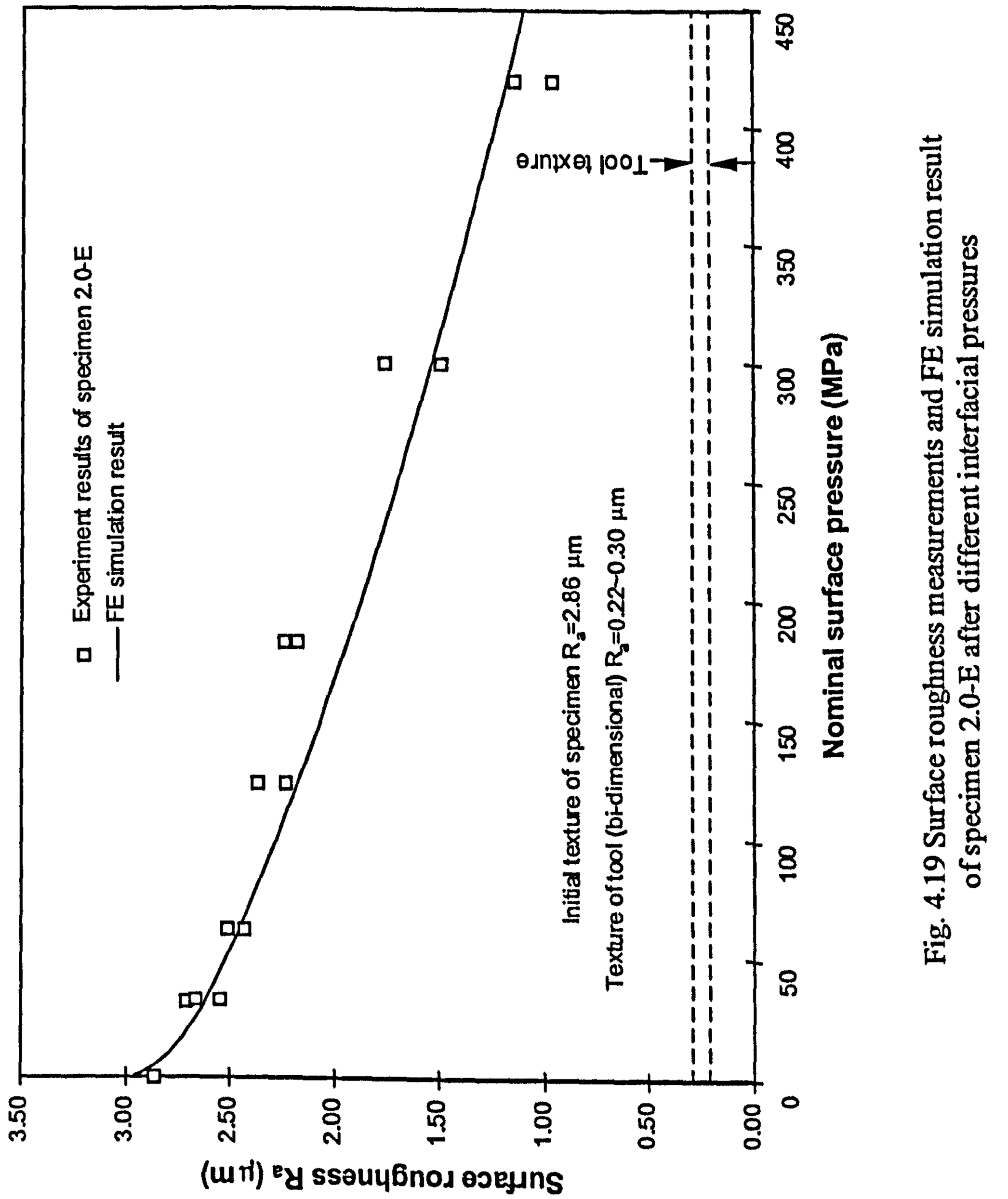

Fig. 4.19 Surface roughness measurements and FE simulation result of specimen 2.0-E after different interfacial pressures

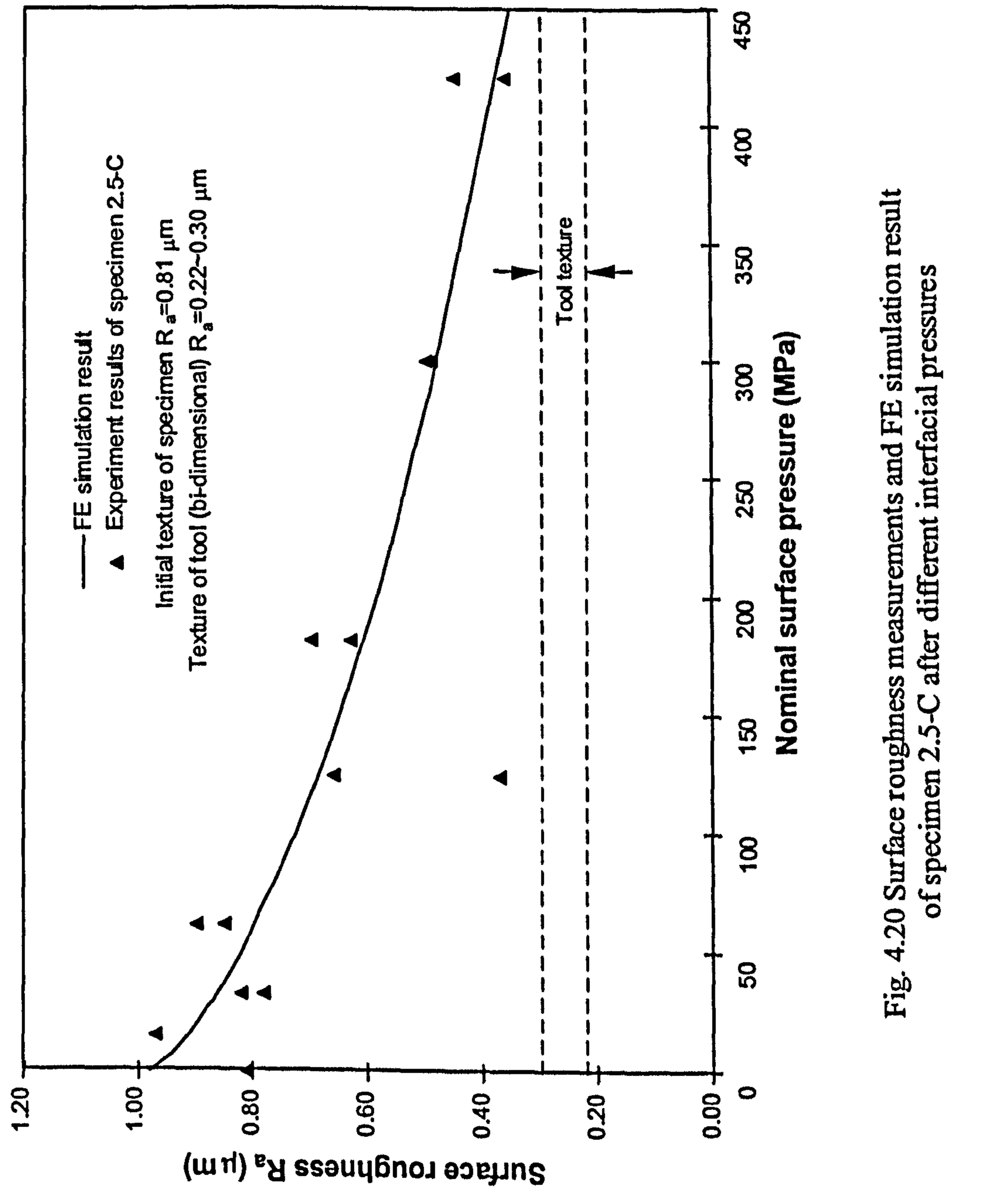

Fig. 4.20 Surface roughness measurements and FE simulation result of specimen 2.5-C after different interfacial pressures

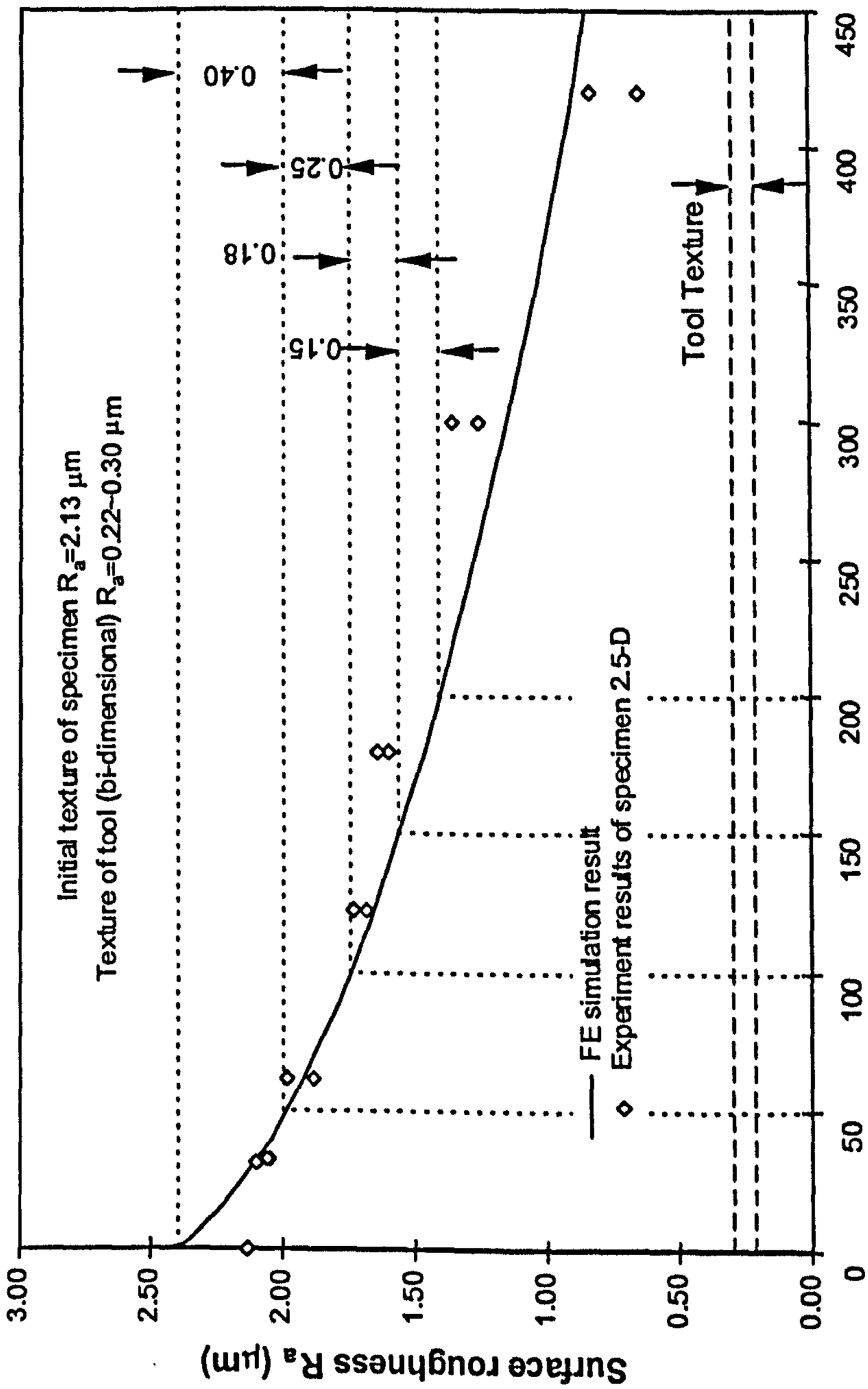

Fig. 4.21 Surface roughness measurements and FE simulation result of specimen 2.5-D after different interfacial pressures

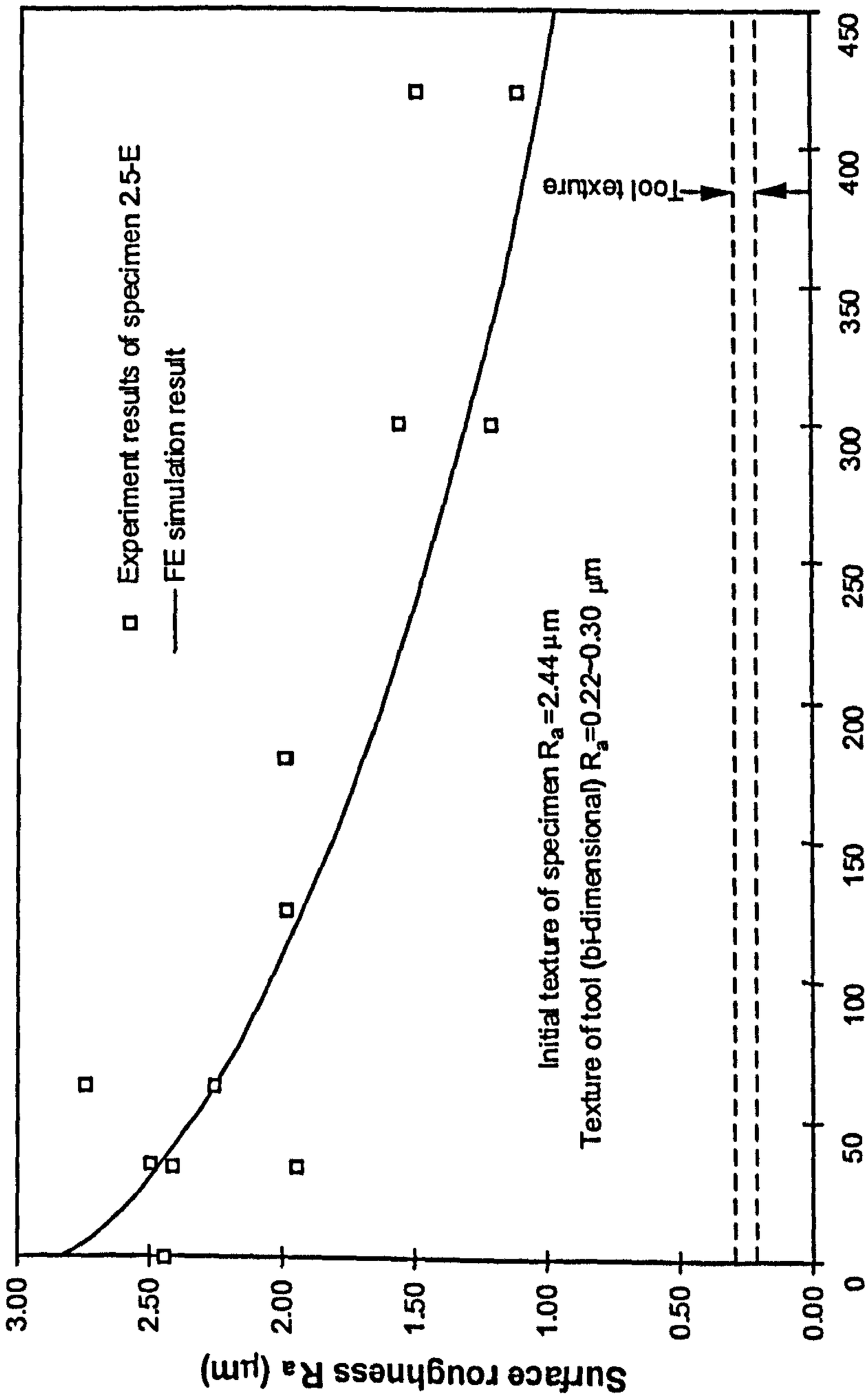

Fig. 4.22 Surface roughness measurements and FE simulation result of specimen 2.5-E after different interfacial pressures

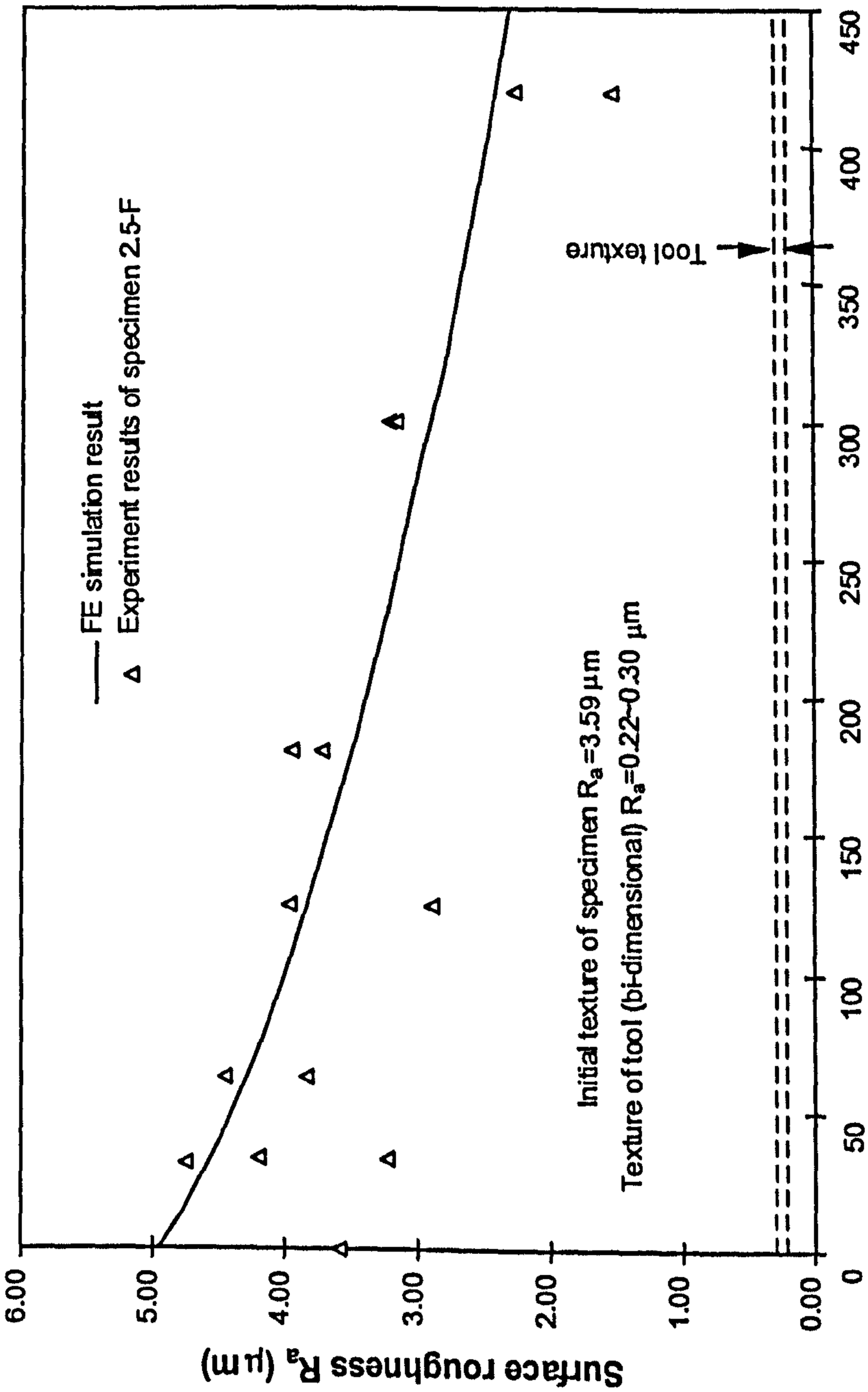

Fig. 4.23 Surface roughness measurements and FE simulation result of specimen 2.5-F after different interfacial pressures

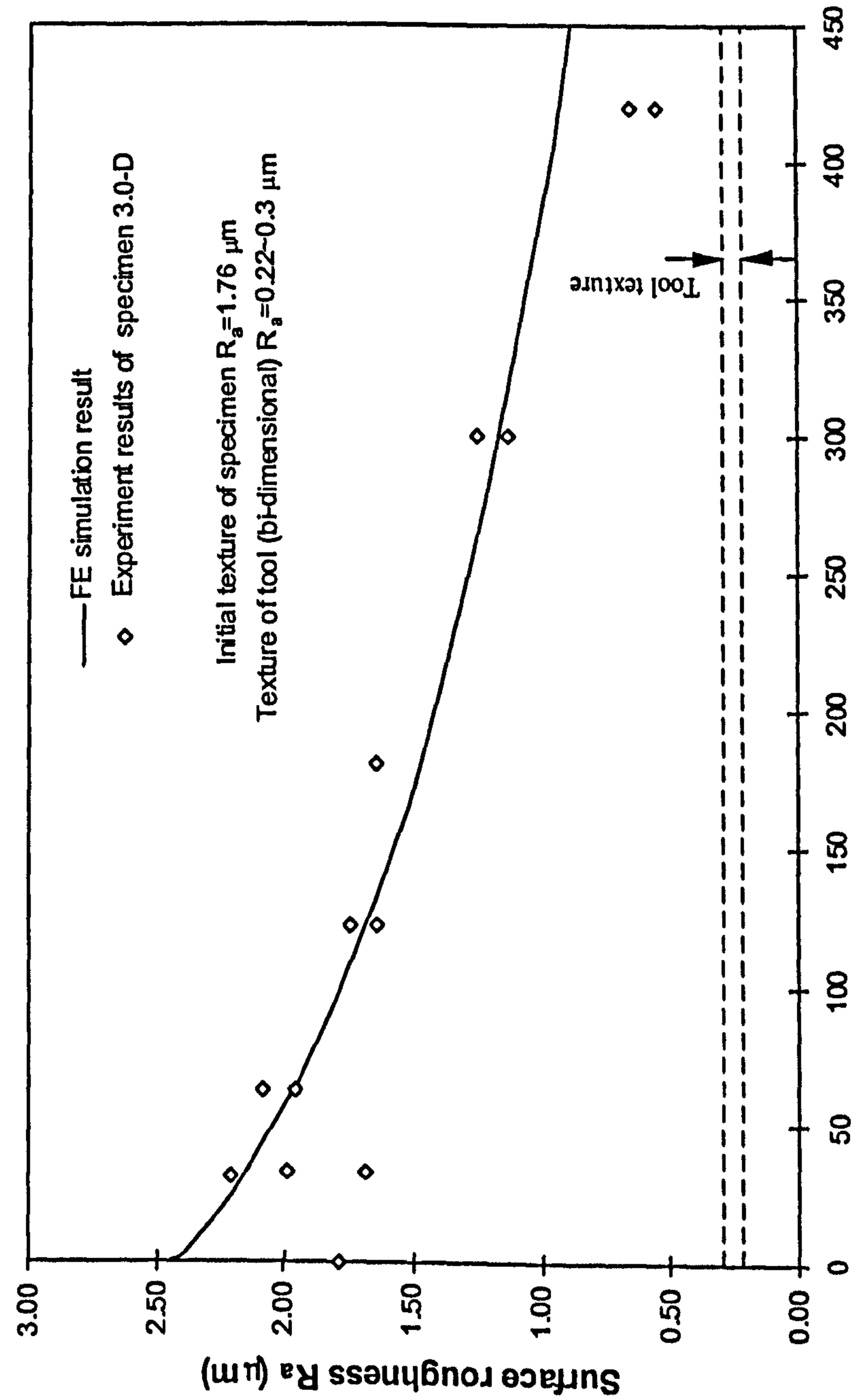

Fig. 4.24 Surface roughness measurements and FE simulation result of specimen 3.0-D after different interfacial pressures

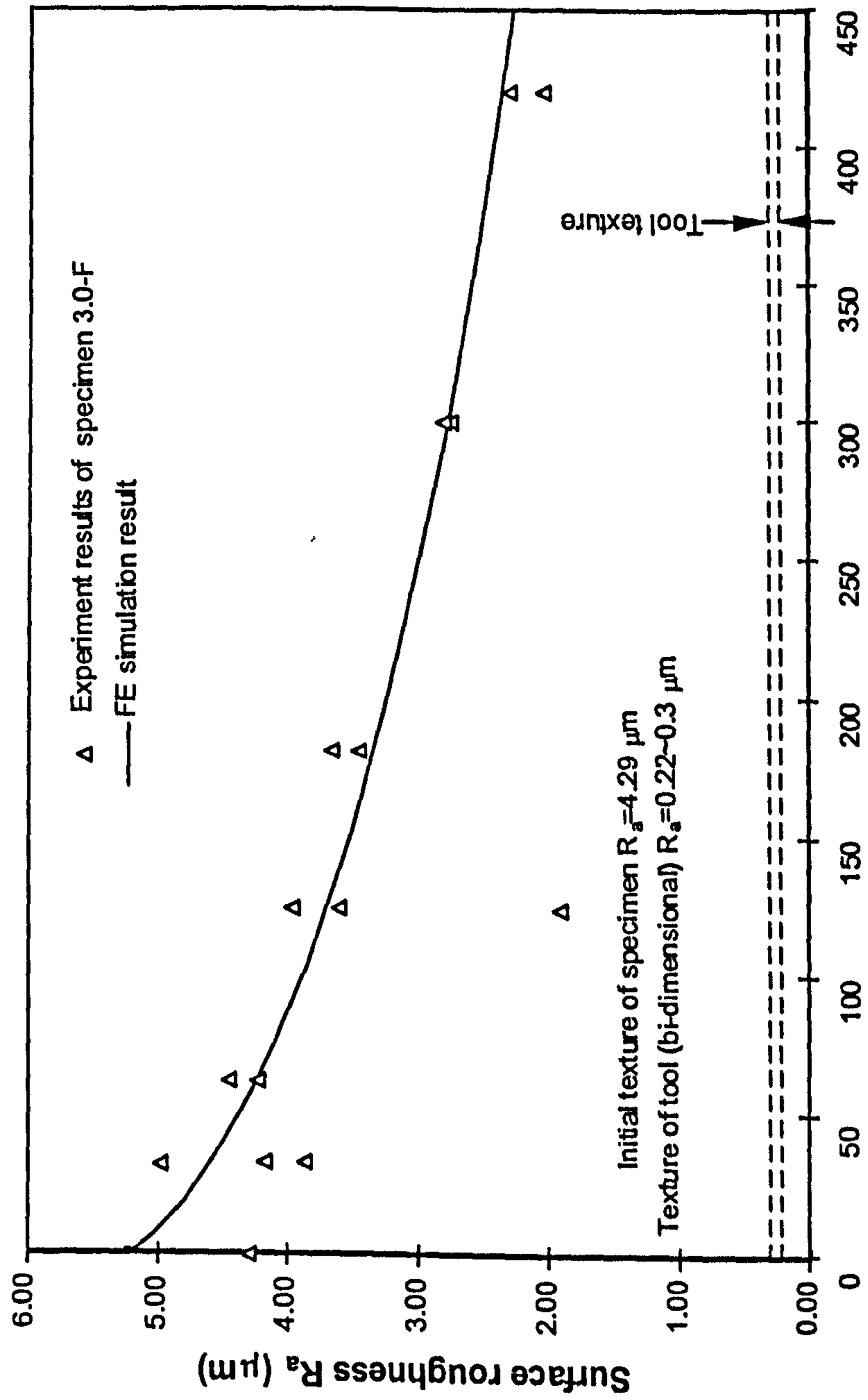

Fig. 4.25 Surface roughness measurements and FE simulation result of specimen 3.0-F after different interfacial pressures

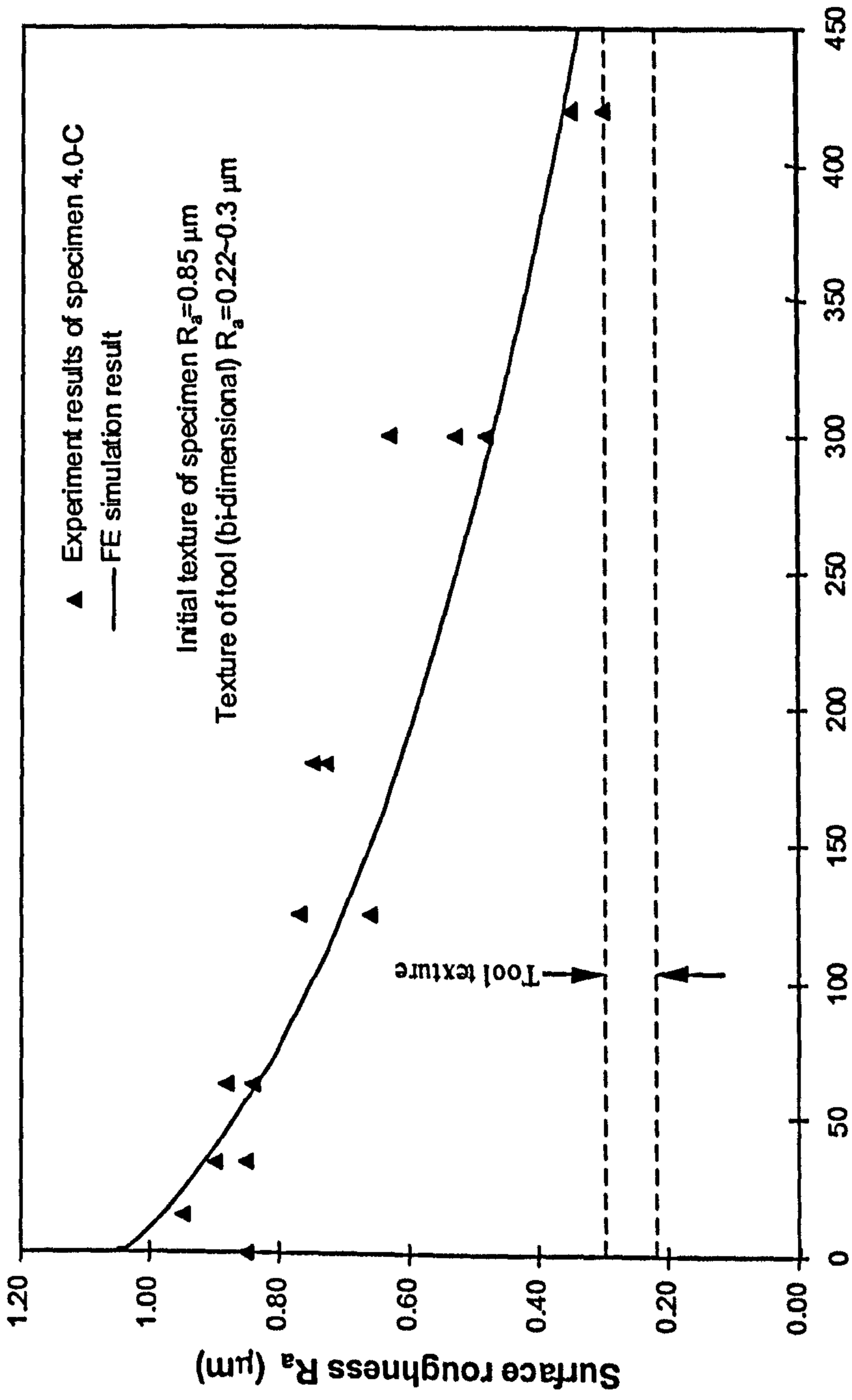

Fig. 4.26 Surface roughness measurements and FE simulation result of specimen 4.0-C after different interfacial pressures

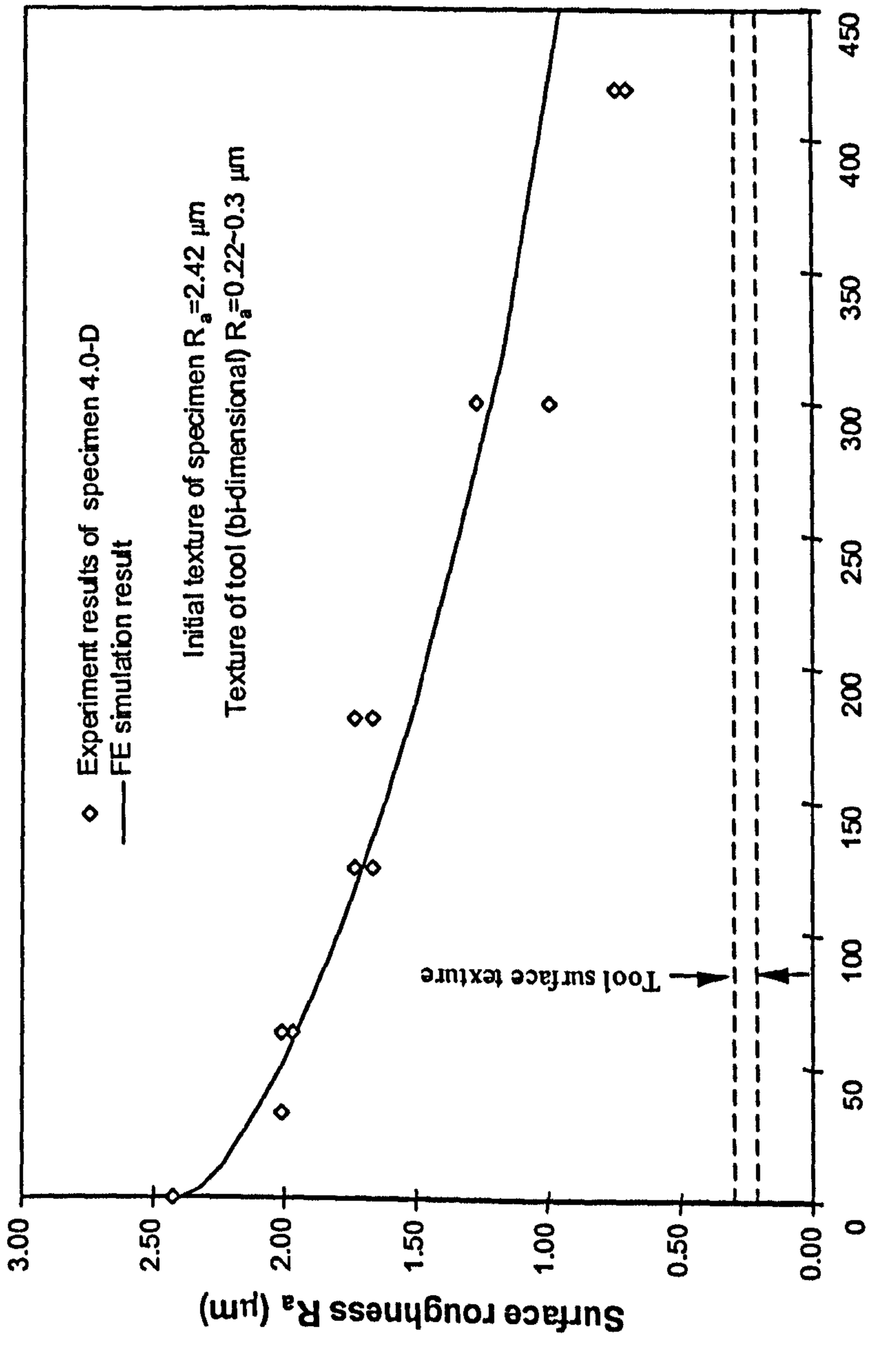

Fig. 4.27 Surface roughness measurements and FE simulation result of specimen 4.0-D after different interfacial pressures

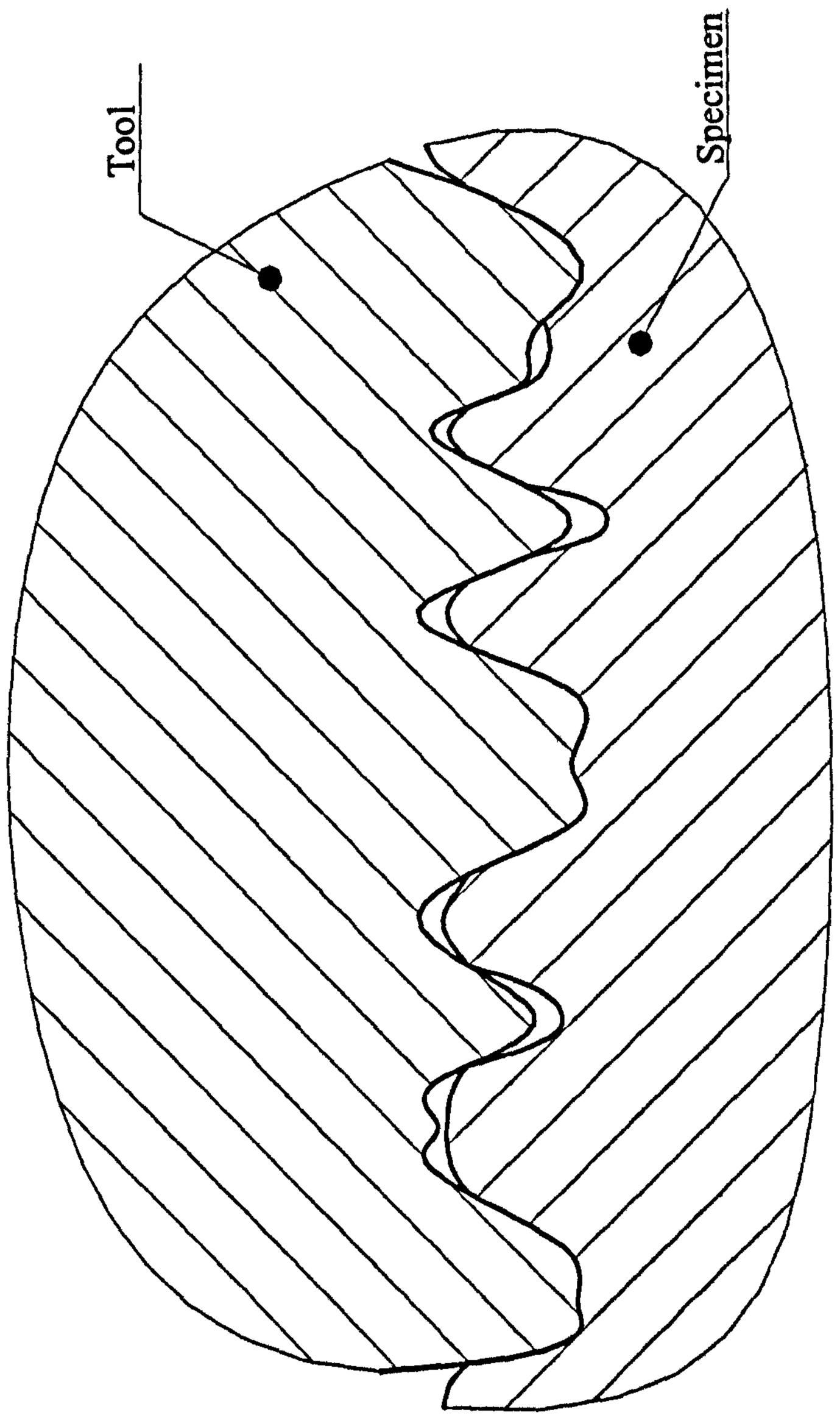

Fig. 4.28 Replication of tool texture on specimen

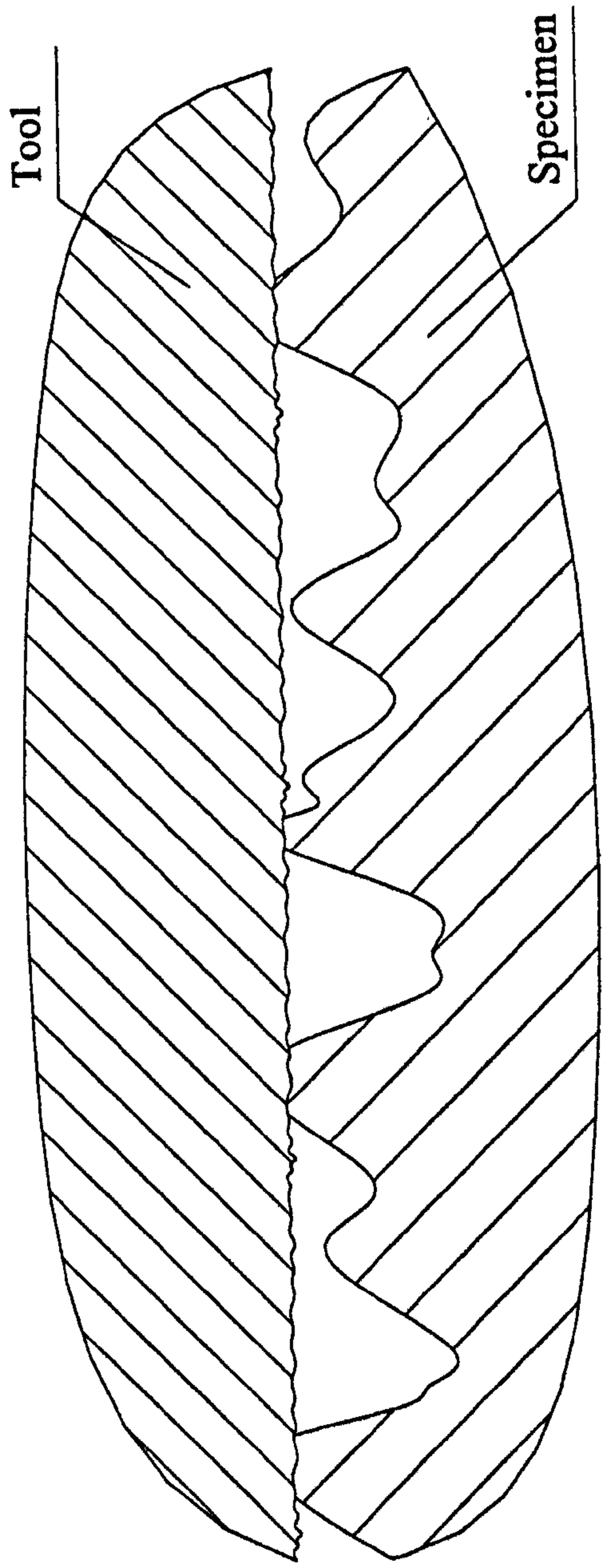

Fig. 4.29 Perfect tool

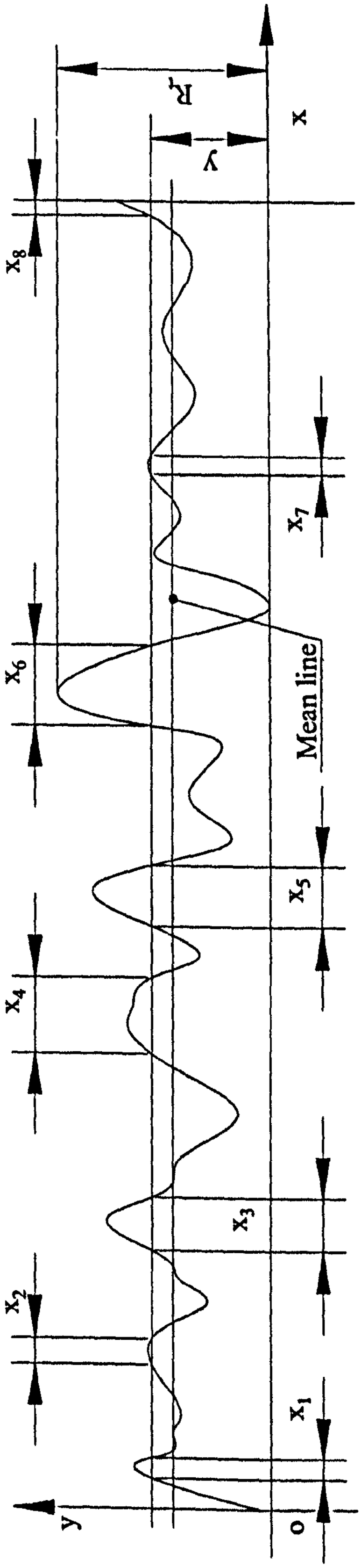

Fig. 4.1.1 Geometric definition of bearing ratio (material ratio) curve

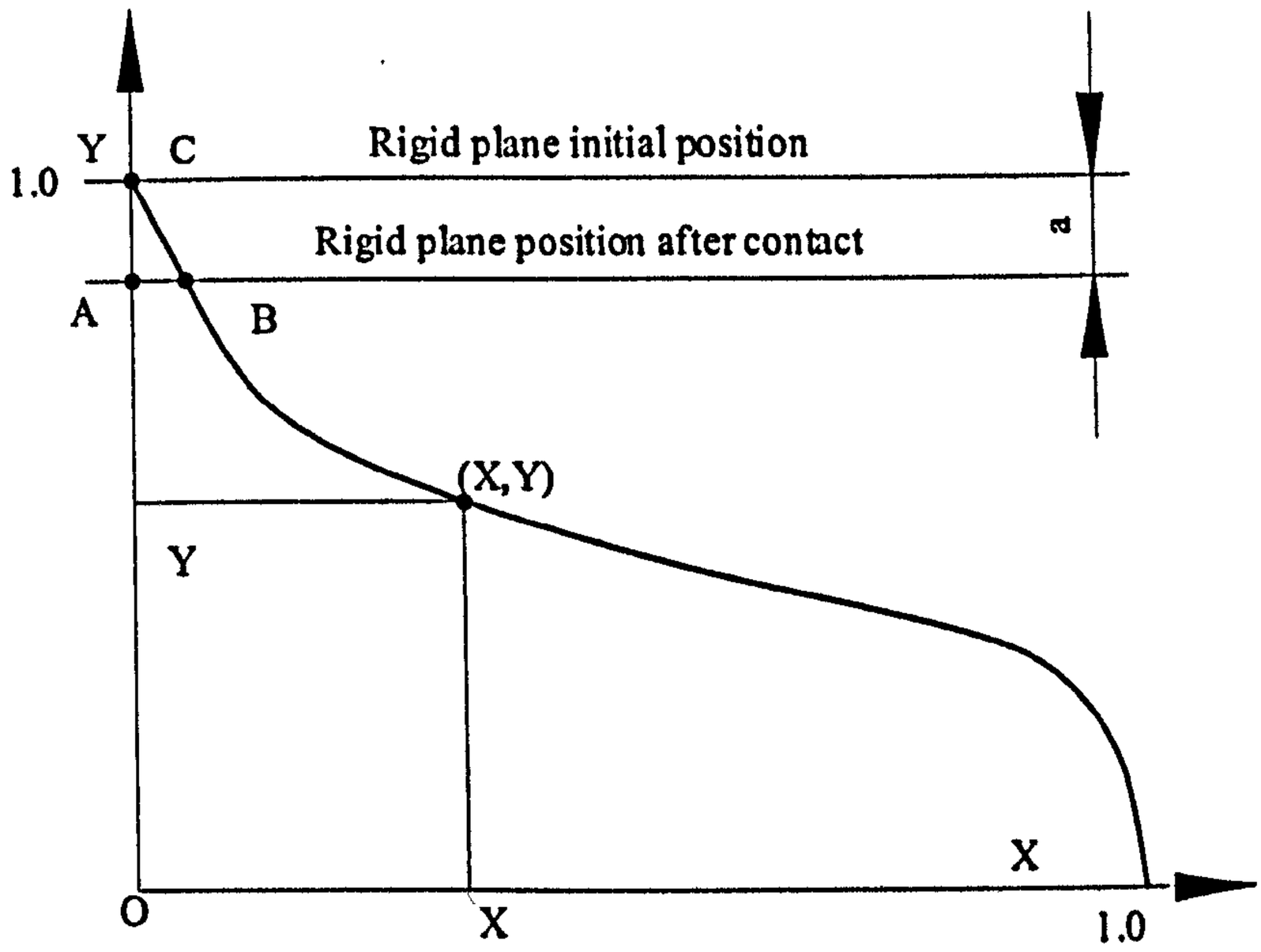

Fig.4.1.2 Bearing ratio curve and its meaning

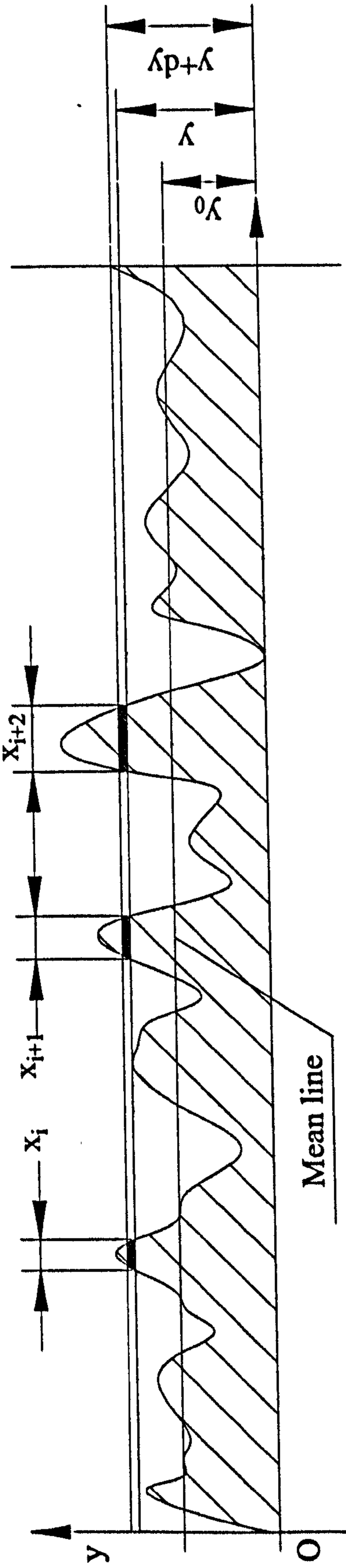

Fig.4.2.1 Geometric meaning of equation (4.2-1)

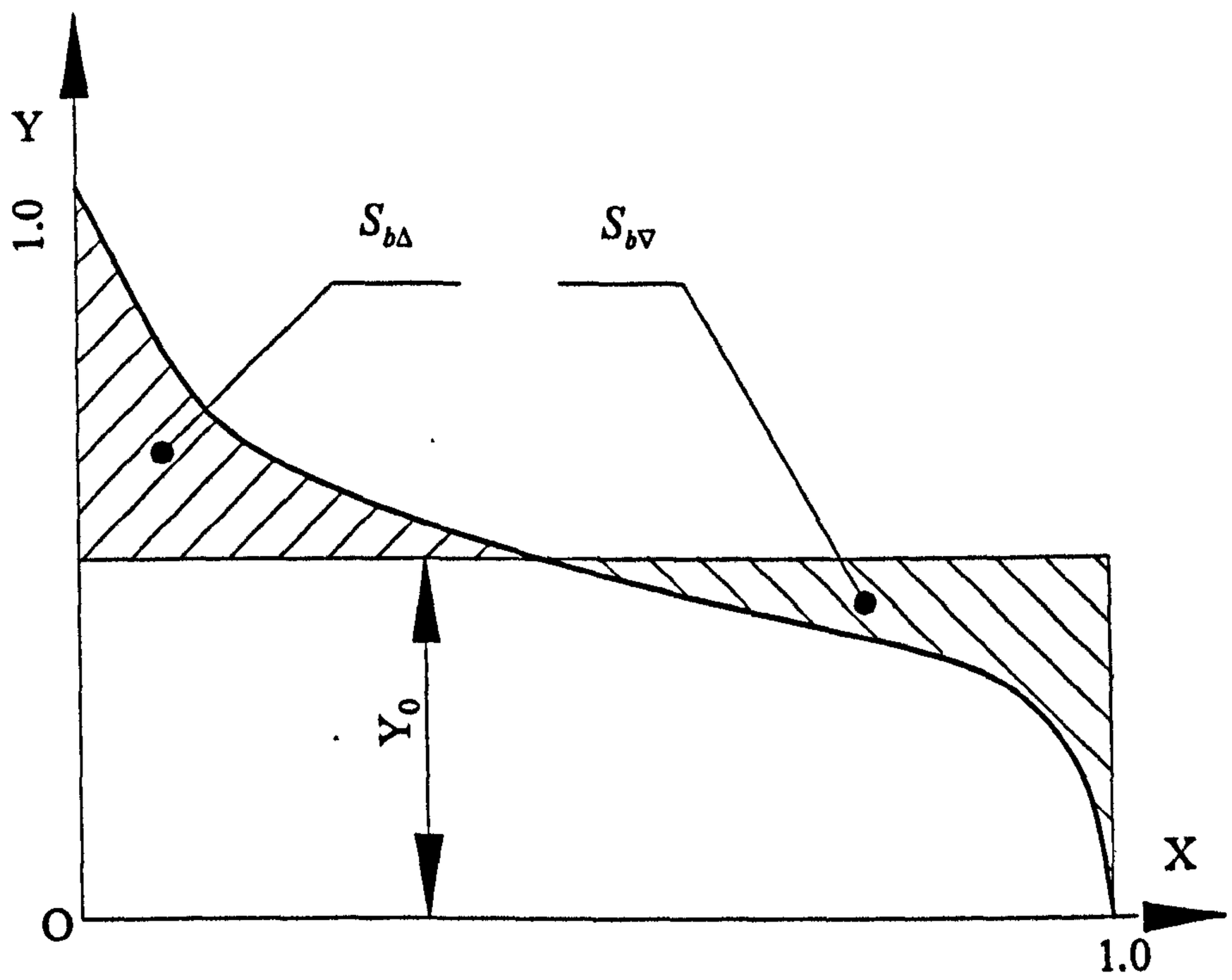

Fig.4.2.2 Mean line position

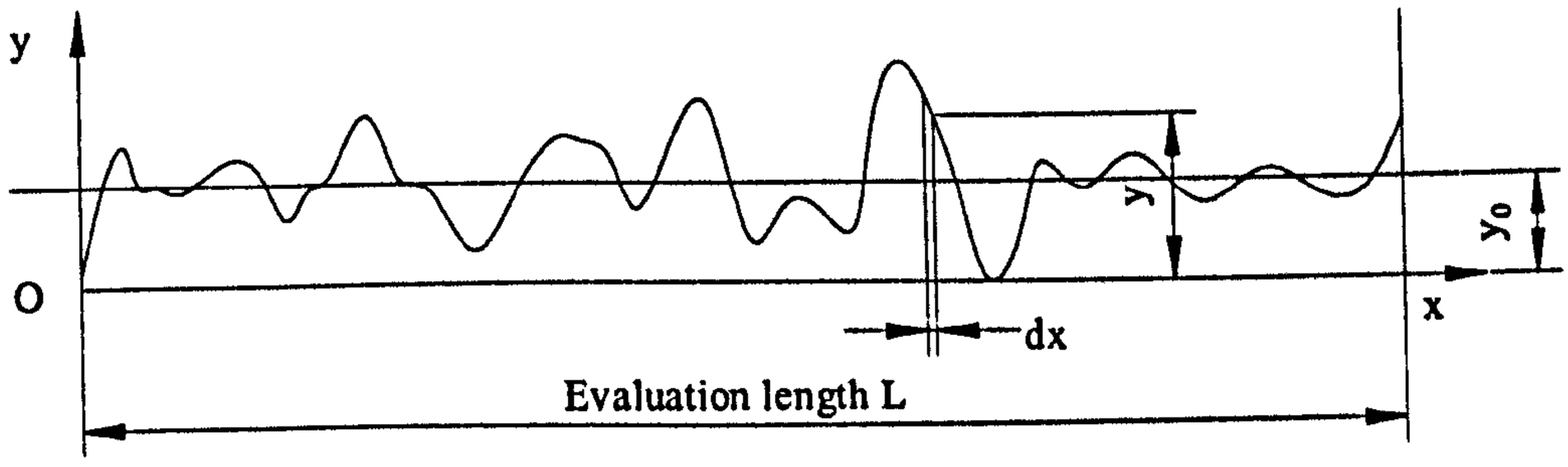

(a) General integration for R_q

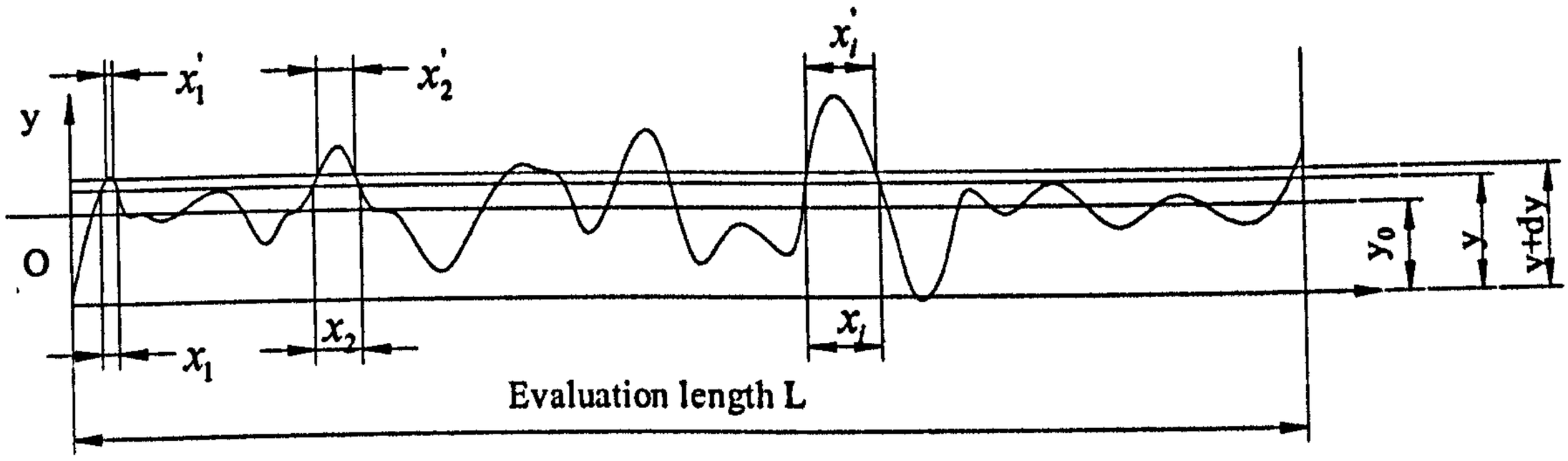

(b) A different integration method

Fig. 4.2.3 The integration approaches for root-mean-square deviation

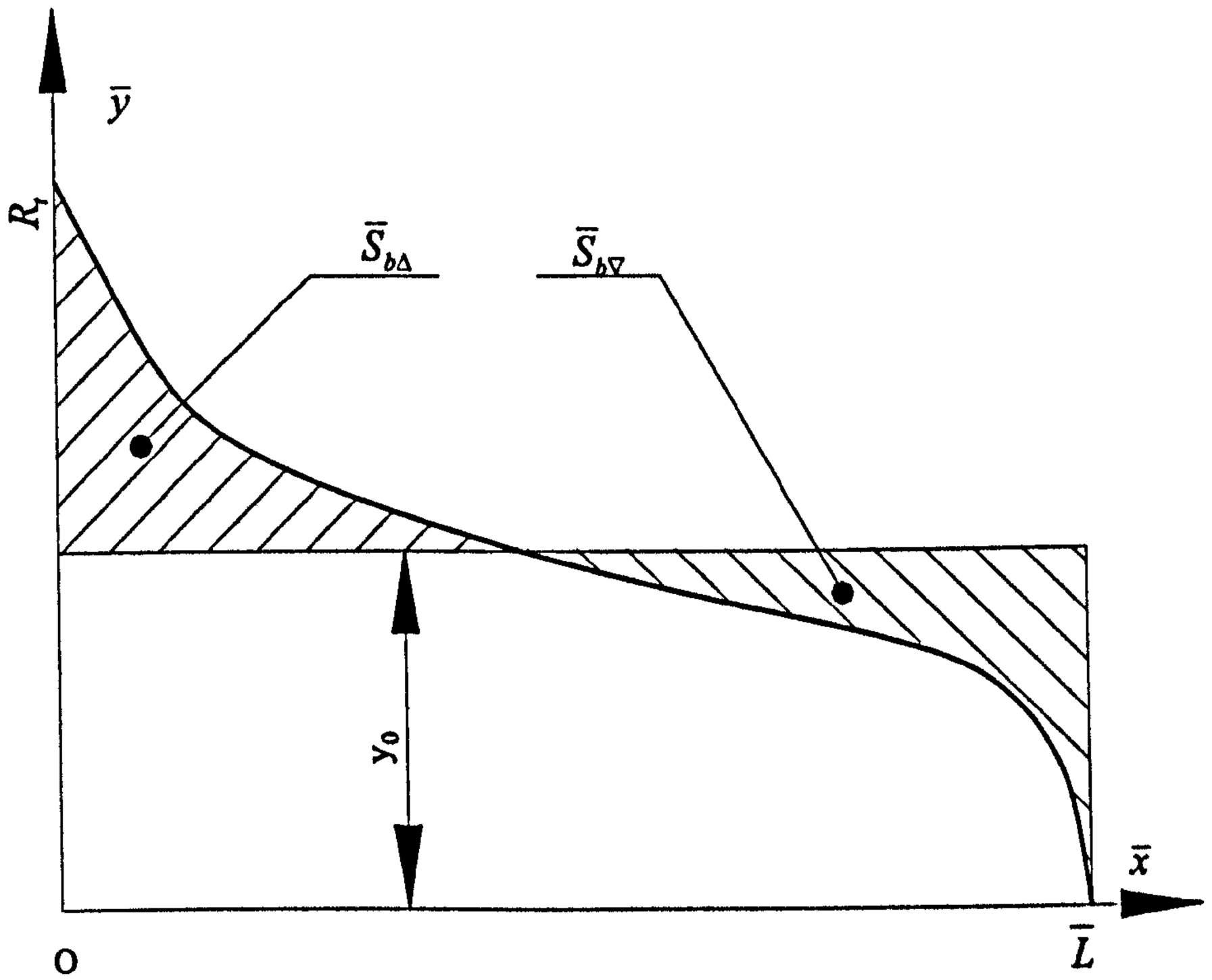

Fig. 4.2.4 Expanded bearing ratio curve

Diagrams for Chapter Five

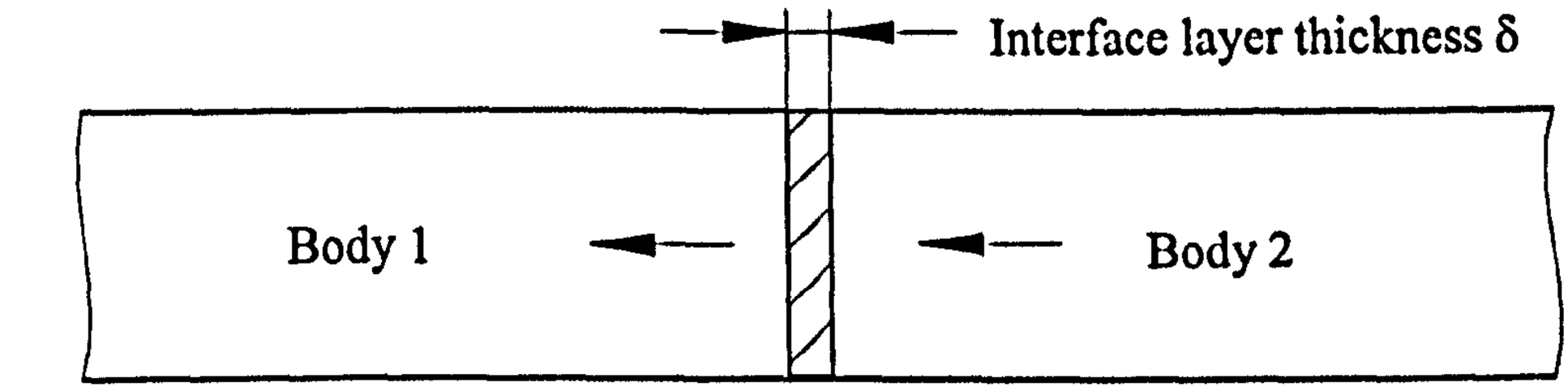

(a)

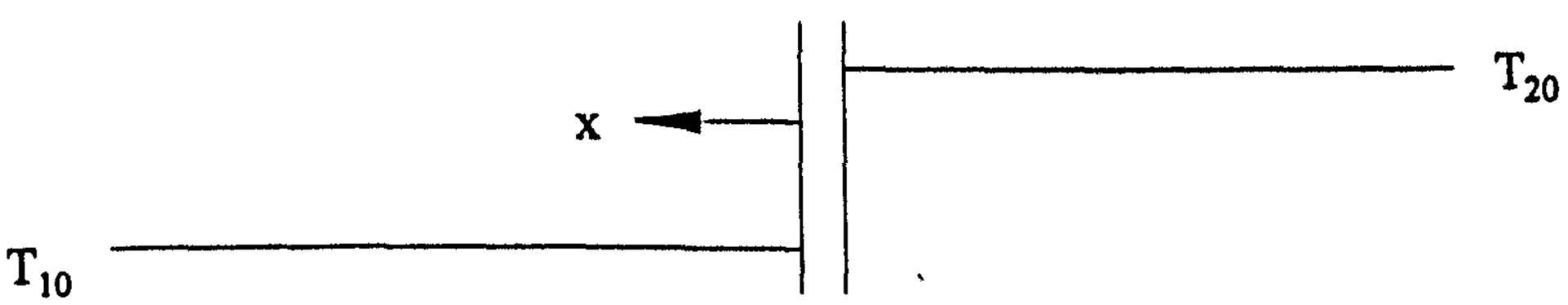

(b)

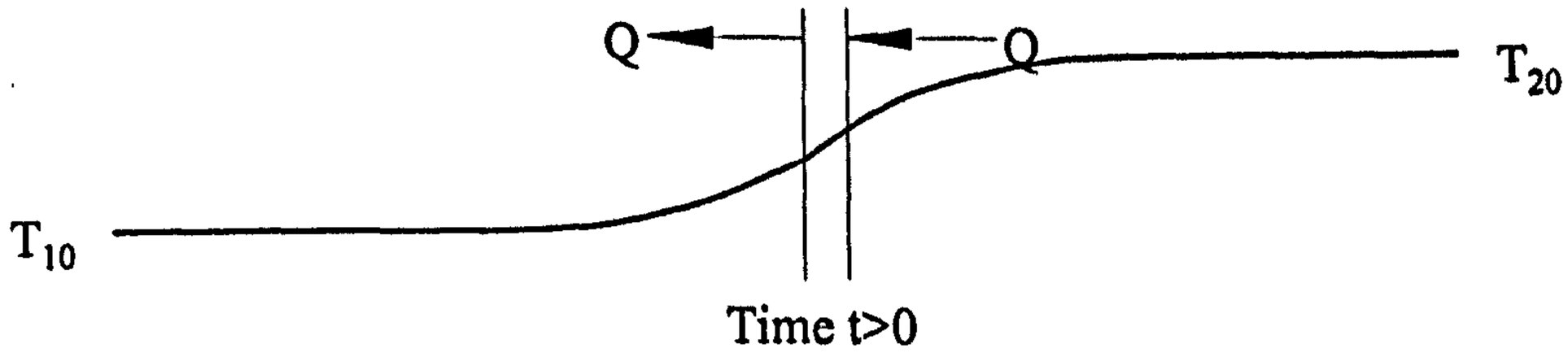

(c)

Fig.5.1 Transient thermal model at higher contact pressure

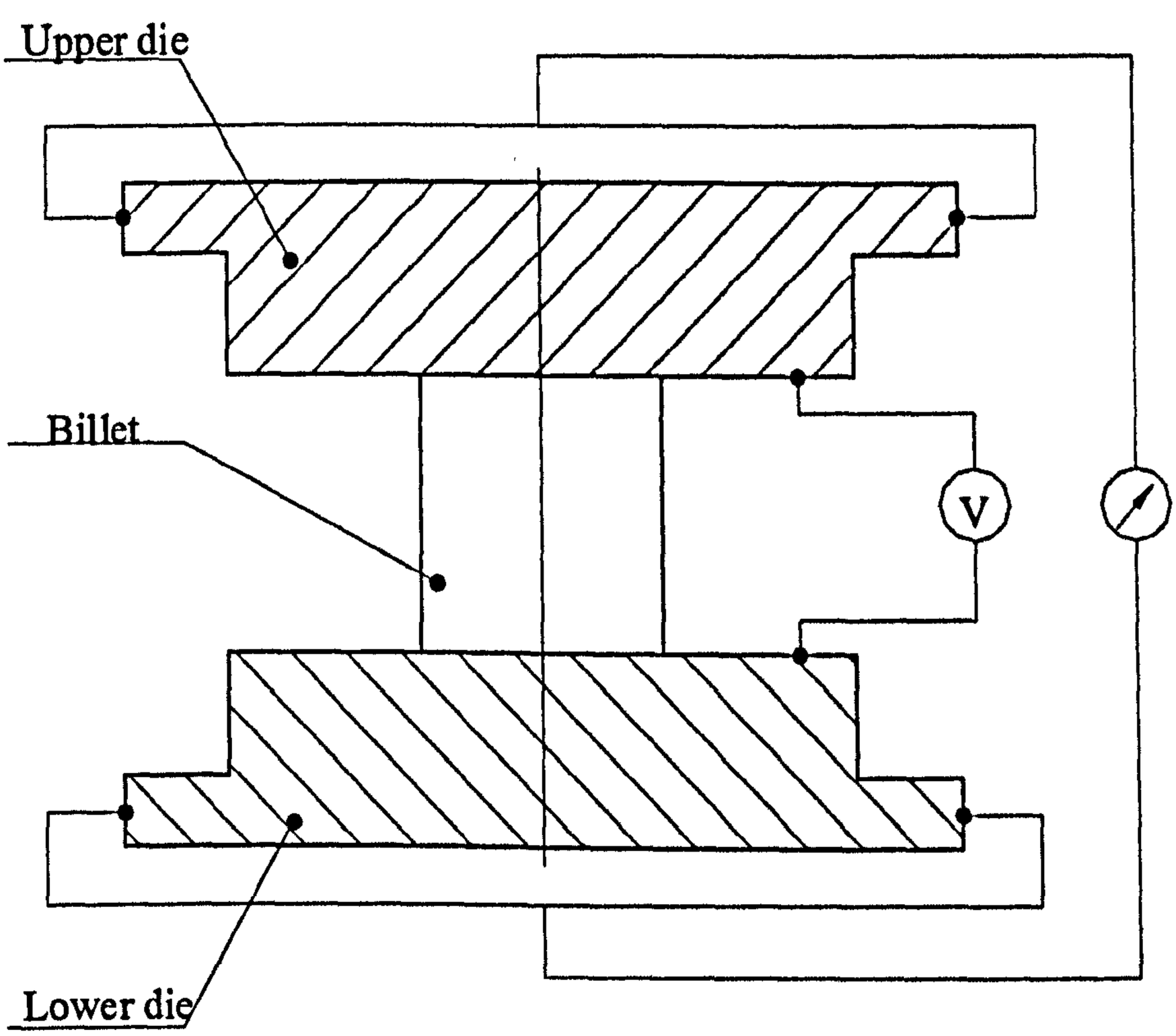

Fig. 5.2 Electrical approach for establishing thermal contact behaviour

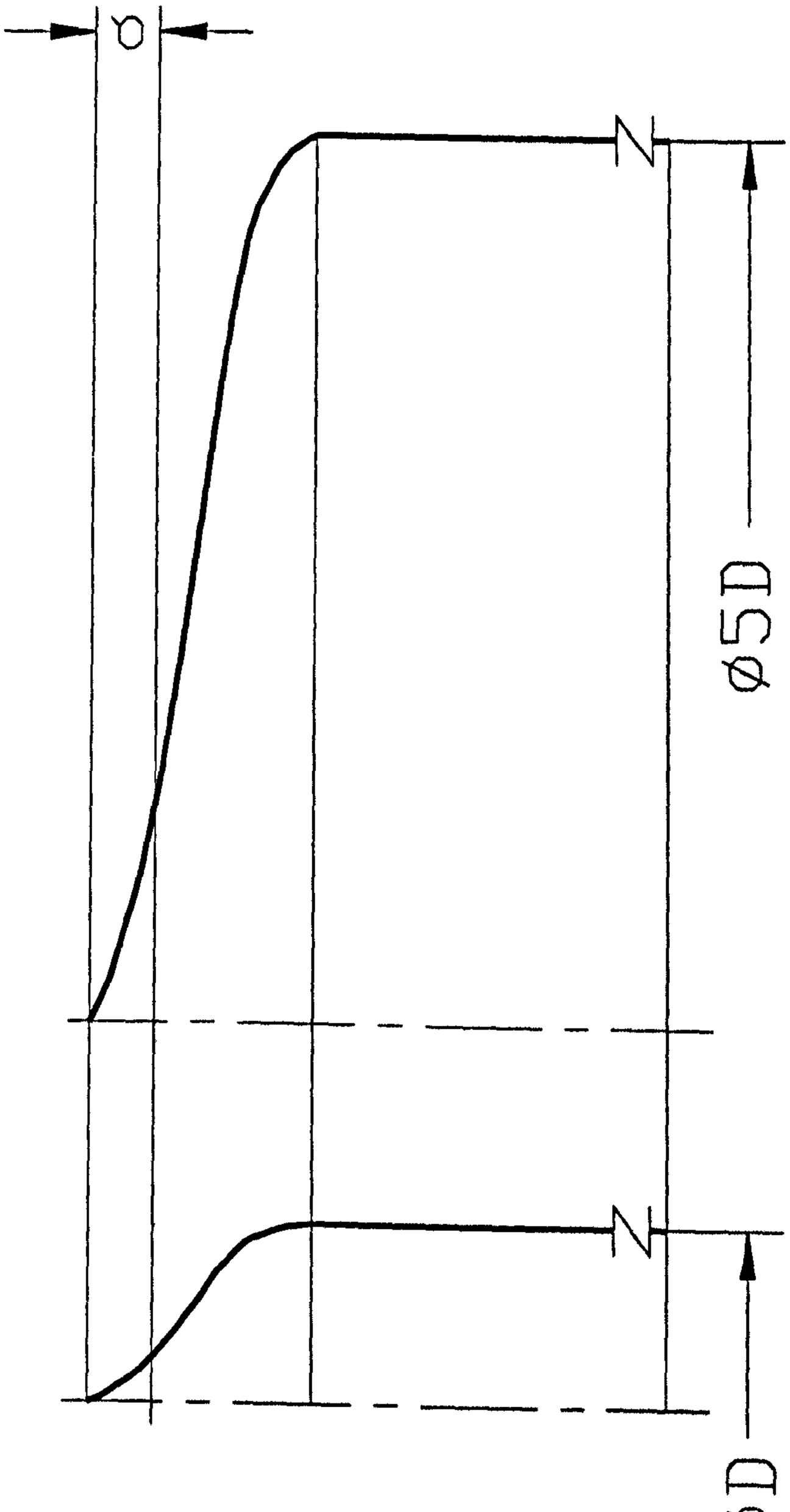

Fig. 5.3 Influence of equivalent asperity diameter on interfacial pressure

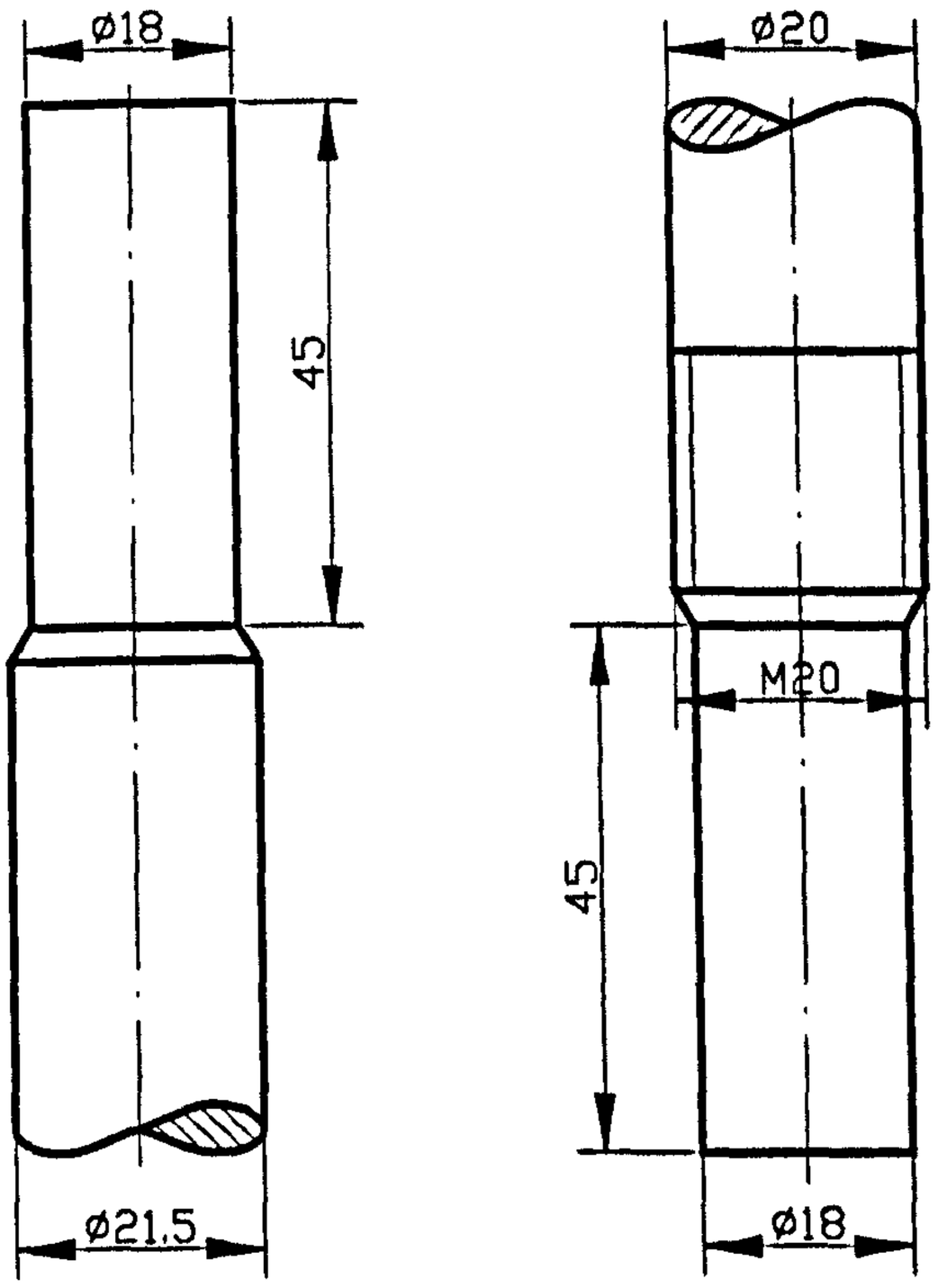

(a) Tools used in the experimental equipment

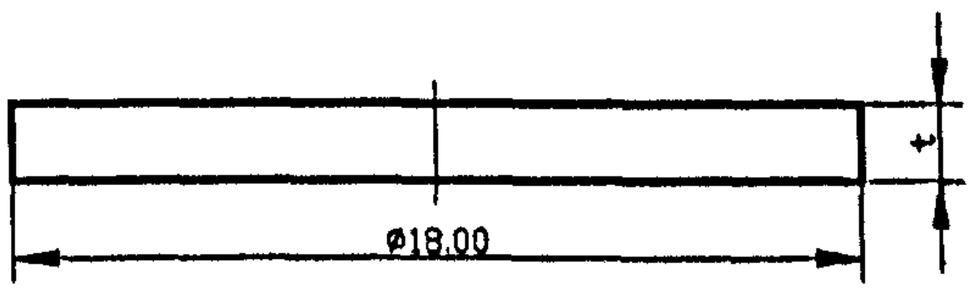

t=1.00, 1.50, 2.00, 2.50, 3.00, 4.00 mm

(b) Dimensions and form of specimen

Fig. 5.4 Tools and specimens used in the experiment

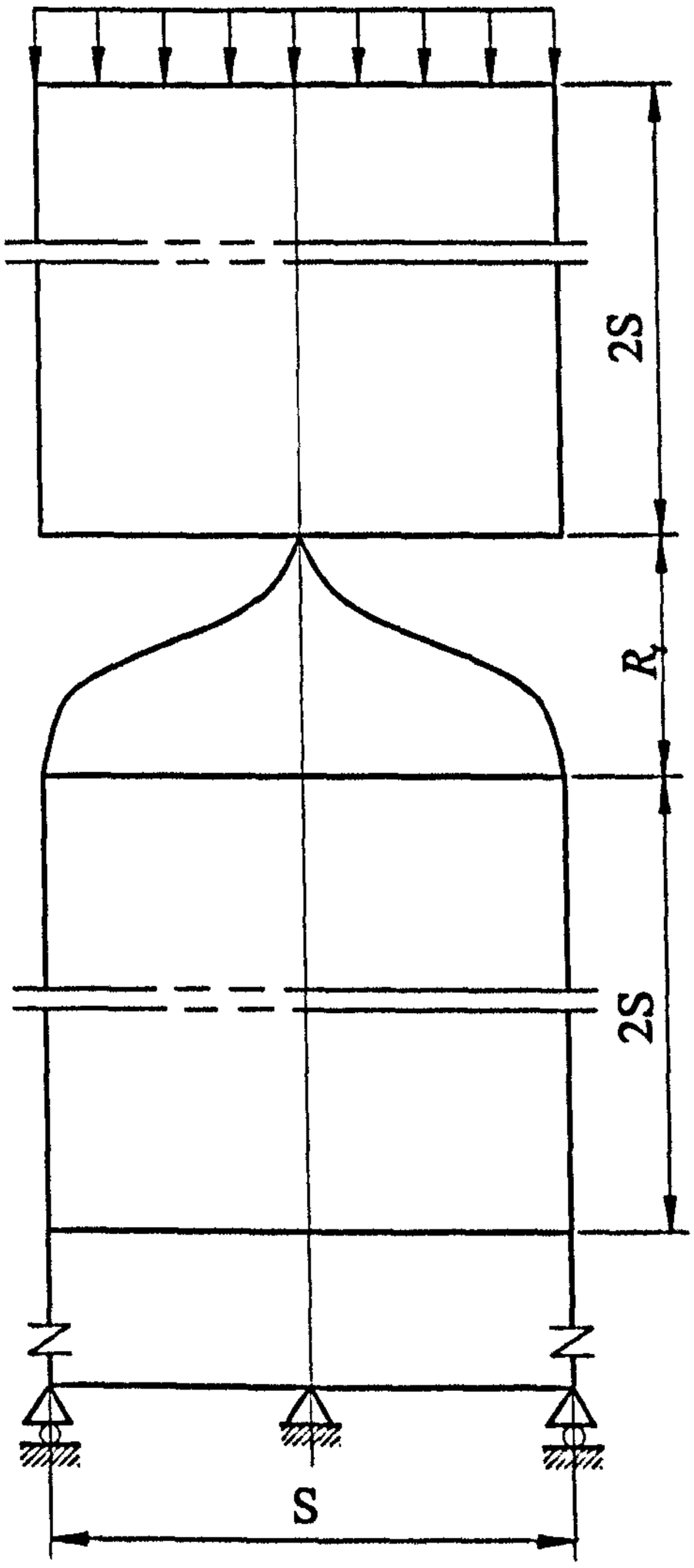

Surfaces AB and CD are used for setting boundary conditions of temperature

Fig. 5.5 Geometry and dimensions of the FE simulation model

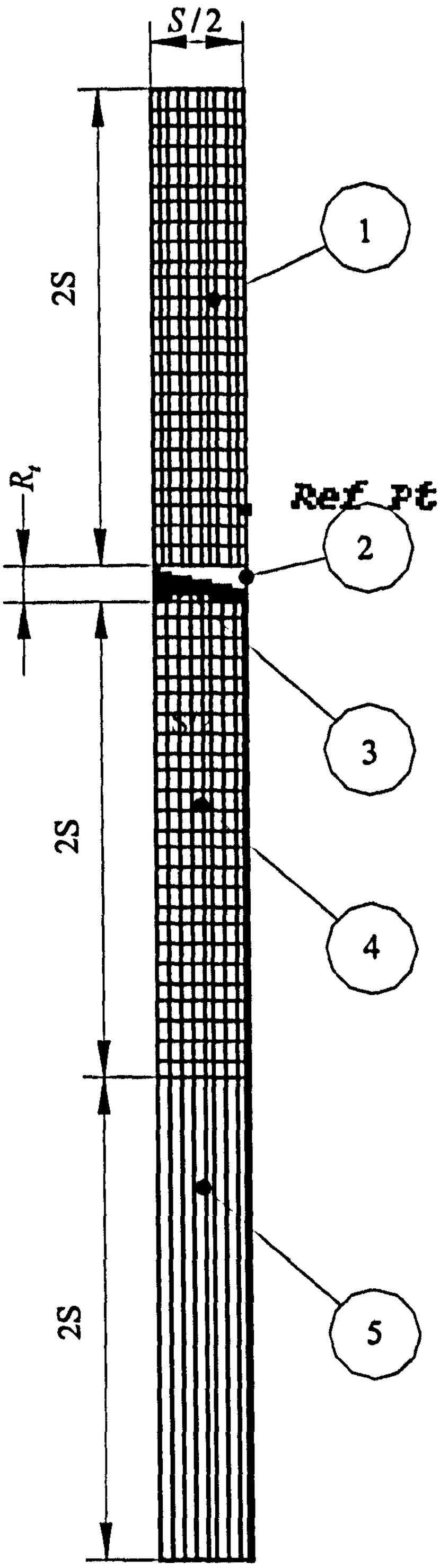

1. Tool geometry and mesh before contact;
2. Virtual cylinder to simulate interaction between asperities;
3. Equivalent asperity;
4. Specimen with two-dimensional solid elements;
5. Specimen with infinite elements.

Fig. 5.6 Geometry and mesh model
of the thermal contact conductance FE simulation

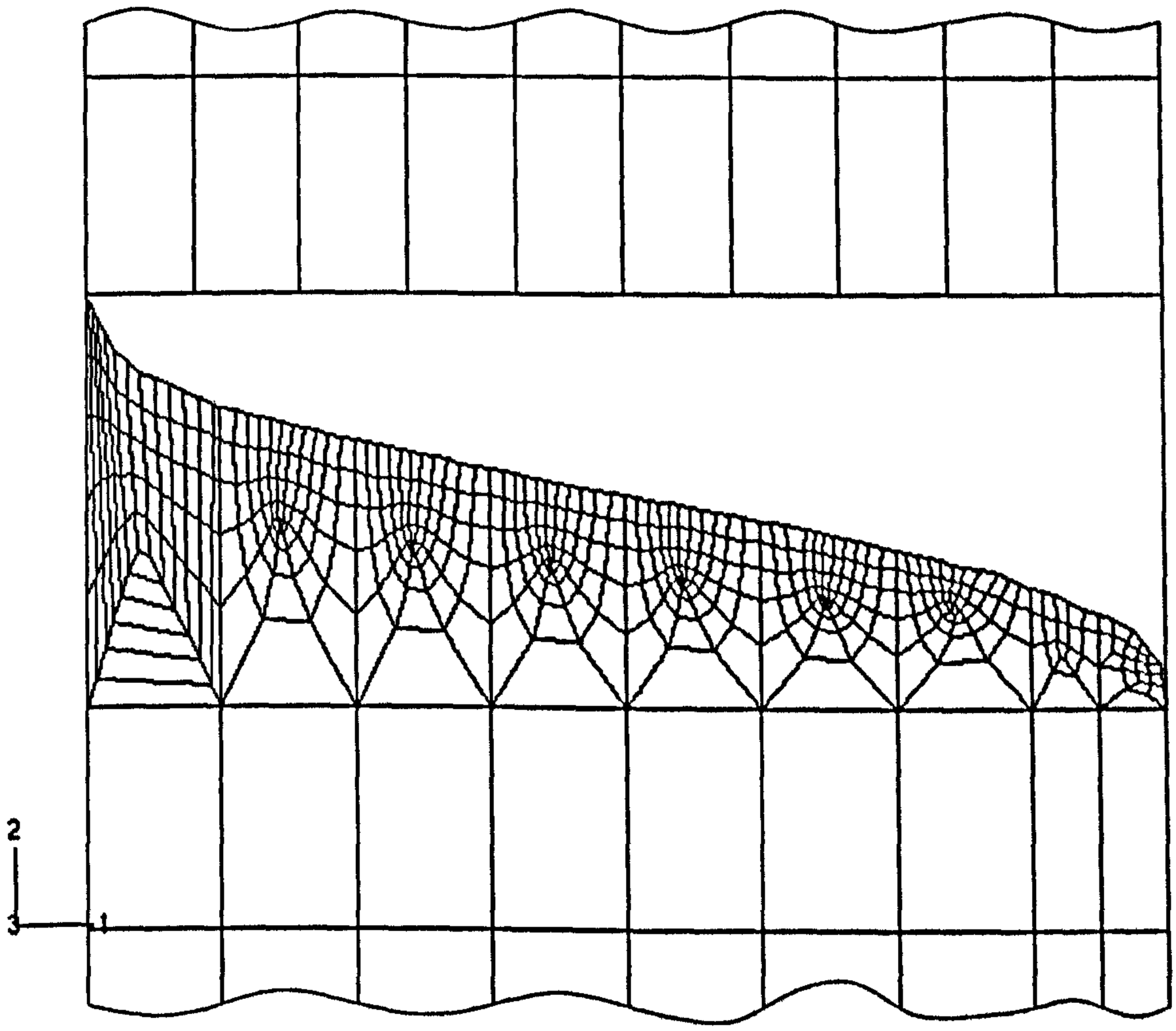

Fig. 5.7 The local mesh of the equivalent asperity before contact

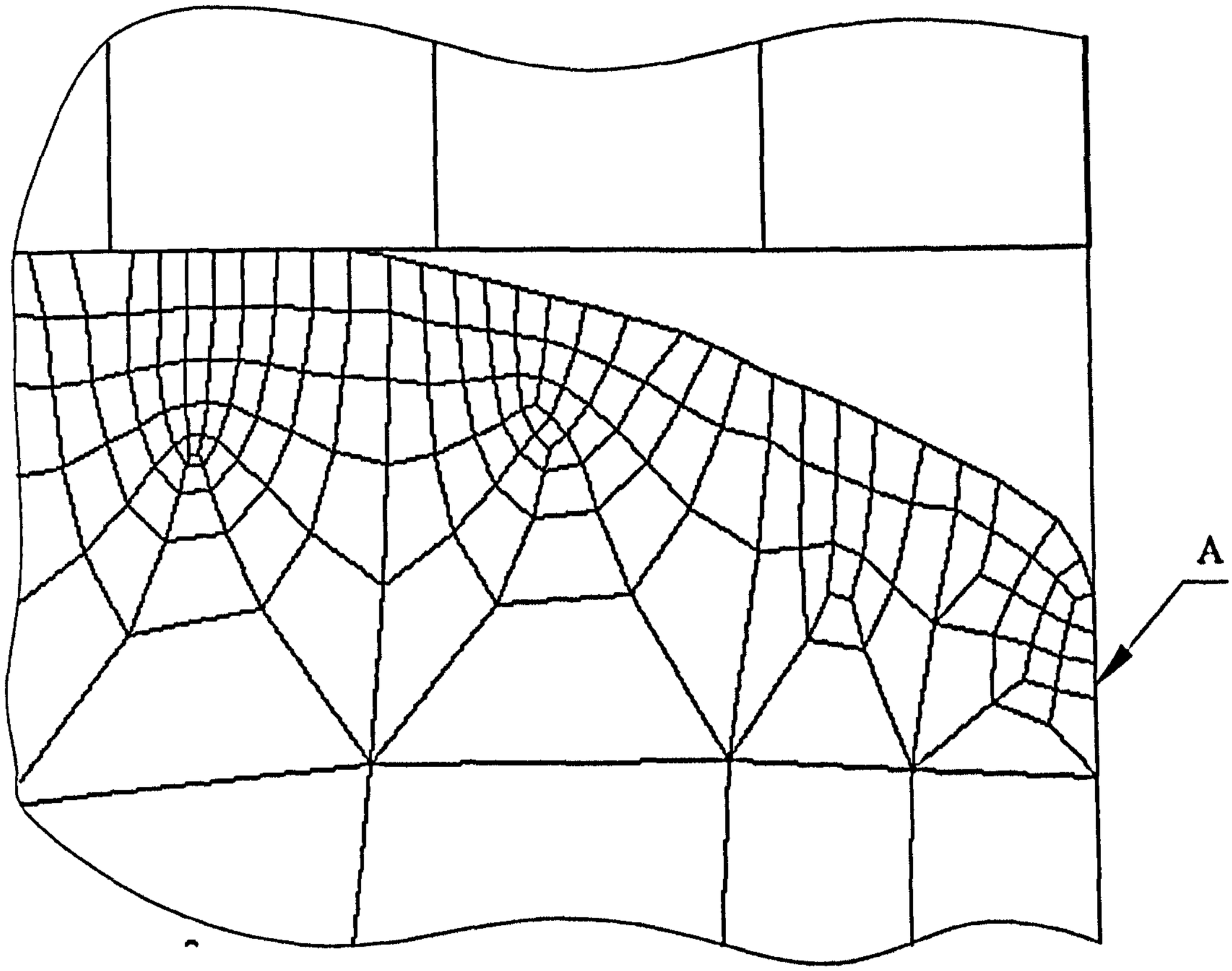

Fig. 5.8 The interaction between asperities

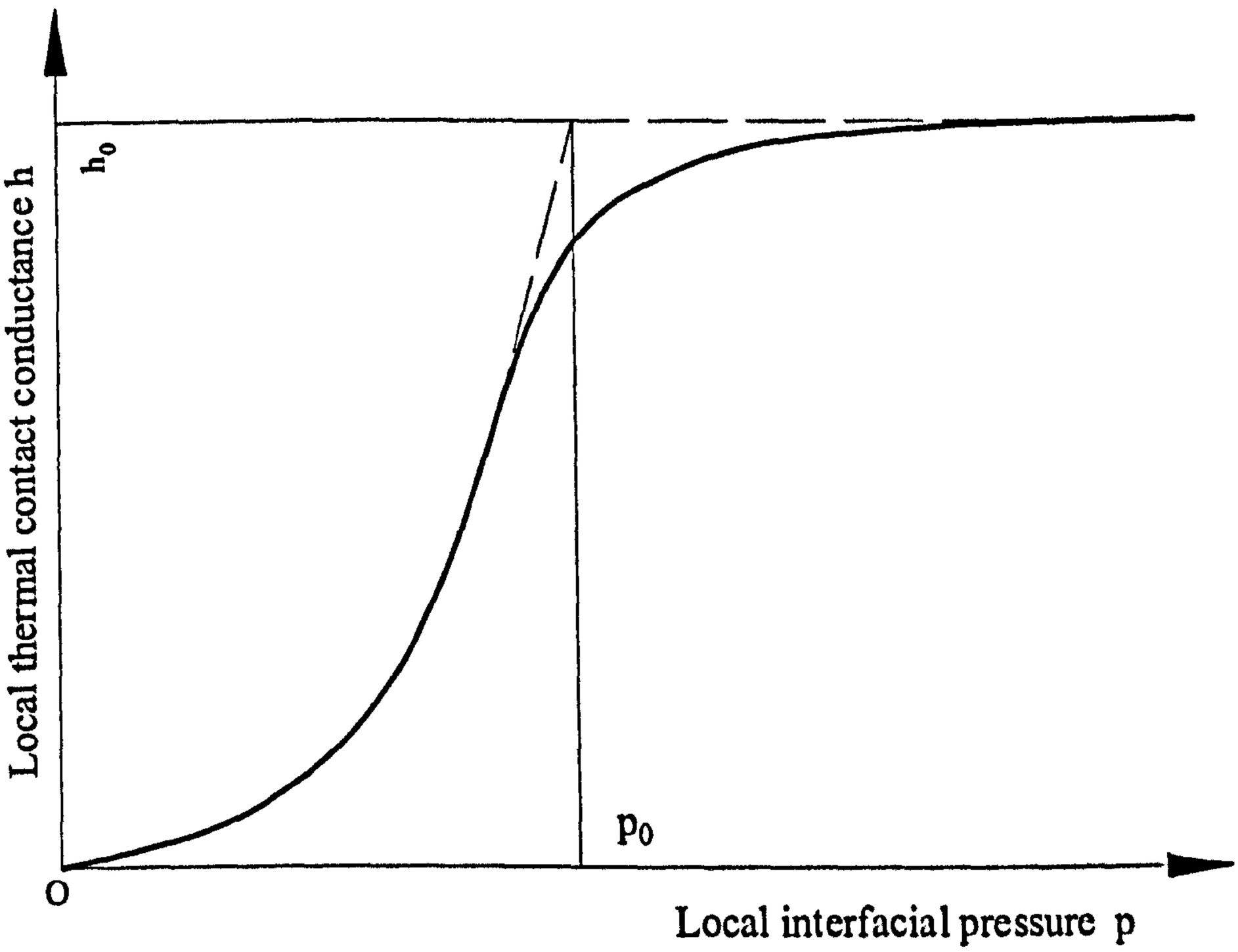

Fig. 5.9 Assumption of local thermal contact conductance

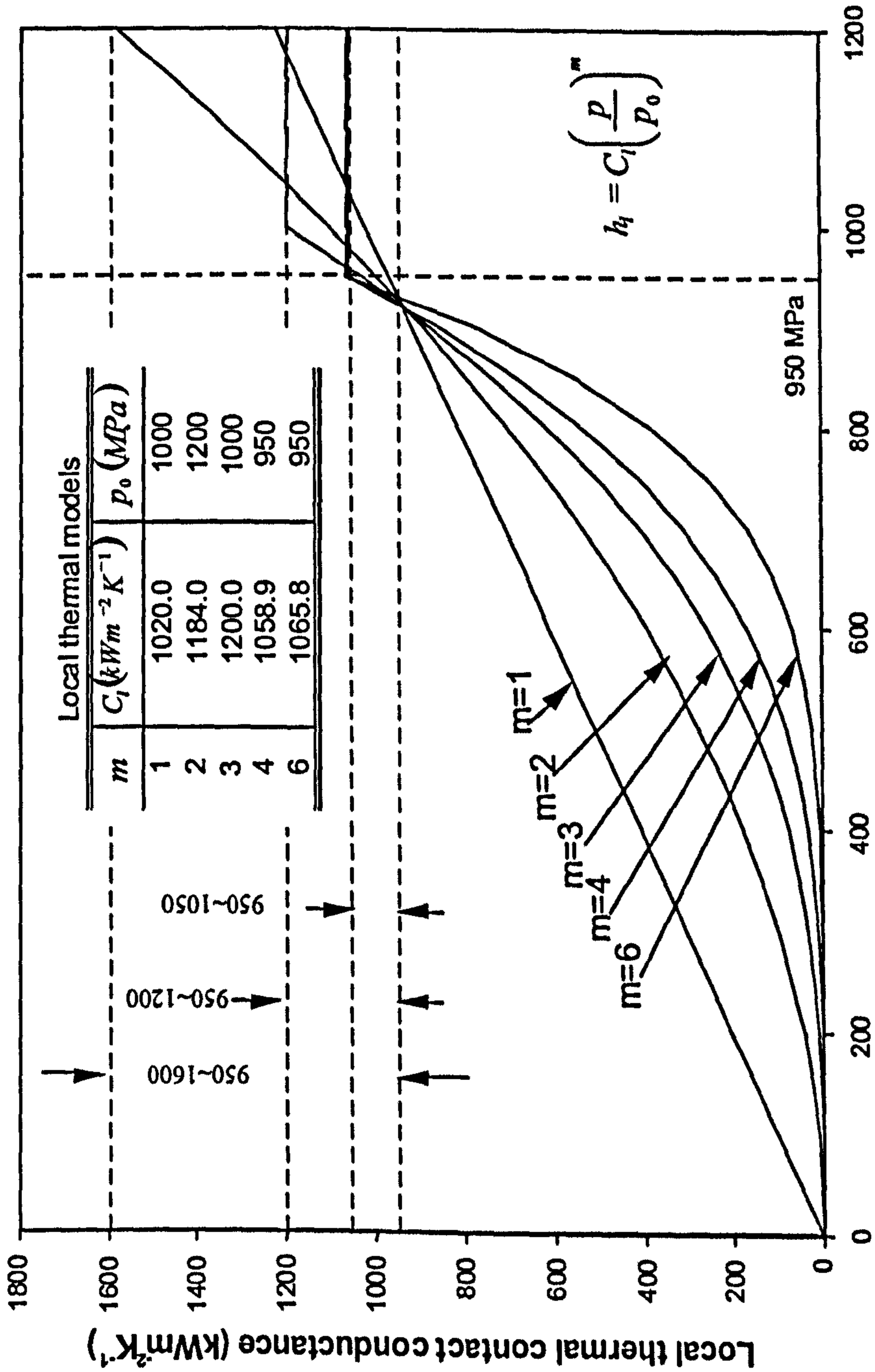

Fig. 5.10 Local thermal models used in h-value FE simulations

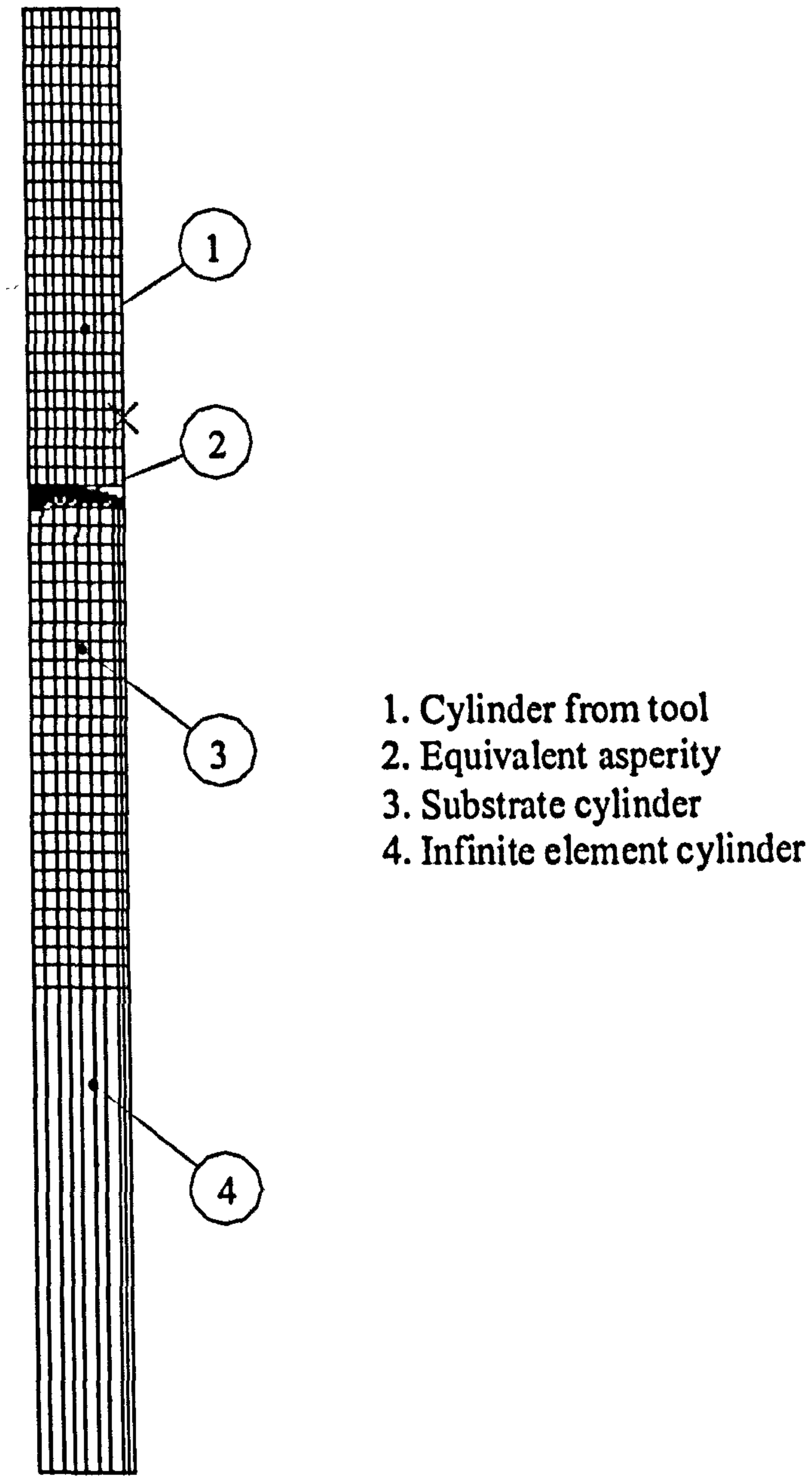

Fi.g 5.11 Mesh of thermal contact conductance
FE simulation model after deformation

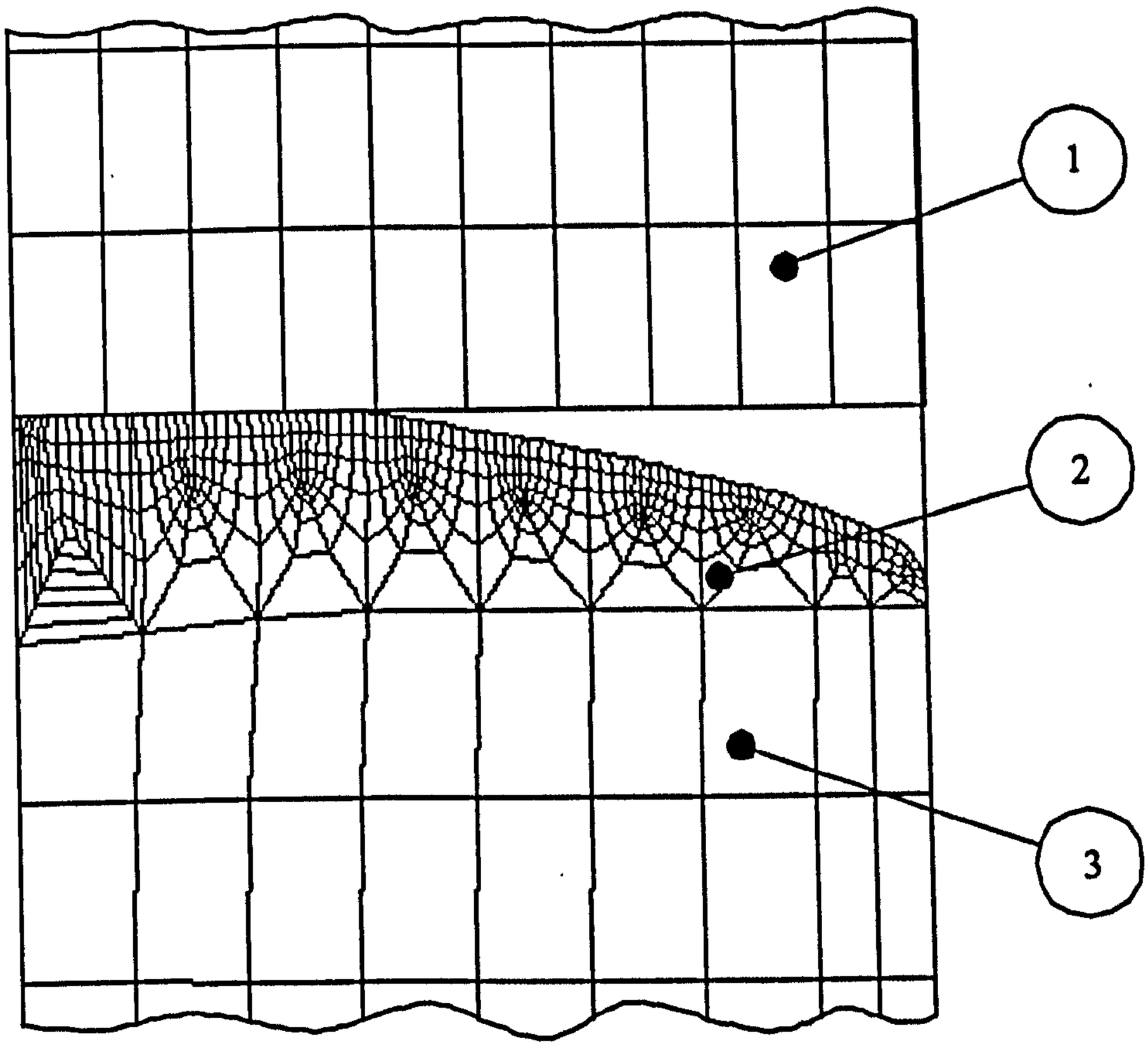

1. Elastic tool mesh
2. Equivalent asperity mesh
3. Substrate mesh

Fig. 5.12 Deformation of the equivalent asperity during contact

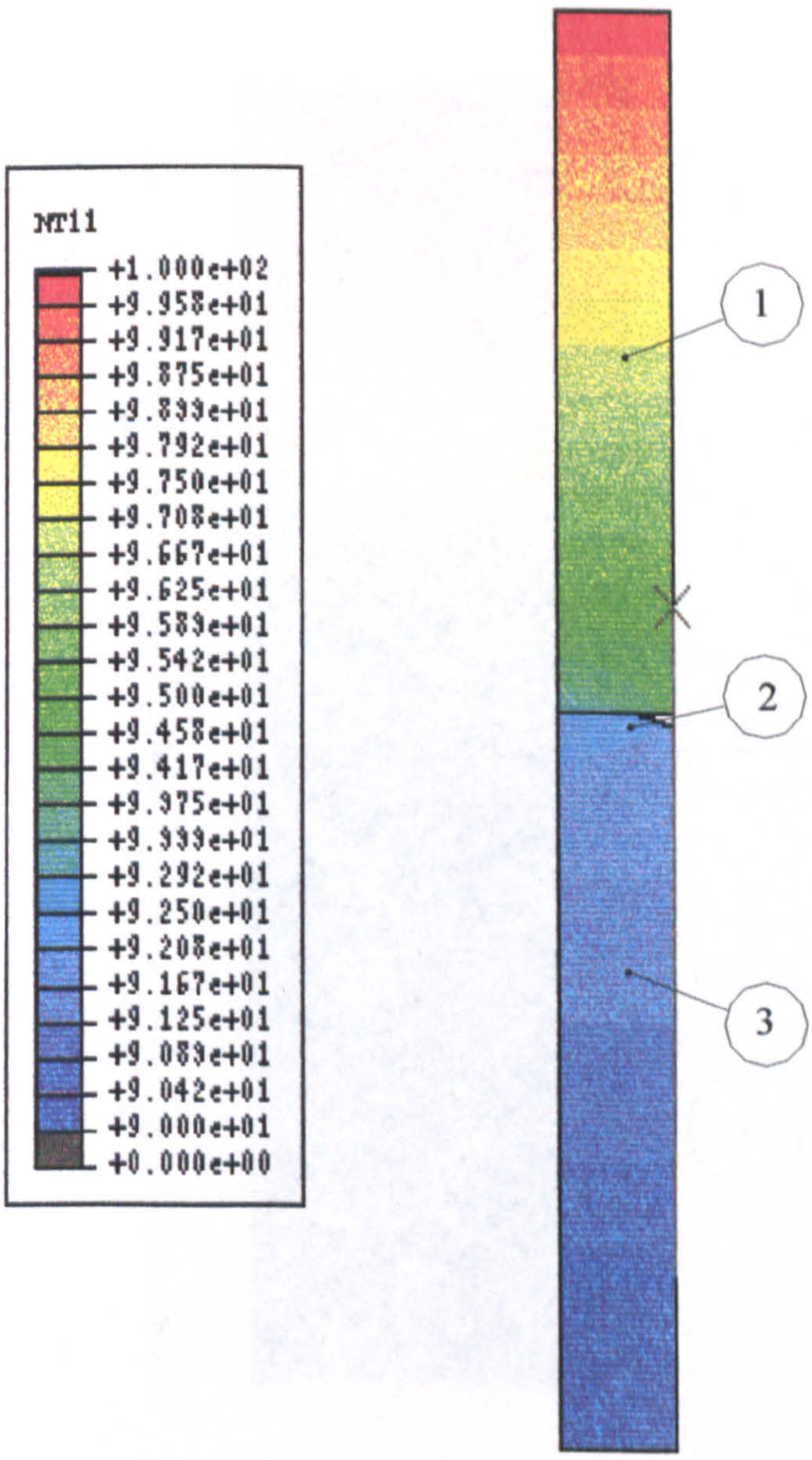

1. Tool;
2. Equivalent asperity of the specimen;
3. Specimen substrate

Fig. 5.13 Temperature distribution of tool, specimen and near the interface

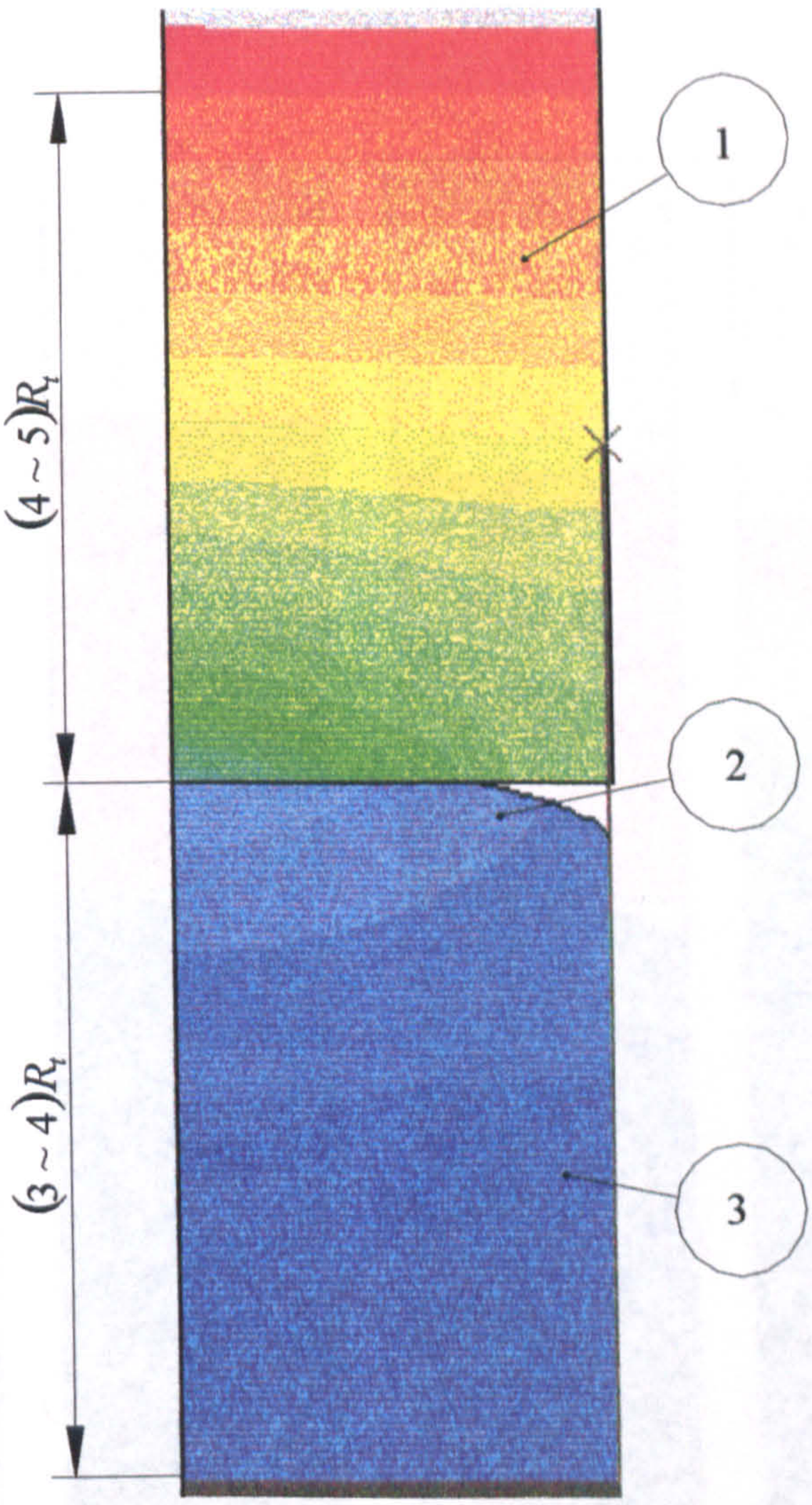

1. Tool;
2. Equivalent asperity in thermal-mechanical contact;
3. Substrate of specimen

Fig. 5.14 Local temperature distribution near the contact interface

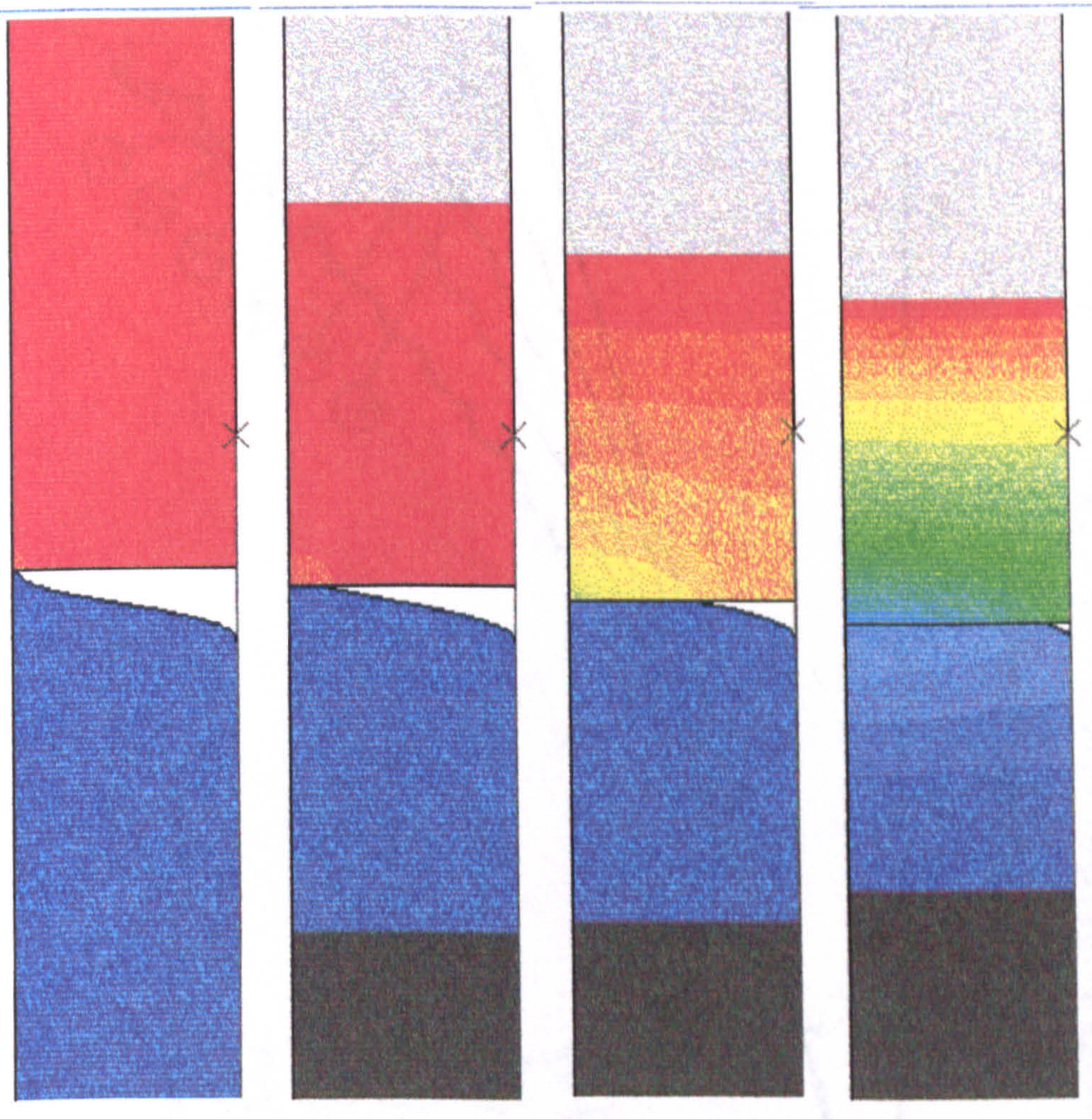

Fig. 5.15 Variation of the temperature disordered area
to different interfacial pressures

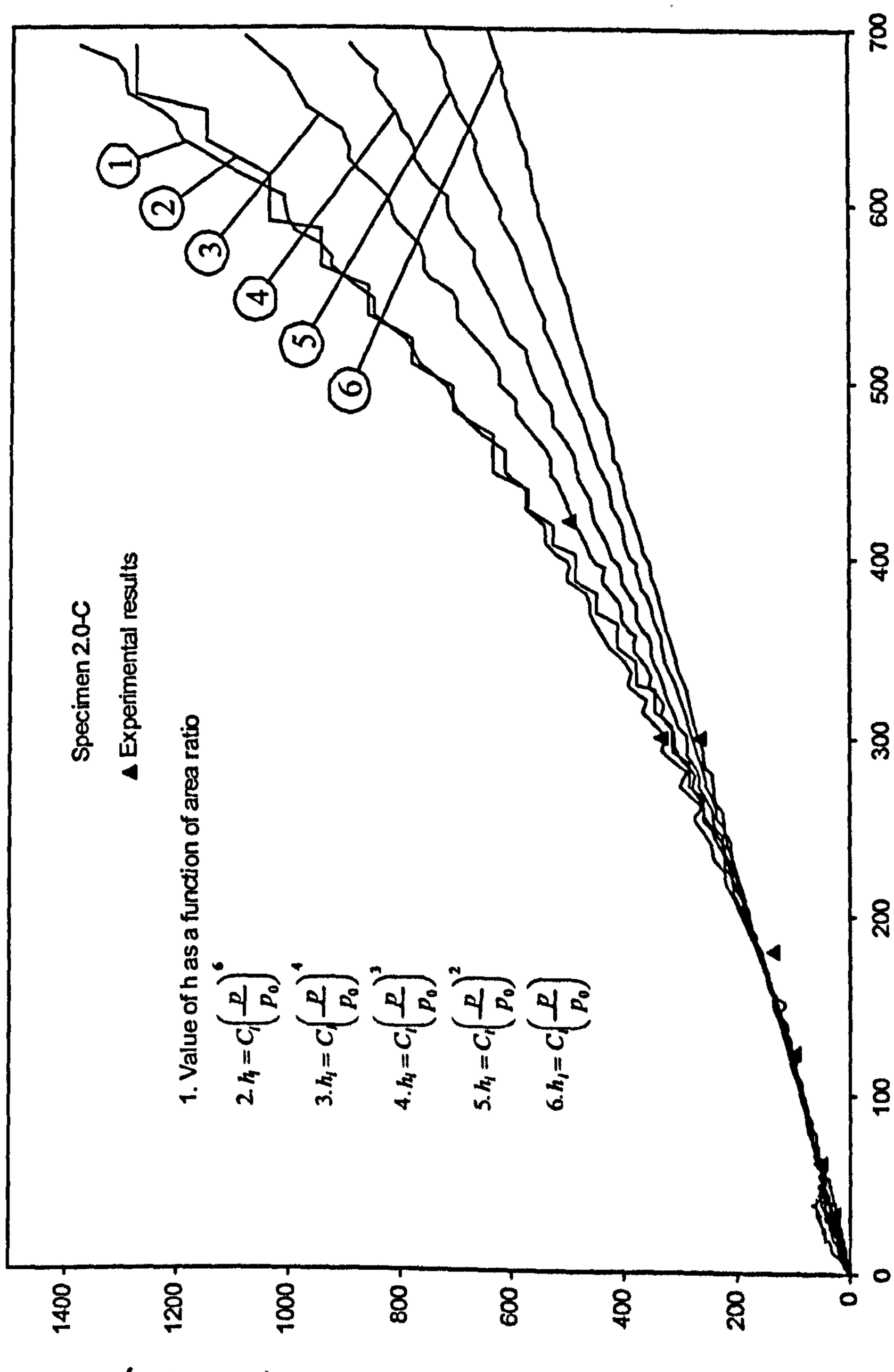

Fig. 5.16 Value of h derived from simulation using different thermal models

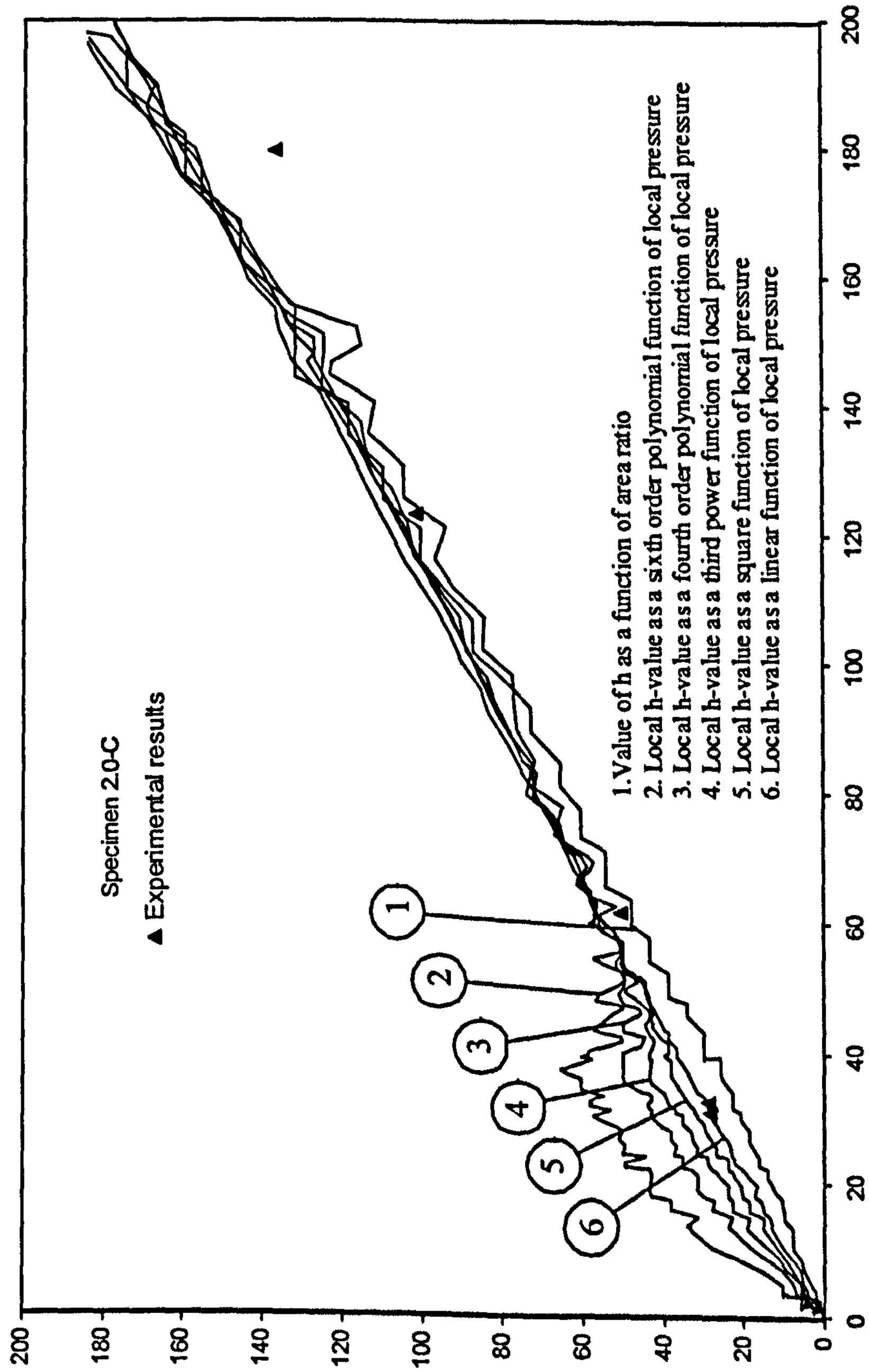

Fig. 5.17 Determination of parameters of local thermal model

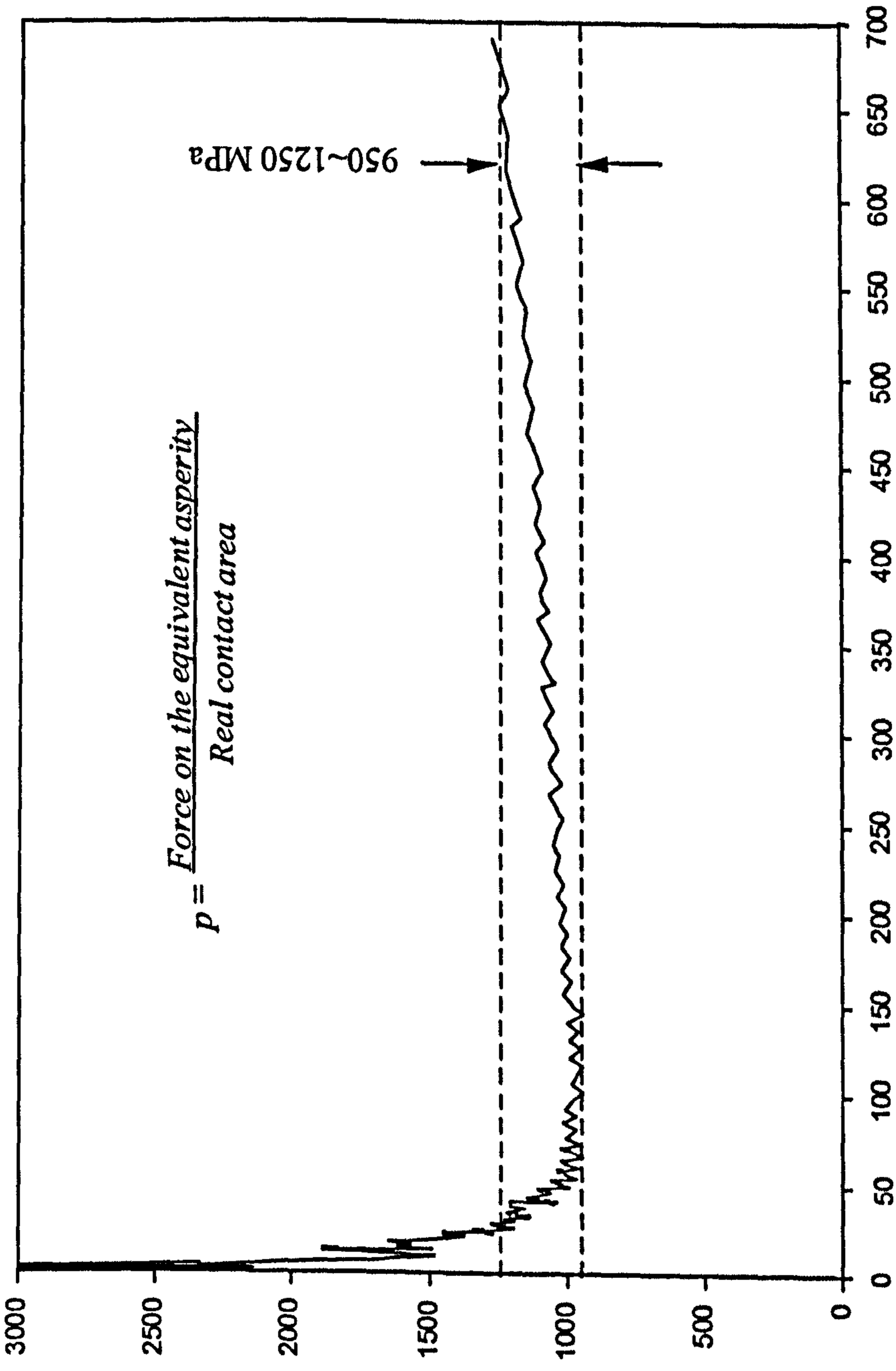

Fig. 5.18 Mean local interfacial pressure distribution

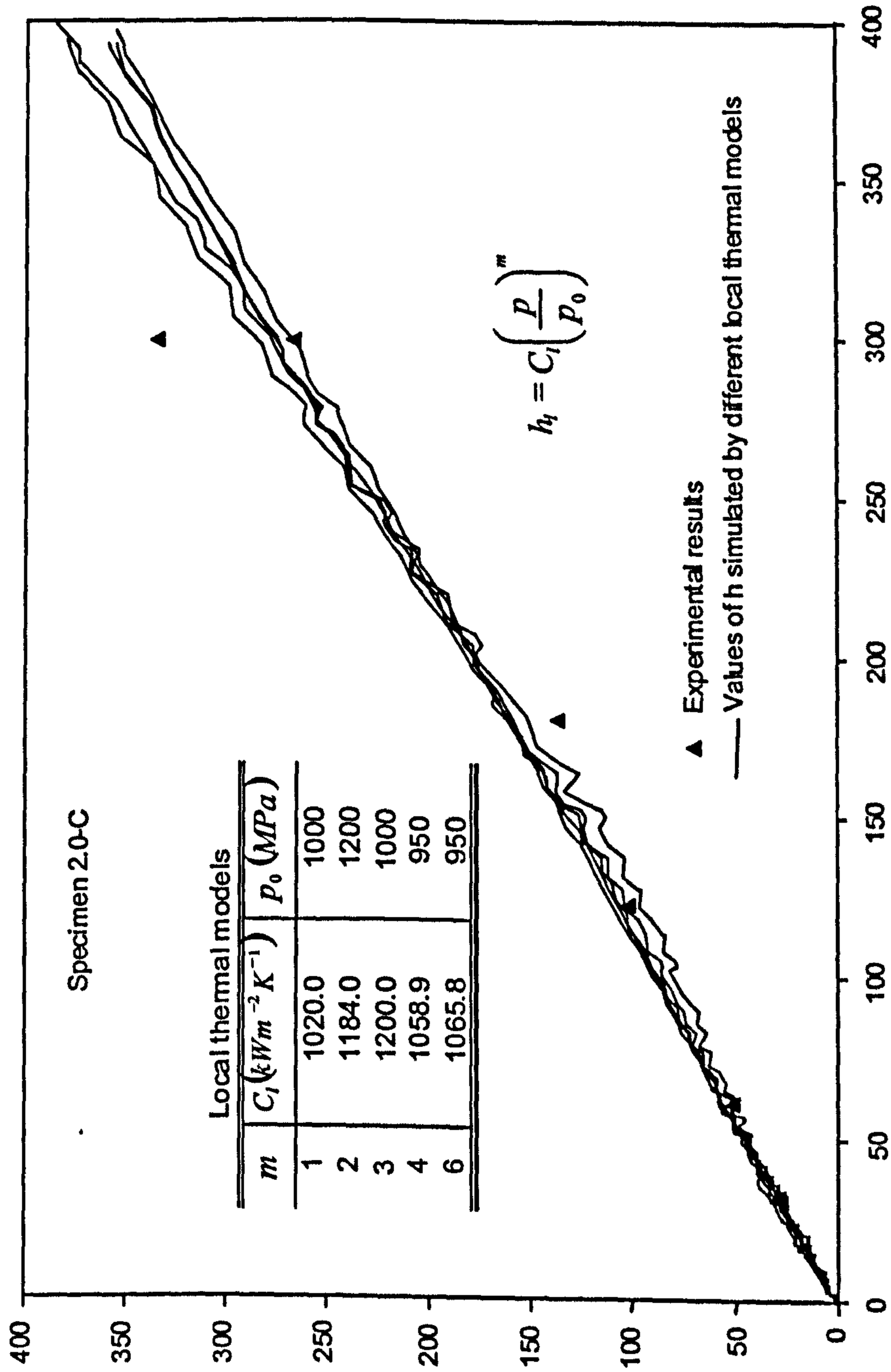

Fig. 5.19 Values of h for different local thermal models

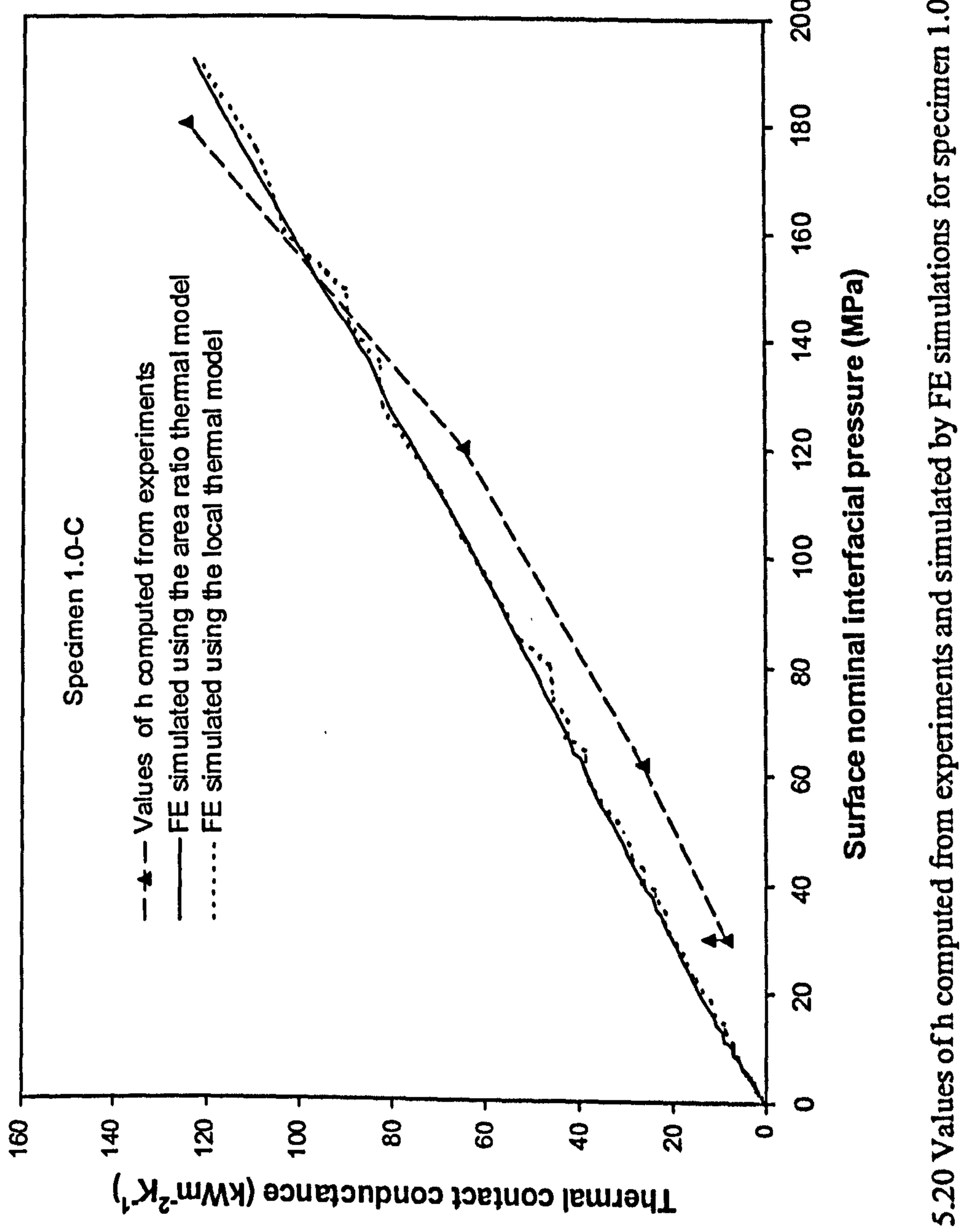

Fig. 5.20 Values of h computed from experiments and simulated by FE simulations for specimen 1.0-C

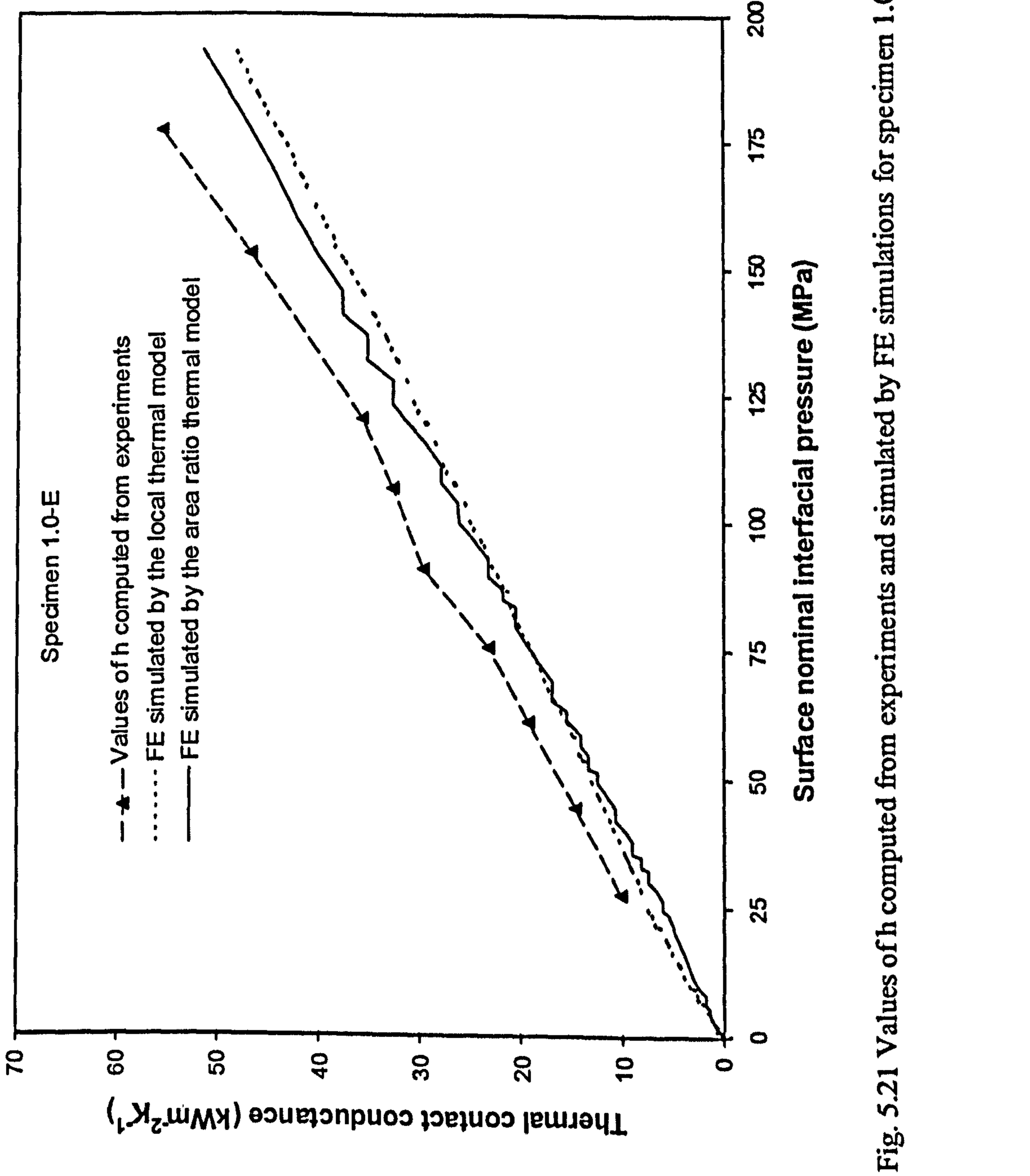

Fig. 5.21 Values of h computed from experiments and simulated by FE simulations for specimen 1.0-E

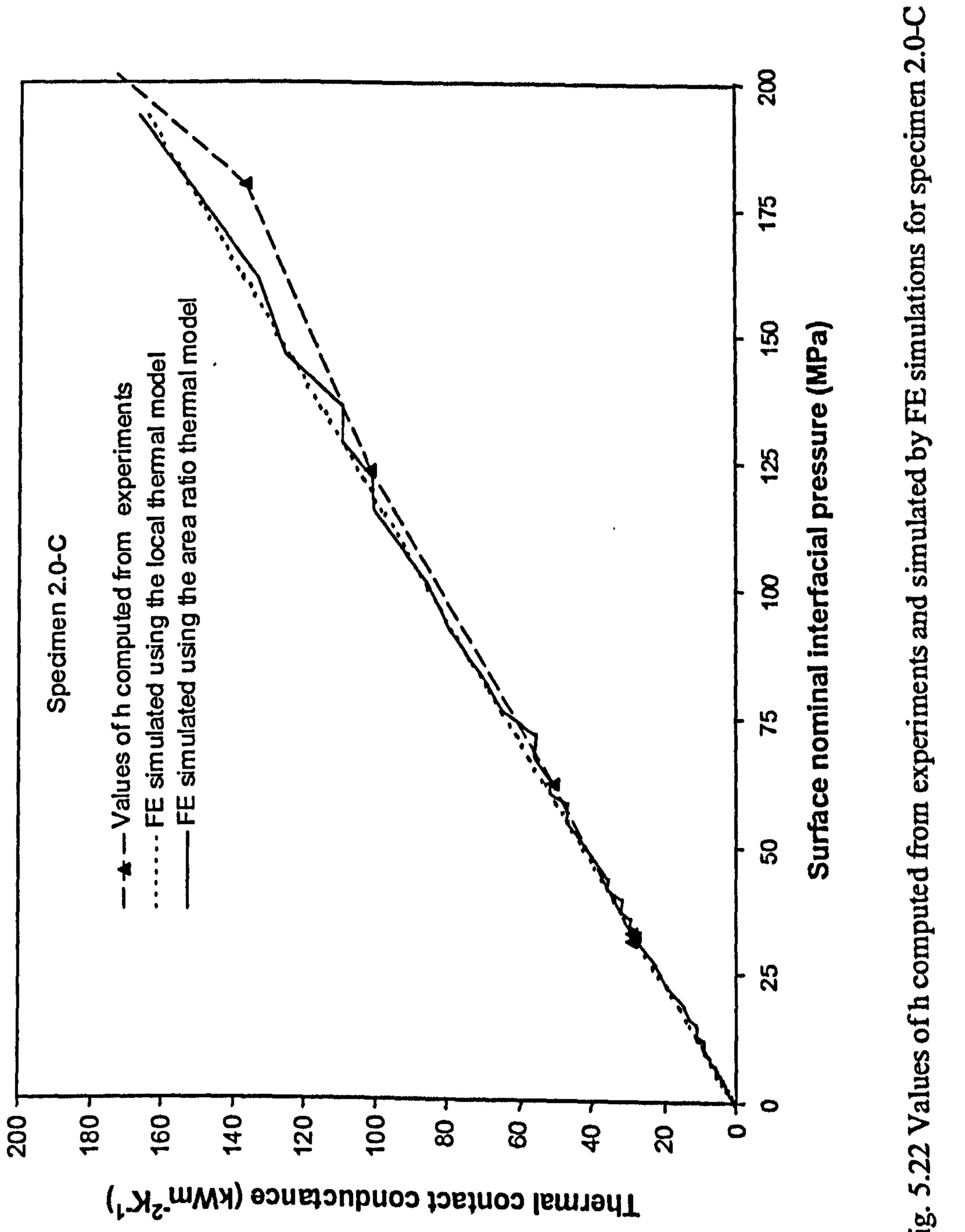

Fig. 5.22 Values of h computed from experiments and simulated by FE simulations for specimen 2.0-C

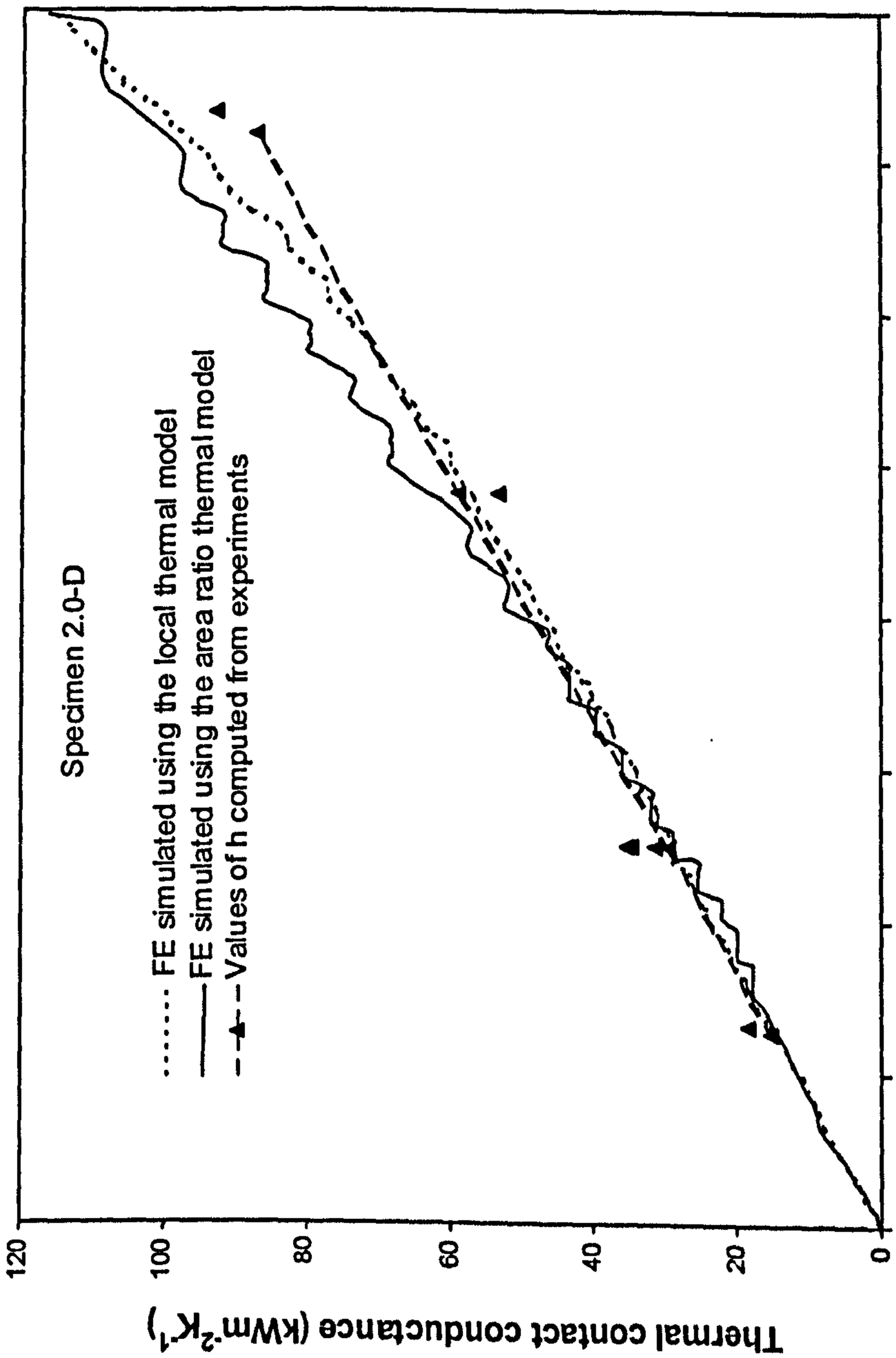

Fig. 5.23 Values of h computed from experiments and simulated by FE simulations for specimen 2.0-D

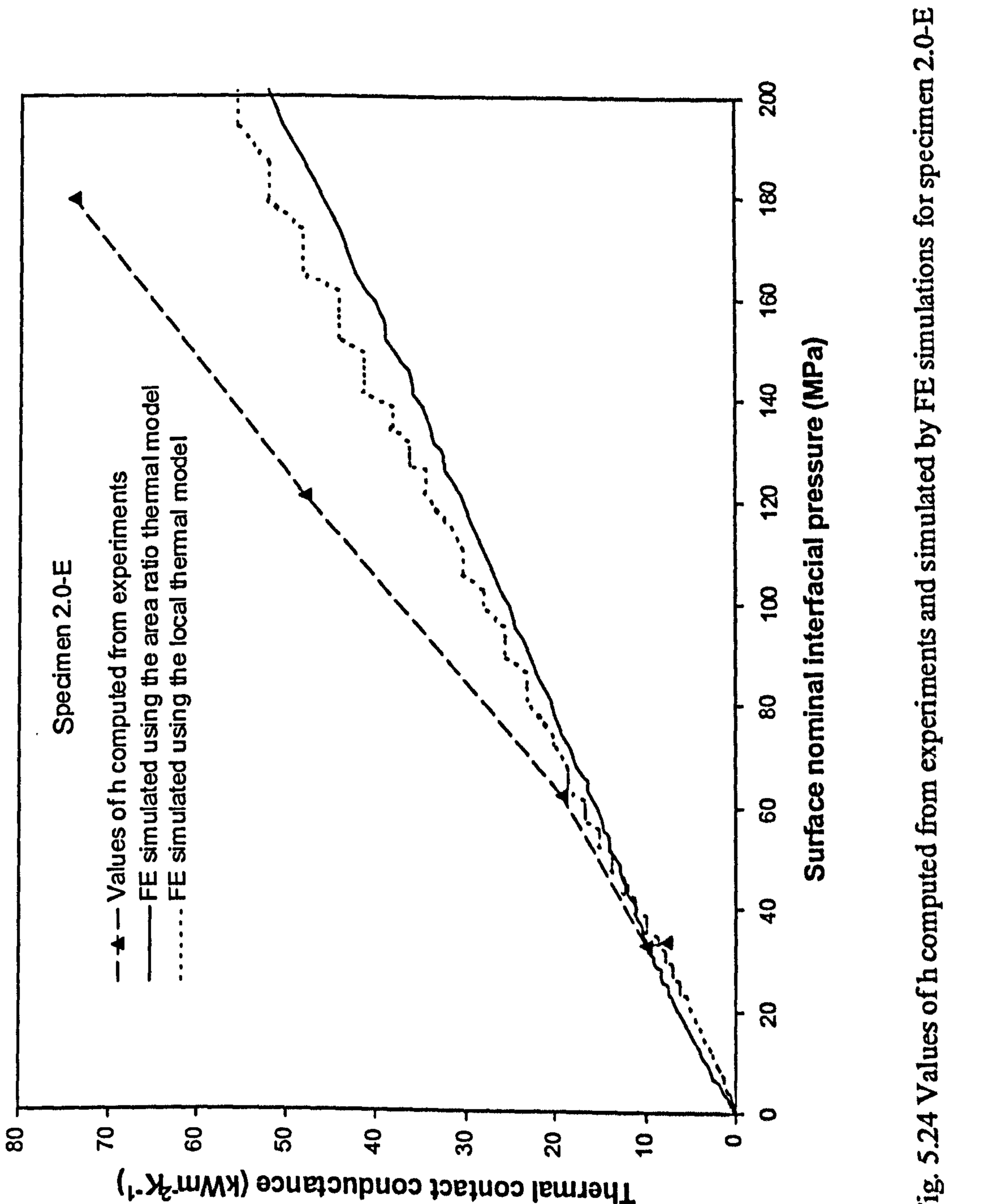

Fig. 5.24 Values of h computed from experiments and simulated by FE simulations for specimen 2.0-E

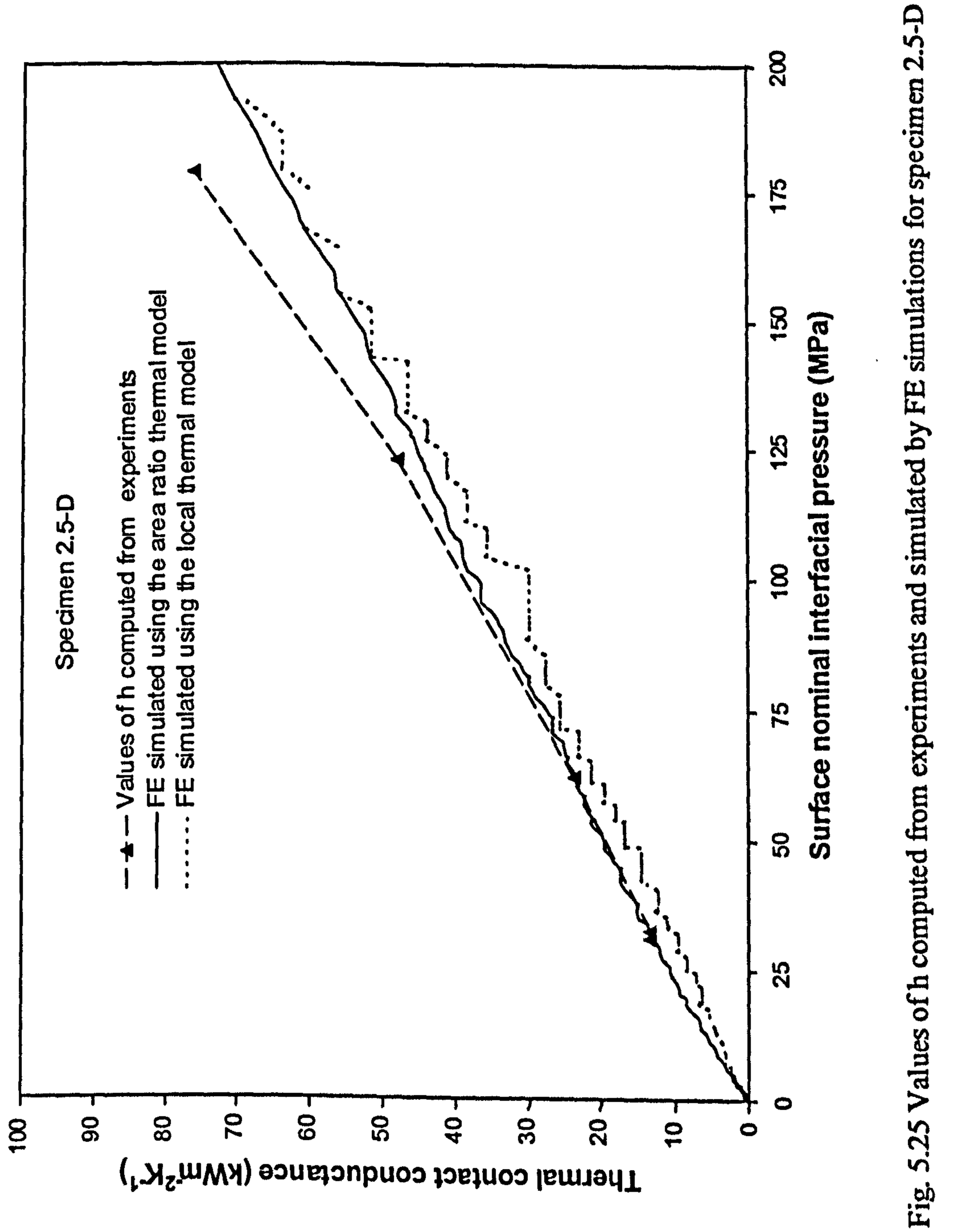

Fig. 5.25 Values of h computed from experiments and simulated by FE simulations for specimen 2.5-D

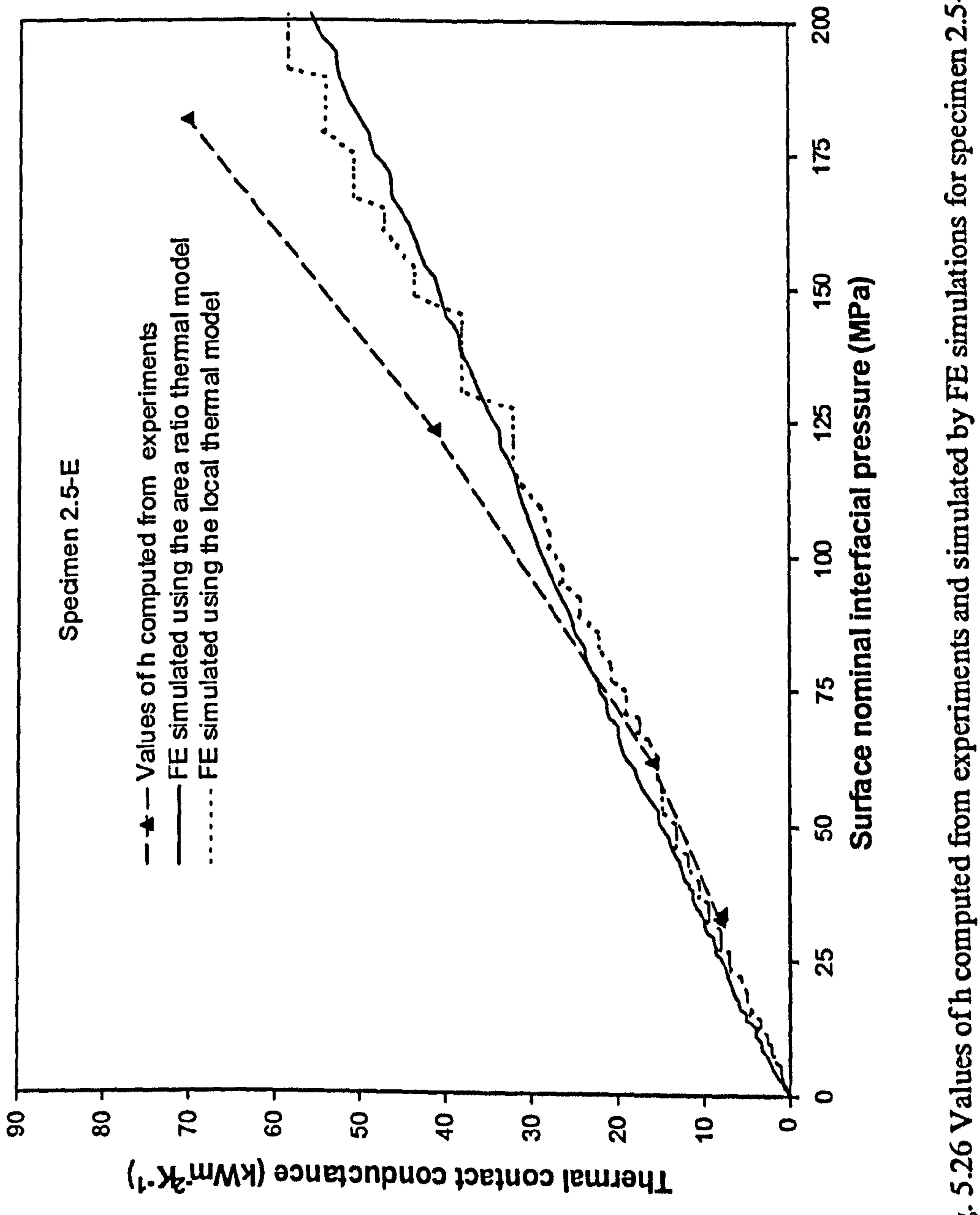

Fig. 5.26 Values of h computed from experiments and simulated by FE simulations for specimen 2.5-E

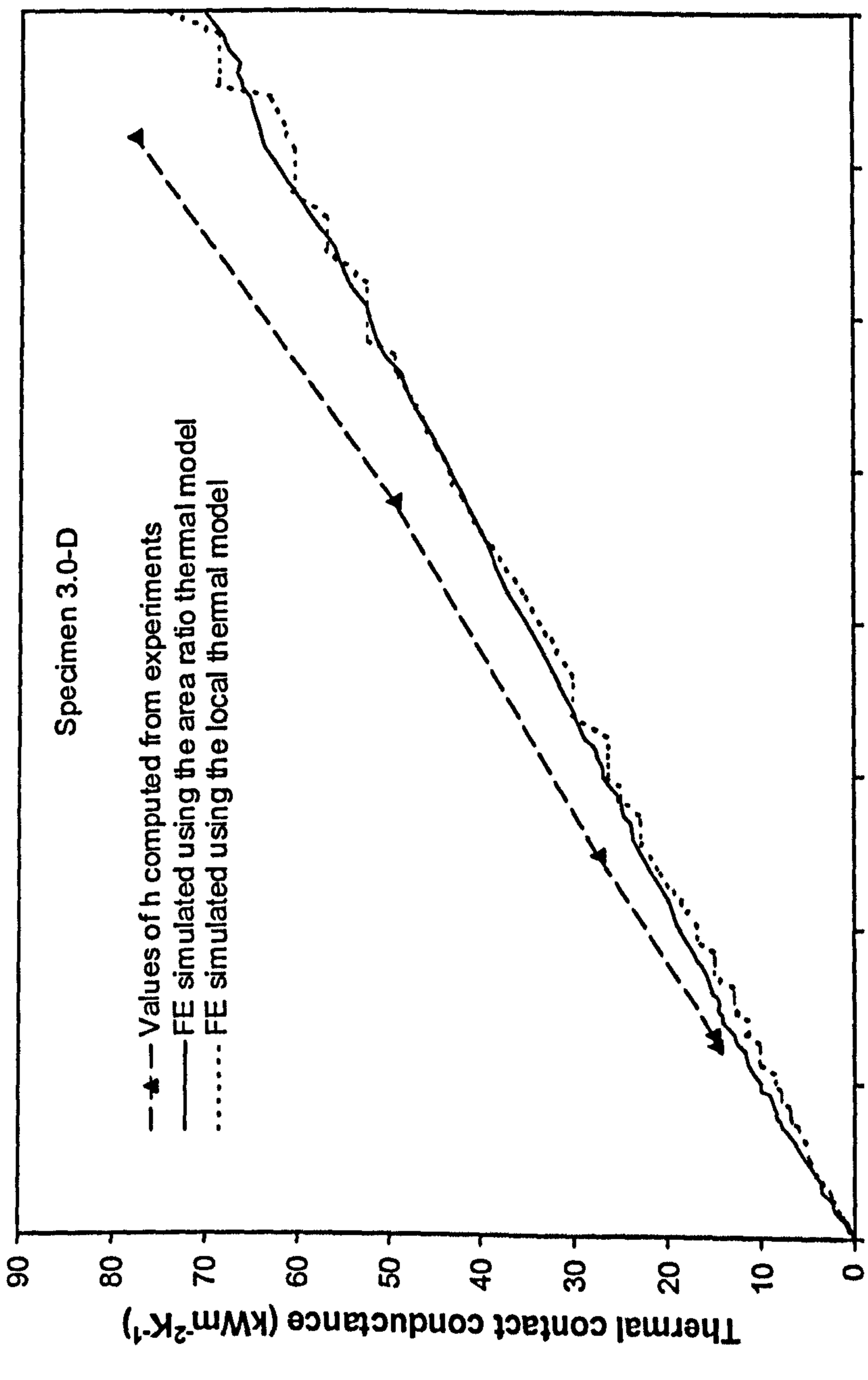

Fig. 5.27 Values of h computed from experiments and simulated by FE simulations for specimen 3.0-D

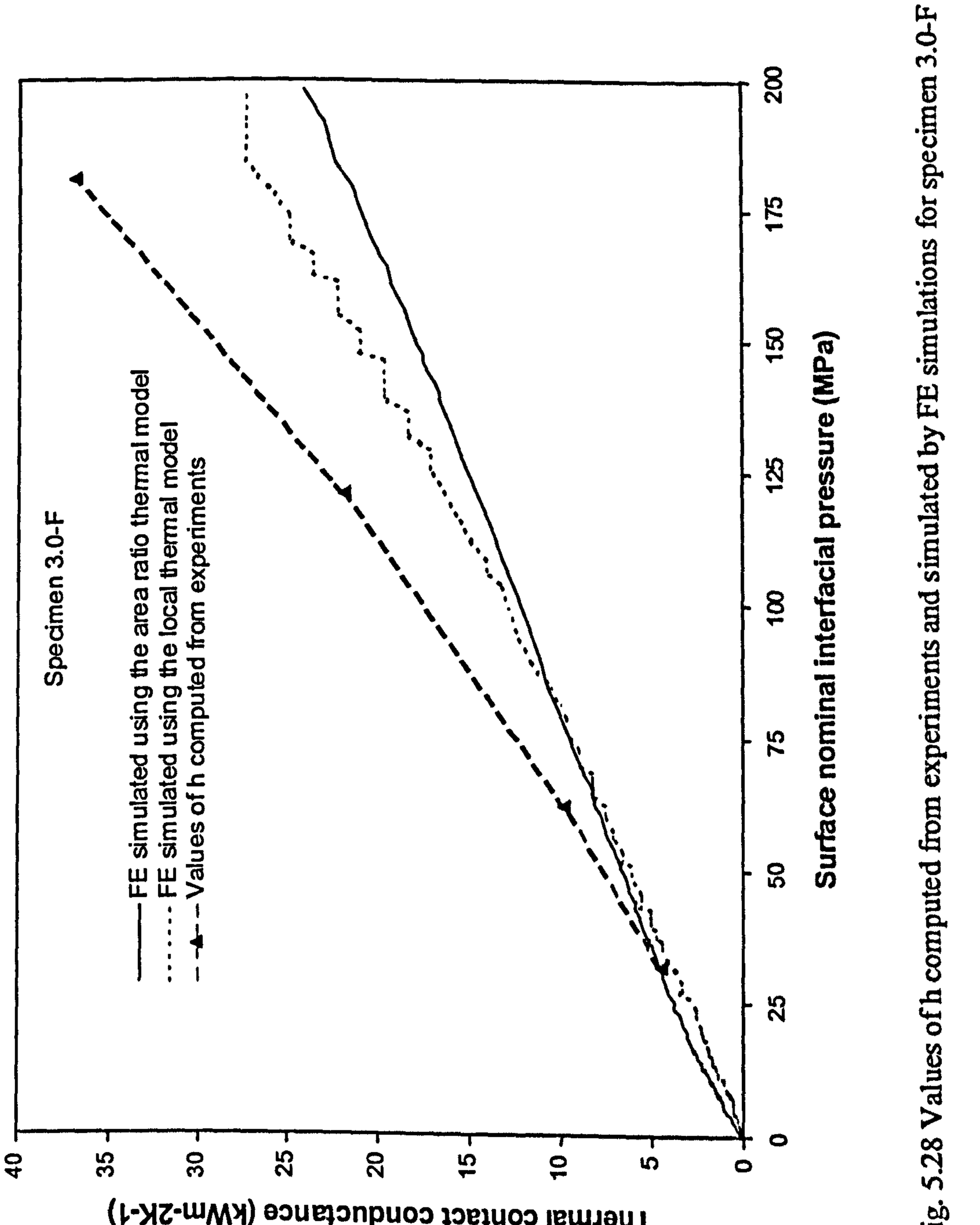

Fig. 5.28 Values of h computed from experiments and simulated by FE simulations for specimen 3.0-F

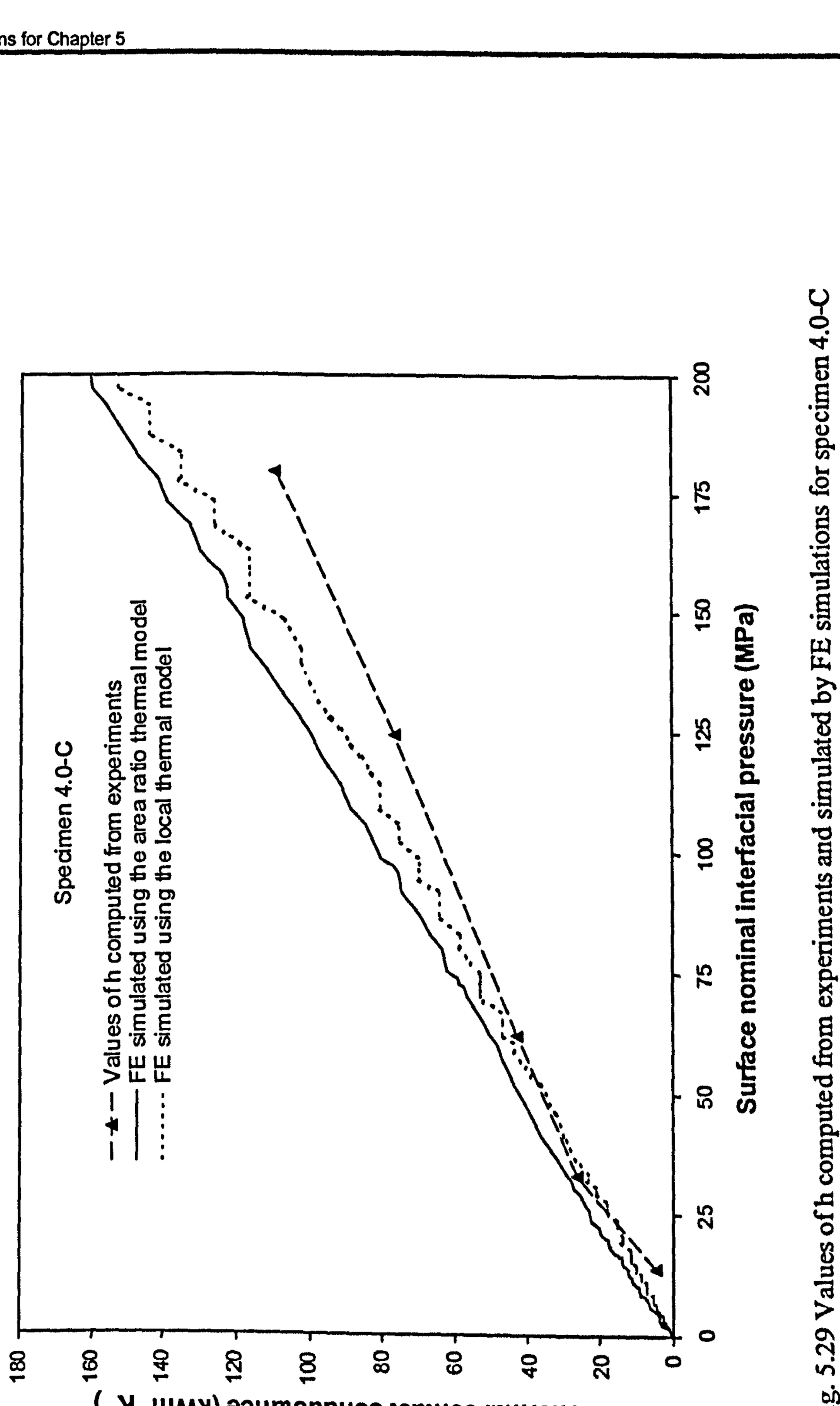

Fig. 5.29 Values of h computed from experiments and simulated by FE simulations for specimen 4.0-C

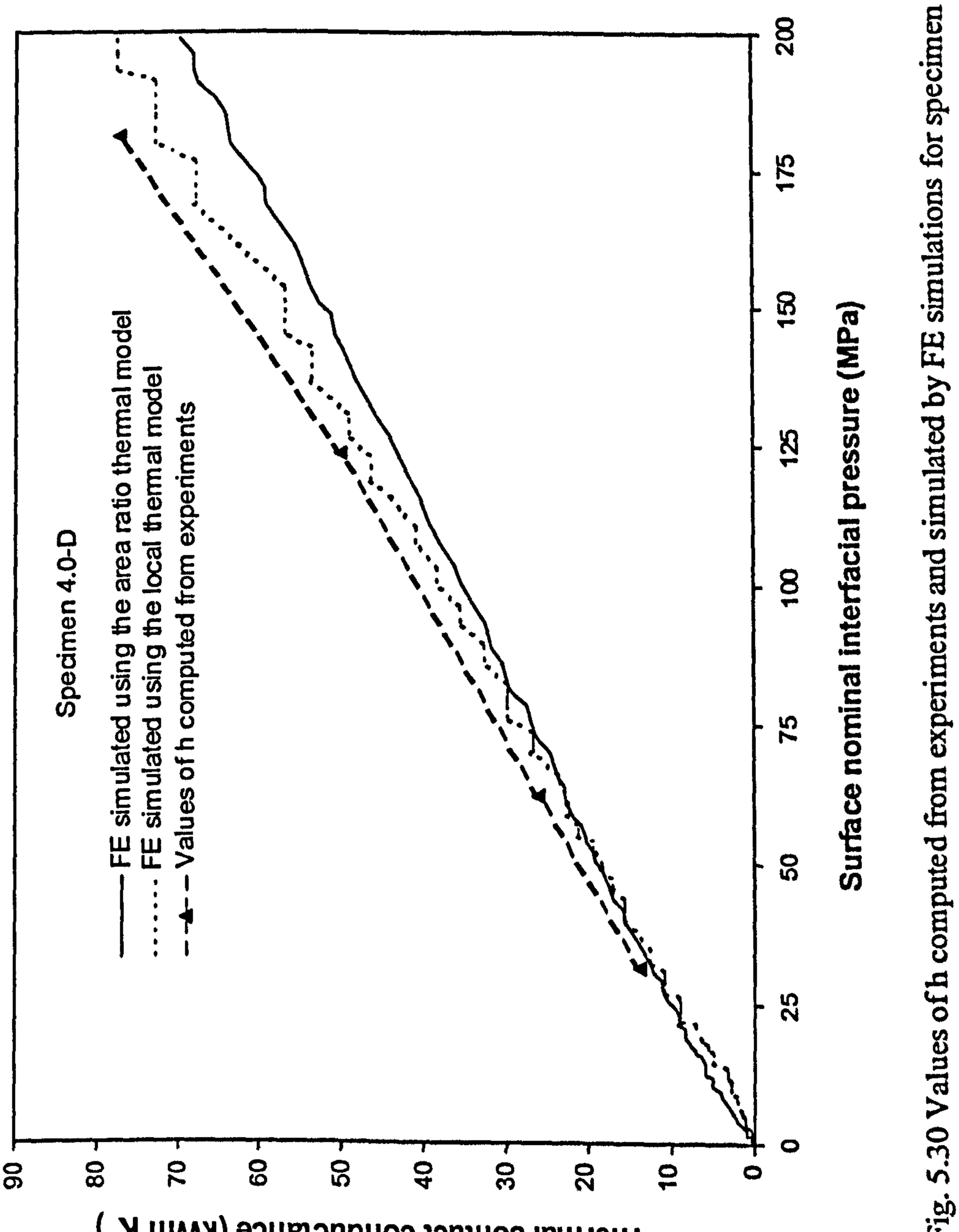

Fig. 5.30 Values of h computed from experiments and simulated by FE simulations for specimen 4.0-C

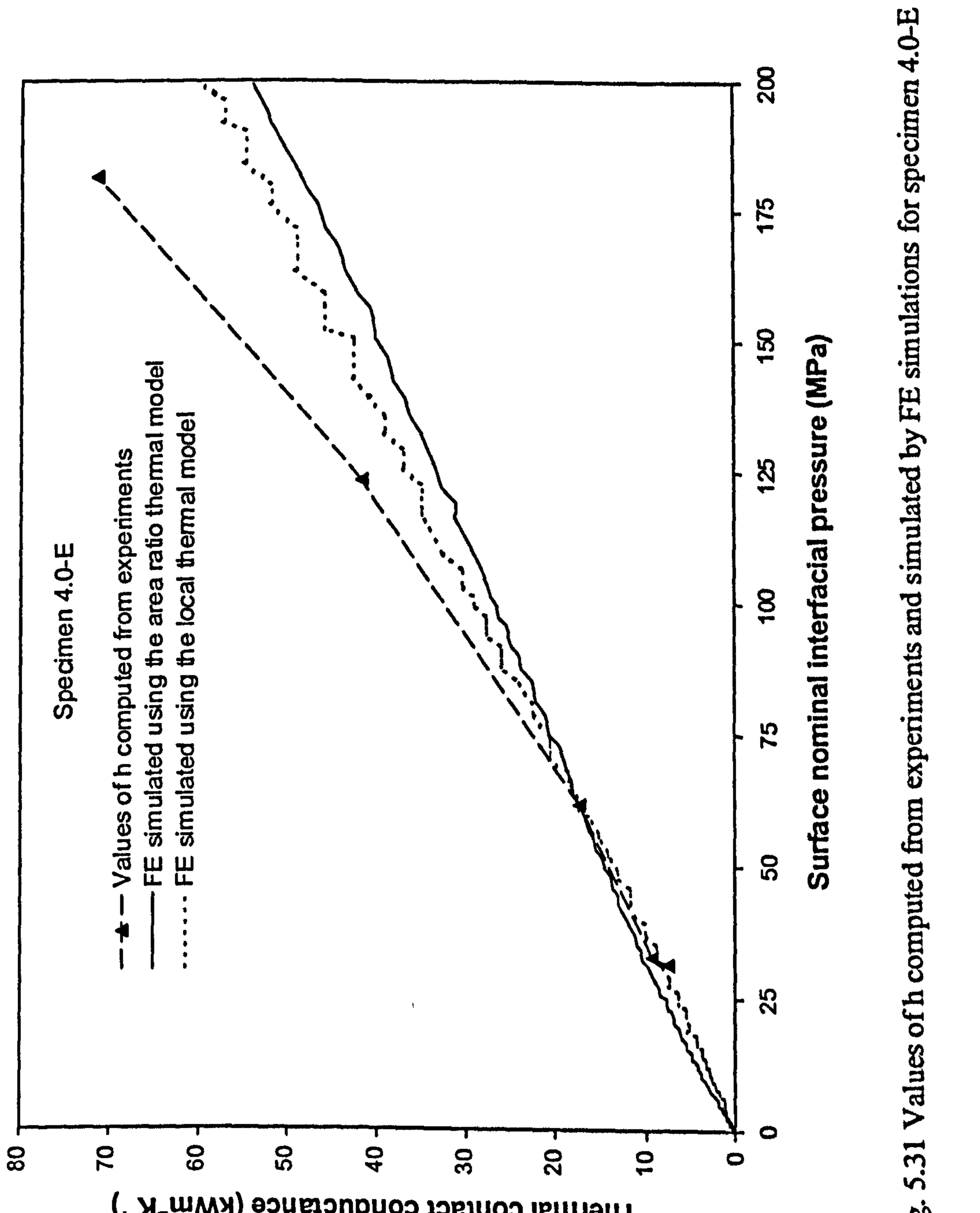

Fig. 5.31 Values of h computed from experiments and simulated by FE simulations for specimen 4.0-E

Diagrams for Chapter Six

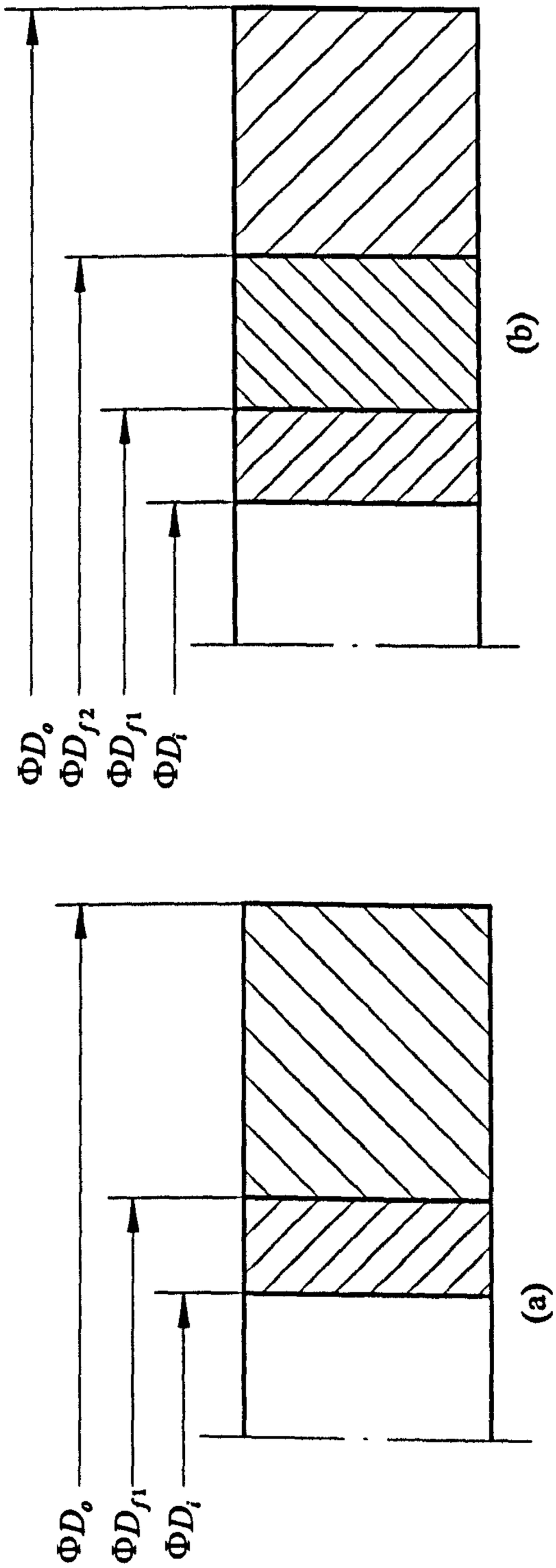

ΦD_o : Outside diameter of die container

ΦD_{f2}: Nominal diameter of outside shrink-fitting surface

ΦD_{f1}: Nominal diameter of inside shrink-fitting surface

ΦD_i : Inside diameter of insert

Fig. 6.1 Diagram of shrink-fitting dies

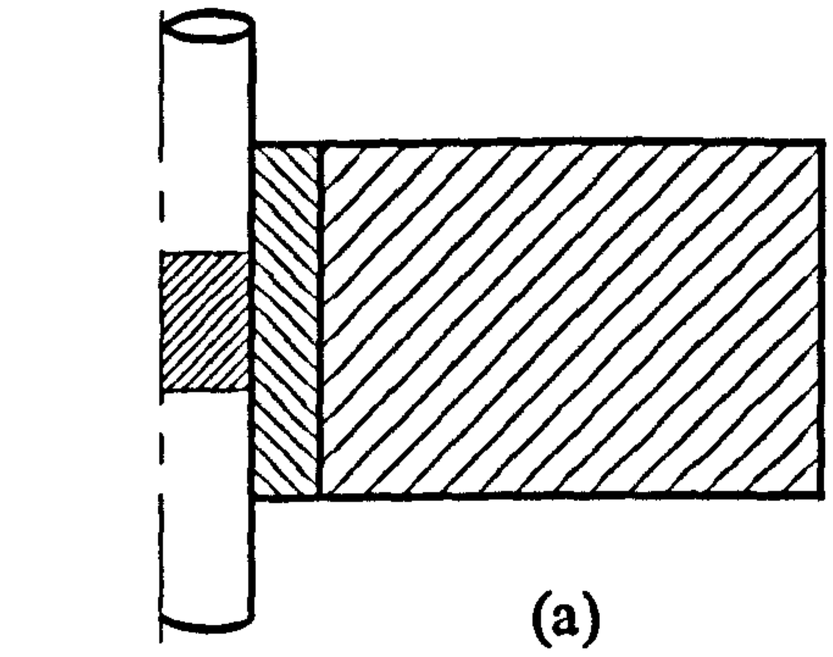

(a)

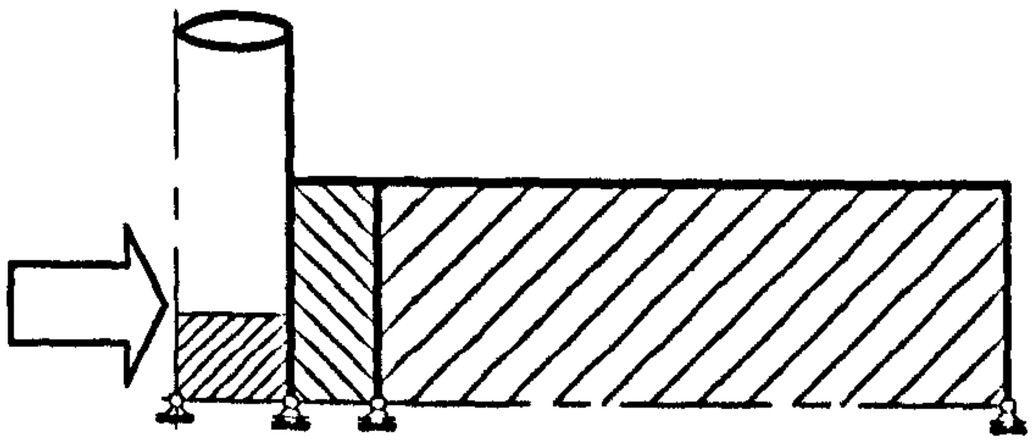

(b)

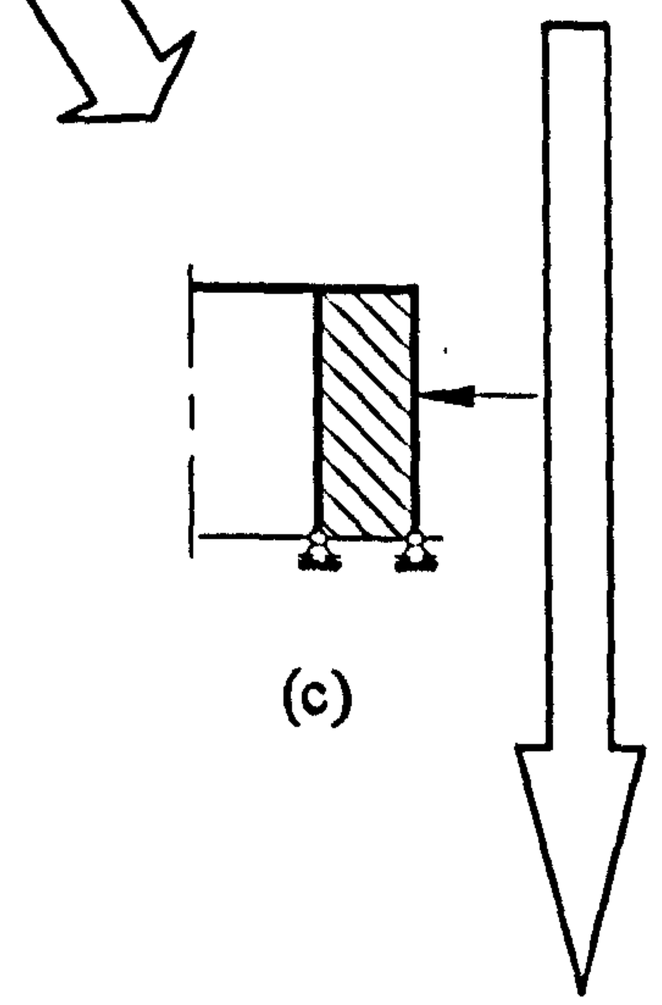

(c)

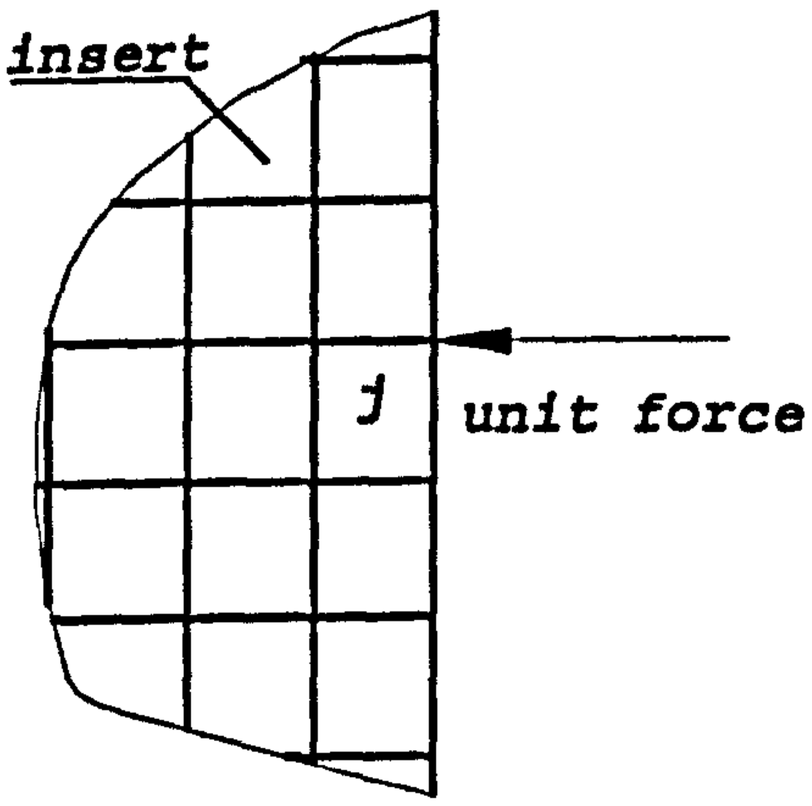

(e)

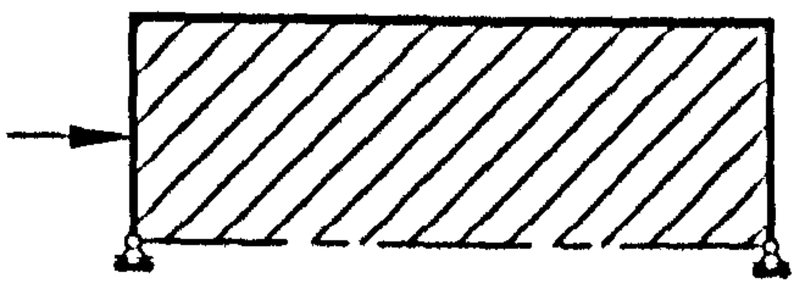

(d)

Fig. 6.2 Unit force method

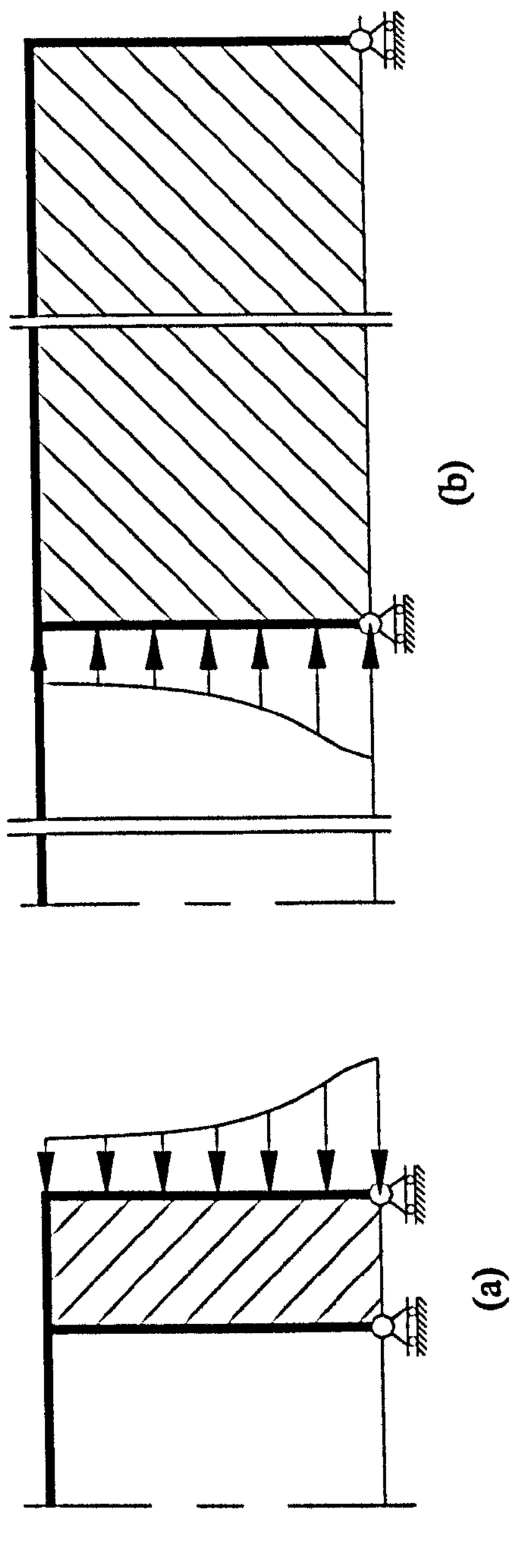

Fig. 6.3 Shrink-fitting mechanics models

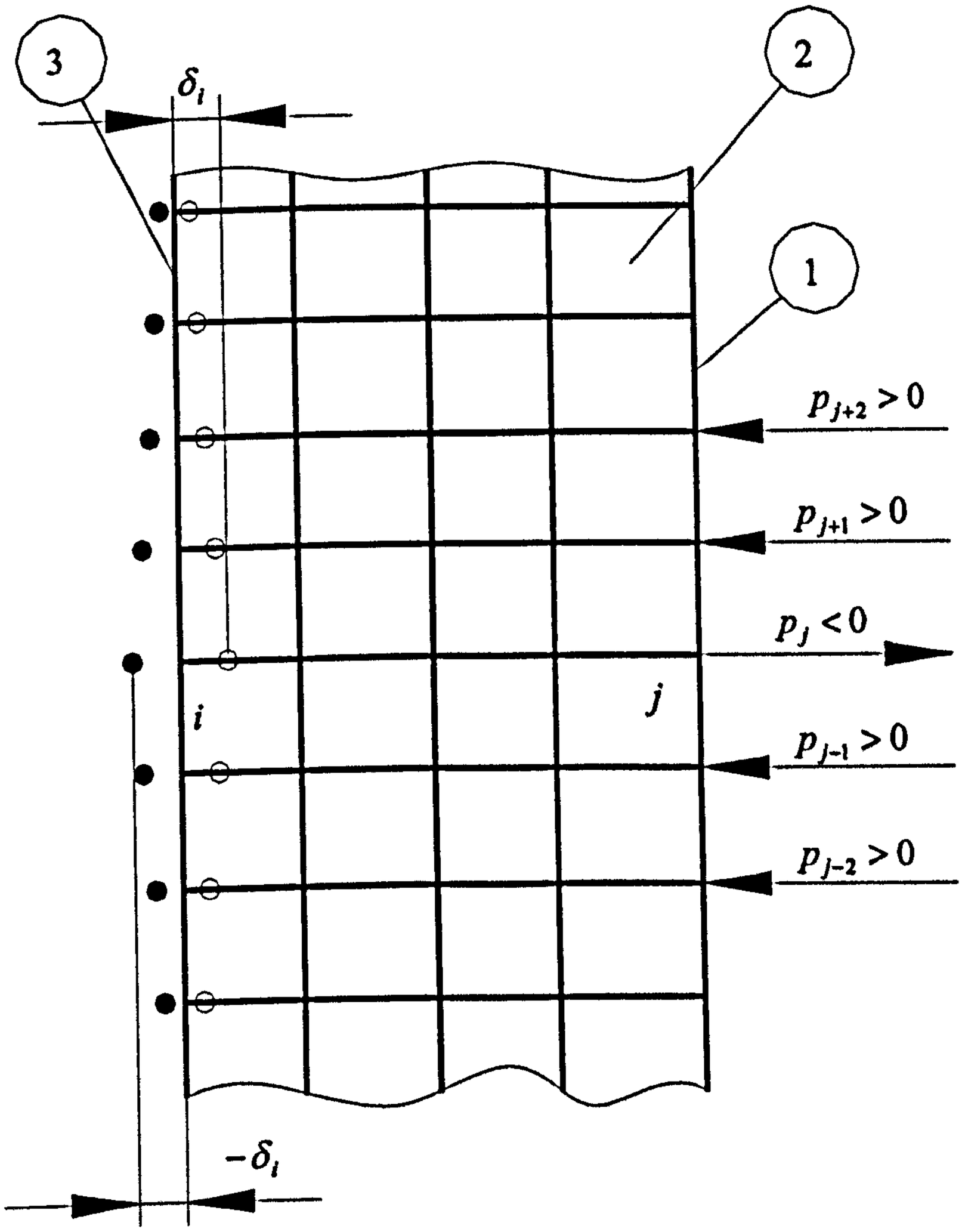

○ : The actual die deflection

● : The required pre-deflection

1. Insert shrink-fitting surface
2. Insert
3. Die surface

Fig. 6.4 Iteration for eliminating negative pressure

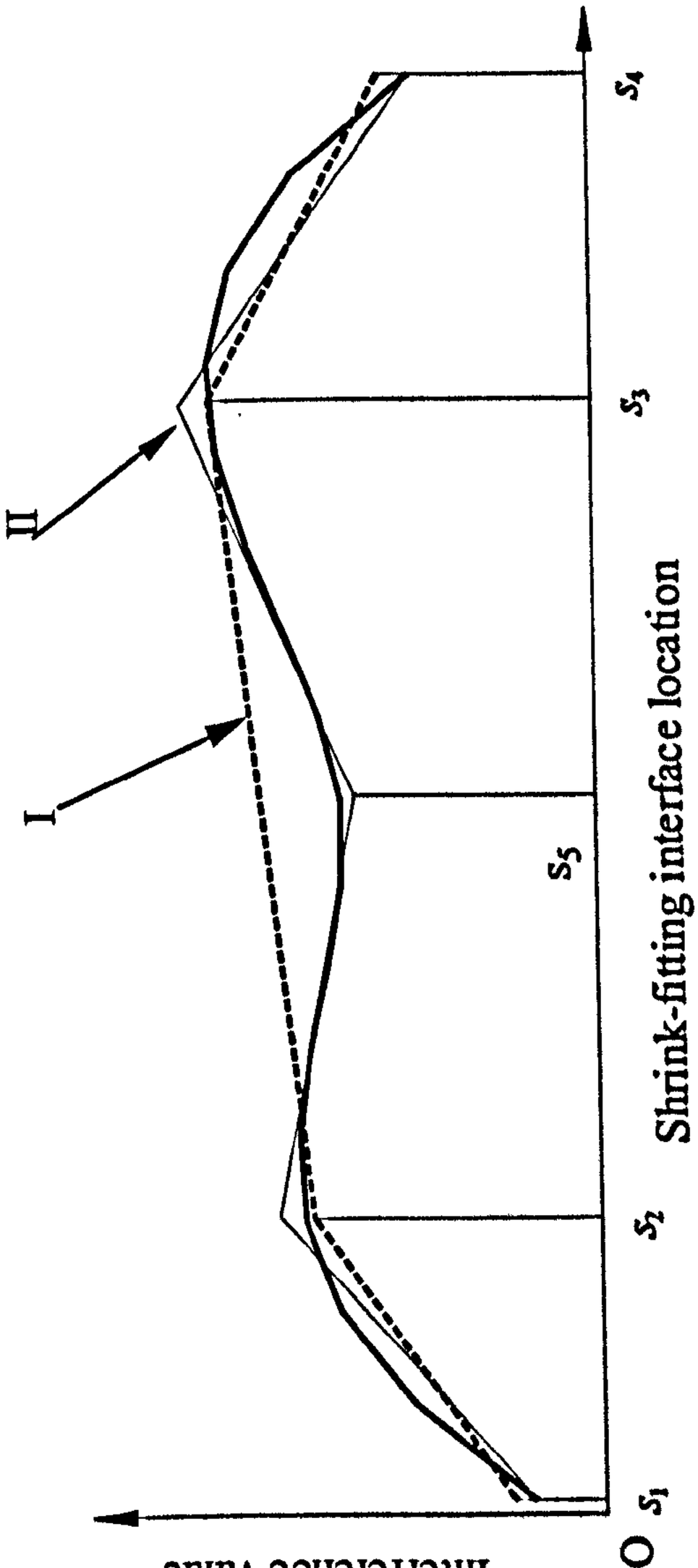

Solid line: General profiled interference
Dashed line: Linear profiled interference I
Thin solid line: Linear profiled interference II

Fig. 6.5 Linear profiled interference

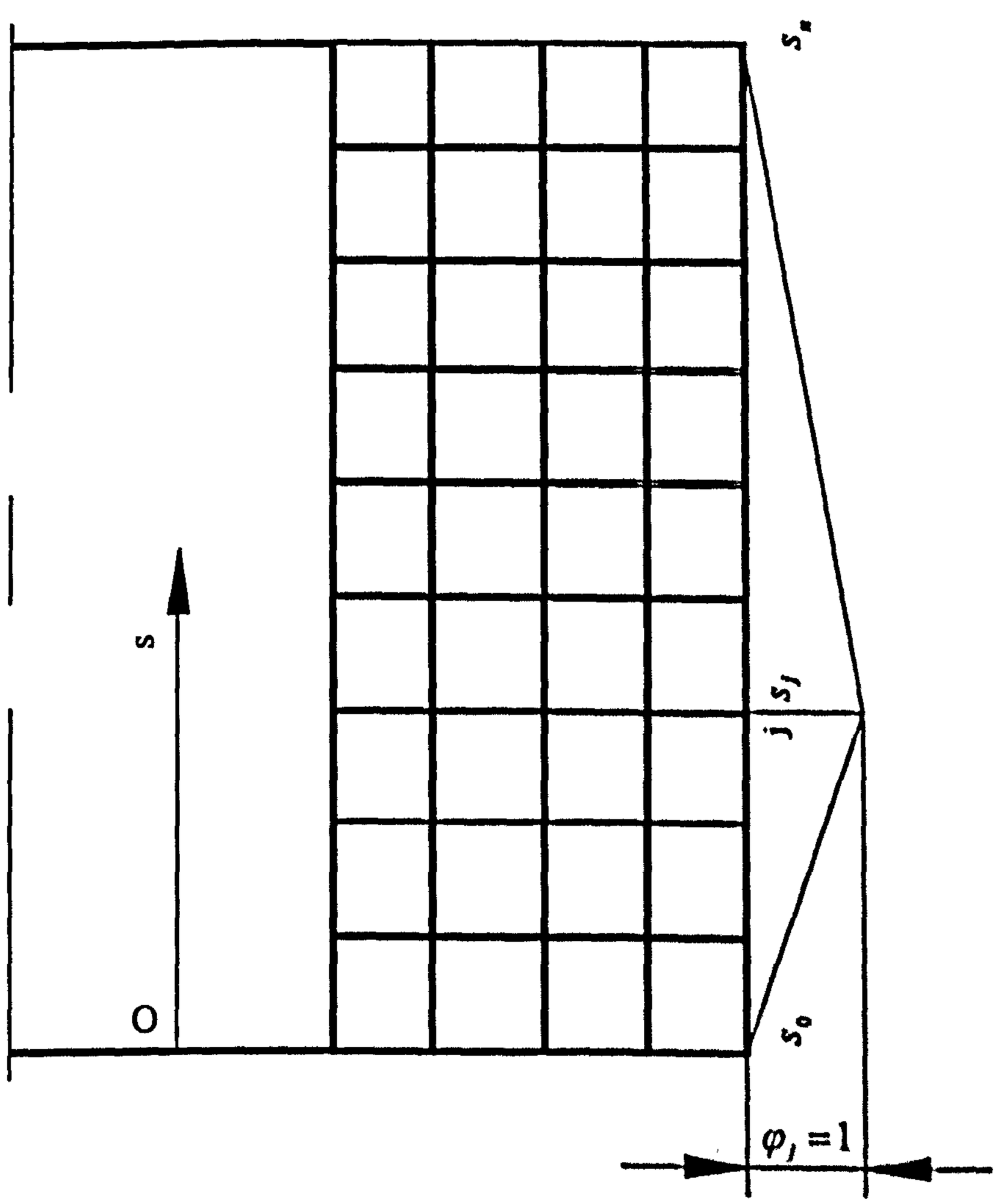

Fig. 6.6 Definition of unit interference

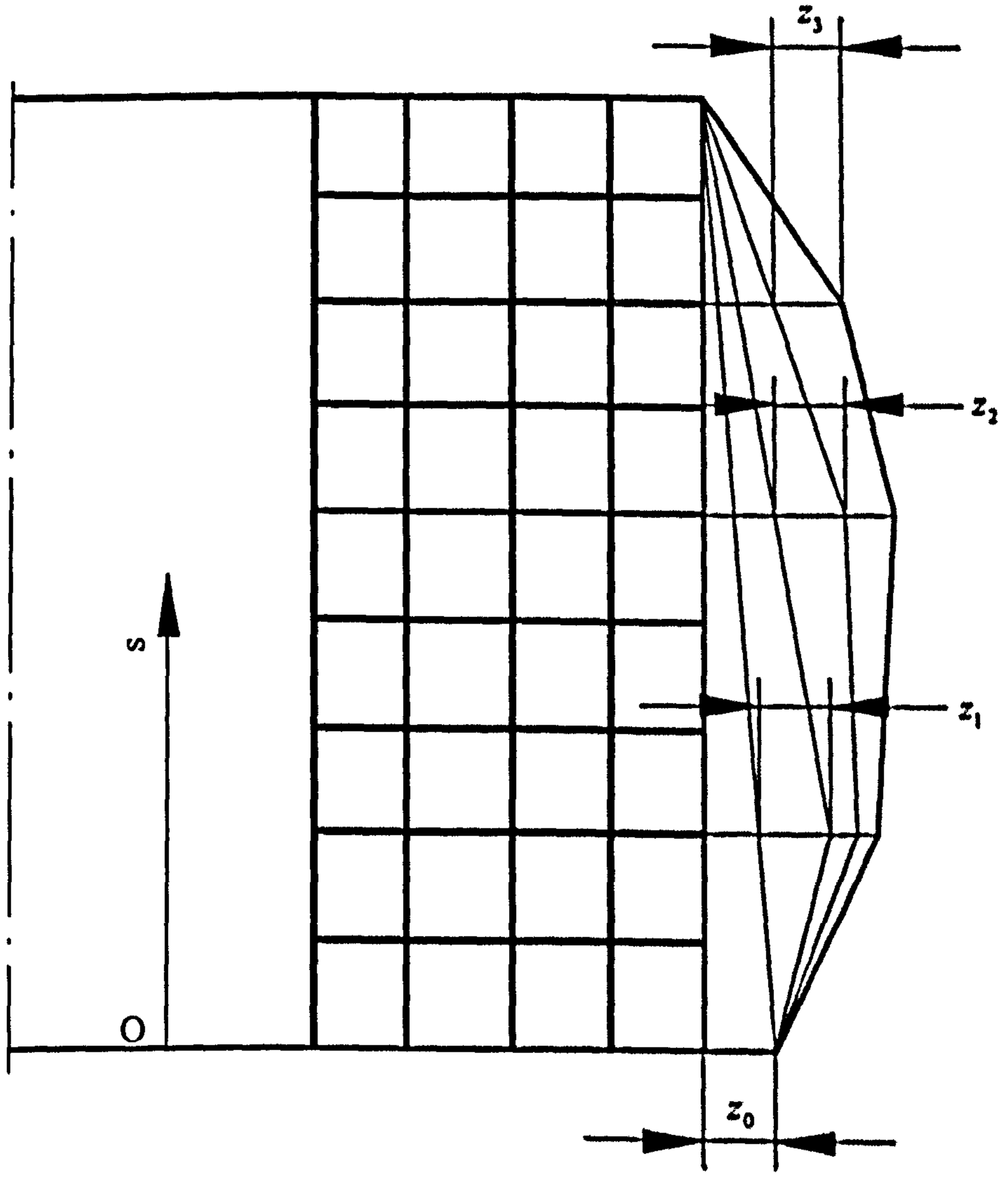

Fig.6.7 Linear superposition of independent interference

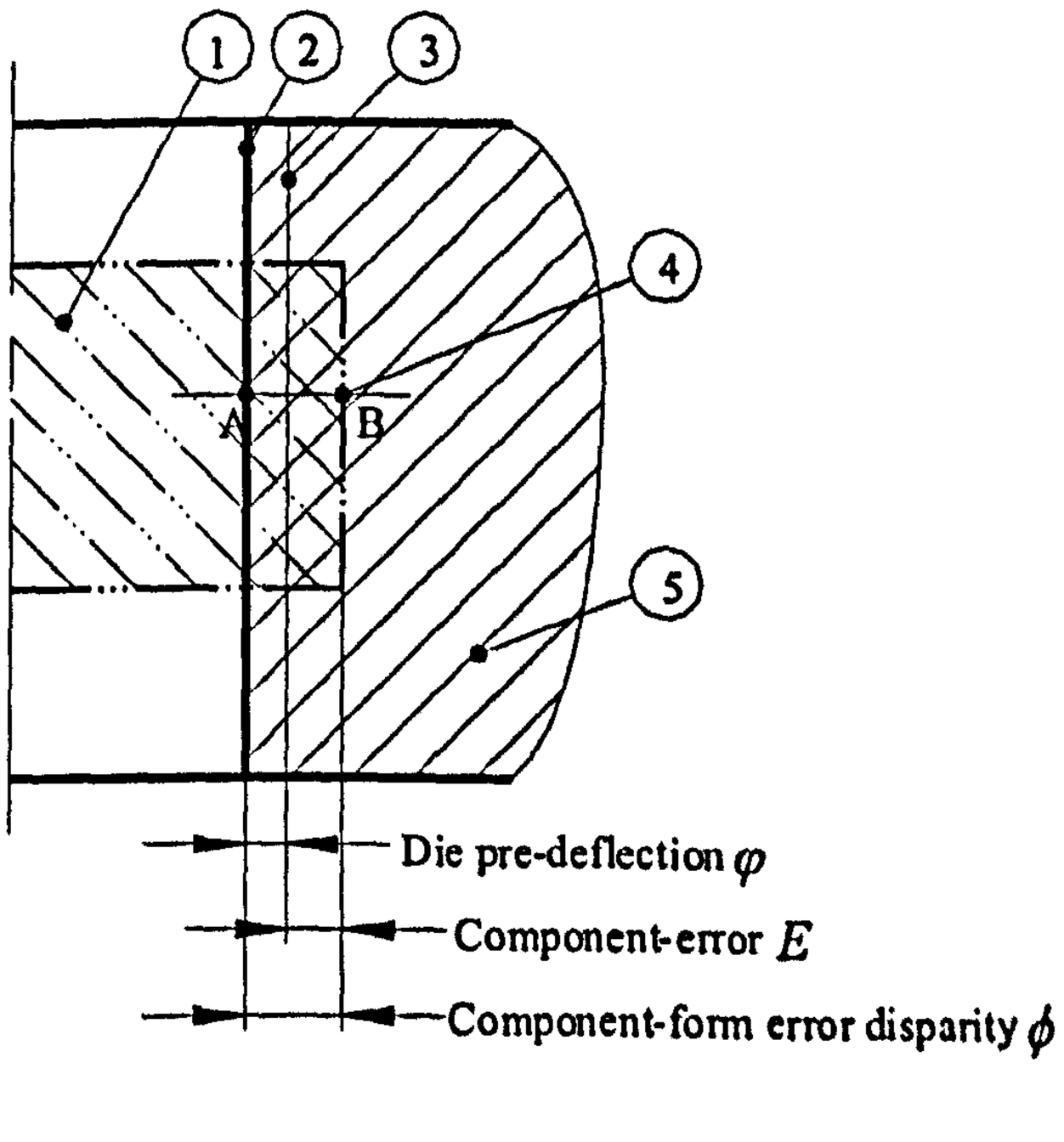

1. Component after ejection
2. Die surface after assembly of insert and stress-ring
3. Ideal/nominal die surface without compensation, or ideal component surface
4. Actual component surface
5. Die

Fig. 6.8 Geometric relation among predeflection, component-error and component dimensional disparity

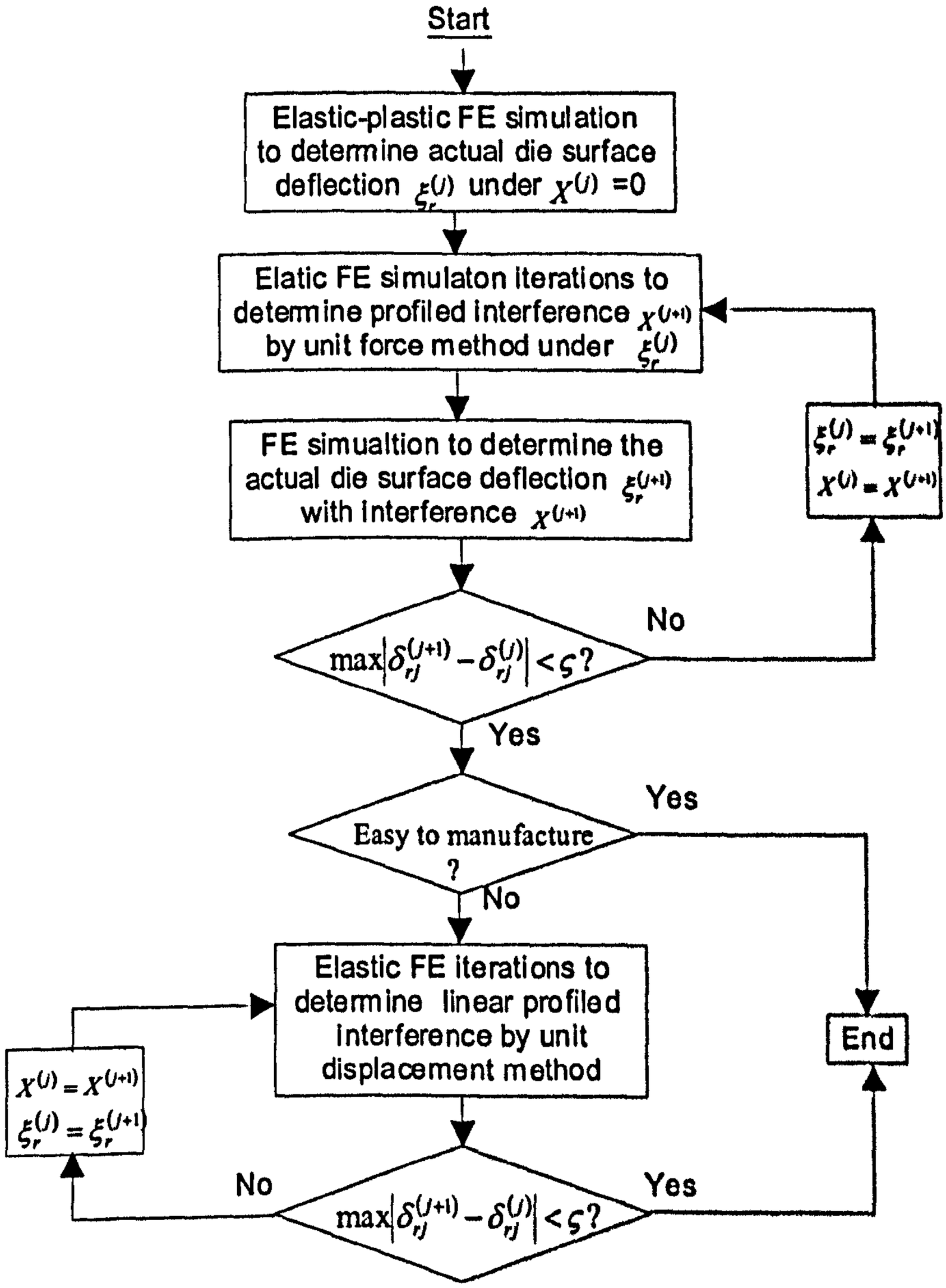

Fig. 6.9 Iteration for die elasticity compensation by shrink-fitting

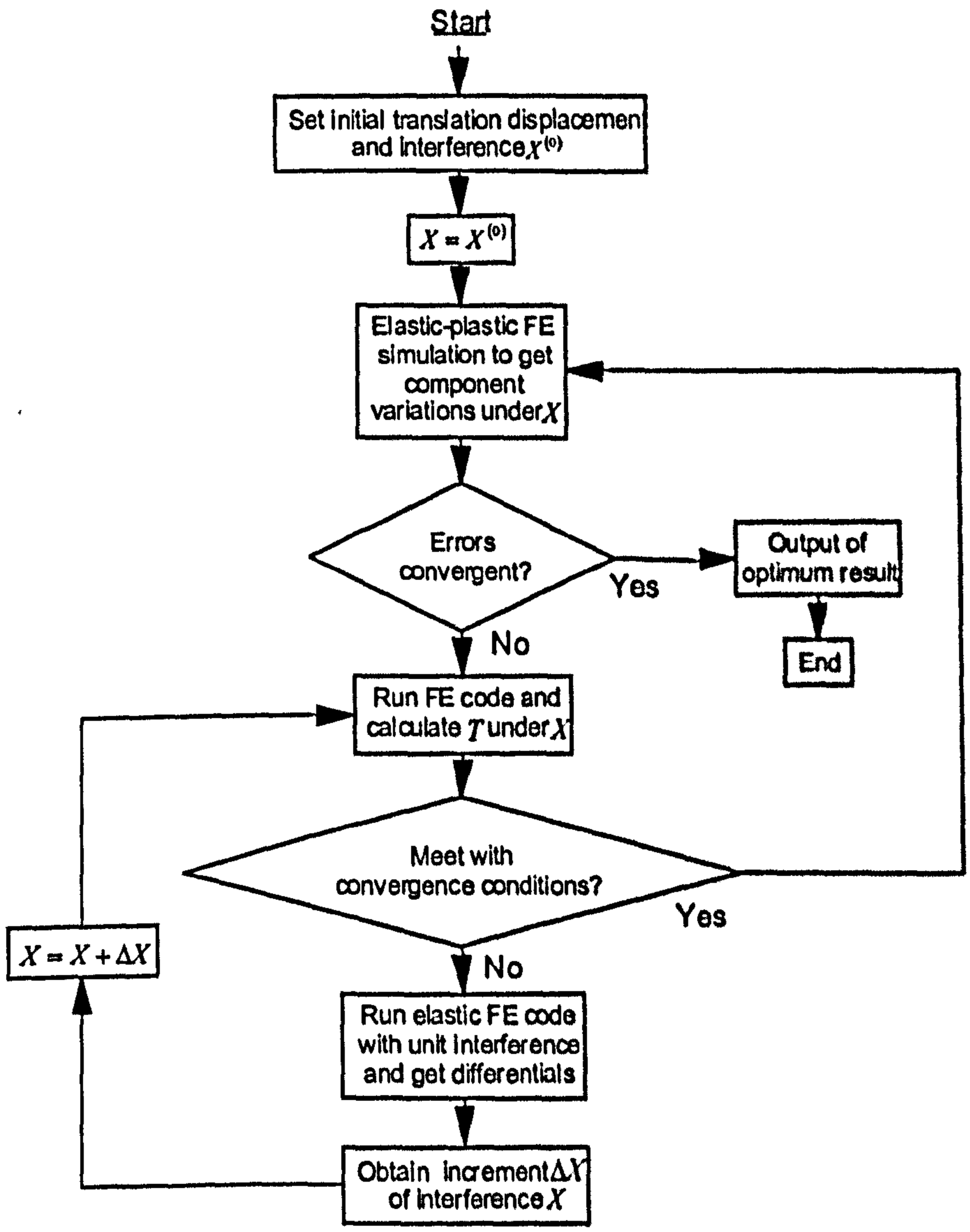

Fig. 6.10 Optimum procedure flow chart

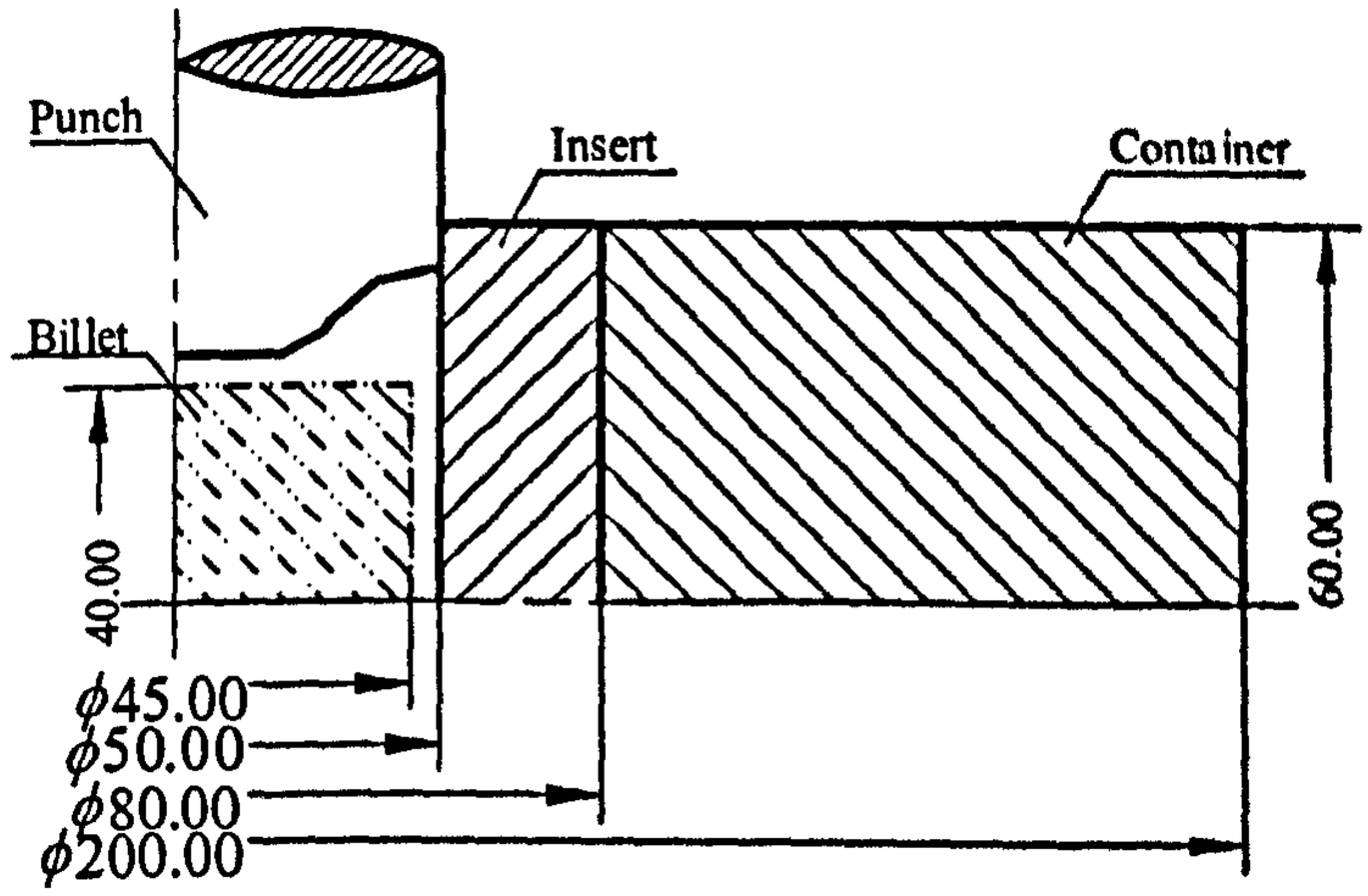

(a) Die diagram of the example

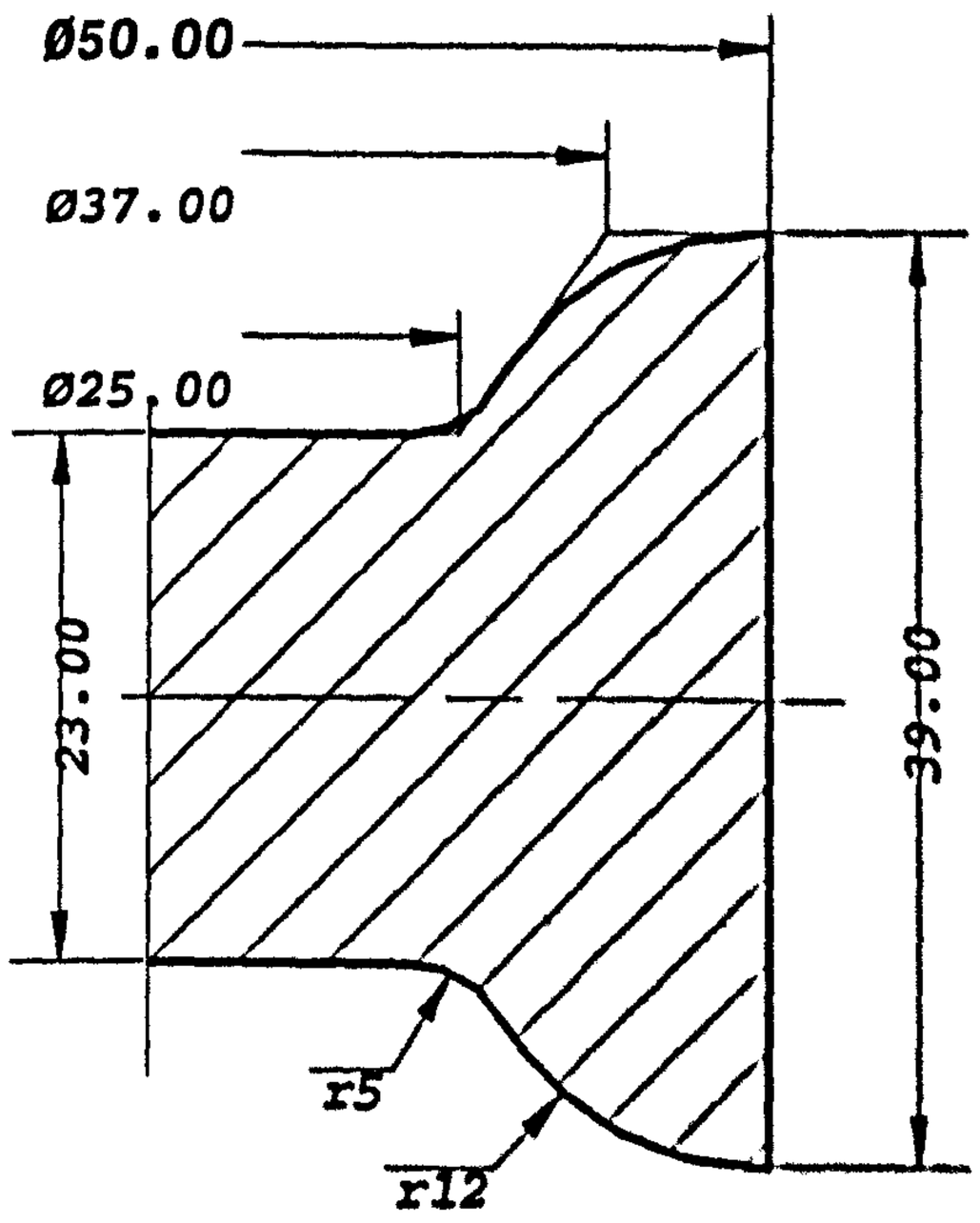

(b) Component geometry

Fig. 6.11 Diagrams of tool configuration and component geometry

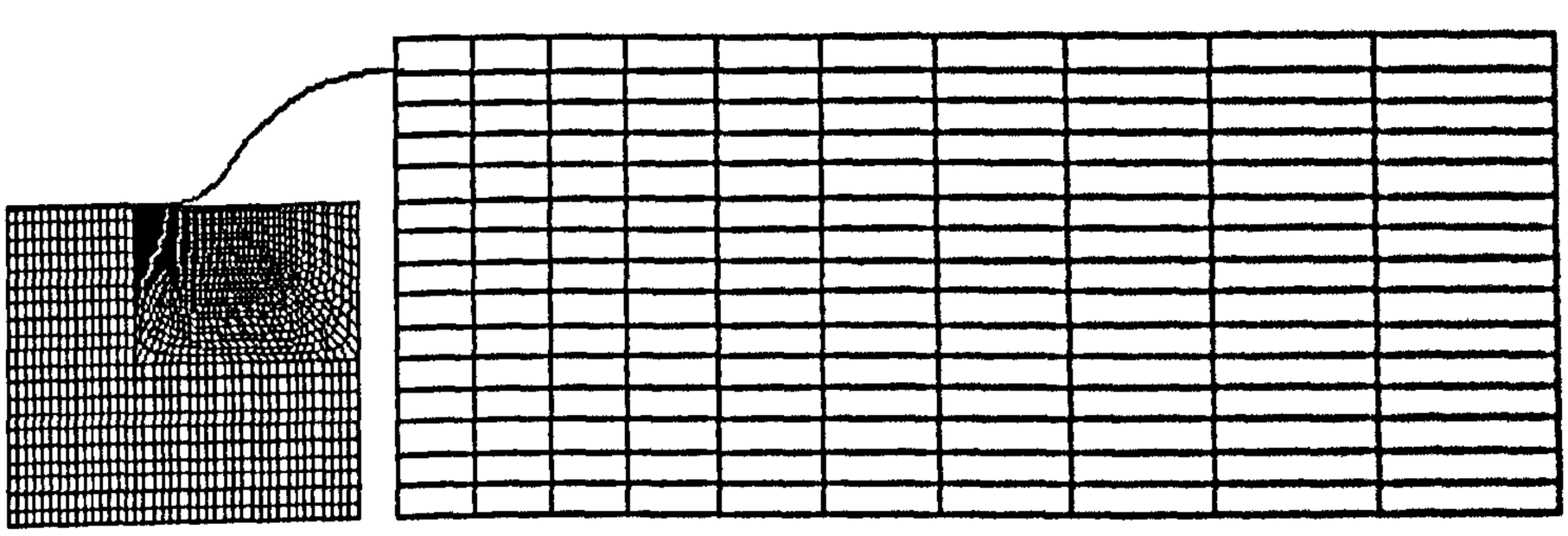

(a) Mesh before deformation

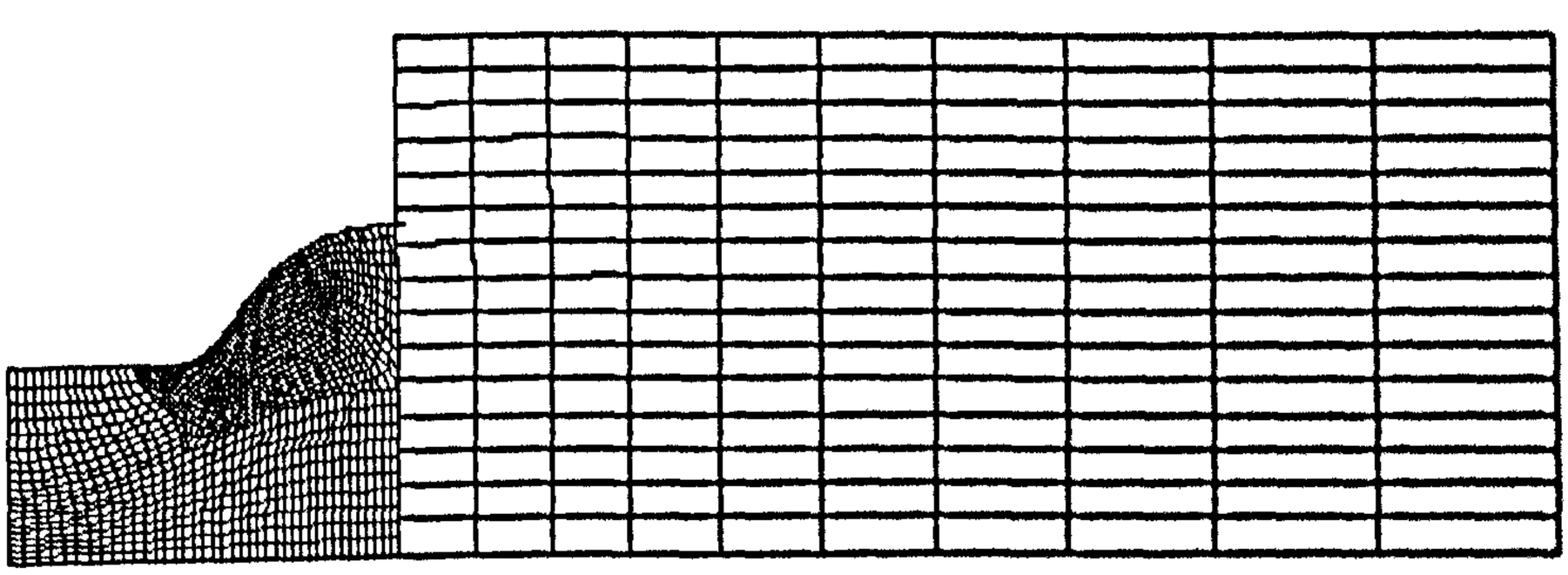

(b) Mesh after deformation

Fig.6.12 Mesh before and after forming

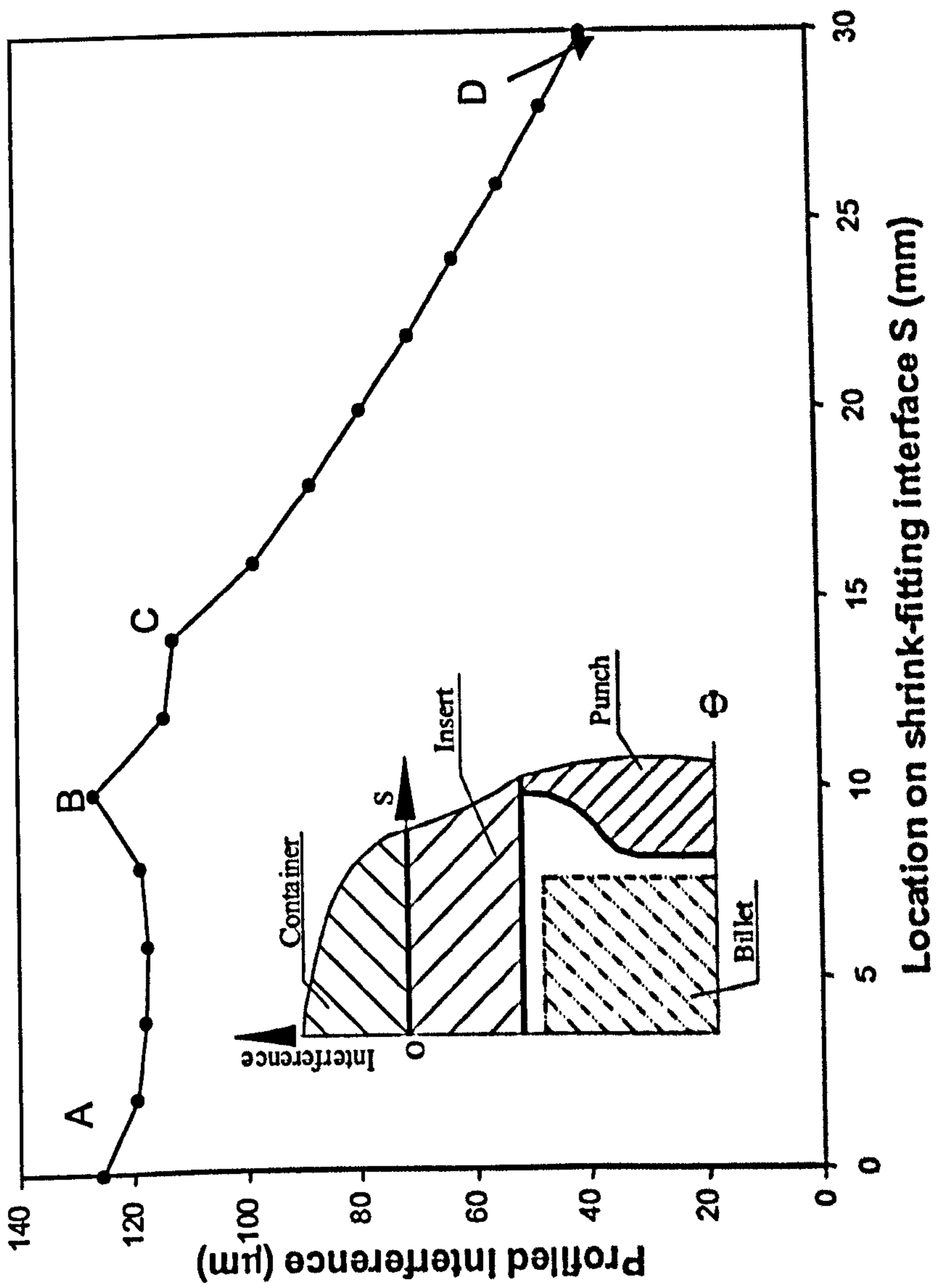

Fig. 6.13 General optimum profiled interference

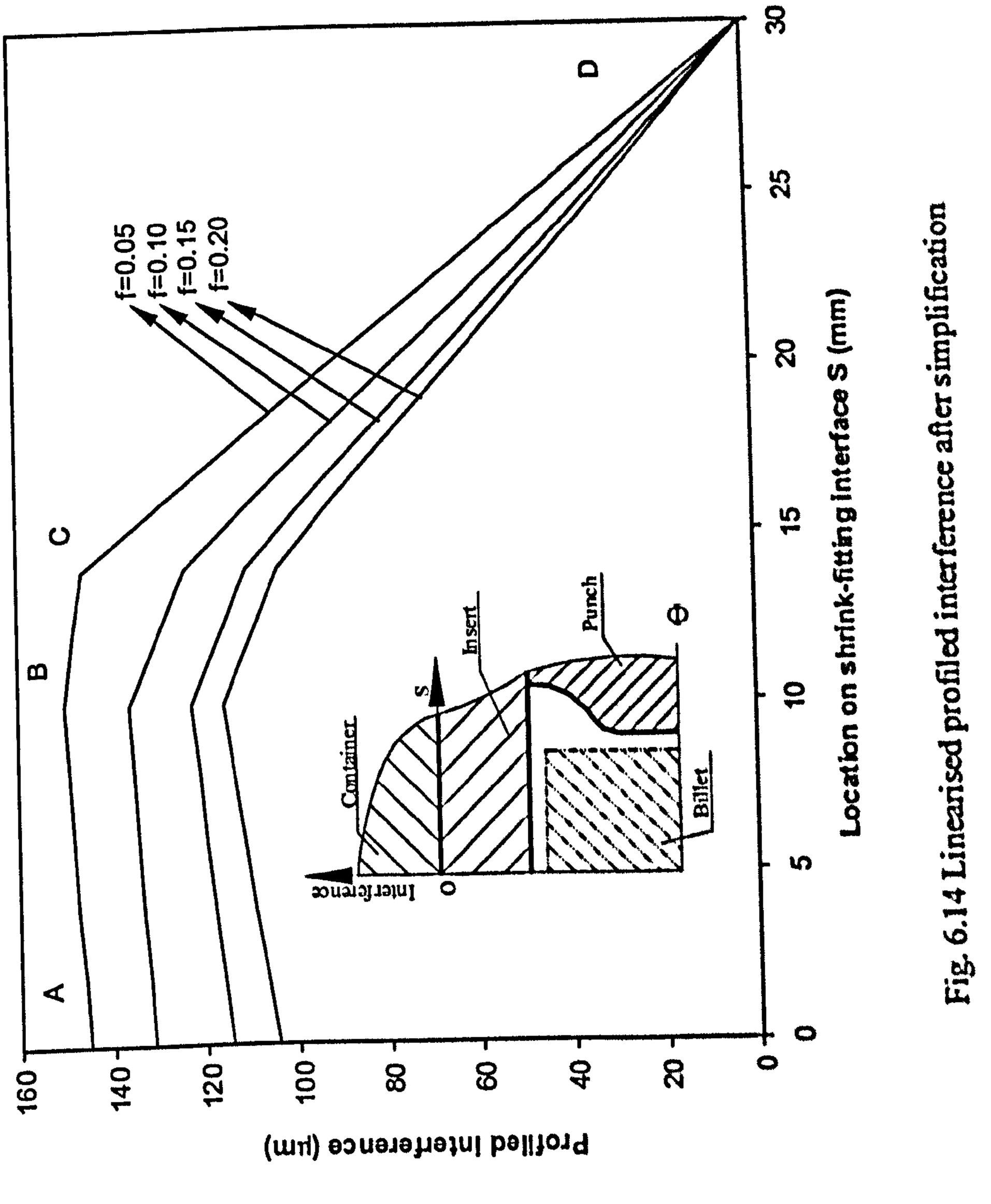

Fig. 6.14 Linearised profiled interference after simplification

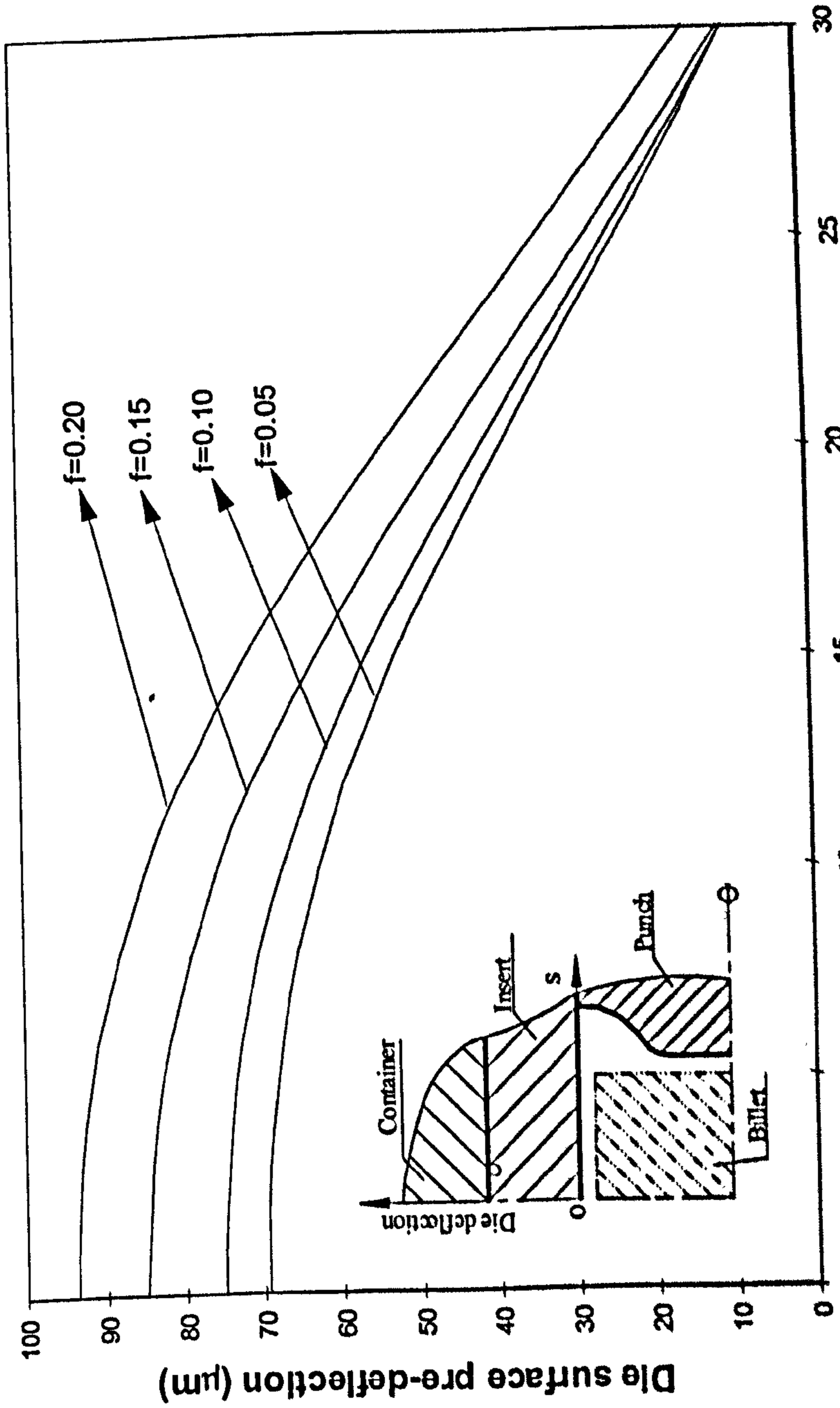

Fig. 6.15 Die deflection without interference

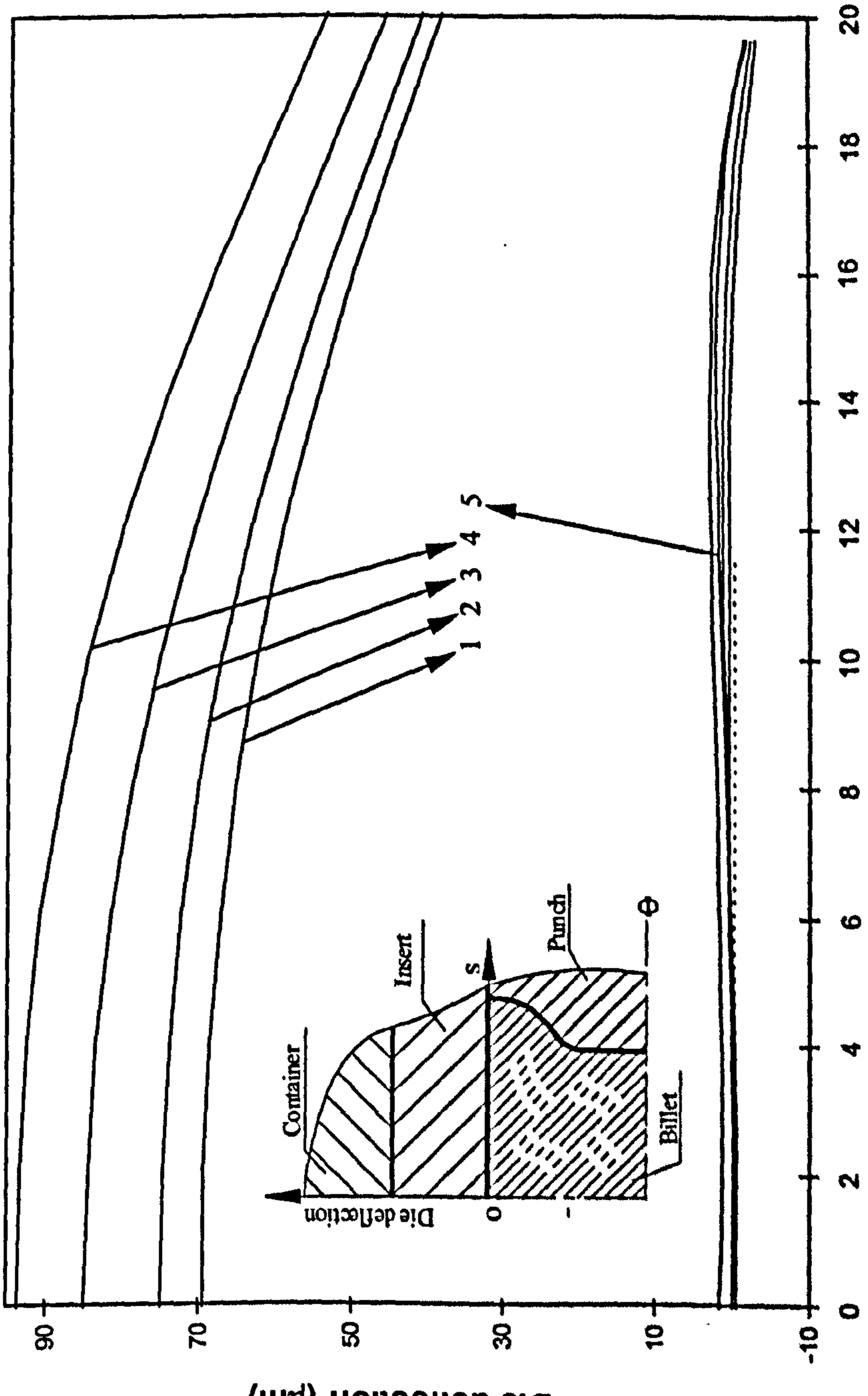

Fig. 6.16 Die deflection comparison

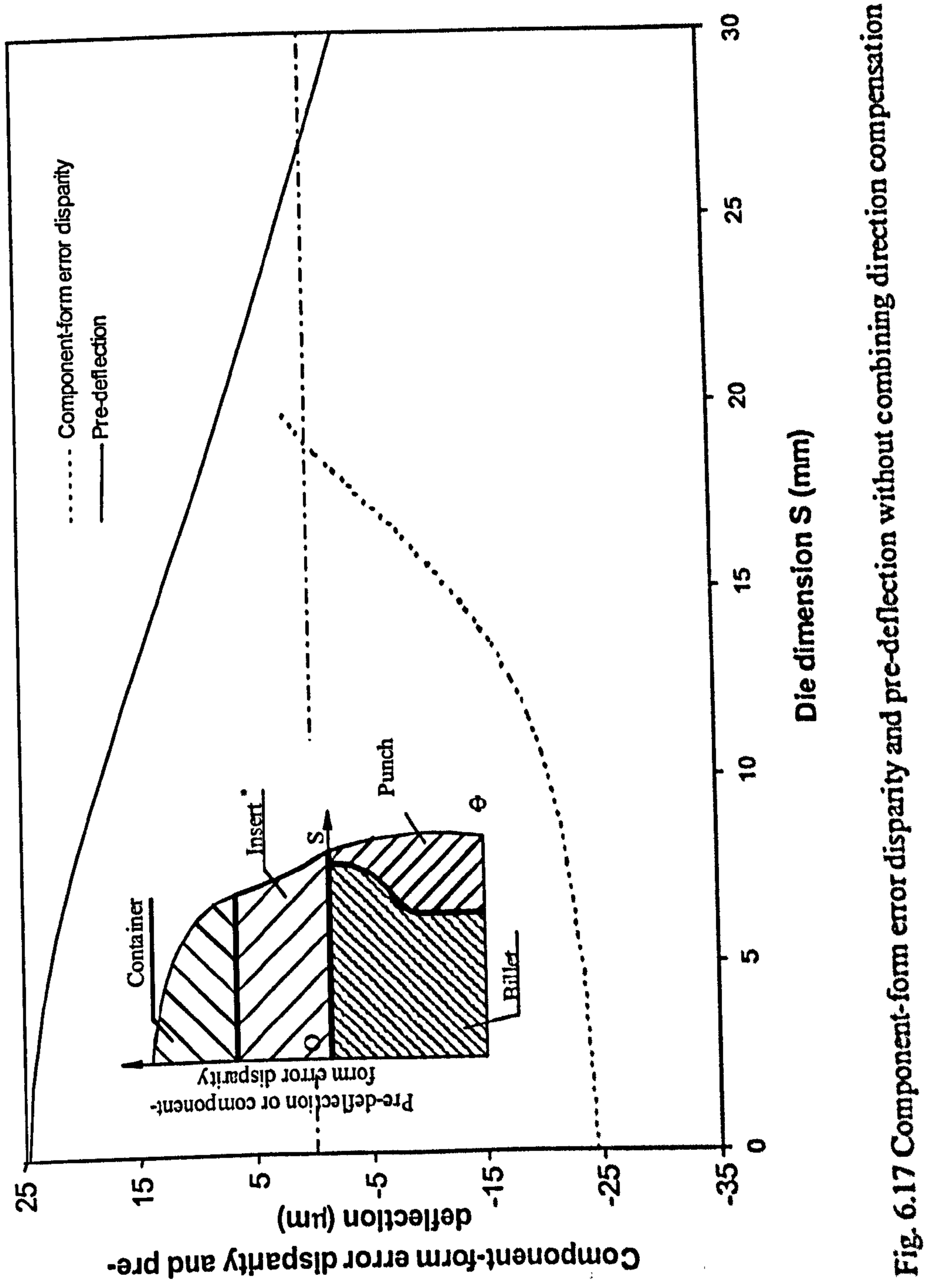

Fig. 6.17 Component-form error disparity and pre-deflection without combining direction com

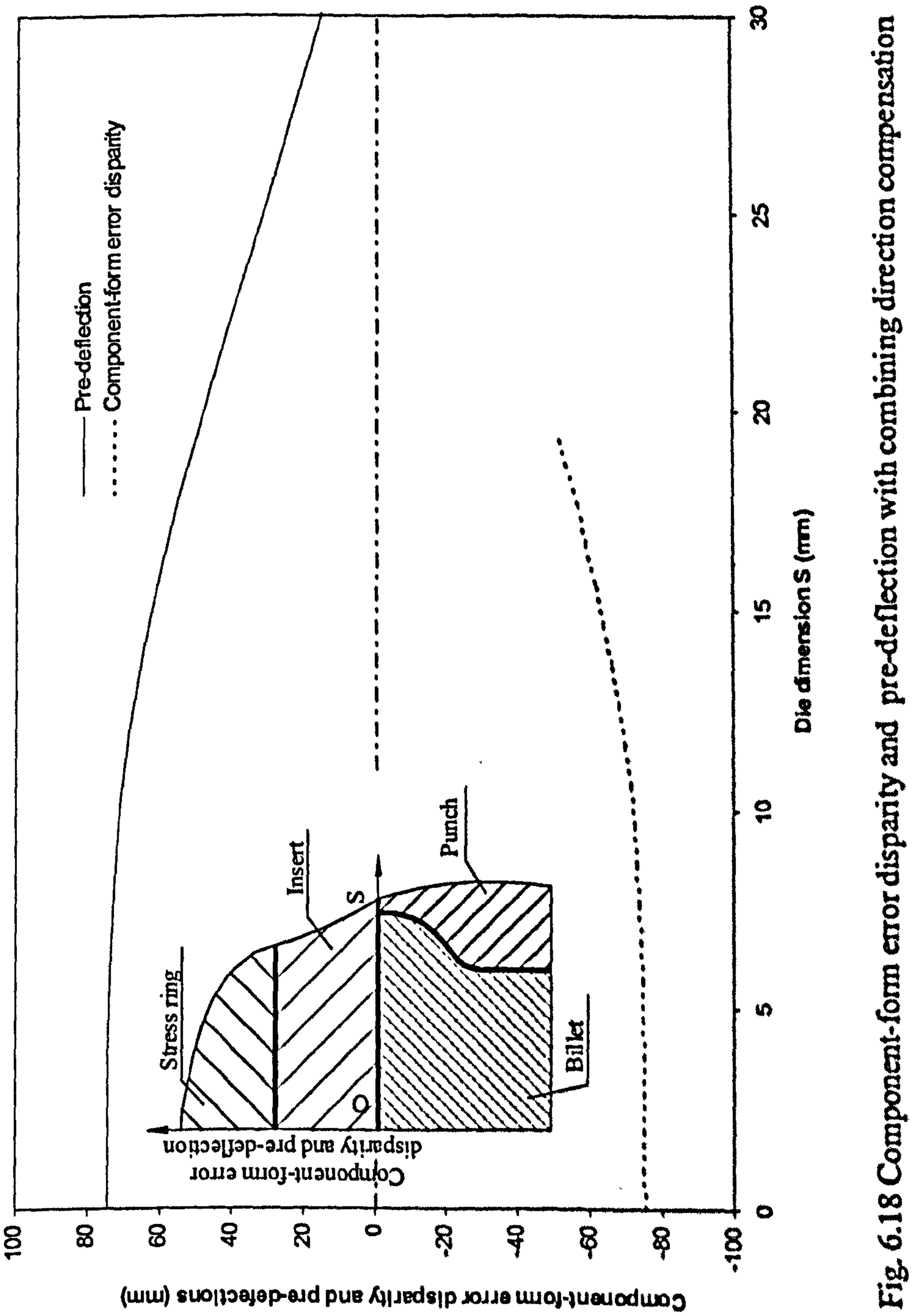

Fig. 6.18 Component-form error disparity and pre-deflection with combining direction compensation

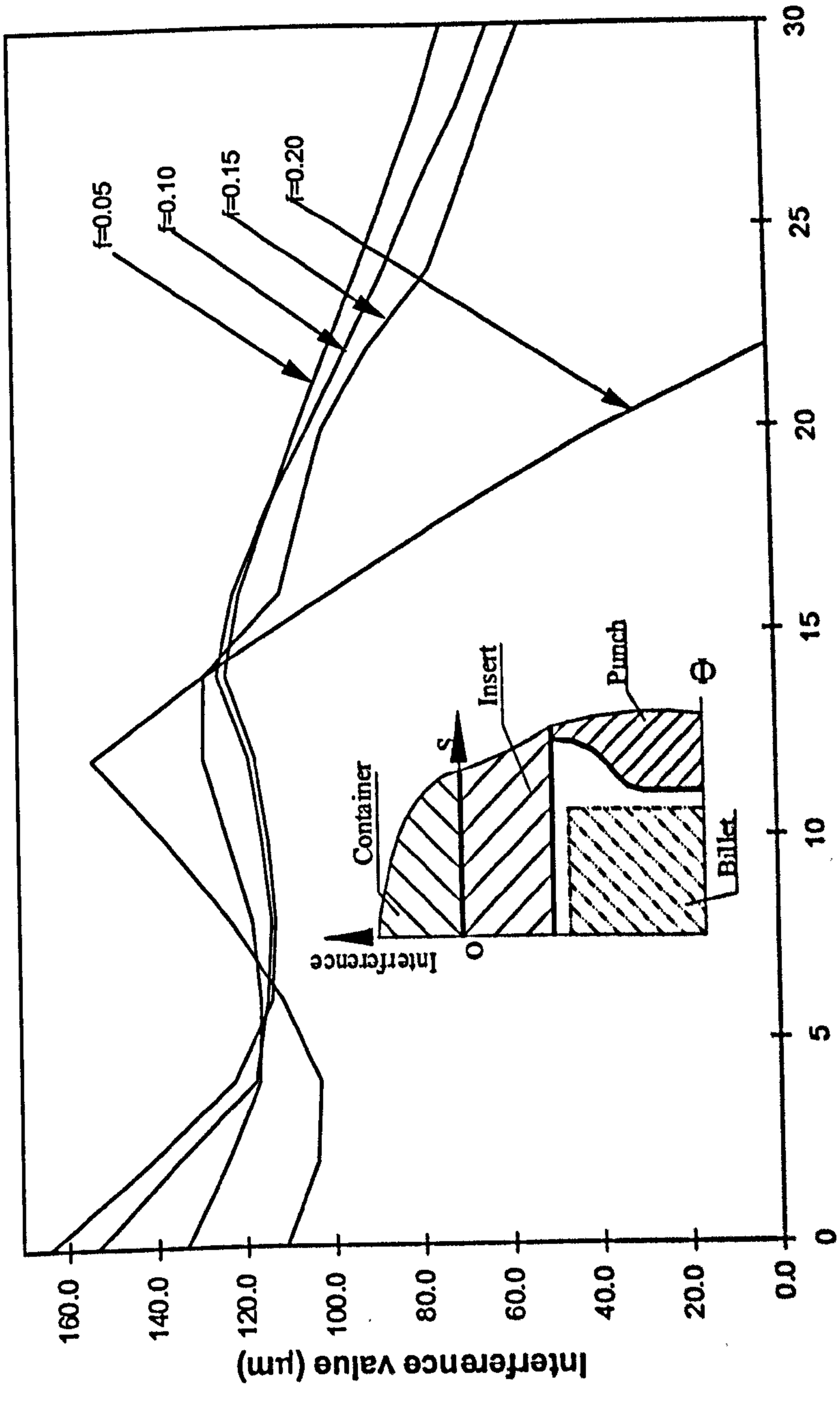

Fig. 6.19 Profiled optimum interference for component-error compensation

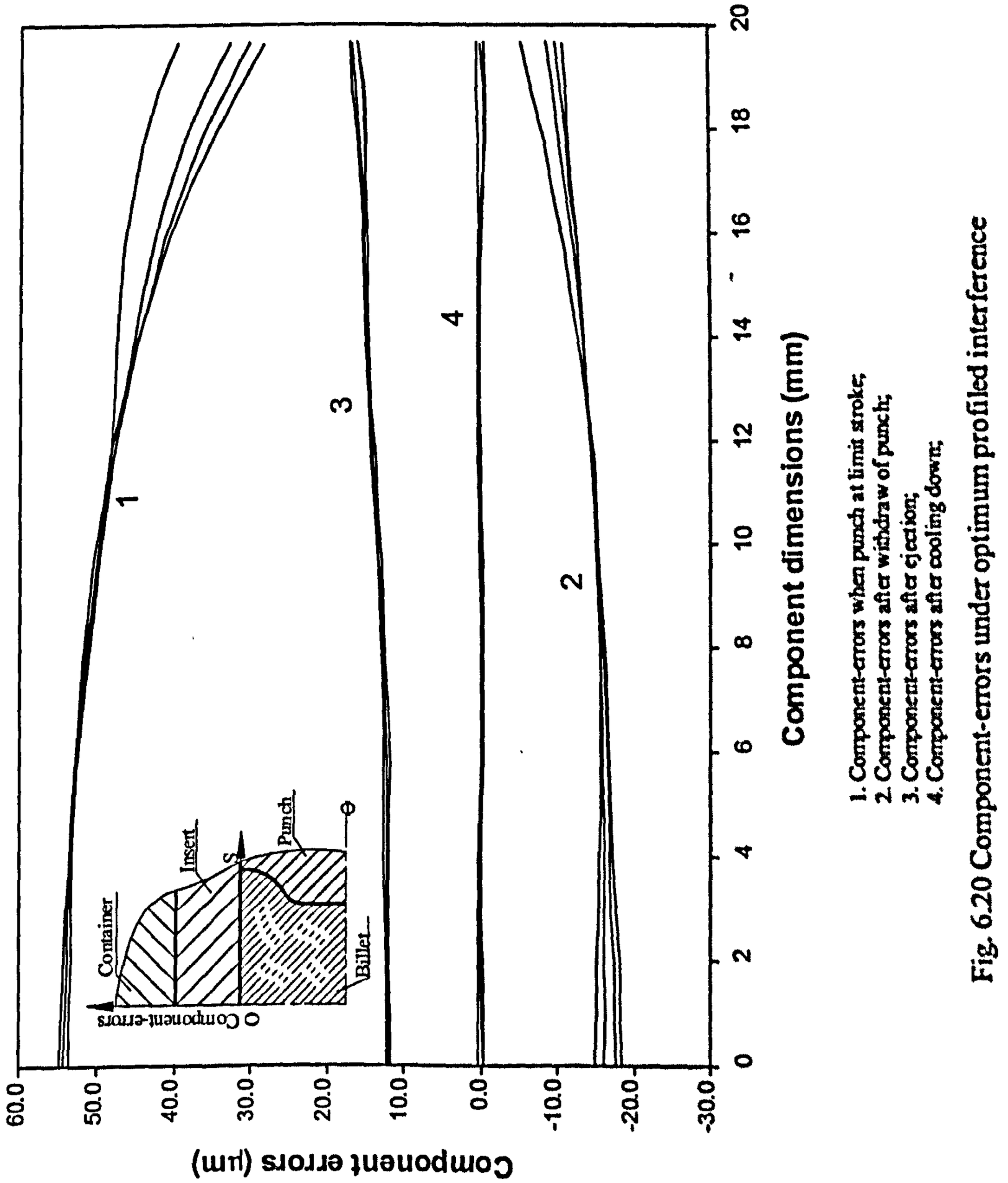

Fig. 6.20 Component-errors under optimum profiled interference

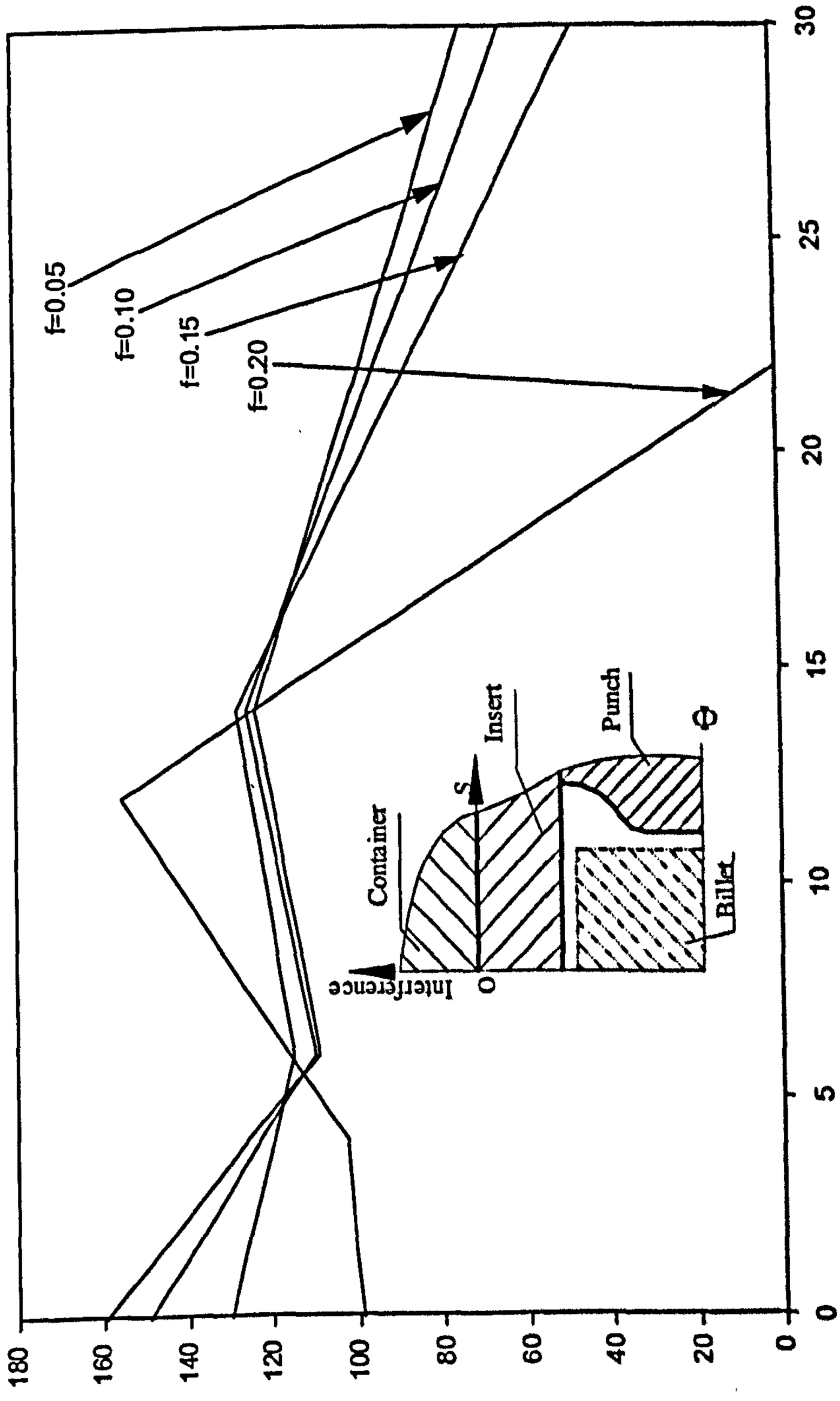

Fig.6.21 Optimum profiled interference with Lineanisation

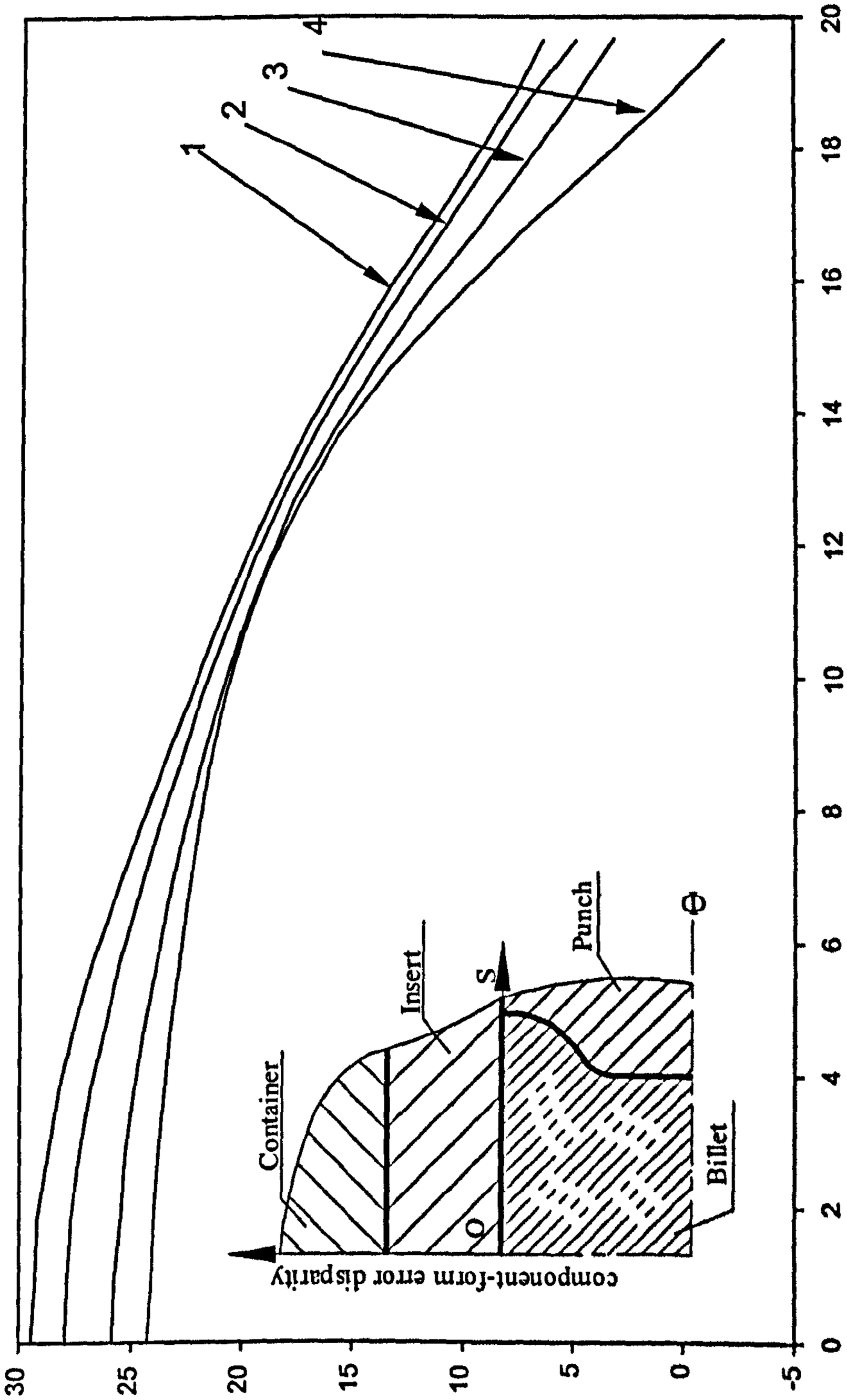

Fig. 6.22 Component-form error disparity under different frictional conditions

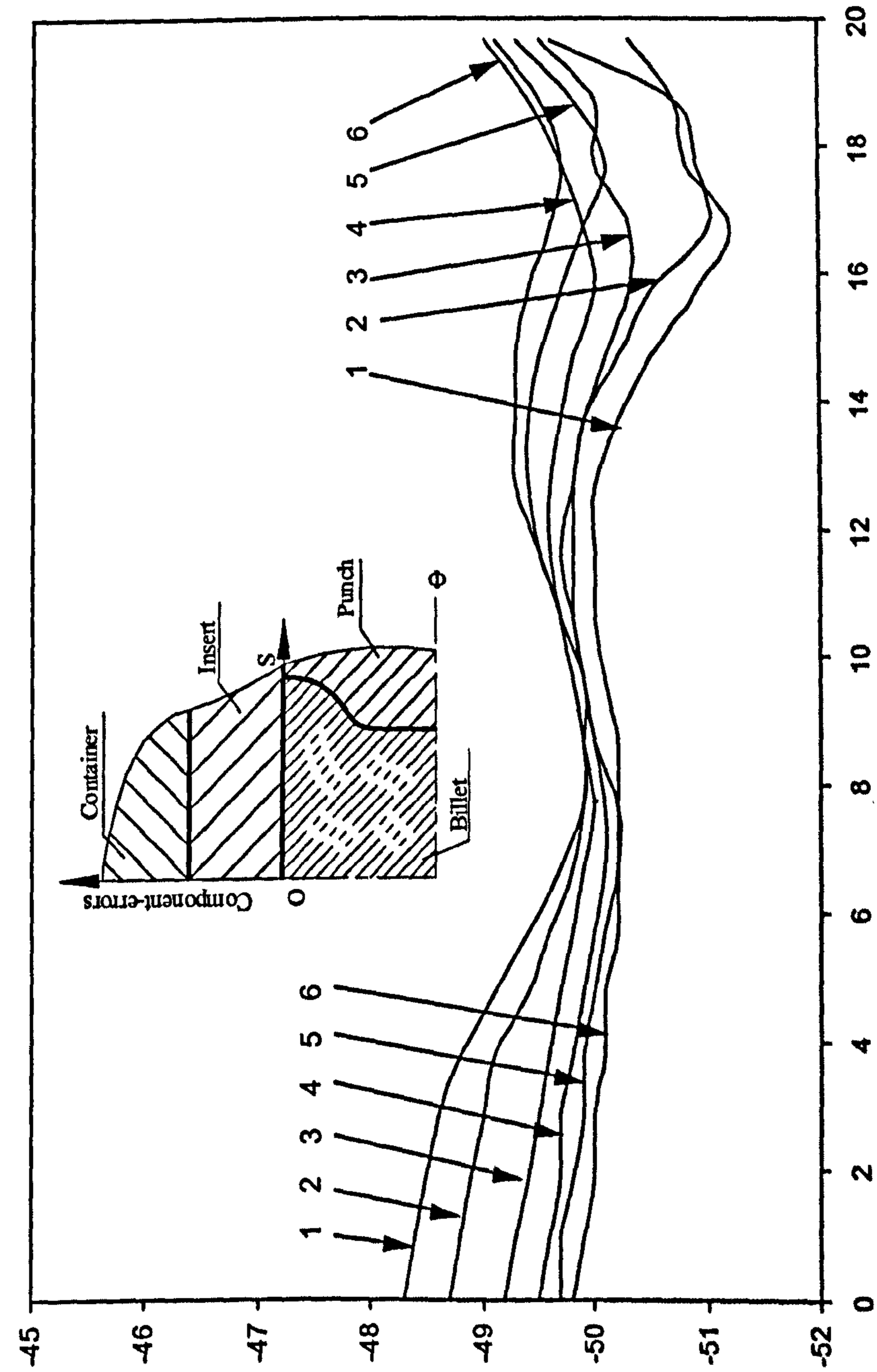

Fig.6.23 Component-errors under different frictional conditions

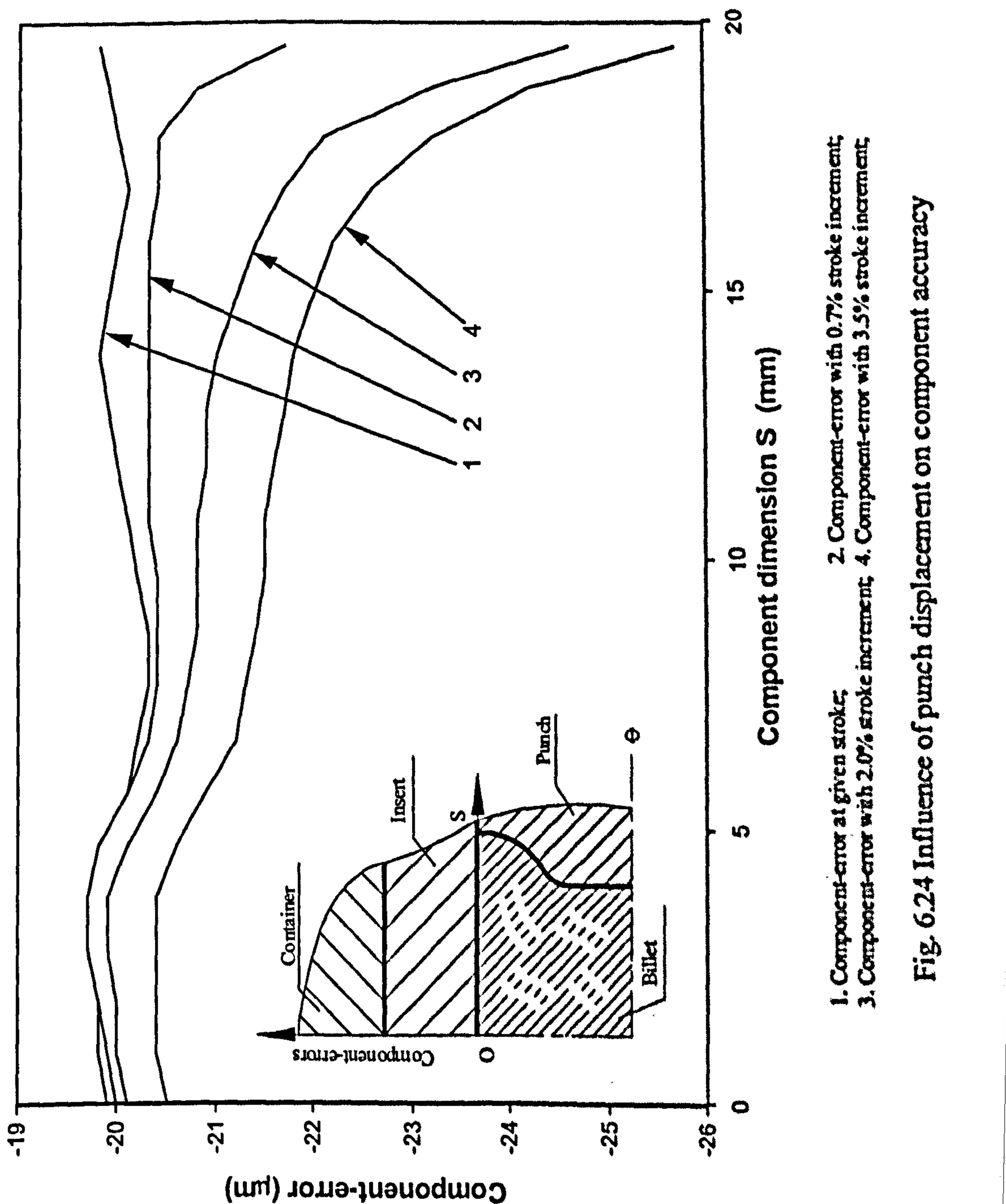

Fig. 6.24 Influence of punch displacement on component accuracy

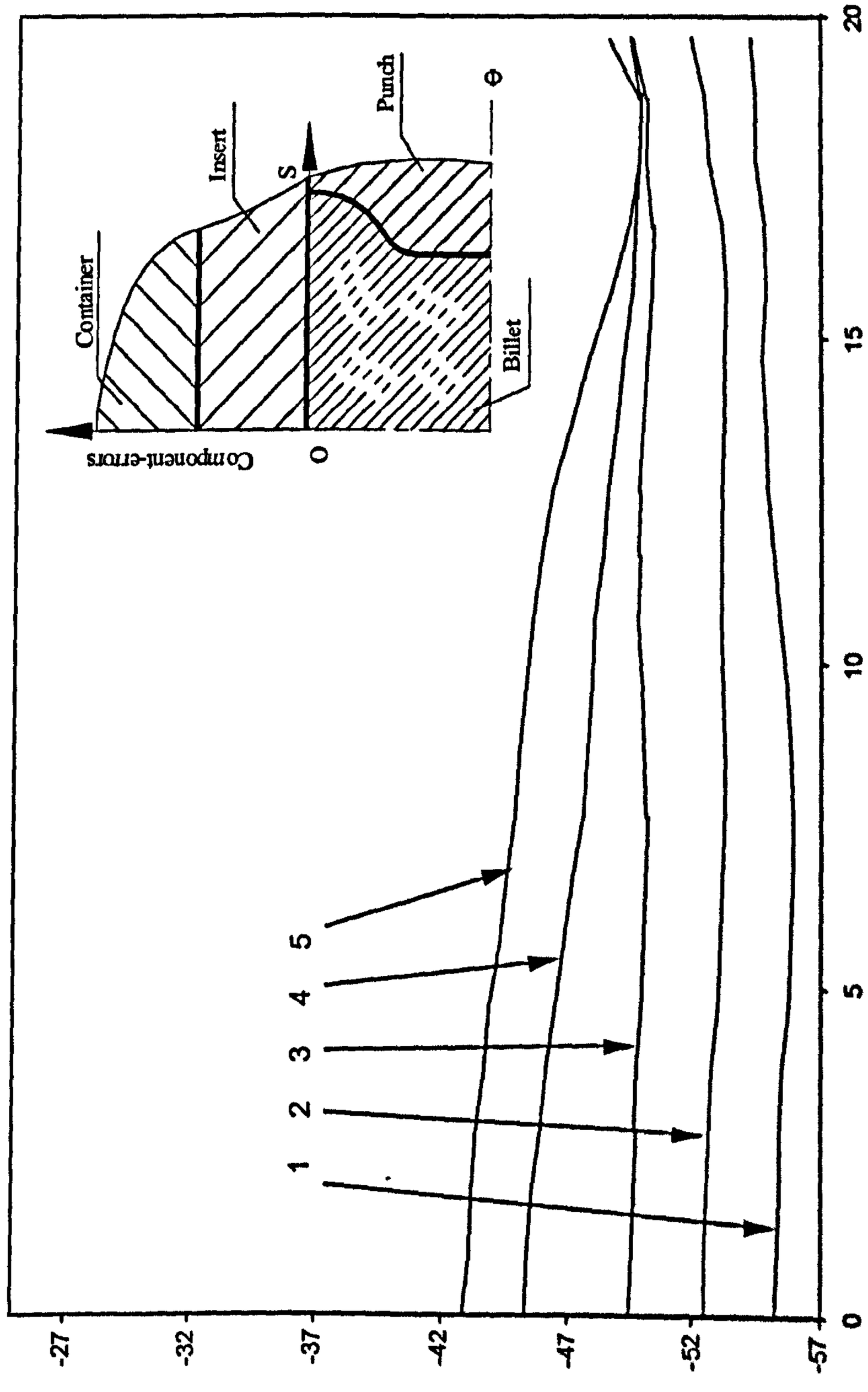

Fig. 6.25 Material property influence on component accuracy

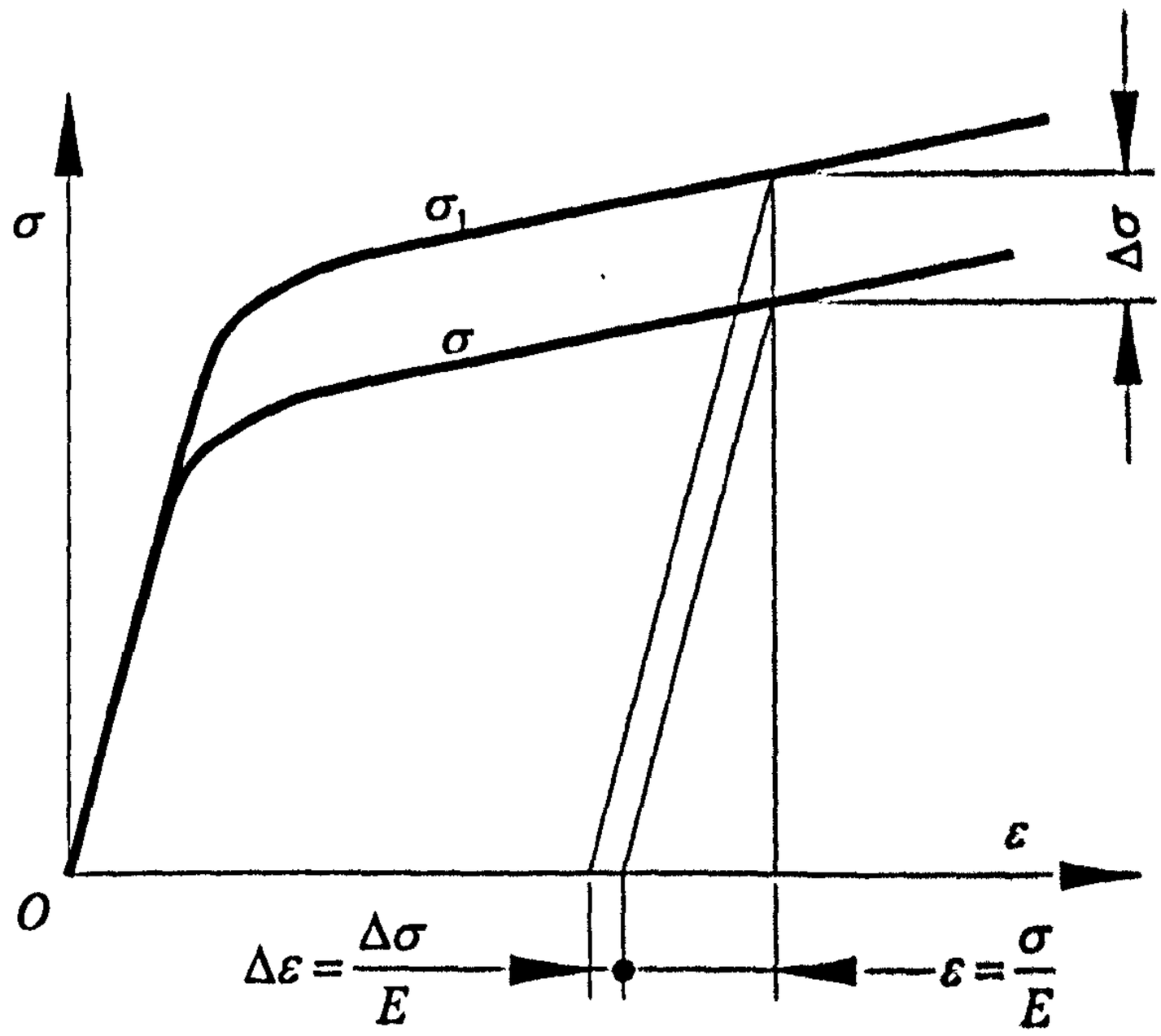

Fig. 6.26 Influence of spring back on component accuracy

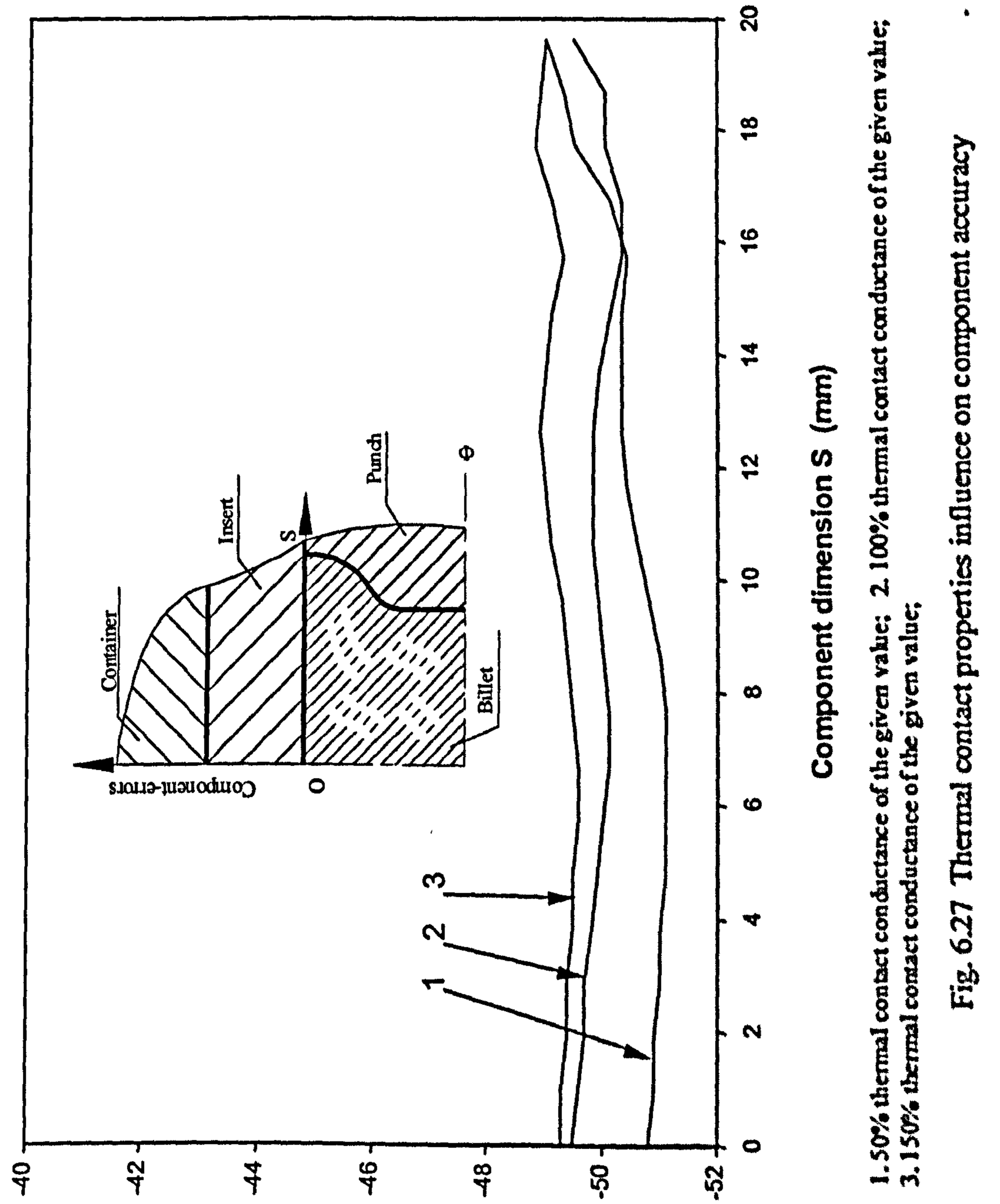

Fig. 6.27 Thermal contact properties influence on component accuracy